Characterization of liquefaction parameters for saturated soil under dynamic loading using laboratory tests and calibration of constitutive laws by numerical modelling

Stefania Gobbi

UNIVERSITÉ PARIS-EST

IFSTTAR

THÈSE DE DOCTORAT DE L'UNIVERSITÈ PARIS EST

Spécialité: **Géotechnique**
Ecole Doctorale: **SIE - Sciences, Ingénierie et Environnement**

par

Stefania GOBBI

Characterization of liquefaction parameters for saturated soil under dynamic loading using laboratory tests and calibration of constitutive laws by numerical modelling

Caractérisation de paramètres mécaniques d'un sol saturé à partir d'essais de laboratoire et calibration de lois de comportement sous charge dynamique par modélisation numérique

Thèse présentée et soutenue le 28 Octobre 2020 devant le jury composé de:

Denis LeBoeuf	Université Laval	Président du Jury, Rapporteur
António Viana Da Fonseca	University of Porto	Rapporteur
Giuseppe Lanzo	Sapienza Università di Roma	Examinateur
Amin Askarinejad	TU Delft	Examinateur
Luca Lenti	Université Gustave Eiffel	Directeur de thèse
Philippe Reiffsteck	Université Gustave Eiffel	Co-Directeur de thèse
Maria Paola Santisi d'Avila	Laboratoire Polytech'Lab	Encadrant de thèse
Jean-François Semblat	ENSTA ParisTech	Encadrant de thèse

Acknowledgements

I would like to express my profound gratitude and sincere thanks to my supervisors, namely Luca Lenti, Maria Paola Santisi d'Avila, Jean-François Semblat and Philippe Reiffsteck, for their wisdom, encouragement, support and patience. They fostered my technical and professional skills. Each of them advised and helped me with his unique way throughout the three years of my thesis.

I would like to thank the members of my thesis committee. Prof. Denis LeBoeuf, Prof. António Viana Da Fonseca, Prof. Amin Askarinejad and Prof. Giuseppe Lanzo. Special thanks to Prof. Denis LeBoeuf and Prof. António Viana Da Fonseca who kindly accepted to be referees and critically appraised my PhD manuscript.

I would like to thank my thesis committee, Fernando Lopez-Caballero and Jean-Claude Dupla, for their time and advices. I would like to extend my appreciation to Prof. Fabian Bonilla for his feedback and encouragement, but also for the numerous fruitful discussions. I would also like to thank Prof. Davide Forcellini, who was the first one to believe and invest in me.

Thanks to all my IFSTTAR colleagues for their company and time spent together. Special thanks to Benoît, Sonia and Roberto for their friendship and coffee breaks. Thanks to Hiba, Chiara, Danilo, Wassim, Carolina, Margot, Quang-Huy and Loren for sharing this journey together during these years. Several people, outside of the IFSTTAR lab, also contributed making this experience unforgettable. Special thanks to my friends in Italy, for their support and their friendship over the years. Special thanks also to Reine for her support during my PhD, especially during the lockdown.

My deepest gratitude goes to my family who have always encouraged and supported me throughout my education.

Characterization of liquefaction parameters for saturated soil under dynamic loading using laboratory tests and calibration of constitutive laws by numerical modelling

---

Abstract

Liquefaction is one of the most devastating instabilities in saturated granular materials and is the major cause of damage to the ground and earth structures during earthquakes. Field observations of liquefaction case histories triggered by strong earthquakes evidence the development of large deformations and strength loss due to the pore water pressure build-up for a broad range of saturated soils. Earlier experimental attempts to study the liquefaction phenomenon of soils date back to the 1960's, nevertheless, soil liquefaction is still one of the most difficult phenomenon to assess, as it is strongly affected by different factors, such as relative density, confining pressure, fine content, overconsolidation, stress or strain amplitude and loading path. Hence, predicting the occurrence of liquefaction of soils is a critical aspect of geotechnical earthquake engineering practice.

The goal of this research is to identify factors affecting liquefaction resistance of silty-sands and investigate their influence on liquefaction susceptibility. To this purpose, in the first part of the work, the behavior of loose, medium and dense silty-sands is analyzed through experimental tests, including monotonic and cyclic consolidated undrained triaxial tests, as well as resonant column tests, using different fine contents and confining pressures. The results show that the behavior of mixtures strongly depends on the packing configuration of coarse and fine particles. The experimental results are analyzed in terms of equivalent intergranular void ratio, which is identified in the literature as an adequate state parameter to characterize the global effect of fine particles. However, the estimation of the equivalent intergranular void ratio requires the determination of the active fine fraction b participating in the force transfer. An original formula is proposed for the b parameter based on packing configuration, thereby allowing a satisfactory prediction of liquefaction triggering in sand-fines mixtures independently from the fine content.

In the second part, the set of laboratory test results are used to calibrate the 3D Iwan-Iai constitutive model for saturated sands, whose main advantage is its small number of geotechnical parameters commonly measured. A parametric study is performed to investigate the effects of the aforementioned factors known to affect liquefaction susceptibility and resistance of silty-sands.

The correlation of liquefaction parameters with the relative density, fine content and confining pressure is proposed.

In the last part of this work, the model parameters obtained by numerical calibration are used in a finite element model, simulating the vertical wave propagation in layered soil profiles, in order to investigate the influence of liquefaction parameters on the seismic response. Then, a dataset of 300 one-dimensional soil profiles are generated through a Monte Carlo method to investigate the reliability and the limit of using the average shear wave velocity in the upper 30 m of the soil profile, as single proxy, to characterize seismic site effects for weak and strong events. Correlations between site-specific amplification factors deduced using the numerical response spectra and other proposed site proxies are analyzed for period ranges and compared to those proposed by different international and national design codes. The results, obtained under assumption of linear and nonlinear behavior of soil, emphasize the need to introduce complementary site parameters proxies to characterize the expected site effects in design response spectra.

Keywords: Silty sand, soil liquefaction, fine content, relative density, confining pressure, equivalent intergranular void ratio, numerical calibration, geotechnical properties, site response.

Caractérisation de paramètres mécaniques d'un sol saturé à partir d'essais de laboratoire et calibration de lois de comportement sous charge dynamique par modélisation numérique

---

Résumé

Le phénomène de liquéfaction est l'une des instabilités les plus dévastatrices des massif sableux saturés et constitue la principale cause de dégâts au sol et aux structures lors des tremblements de terre. Les observations sur le terrain des cas historiques de rupture par liquéfaction déclenchés par de forts tremblements de terre montrent le développement de grandes déformations et la perte de résistance due à l'augmentation de la pression de l'eau interstitielle pour une large gamme de sols saturés. Les premières travaux qui ont permis de mettre en évidence le phénomène de liquéfaction au laboratoire remontent aux années 1960, mais la liquéfaction des sols reste néanmoins l'un des phénomènes les plus difficiles à évaluer, car elle est fortement influencée par différents facteurs, tels que la densité relative, la pression de confinement, la teneur en fines, l'amplitude des contraintes ou des déformations et le chemin de chargement. Par conséquent, la prévision de l'occurrence de la liquéfaction des sols est un aspect essentiel de l'ingénierie géotechnique parasismique.

L'objectif de cette thèse est d'identifier les facteurs affectant la résistance à la liquéfaction des sables silteux et d'étudier leur influence sur la susceptibilité à la liquéfaction. À cette fin, dans la première partie du travail, le comportement des sables limoneux lâches, moyens et denses est analysé par des essais au laboratoire, qui comprennent des essais triaxiaux non drainés monotones et cycliques, ainsi que des essais à la colonne résonante, en utilisant différents teneur en fines et pressions de confinement. Les résultats montrent que le comportement des mélanges dépend fortement des caractéristiques des particules grossières et fines. Les résultats expérimentaux sont analysés en termes d'indice des vides intergranulaire équivalent, qui est identifié dans la littérature comme un paramètre d'état adéquat pour caractériser l'effet global des particules fines. Cependant, l'estimation de l'indice des vides intergranulaire équivalent nécessite la détermination de la fraction fine active b participant au transfert de force. Une formule originale est proposée pour le paramètre b, basée sur l'arrangement des particules, permettant ainsi une prédiction satisfaisante du déclenchement de la liquéfaction dans les mélanges sable-fines indépendamment de la teneur en fines.

Dans la deuxième partie, l'ensemble des résultats des essais de laboratoire est utilisé pour calibrer le modèle constitutif 3D d'Iwan-Iai pour les sables saturés, dont le principal avantage est le nombre limité de paramètres géotechniques couramment mesurés. Une étude paramétrique est réalisée pour étudier les effets des différents facteurs sur la résistance à la liquéfaction des sables limoneux. La corrélation des paramètres de liquéfaction avec la densité relative, la teneur en fines et la pression de confinement est proposée.

Dans la dernière partie de ce travail, les paramètres du modèle obtenus par calibration numérique sont utilisés dans un modèle éléments finis simulant la propagation verticale des ondes dans des profils de sol stratifiés afin d'étudier l'influence de ces paramètres dans la réponse sismique. Ensuite, une base de données de 300 profils de sol est générée par la méthode de Monte Carlo afin d'étudier la fiabilité et la limite de l'utilisation de la vitesse moyenne des ondes de cisaillement dans les 30 m supérieurs du profil de sol, en tant que paramètre unique, pour caractériser les effets de site. Des corrélations entre les facteurs d'amplification et les paramètres de site sont analysées pour différentes gammes de périodes et comparées à celles proposées par différents codes de conception internationaux et nationaux. Les résultats, obtenus dans l'hypothèse de comportement linéaire et non linéaire du sol, soulignent la nécessité d'introduire des paramètres de site complémentaires pour mieux caractériser les effets de site dans les spectres de réponse de conception.

Mots clés: Sable silteux, liquéfaction du sol, teneur en fines, densité relative, pression de confinement, indice des vides intergranulaire équivalent, calibration numérique, propriétés géotechniques, réponse du site.

Contents

List of Figures

List of Tables

Notations and abbreviations

For the sake of brevity, the notations and abbreviations are described by its most common meaning in the present thesis, however, some symbols were not included in this list because they concern single cases.

Latin alphabet

a_g	surface peak ground acceleration
a_{gR}	peak ground acceleration
b	fraction of active fines
B	Skempton coefficient
B_{30}	shear wave velocity gradient
C_u	coefficient of uniformity
c_1	liquefaction parameter (Iai model parameter)
c'	cohesion
D	soil damping
D_{min}	minimum damping ratio
D_R	relative density
$D_{R,cs}$	critical relative density
dt	time step
D_{50}	mean grain size of sand
d_{50}	mean grain size of fine
D_{10}	size of sand at 10% finer
e	void ratio
e_{cs}	critical void ratio
e_g	intergranular void ratio
e^*_{cs}	equivalent intergranular critical void ratio
e^*_g	equivalent intergranular void ratio
e_{max}	maximum void ratio
e_{min}	minimum void ratio
f	frequency
FC	fine content
FC_{th}	fine content threshold
$f(e)$	void ratio function
f_{max}	maximum frequency
f_0	site dominant frequency
G	shear modulus

G_0 or G_{max}	maximum shear modulus
h_i	thickness of the i-th soil layer
H_{800}	shear wave velocity reaches 800m/s
K_σ	overbudden correction factor
m_1	failure line slope (Iai model parameter)
m_2	phase transition line slope (Iai model parameter)
m_3	reduced phase transition line slope (Iai model parameter)
M_w	moment magnitude
N	number of cycles
N_L	number of cycles required to reach liquefaction
p	mean stress
P_a	atmospheric pressure
PSA	acceleration spectrum
PSV	velocity spectrum
p_1	liquefaction parameter (Iai model parameter)
p_2	liquefaction parameter (Iai model parameter)
p'	mean effective stress
p'_0	initial effective stress
q	deviatoric stress
q_{cyc}	cyclic deviatoric stress
q_{cr}	critical deviatoric stress
r	deviatoric stress ratio (Iai model parameter)
R^2	Coefficient of determination
$RMSD$	root mean square deviation
r_u	excess pore water pressure ratio
S	state variable (Iai model parameter)
SA	spectral amplification factor
SA_L	spectral amplification factor for long periods of vibration
SA_M	spectral amplification factor for middle periods of vibration
SA_S	spectral amplification factor for short periods of vibration
S_S	soil amplification factor
SV	spectral velocity factor
SV_L	spectral velocity factor for long periods of vibration
SV_M	spectral velocity factor for middle periods of vibration
SV_S	spectral velocity factor for short periods of vibration
S_0	limit value of liquefaction front (Iai model parameter)
S_1	liquefaction parameter (Iai model parameter)
t	time
T	period
T_{VA}	period of equivalent harmonic wave
T_0	dominant period of the soil

u	pore water pressure
u_0	initial pore water pressure
v_{gR}	peak ground velocity
v_p	p-wave velocity
v_s	shear wave velocity
v_{sb}	bedrock shear wave velocity
v_{si}	shear wave velocity in the i-th soil layer
$v_{s,30}$	average shear wave velocity in the upper 30 meters
w	normalized shear work (Iai model parameter)
dW_{se}	elastic shear work (Iai model parameter)
w_1	liquefaction parameter (Iai model parameter)
z	depth

Greek alphabet

α	angle related with the failure line slope
α_P	angle related with the phase transformation line slope
Δu	excess pore water pressure
ε_a	axial strain
ε_v	volumetric strain
η	effective stress ratio
η_{IS}	instability effective stress ratio
γ	shear strain
γ_{ref}	reference shear strain
ν	Poisson ratio
ϕ_{car}	characteristic angle
ϕ'	internal friction angle
ϕ'_P	phase transformation angle
ρ	soil density
ρ_b	bedrock density
σ	total stress
σ_{max}	maximum principal stress
σ_{min}	minimum principal stress
σ'	effective stress
σ'_c	initial effective stress
τ	shear stress
τ_{cyc}	cyclic shear stress

τ'	effective shear stress
χ	particle size ratio
Ψ	state parameter
Ψ^*	equivalent state parameter

Abbreviations

ADVDCSS	ADVanced Dynamic Cyclic Simple Shear
CGS	Coarse Grains Sand contact
CRR	Cycliv Resistance Ratio
CSL	Critical State Line
CSR	Cyclic Stress Ratio
CTU	Consolidated Undrained Triaxial
CTX	Cyclic TriaXial
CU	Consolidated Undrained
CV	Coefficient of Variation
EGCSL	Equivalent Granular Critical State Line
FEM	Finite Elements Model
FF	Free Field
ITACA	Italian Strong Motion Database
ISESD	European Strong Motion Database
L	Linear
LS	Liquefiable Soil
MPII	Masing-Prandtl-Ishlinskii-Iwan model
NL	Non-Linear
NLS	Non-Liquefiable Soil
PEER	Pacific Earthquake Engineering Research Center
PI	Plastic Index
PSA	Pseudo-Spectra of Acceleration (or acceleration response spectra)
PSV	Pseudo-Spectra of Velocity
RC	Resonant Column
SD	Standard Deviation
SFFS	Sand-Fine-Fine-Sand contact
SFS	Sand-Fine-Sand contact
SSL	Steady State Line
TF	Transfer Function

Chapter 1

Introduction

1.1 Motivation

Characterizing the potential effect of local site conditions on the amplification of ground motions is a critical aspect of seismic hazard and risk assessment. Recent and past earthquakes, such as 1985 Mexico City, 1989 Loma Prieta, 1994 Northridge, 1995 Kobe events, among others, underline the need to characterize the effect of the local soil conditions on seismic site response prediction. It has been widely recognized that the seismic site effects are generally related to the stratigraphy, the surface topography, the impedance contrast and the rheology of the soils involved during the propagation of seismic waves. However, such detailed effects are not taken into account in building codes, where amplification factors depend only on the intensity of the motion, the period of interest and some information of the soil deposit, often limited to the average shear wave velocity in the upper 30 meters ($v_{s,30}$). Additionally, field historical cases, past experimental and numerical studies evidence that granular soils exhibit nonlinear behavior under cyclic loading, which may lead to a sudden change in shear modulus and material damping, hence to a significantly loss in its strength. Moreover, the stiffness of granular saturated soils may change further due to excess pore water pressure generation under undrained cyclic loading, and may induce phenomena such as cyclic mobility and liquefaction.

Soil liquefaction phenomenon has been identified as one of the main causes of damage to land and structures, serious lives and economic loss during earthquakes. Liquefaction is defined in the literature as the phenomenon of seismic generation of excess pore water pressures and consequent softening of granular soils. Although several important achievements in the characterization of soil liquefaction have been accomplished over the decades, liquefaction assessment can be challenging. In particular, whether or not liquefaction is triggered largely depends on various factors, such as relative density, confining pressure, fine content, overconsolidation, stress or strain amplitude, type and frequency of loading. To this regard, accurate liquefaction assessment is essential to enhance the seismic safety of existing

and new structures, but the factors affecting liquefaction are often difficult to measure or predict, and thus liquefaction analyses may lead to contradictory results.
Uncertainties are introduced into liquefaction assessments from many sources. For instance, the in situ or laboratory test methods used to evaluate soil liquefaction resistance introduce uncertainties given the lack of fully standardized protocols for their use, as well as the additional uncertainties of the influence of earthquake characteristics (e.g. magnitude, intensity and duration) and the soil site profile properties (e.g. in situ effective confining stress, amount of fine particles in the soil). That shows how much field and laboratory test data are important for the improvement, calibration, and validation of the different approaches to predict liquefaction triggering and its consequences.

Recent earthquake case histories, such as 2010 Darfield and 2016 Ecuador earthquakes, reveals that deposits of uniform, clean sand are rare and natural soils at liquefaction sites are mostly silty sands and sandy silts, and thus also sites containing a significant percentage of finer grains can liquefy during seismic loading. Although the influence of fines content on the liquefaction potential of silty sand has been the topic of numerous experimental researches over the past decades, literature regarding the role of non-plastic fines on the undrained behavior of silty sand mixtures is still confusing. It has been widely recognized that the presence of silt particles may affect the mechanism of resistance distribution in clean sand, but there is a need for understanding the undrained response of silty sand under seismic loading and laboratory testing plays an important role in this regard.

An other source of uncertainties is associated with the application of numerical methods to predict soil liquefaction. To this regard, advanced constitutive models can be used to solve different geotechnical problems, however, their capability in representing cyclic soil behavior depends largely on the accuracy of the constitutive relations and input parameters employed. Thus, these computational models need to be supplemented by laboratory and field data in order to better understand key aspects of the behavior of soils before and subsequent to liquefaction triggering and clarify limitations of models.

Lastly, seismically-induced soil liquefaction may alter the characteristics of shear wave propagation at a site, however, these effects are not included in current site amplification factors and building codes. In geotechnical engineering practice, the complexity of liquefaction phenomena are currently

estimated through semi-empirical methods based on field reconnaissance or by simulations of the soil response. Nevertheless, empirical approaches cannot take into account all of the effects due to site-specific geology and topography, engineered structure configurations, and ground motion characteristics and hence computational models are recommended to assess liquefaction problems, such as the deformation and pore-pressure response of a soil deposit with an overlying structure subjected to dynamic loading.

Hence, a robust validation of non-linear behaviour models during seismic loading and a more precise knowledge of the expected seismic response are necessary to reduce the seismic risk and improve the earthquake engineering practice in the prediction of potential damage to structures.

1.2 Objectives

The goal of this thesis is to identify the factors affecting liquefaction resistance of silty-sands, investigate their influence on liquefaction susceptibility, and to advance towards a better understanding of soil behavior under dynamic loading via experimental tests and numerical modeling. In particular, this work focuses on liquefaction evaluation through the calibration of constitutive models. To this purpose, a laboratory testing program, including monotonic and cyclic consolidated undrained triaxial tests, as well as resonant column tests, is carried out on sandy soil in order to produce a wide set of data for the same soil type, under different conditions, to define a standardized experimental program and to overcome previous difficulties on the characterization of the behavior of silty sand with respect to clean sand.
In pursuit of the main objective, several subordinate objectives are also addressed:

- Analysis of the effects of various parameters, such as relative density, confining pressure, fine content and rate of the loading, on the undrained behavior of silty sand under static and cyclic loading;

- Investigate the main factors affecting the binary packing of mixtures and the b value, representing the fraction of fines actively participating in the mechanical resistance of the solid skeleton, in order to reduce the complexity for predicting the behavior of fines-sand mixtures;

- Calibration of a constitutive soil model based on different laboratory test results and definition of correlations between model parameters and soil parameters;

- Parametric analyses of the seismic response of 1D columns considering different hazard levels and various stratigraphic conditions.

1.3 Outline

This research can be divided into three main parts. The first part of this work is devoted to show the effect of relative density, confining pressure, fine content and rate of the loading on the undrained behavior of silty-sand mixtures under static and cyclic loading. To this regard, an experimental program is undertaken using reconstituted samples of silty sand mixtures to understand how fine particles contribute to the mixture strength in undrained conditions. Monotonic and cyclic triaxial tests and resonant column tests are carried out using HN31 Hostun sand and various amounts of commercial Silica C500 fines. Different relative densities are selected to investigate loose, medium and dense soils. Fine content is varied below a threshold of 20% to considered mixtures having sand-dominated behavior. Initial confining pressure is modified to consider the liquefaction susceptibility at different depths. A detailed characterization of the static and dynamic properties of the analyzed mixtures is obtained.
The second part is focused on the calibration process of 3D Iwan-Iai constitutive model through the set of laboratory tests of each soil type. This elasto-plastic constitutive model with hardening, pressure-dependent through Iai's correction of the shear modulus is able to model the cyclic behavior of saturated soil and to predict cyclic mobility and liquefaction of sands when undrained conditions are supposed.
Lastly, in the third part, the influence of model parameters on the site amplification is investigated. First, the effect of liquefaction numerical parameters on the seismic response is investigated via the simulation of nonlinear 1D wave propagation in layered soil profiles. Then, a dataset of 300 one-dimensional soil profiles is generated through a Monte Carlo method in order to assess the correlation with the site amplification of some site parameters, with the aim of improving the expected ground motion prediction.

More in particular, the thesis consists of seven chapters, which can be briefly described as follows.
Chapter 1 presents an introduction on this research work.
Chapter 2 presents a literature review on the undrained response of satured granular soils, in particular on the liquefaction phenomena, via experimental test and numerical modeling. This chapter highlights the performed works on the main factors affecting soil liquefaction.

Chapter 3 presents the experimental program, the material tested and the test devices and experimental techniques adopted in this work.
Chapter 4 discusses the experimental results on the undrained behavior of silty soils. In particular, the behavior of loose, medium and dense mixtures is analyzed, using different fine contents and confining pressures. Equivalent intergranular void ratio concept is used to discuss the observed experimental results. Furthermore, an original formula is proposed for the evaluation of the equivalent intergranular void ratio parameter.
Chapter 5 assesses the influence of relative density, confining pressure and fine content on the liquefaction numerical parameters characterizing the soil behavior according to the extended 3D Iwan-Iai model. Correlations between these factors and the numerical parameters are proposed. In the second part of this chapter, the soil data obtained by numerical calibration are used in a finite element model simulating the vertical wave propagation in a horizontally layered soil (in free-field conditions). The influence of liquefaction parameters on the seismic response of soil profiles is discussed.
In Chapter 6, a dataset of 300 one-dimensional soil profiles, with a given average shear wave velocity, are generated through a Monte Carlo method in order to investigate the reliability and the limit of using the average shear wave velocity in the upper 30 m of the soil profile, as single proxy, to characterize seismic site effects for weak and strong events. The site dominant frequency and the shear wave velocity gradient in the profile are proposed as proxies to characterize seismic site effects and the variability of the response spectra at the free surface of the set of columns, for the numerical signals considered as inputs, is discussed. Correlations between site-specific amplification factors deduced using the numerical response spectra and the proposed site proxies are analyzed for various period ranges.
Chapter 7 presents the conclusions of this work and gives some suggestions for future research.

Chapter 2

Literature Review

Soil liquefaction is one of the most devastating instabilities that occurs in a broad range of saturated granular materials and is the major cause of damage to the ground and earth structures during strong earthquakes. At this regard, well-known past examples are the 1964 Niigata (Ishihara and Koga, 1981), the 1976 Tangshan (Shengcong and Tatsuoka, 1984), and the 1999 Chi–Chi earthquakes (Yuan et al., 2004).
The liquefaction mechanism is typically associated with a build-up of pore water pressure due to static or cyclic loading, and a consequent reduction in effective mean stress, hence lowering the shear strength of the soil. In this case, soil liquefaction can produce very large displacements, also in the order of tens of metres or more, and consequently severe damage to buildings and infrastructures.
Nevertheless, recent seismic events during the twenty-first century, such as 2010 Darfield and 2016 Ecuador earthquakes, have highlighted the fact that major damages are due to different scenarios of liquefaction phenomena, such as liquefaction in areas with moderate seismic intensity, liquefaction of gravelly soils, liquefaction of deeplevel sandy soils, re-liquefaction during aftershocks, and liquid-like behavior of unsaturated sandy soils (Huang and Yu, 2013).

In the following, basic concepts of laboratory tests and numerical methods dedicated to investigate liquefaction phenomena as well as previous findings on this topic are introduced.

2.1 Field liquefaction case histories

It is widely known that ground failures associated with liquefaction are potentially very damaging in buildings and can be associated with loss of human lives as observed during past earthquakes. To this regard, field and laboratory investigation data represents an important information concerning the liquefaction phenomenon and its analysis.

One of the first historical case is the 1964 M_w 7.5 Niigata earthquake where the widespread of liquefaction of the sandy ground and lateral spreading brought extensive damage to various engineering structures such as buildings, bridges, highways, railways, harbours, airports, river dikes and lifeline facilities (Iwasaki, 1986). During the Niigata earthquake, approximately 310 reinforced concrete buildings were damaged, 200 of which tilted or settled without affecting the superstructure (Fig. 2.1). Detailed soils investigations were conducted to clarify the mechanism of liquefaction and it was found that most of those damages were caused by liquefaction of recent sedimentary deposits, of low relative density, with a shallow water table (Ishihara and Koga, 1981).

(a)

(b)

Figure 2.1: Tilt and settlement of some buildings in Kawagishi-cho (a); Showa Bridge collapse (b) during 1964 Niigata Earthquake (Ishihara and Koga, 1981)

At the end of the 20th century, two great earthquakes have witnessed soil liquefaction. The 1999 M_w 7.6 Chi-Chi Taiwan earthquake caused the destruction of buildings, bridges, and other facilities, as well as a death toll of more than 2400 due the widespread liquefaction. Many sand boiling

phenomena were observed in central Taiwan, which caused severe ground settlement and structure damages (Fig. 2.2a). On the other hand, during the 1999 M_w 7.4 Kocaeli earthquake (Turkey), over 15.000 people lost their lives and about 1200 buildings collapsed or were damaged because of both liquefaction and faulting along the southern coasts of Izmit Bay and Sapanca Lake, as well as the city of Adapazari (Yoshida et al., 2001) (Fig. 2.2b). Furthermore, field investigations showed that the soils that led to severe damage were generally fine-grained soils, which did not typically meet the Chinese criteria as defined by Youd et al. (2001). Hence, the historical case of the 1999 Kocaeli earthquake highlight unforeseen issues and the importance of better understanding the susceptibility to liquefaction of fine-grained soils. (Bray et al., 2004).

(a) (b)

Figure 2.2: The 1999 M_w 7.6 Chi-Chi Taiwan earthquake (a); The 1999 M_w 7.4 Kocaeli earthquake (b)

More recently, the 11th March 2011 Mw 9.0 Tohoku earthquake is up to now the largest earthquake ever recorded in Japan. About 27,000 houses settled substantially and tilted seriously in Tohoku due to liquefaction, about half of the damaged houses are located in the Tokyo Bay area where severe liquefaction occurred although the epicentral distance was very large, about 380–400 km (Yasuda et al., 2012). For this event, the observed damage due to liquefaction seems to be strongly dependent on the long-duration and the magnitude of the ground motion, the age of the deposit, the type of material (pure sand, silty or clay sand). Fig. 2.3 shows some of the ground devastation caused by liquefaction.

The 2010–2011 Canterbury earthquake (New Zealand) sequence includes up to ten events that induced liquefaction. In particular, the M_w 6.3 eartquake occurred on 22 February 2011 in the city of Christchurch caused

(a) (b)

Figure 2.3: Destruction of the ground due to liquefaction in the Tokyo Bay area: spreading of sand over the road (a); Offset between an undamaged building and settlement of the surrounding ground (b) (Ishihara et al., 2011)

the largest number of casualties in the history of the country (Fig. 2.4). This earthquake affected nearly half of the urban area of Christchurch and caused widespread liquefaction in residential, commercial and industrial areas, including 60,000 residential buildings (Quigley et al., 2013; Cubrinovski et al., 2019). Also after this event, several samples of liquefaction ejecta were collected from different sites around Christchurch and Kaiapoi to analyze the grain characteristics. In the majority of cases, it was found that predictions from the simplified methods were conflicting with field observations. In particular, results show that the characteristics of liquefied soils are highly varied, but most of the sample can be described as silty fine sand having particles characterized by subrounded shapes.

Most recently, in Kumamoto, Japan, an intense seismic event occurred on the 14th of April 2016 (M_w 6.5) followed by the main shock of M_w 7.3 on the 16th of April. During these two major earthquakes, soil liquefaction induced catastrophic damage to infrastructures and buildings in the Kumamoto city, as well as in the Kumamoto plain and caused large settlements and a number of cracks at the embankement along the Midorikawa River. Figure 2.5a shows the liquefaction-induced damage to buildings in Karikusa district, while Fig. 2.5b shows the damage at the right river embankment of Midorikawa River. From the observation of the sand boils, it was observed that the liquefied soils contained fine fractions and also the fact that some regions experienced liquefaction both during the foreshocks and the mainshock, whilst other regions only at the occasion of the mainshock. In fact, it is unclear if liquefaction during the mainshock is a re-liquefaction, or if the ground had not yet stabilized after the dissipation of excess pore water pressure (Kiyota et al., 2017).

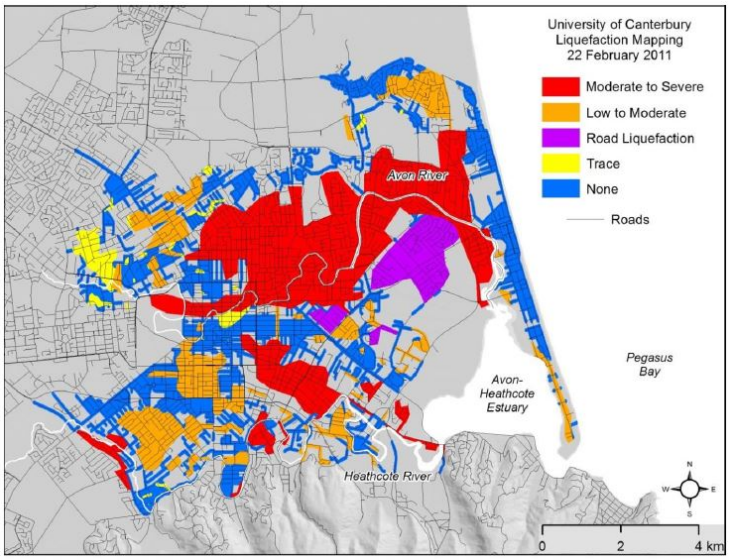

Figure 2.4: Liquefaction mapping for the 22 February 2011 Christchurch earthquake based on street reconnaissance drive-through conducted by the University of Canterbury (Cubrinovski and Taylor, 2011)

(a) (b)

Figure 2.5: Liquefaction-induced damage to buildings in Karikusa district (a) (Kiyota et al., 2017); Large longitudinal crack and settlement at the right river embankment of Midorikawa River (b) (Mukunoki et al., 2016)

A very recent strong earthquake M_w 7.5 occurred on the island of Sulawesi, Indonesia, on the 28 September 2018 causing more than 2000 fatalities due to extensive liquefaction and liquefaction-induced flow slides. The field investigations confirm the presence of sandy soils containing a certain amount of silt and clay, which may have facilitated the flowability of

the liquefied soil, as in the case of the 2011 Tohoku earthquake. Furthemore, field investigations revealed new evidence of extensive liquefaction in coastal areas (Fig. 2.6) where liquefied sediment flows occurred and consequently induced multiple tsunamis (Sassa and Takagawa, 2019).

Figure 2.6: Evidence of extensive coastal liquefaction during the 2018 Indonesia Sulawesi earthquake (Sassa and Takagawa, 2019).

Although, historical case histories have been studied over the time to understand soil liquefaction, significant damage still occurs. This indicates that, further efforts are required for the development, calibration and validation of liquefaction analyses to improve the current simplified methods and to contribute to a better assessment of liquefaction and its consequences. Thus, to evaluate liquefaction hazards, it is necessary to assess the susceptibility of a soil to liquefaction, the potential for liquefaction triggering taking into account in-situ as well as laboratory test data and observations from case histories.

2.2 General concepts of soil mechanics

2.2.1 Effective stress and pore pressure in saturated soils

Soil is a porous material, consisting of particles, which form the grain skeleton, and of water and air. In the case of a saturated granular material, the volume of void is completely filled by the pore water. When a saturated soil is subjected to an external force, the total stresses, denoted by σ_{ij}, are divided into two portions: one called effective stresses, σ'_{ij}, related to the internal forces acting on the contact points of the particles, and the second one constituted by the pore water pressure, u, acting on the fluid.
The corresponding formulation, after the postulate of Terzaghi (1943), in terms of the components of the stress tensors is defined as the following

$$\sigma_{ij} = \sigma'_{ij} + \delta_{ij} u \tag{2.1}$$

where δ_{ij} is the unit second order Kronecker tensor.
Based on this formulation, the deformations of a satured granular material strongly depends on effective stress which determines changes of the concentrated forces in the contact points of the grains causing rolling and sliding at the contact points.

2.2.2 Stress path

The soil properties strongly depend on the stress state in the soil induced by the loading. In general, the stress state at a given point in a soil mass is characterized by the normal stress σ and the shear stress τ, which act on a particular plane passing through that point.
Fig. 2.7 represents the sign conventions in geotechnical engineering for normal stresses σ_x and σ_y to the the x and y axes respectively which are positive if compressive, and the shear stresses τ_{xy} and τ_{yx}, which are positive when they cause the counterclockwise rotation. To this regard, σ_α and τ_α are the stresses on the plane inclined at an angle α that can be expressed as the following:

$$\sigma_\alpha = \frac{\sigma_x + \sigma_y}{2} + \frac{\sigma_y - \sigma_x}{2} cos2\alpha - \tau_{xy} sin2\alpha \tag{2.2a}$$

$$\tau_\alpha = \frac{\sigma_x - \sigma_y}{2} sin2\alpha - \tau_{xy} cos2\alpha \tag{2.2b}$$

Eqs 2.2 represent the Mohr circle in the plane $(\tau - \sigma)$, having center at $(\sigma = (\sigma_x + \sigma_y)/2; \tau = 0)$ and radius equal to $\sqrt{[(\sigma_y - \sigma_2)/2]^2 + \tau_{xy}^2}$. This circle describes the stress state at any inclinations α, induced by loading, as shown as an example in Fig. 2.8, where the soil element is subjected to

normal stresses σ_x and σ_y.
The Mohr cicle is characterized by a particular point, the so called pole P. For instance, as shown in Fig. 2.8, the known stress conditions is point A, where $\sigma = \sigma_y$ and $\tau = 0$, and the plane for those stress conditions is horizontal. Hence, if a horizontal secant line is drawn using the location of the point A, it will intersect the Mohr circle at the pole P.

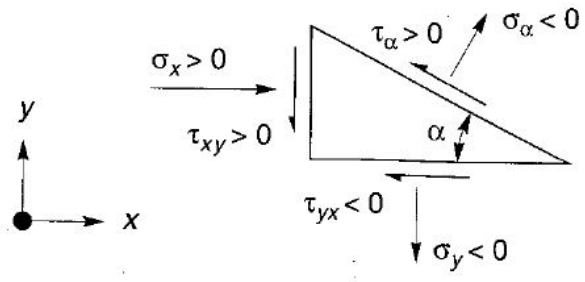

Figure 2.7: Sign conventions for normal and shear stresses (Kramer, 1996)

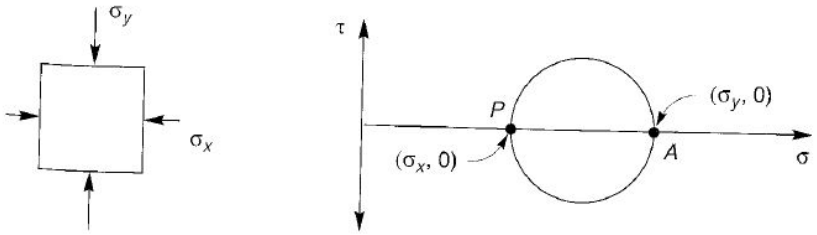

Figure 2.8: Mohr circle of stress for a soil element subjected to normal principal stresses; P is the location of pole. (Kramer, 1996)

If a different external loading is considered, the stress state changes and also the location of the pole changes, as shown in Fig. 2.9. In this case, the known stresses on the horizontal plane are $\sigma = 4$ and $\tau = 1$, while those on the vertical plane are $\sigma = 2$ and $\tau = -1$. Then, the location of the pole P can be determined by the intersect between the horizontal line drawn through the first point and the vertical line through the second point. Once the location of the pole is determined, the stress conditions of any plane can be identified.

Thus, in order to known the stress state at any plane in a soil mass, the representation of the Mohr circle of stress is important. In particular, two points of the circle are very useful: the intersects with the σ axis that define the normal stresses on planes where the shear stresses are equal to

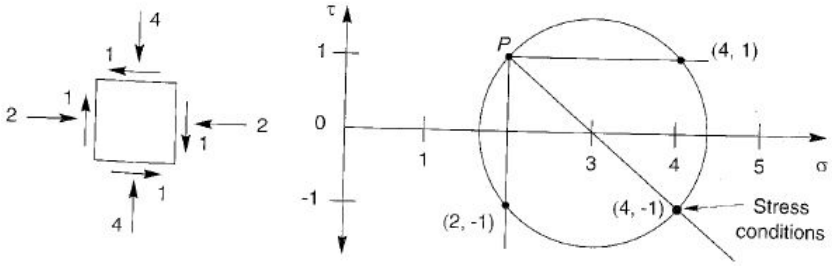

Figure 2.9: Mohr circle of stress for a soil element subjected to normal and shear stresses; P is the location of pole. (Kramer, 1996)

zero. These normal stresses are called principal stresses and the major one is defined as σ_1, the smallest as σ_3 and the intermediate as σ_2. The pole can be used to determine the orientation of the principal stress axes.

In triaxial test conditions, a cylindrical specimen is stressed along the three perpendicular directions of space. The major principal stress σ_1, acting in the direction of the specimen's axis, represents the vertical stress, while the minor principal stress σ_3 is of constant value at all locations and simulates the confining stress and in particular it is assumed that $\sigma_3 = \sigma_2$.
The variation in stress conditions acting on the specimen can be described by plotting the Mohr circle at different times during the application of the loading, but that plot can result difficult to interpretate due to the numerous circles. For that reason, generally only the variation of the top point of the circle, called stress point, is tracked, as shown by the blue points in Fig. 2.10, and its location is called the stress path and it can be drawn for the total stresses as well as the effective stresses, in the same diagram (the difference is the pore pressure).
The Mohr-Coulomb failure criterion is a straight line, defined by the stress path, in the (τ, σ, σ') plane and described by the following equation

$$\tau = c' + \sigma' tg(\phi') \tag{2.3}$$

where ϕ' is the internal friction angle of the granular material and c' is the cohesion.
In particular, in case of non-cohesive soils the cohesion is $c' = 0$.

The stress path can be also represented in the Cambridge (q, p, p') plane where $q = \sigma_1 - \sigma_3$ is the deviatoric stress, $p = (\sigma_1 + 2\sigma_3)/3$ is the mean stress and $p' = p - u$ is the mean effective stress. By analogy to the Mohr representation, the points of the stress states in the (q, p, p') plane also describe

a straight line with a slope:

$$M = \frac{6sin(\phi')}{3 - sin(\phi')} \tag{2.4}$$

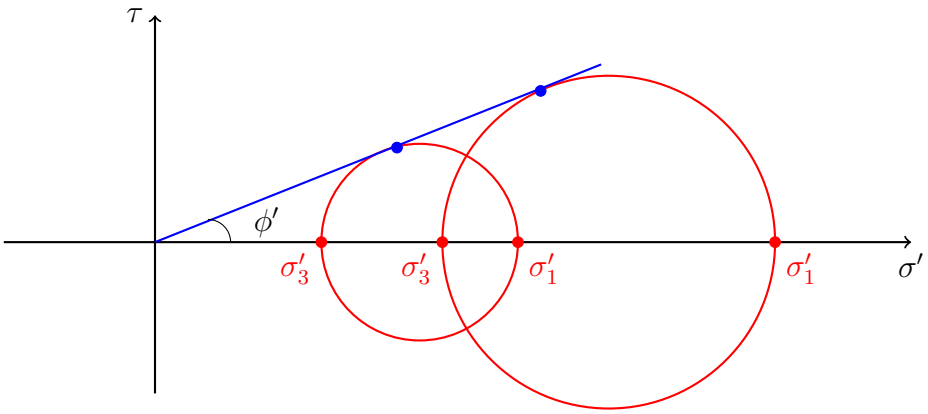

Figure 2.10: Location and definition of the stress point of the stress path

2.2.3 Drained and undrained behaviour

In the laboratory, there are two drainage conditions: perfectly drained test or perfectly undrained test.

The drained behavior is the case where the pore water can flow out of the soil throughout the loading avoiding any overpressure within the sample. Under these conditions, total and effective stresses are equal due to the fact that there is no variation in pore water pressure ($\Delta\sigma' = \Delta\sigma$, $\Delta u = 0$), while volumetric strains variations are possible ($\varepsilon_v \neq 0$).

Conversely, the undrained behaviour consists in preventing any fluid exchange between the outside and the inside of the sample. Consequently, excess pore water pressures will then develop within the material, leading to an evolution of the effective stresses which may be very different from that of the total stresses. On the other hand, the material will deform at constant volume. The undrained behaviour is therefore characterised by a non variation in volumetric strains ($\varepsilon_v = 0$) and the development of excess pore water pressure ($\Delta u \neq 0$).

Usually, laboratory tests are conducted under undrained conditions to take into account the fact that during an earthquake water has not the time to drain out from soil.

2.2.4 Contractancy and dilatancy

Shear deformations of soils are generally characterized by volume changes. In nature, the irreversible volume deformations of the soil can be compressive (contractancy) or expansive (dilatancy).
Dilatancy is the volume increase that may occur during shear (Fig. 2.11). When a dilatant soil (i.e. dense sand) is subjected to shear stresses, the only possible mode of deformation is the sliding and rolling of granular particles, creating some moving space between them and making the sand looser (i.e. an increase of the porosity). Thus, in the case of a saturated soil, this means that water will fill the additional pore space producing a negative water pressure.
Conversely, a reverse effect can occur in case of very loose sand (Fig. 2.12). In fact, when a loosely packed sand is subjected to shear stresses, the volume tends to decrease, which corresponds to a densification mechanism of the granular soil resulting from the intergrain sliding and rolling caused by the stress.
The existence of these two different behaviors in soils, show that the density of granular soils is very important for the understanding of the mechanical behavior, especially when the soil is saturated. In fact, in this case, the contracting and dilatant behaviors result in a positive and negative rate of development of pore water pressure respectively, which can lead to a large increase in the pore water pressures in the contracting case and strongly negative pressure of water in the dilatant case.

The contracting or dilatant behavior of a sand depends on the initial state of the material, expressed in terms of the void ratio e, and on the state of initial stress applied (state of consolidation). Additionally, the two mechanisms can be observed simultaneously on the same material if it is moderately loose or moderately dense.

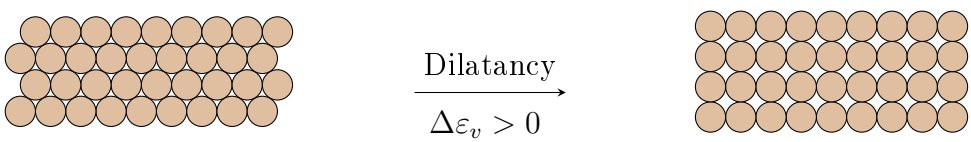

(a) Before shearing (b) After shearing

Figure 2.11: Densely packed sand

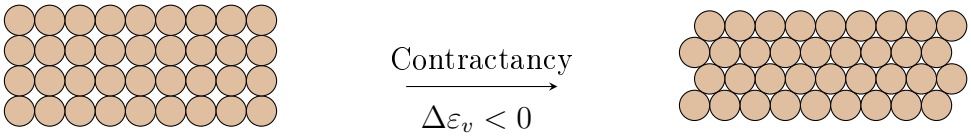

(a) Before shearing (b) After shearing

Figure 2.12: Loosely packed sand

2.2.5 Characteristic state - Phase transformation state

As already mentioned above, volume variations of samples subjected to shear loading under undrained conditions are important for the understanding of the behavior of granular soils. To this regard, the transition from contracting to dilative behavior occurs along a line through the origin of stress space, whose slope is characterized by the angle ϕ_{car}, defined as

$$\phi_{car} = \arcsin \frac{3\eta_{car}}{6 + \eta_{car}} \tag{2.5}$$

where η_{car} is the ratio of the effective stress $\eta = q/p'$ corresponding to the characteristic state. This line is denoted as characteristic line in case of drained condition or phase transformation line in case of undrained condition. The characteristic state marks the separation between contracting and dilative behavior in drained tests and occurs when the rate of volume change is equal to zero ($\dot{\varepsilon}_v = 0$) (Luong, 1978). The state of phase transformation in undrained conditions is defined as the point where the path of effective stress p' changes its direction in the q, p' plane (Ishihara et al., 1975). This state is associated with the phase transformation angle ϕ'_p and can be determined either as the minimum point of the effectives stresses ($\dot{p}' = 0$) before their increase in the (q, p') plane, or as the maximum point of the excess pore water pressure ($\Delta u = 0$). According to Lade and Ibsen (1997), the phase transformation state determined in undrained test conditions is similar to the characteristic state determined in drained test conditions. Furthermore, that line is unique for a given sand and is influenced by relative density, initial isotropic stress and fine content.

2.2.6 Critical state - Steady state

At continuing deformations both dense and loose sand tend towards a unique state of average density, independently of its initial density state, denoted as the critical density or critical void ratio (Casagrande, 1936).
On the other hand, Poulos (1981) proposes the concept of a steady state, denoted as a state in which the soil mass deforms continuously at constant

volume, constant normal stress, constant shear stress and constant velocity.

The critical state or steady state relates the effective confining pressure (p') with the void ratio (e) of a soil during shearing, identifying a unique critical state line (CSL) or steady-state line (SSL), which have been proved to be an useful method to predict the behavior of sand under both drained and undrained behaviors (Fig. 2.13a). Laboratory experiments have shown the critical state line is equivalent to the steady-state line (Been and Jefferies, 1985; Wood, 1990; Verdugo and Ishihara, 1996; Bobei and Lo, 2005). This curve is commonly plotted in the ($e - logp'$) plane, identifying a critical state line having the following equation (Li and Wang, 1998)

$$e_{cs} = \Gamma - \lambda(\frac{p'}{p_a})^{\varepsilon} \tag{2.6}$$

where p' is the mean effective stress at the critical state, Γ, λ and ε are dimensionless constants and $p_a = 100$ kPa is the atmospheric pressure.

Been and Jefferies (1985) introduce the state parameter Ψ, based on critical state soil mechanics, as a reference point to characterize liquefiable soil behaviour during undrained monotonic loading (Fig. 2.13b). It is defined as the void ratio difference between the current state of the soil and the critical state at the same mean effective stress

$$\Psi = e - e_{cs} \tag{2.7}$$

where e is the intial void ratio and e_{cs} is the void ratio at critical state conditions. In particular, when the initial state of a sand is above the CSL ($\Psi > 0$), the sand has the tendency to contract during shearing, while if the initial state point is located below the CSL ($\Psi < 0$), the tendency of sand is to dilate upon shearing. Hence, the state parameter allows quantification of many aspects of sand behaviour using a single variable.

2.3 Soil liquefaction phenomenon from laboratory tests

Field evidences of soil liquefaction, associated ground failure and damage to structures and earthstructures during past earthquakes have led to extensive laboratory investigation on the liquefaction behavior of soils and procedures for assessing liquefaction potential by numerous researchers since 1960's (Castro, 1969; Vaid et al., 1981; Vaid and Chern, 1985; Sladen et al., 1985; Been

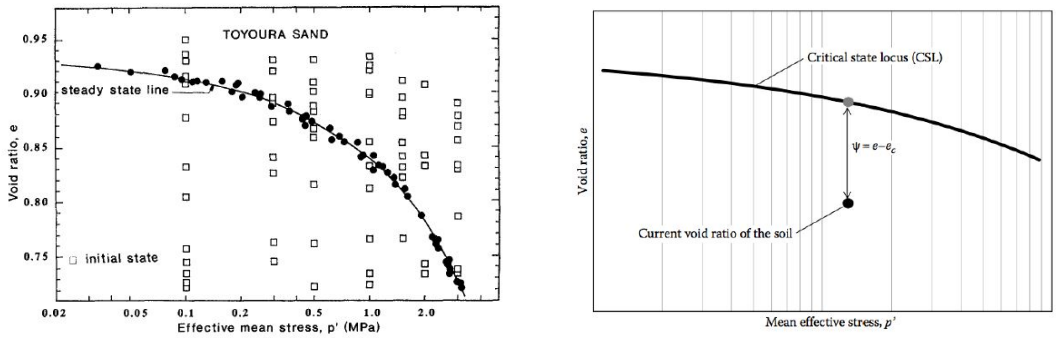

(a) (b)

Figure 2.13: Steady state line and initial states (Verdugo and Ishihara, 1996) (a); Definition of state parameter Ψ after Been and Jefferies (1985)

and Jefferies, 1985; Ishihara, 1993; Verdugo and Ishihara, 1996).
Soil liquefaction is a phenomenon caused by static or dynamic loading, in which the strength and stiffness of saturated granular soils are significantly reduced by pore pressure build-up and decreasing of effective stressess.
Soil liquefaction occurring under static load conditions is called static liquefaction, while it is called cyclic liquefaction or cyclic mobility when induced by cyclic loads (Kramer, 1996).

2.3.1 Undrained monotonic loading

The phenomenon of flow/static liquefaction is associated with undrained softening behavior which can lead to large displacement and devastating failures. Fig. 2.14 depicts the typical observed behavior of soils under undrained monotonic loading. In particular, Figs 2.14a and 2.14c show the deviatoric stress (q) and the excess pore water pressure (Δu) with respect to the axial deformation (ε_a), while Fig. 2.14b depicts the stress path of soil specimens in the ($q - p'$) plane and Fig. 2.14d the behaviour in the ($e - p'$) plane.

When the state of the soil material is very loose (case A; e.g. with a relative density $D_R < 35\%$ on average), undrained softening occurs with a significant loss of strenght. The soil contracts and reaches the critical state line at very low mean effective stress; in particular, in Fig. 2.14a it can be observed that after a peak at a low level of deformation, a sudden reduction of the strength and stiffness occurs. On the other hand, the excess pore water pressure increases rapidly coinciding with the increase of the deviatoric stress up to a value close to the confining stress, then begins to stabilize and

becomes constant (Fig. 2.14c). This behaviour is call "true liquefaction" (Carrera et al., 2011) and it is characterized by a deviator stress equal to zero at the end of undrained softening (Castro, 1969; Casagrande, 1975; Seed, 1979; Chern, 1985).

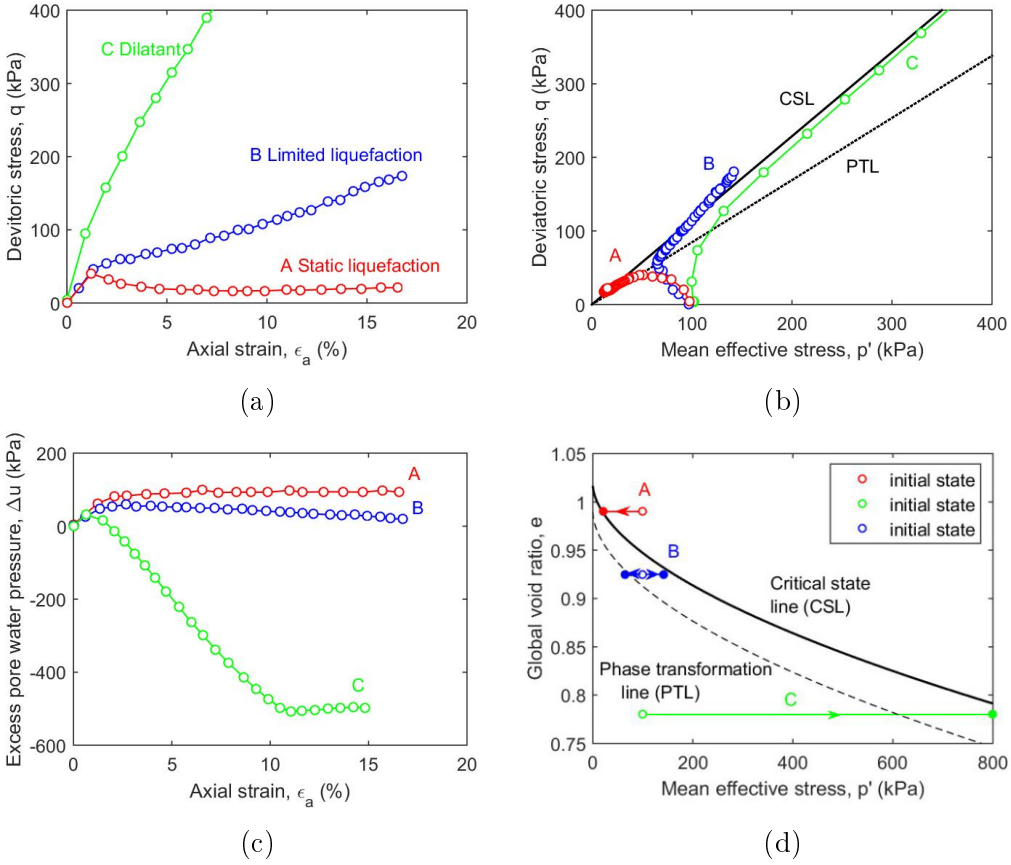

Figure 2.14: Monotonic undrained behaviour of Hostun sand for three soil specimens having different relative density: loose (A), medium (B) and dense (C) samples in terms of deviatoric stress and excess pore water pressure versus axial deformation (a,c), deviatoric stress and global void ratio versus the mean effective stress (b,d)

In the case of intermediate soil (case B), the initial state is located below the critical state line but above the phase transformation line (Fig. 2.14d). Thus, the soil initially contracts reaching the phase transformation line, and then it dilates back towards the critical state line. In this case, the final dilatant phase is preceded by a compressive phase characterized by limited undrained softening; from Fig. 2.14a it can be observed that the deviatoric stress initially increases to a maximum value from which it begins

to decrease slightly to stabilize until the phase transformation line, and then it increases again to reach the critical state. The excess pore water pressure (Δu) increases to a maximum value lower than the confining stress, and then begins to decrease (Fig. 2.14c). This is referred to as "limited liquefaction".

When the soil material is very dense (case C), the initial state is located below both the critical state line and the phase transformation line (Fig. 2.14d). In this case, the soil after a very small phase of contraction expands continuously (Fig. 2.14b), hence the deviatoric stress increases to a less pronounced peak beyond which it continues to increase linearly (Fig. 2.14a). This development is accompanied by an initial increase in the pore water pressure and then a decrease to a level that can even become negative (Fig. 2.14c).

As shown from Fig. 2.14, the stress state and density of the soil are intrinsically linked. Hence, the type of behaviour of the granular soil depends mainly on its initial state (state parameter), which includes void ratio and effective stress.

2.3.1.1 Static instability

It is well known that granular soil may become unstable even before the stress state reaches failure (Lade, 1992; Chu et al., 1993; Leong et al., 2000). In fact, fully saturated soils that tend to compress during shear may become unstable leading to liquefaction. This type of instability has been observed under undrained conditions for both satured loose and medium to dense granular soils (Lade et al., 1988; Lade and Pradel, 1990; Leong et al., 2000). The term instability corresponds to a condition in which the soil may not be able to sustain the current stress state and can develop large plastic strains caused by the increasing of the pore water pressure under undrained conditions. Conditions for stability and instability of granular materials have been derived from experimental results.

To this regard, Sladen et al. (1985) present the collapse surface approach through a series of undrained triaxial tests of varying initial confining pressures with the same initial density. The experimental results show that the locus of the peak shear stresses fall into a unique line called instability line (Fig. 2.15a). The position of this line changes with the variation of the void ratios while the slope remains unchanged. Thus, in the three-dimensional ($e - p' - q$) plane, there would exist an infinity of parallel lines, which describe a cylindrical surface resting on the steady state line and representing the collapse surface (Fig. 2.15b). In particular, the

collapse surface defines three zones that divide the domain from stable to unstable (Fig. 2.15c). The zone C is very unstable and liquefaction can develop under any initial conditions. Zone A is considered as stable because the shear level is below the steady state. Finally, in the zone B, the initial conditions are below the collapse surface but above the steady state and liquefaction can only take place if the effective stress paths cross the collapse line.

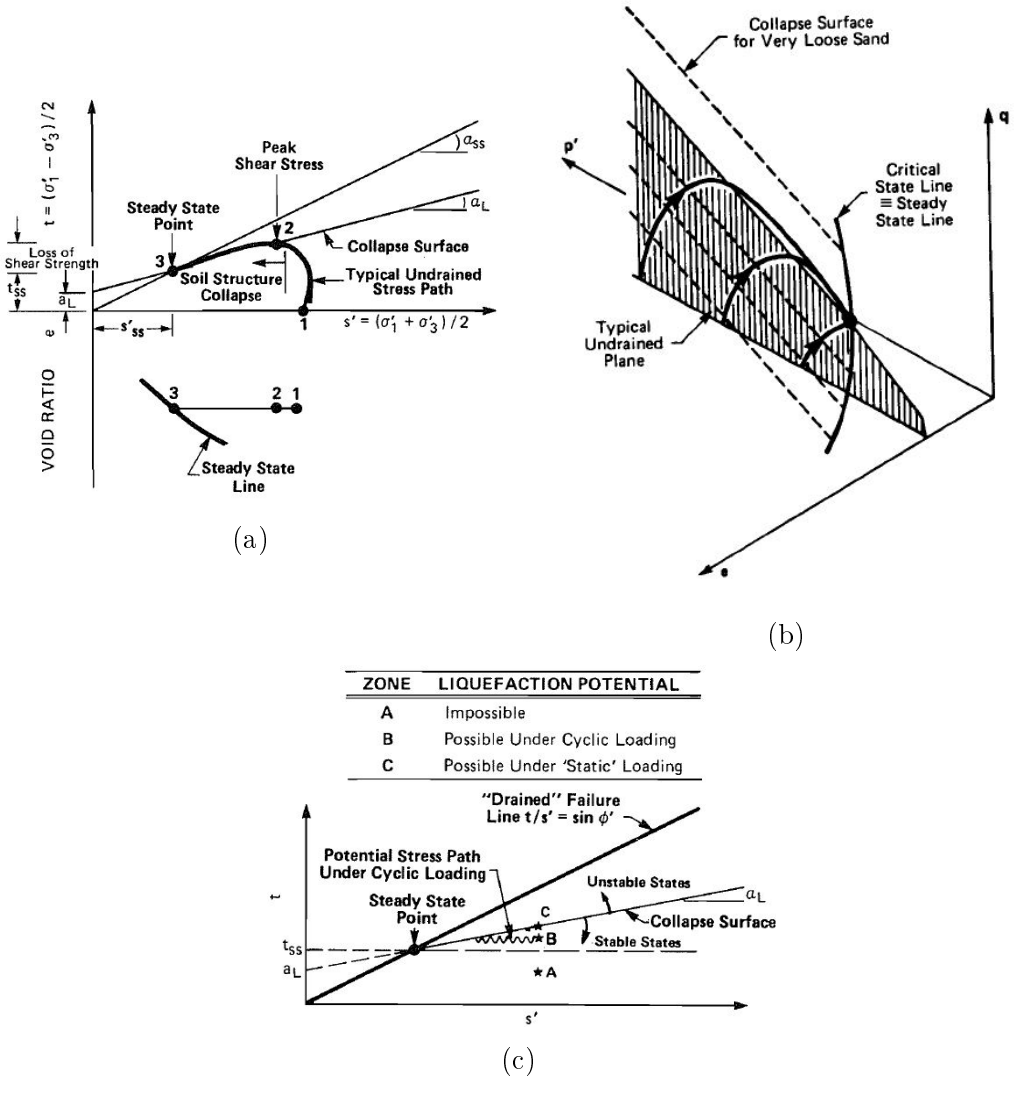

Figure 2.15: The collapse surface in the $(t - s')$ space (b) in the $(p' - q - e)$ space (a) showing typical stress - void ratio paths followed by samples in triaxial compression in undrained conditions; effect of soil state on liquefaction potential (c) (after Sladen et al. (1985))

On the other hand, Vaid and Chern (1985) come to a similar conclusion, defining a potential instability zone that is located between the locus of the peak shear stresses as an inferior limit and the phase transformation line as a superior limit (Fig. 2.16). The slope of the collinear line is determined by the critical effective stress ratio σ'_1/σ'_3 corresponding to the peak of the shear stress beyond which liquefaction is triggered. This means that the onset of liquefaction depends only upon the ratio of stress and it is independent of the initial state.
Furthermore, Vaid et al. (1990a) investigate the instability of granular materials performing experimental studies in both triaxial compression and extension. The experimental results confirm the existence of a single value of critical stress ratio in the case of compression, whereas the value of the critical stress ratio is dependent on the void ratio in the case of extension (Fig. 2.16b). The same results are found by Vaid and Thomas (1995) and Vaid and Sivathayalan (1996).

After performing several series of triaxial compression tests, Lade and Pradel (1990) show that the initiation of instability in granular materials occurs at small strains and requires that the stress states are located above the instability line, which is defined as the line connecting the peak of a series of effective stress paths (Fig. 2.17). The instability line provides the inferior limit of the region of potential instability, while the failure line corresponds to the upper limit of the zone. Thus, for a granular material to become unstable inside the failure surface, the state of stress must be located on or above the instability line. Lade (1993) divides the region of potential instability into three small zones: a zone of potential instability, a zone of temporary instability and a zone of stable behaviour. According to this theory, the temporary instability is located in the upper part of the dilating zone, where the instability may initially occur, but once the soil reaches the phase transformation line, it recovers strength and becomes stable again. Instead, in case of very loose soils, the region of potential instability reaches down to the origin of the stress diagram. Moreover, it is observed that the instability line is not unique, but it is dependent of the void ratio and the effective stresses applied.

Yang (2002) propose a new interpretation of the two concepts, based on the state parameter. He shows that the locus of peak points in the effective stress paths is not a unique line that passes through either the steady-state point or the origin in stress path space, but rather varies with the state of soil. In particular, from experimental analyses, it is evident that the slope of the flow liquefaction line increases with decreasing confining pressure, and the critical-state line provides an upper bound, as can be observed in Fig. 2.18.

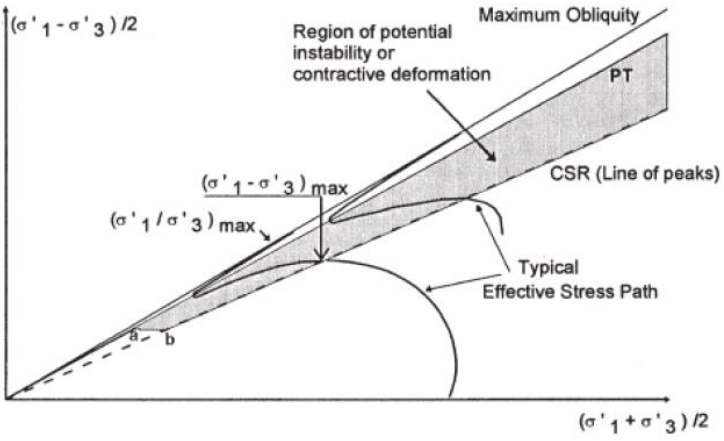

(a)

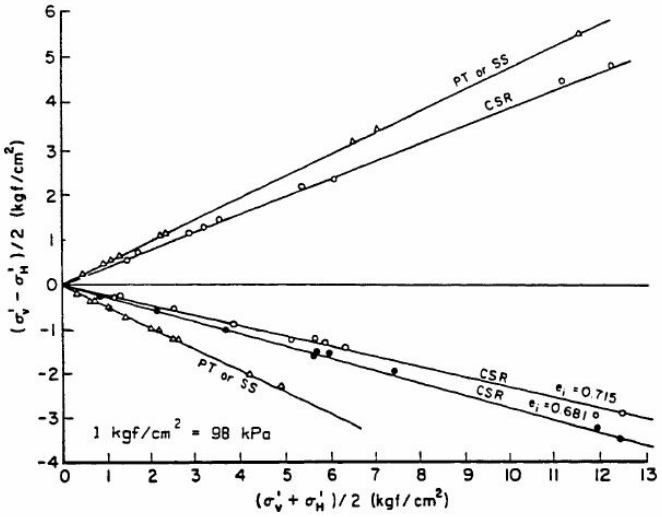

(b)

Figure 2.16: Zone of potential instability according to Vaid and Chern (1985) (a); initiation of liquefaction in compression and extension (after Vaid et al. (1990a))

Thus, according to these findings, flow liquefaction line (or instability line) is defined as the locus of the peak points only of those samples that reached true liquefaction (i.e. deviatoric stress equal to zero) and if the stress conditions in a soil reach this line, flow liquefaction is to be triggered and the shear resistance will be reduced rapidly to the critical-state strength Yang (2002); Carrera et al. (2011).

Furthermore, Carrera et al. (2011) investigate the positions of the peak points for soils exhibit strain softening but no liquefaction. Fig. 2.19a shows

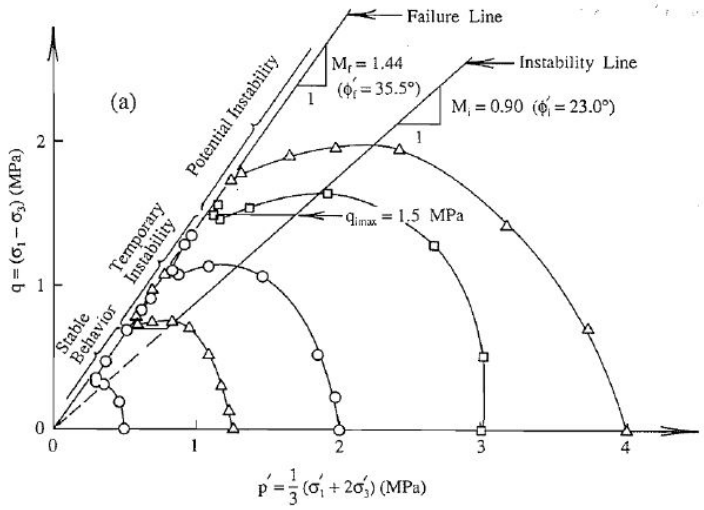

Figure 2.17: Schematic diagram of location of instability line in $p' - q$ diagram (after Lade (1993))

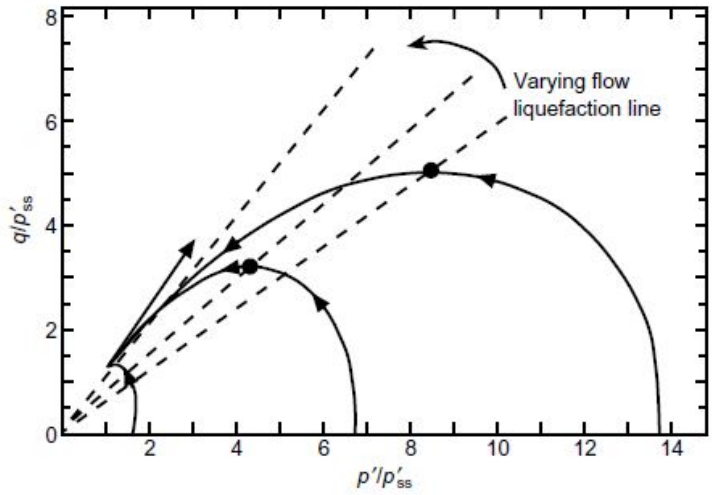

Figure 2.18: Test results for Toyoura sand in stress path space (after Yang (2002))

the stress paths of five tests carried out on clean sand, which exhibit strain softening and have different consolidation pressures and void ratios. As shown in this Figure, only one of them exhibit true liquefaction and lies on the instability line. Then, it can be observed that the peak points for the others tests tend to move towards the critical state line as the void ratio decreases and the mean effective stress increases.

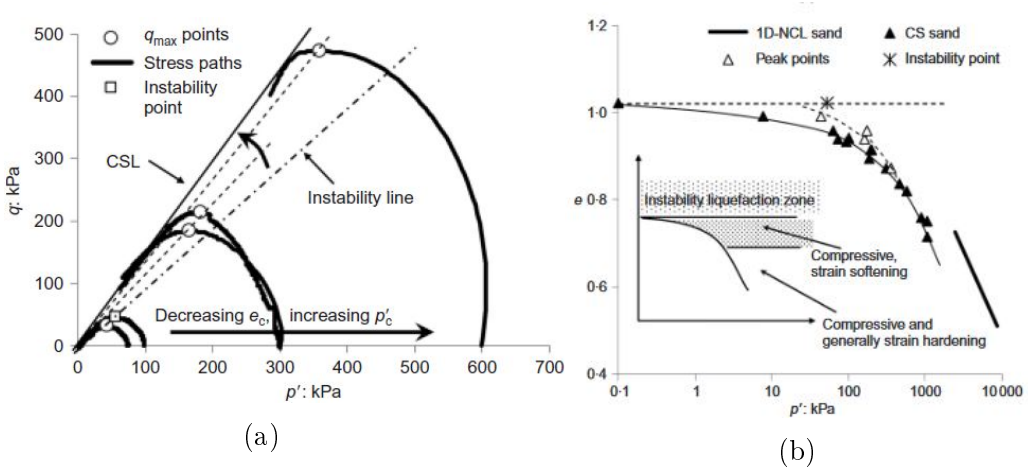

Figure 2.19: (a) Stress paths and locus of peak points from tests on clean sand; (b) scheme of subdivision of the area above the CSL into three different regions connected to different behavior (after Carrera et al. (2011))

In the (e, ln(p')) plane (Fig. 2.19b), three different zones can be defined. According to this approach, samples with initial states the horizontal asymptote of the critical state line (e_{liq}), which defines the instability zone, will exhibit strain softening followed by true liquefaction, under undrained conditions. Samples at lower initial void ratios, on the curved part of the critical state line, will exhibit strain softening, reaching stable critical states but no liquefaction. On the other hand, at the highest stresses, samples will reach stable critical states on the straight part of the critical state line and will exhibit strain hardening (Bedin et al., 2012).

2.3.1.2 Influence of void ratio

The behavior of granular soil materials subjected to shear stress is mainly governed by the associated volume variations, which are controlled by the void ratio (or relative density) and the stress level of the soil material. To characterize the shear behavior of sands in undrained conditions, different parameters are identified (Ishihara, 1993). The void ratio e, defined as the void to solid volume ratio, represents a state parameter correlated to strength, stiffness and dilatancy of sands.
To this regard, Yoshimine and Ishihara (1998) present a summary of the results of undrained triaxial tests carried out by Verdugo (1992) on Toyoura sand at a fixed isotropic consolidation stress ($p'_0 = 490$ kPa) for various void ratios (Fig. 2.20). From this figure, it can be observed that when the void ratio is high ($e = 0.910; 0.901$) the sand shows a contracting behaviour, and therefore liquefies with a strong softening, even reaching a total loss of shear

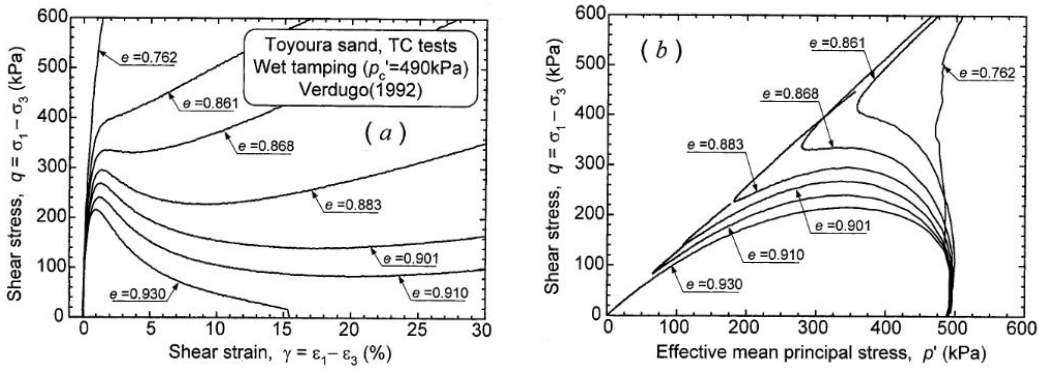

(a) (b)

Figure 2.20: Undrained triaxial tests with $p'_0 = 490$ kPa (Verdugo, 1992)

strength in the case of $e = 0.930$. However, if the void ratio decreases, the sand behavior changes from contracting to dilating by passing through an intermediate phase corresponding to limited liquefaction (point of minimum effective mean stress). On the other hand, when the void ratio is lower ($e = 0.762$), the mean effective stresses show almost no reduction and the behaviour is described as stiff.
Furthermore, the peak of the deviatoric stress increases with decreasing void ratio (e.g. increasing density), implying that the liquefaction susceptibility decreases with decreasing void ratio. This means that the void ratio (or relative density) strongly affects the liquefaction characteristics of the granular soil (Castro, 1969; Kramer and Seed, 1988; Canou, 1989; Yamamuro and Lade, 1997; Yoshimine et al., 1999; Igwe et al., 2012).

2.3.1.3 Influence of confining pressure

Experimental results have shown that the confining stress is an important factor determining the liquefaction susceptibility of a saturated soil. At the same void ratio, the confining stress has an important influence on the peak value of the deviatoric stress as well as on the volume behaviour of the granular material.

In Fig. 2.21 the undrained soil behavior for the Sacramento River sand (Lee, 1965) is shown in terms of stress–strain curve (Fig. 2.21a) and effective stress paths (Fig. 2.21b). In particular, from Fig. 2.21b, it can be noted that the stress paths exhibit more dilatant behavior at low confining pressures and when the confining pressure increases, the soil exhibits more contractive volumetric behavior (positive pore pressures). In fact, the tests performed

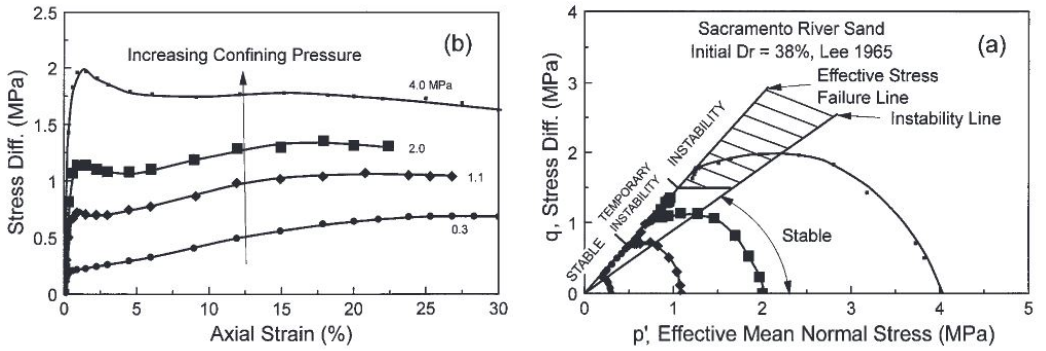

(a) (b)

Figure 2.21: Undrained triaxial tests performed on Sacramento River sand (Lee, 1965)

at lower confining pressure exhibits dilatant behaviour, and the increase in consolidation stress leads to an increase in the contracting behavior. Moreover, the consolidated sample at the highest confining stress shows a very pronounced peak strength, which decreases as the consolidation stress decreases (Fig. 2.21a).

On the other hand, Yamamuro and Lade (1997) investigate the behavior of loose sand under static loading conditions, finding an inverse behavior with respect to the confining stress. As shown in Fig.2.22a, their results clearly indicate that static liquefaction occurs only when the confining pressures is low. Furthermore, at these low densities, as confining pressures increase the effective stress paths indicate increasing resistance to liquefaction by showing increasing dilatant tendencies. Thus indicating that static liquefaction resistance increases with increasing confining pressure. This type of behavior has been widely reported in the literature (Vaid and Chern, 1985; Alarcon-Guzman et al., 1988; Ishihara, 1993).
The reason is related to the compressibility of the soil. In fact, as illustrated in Fig. 2.22b, sands show decreasing compressibility with increasing confining pressure but the Ottawa and Nevada sands present much more compressibility than the Sacramento River sand. Thus, the rapid reduction in compressibility in the case of Ottawa and Nevada sands leads to a significant densification increasing the confining stress. Whereas, the Sacramento River sand presents an almost flat compressibility curve, resulting in decreasing volumetric dilatant behavior with increasing confining pressure.

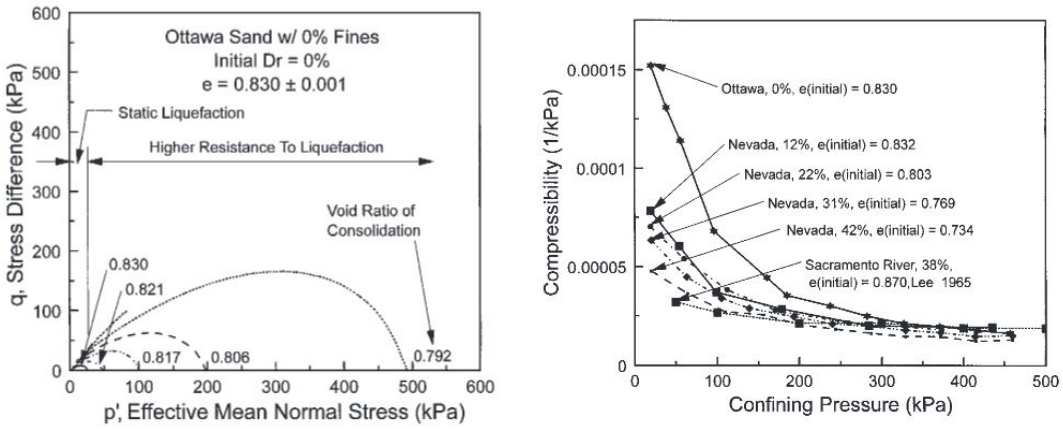

(a) (b)

Figure 2.22: Undrained triaxial tests performed on Ottawa sand with $D_R = 0\%$ and subjected to various confining pressures (a); isotropic compression tests on different initial densities of Nevada, Ottawa, and Sacramento River sands (after Yamamuro and Lade (1997))

2.3.1.4 Influence of non-plastic fines on clean sand

The influence of fine content on the liquefaction potential of silty sand has been the topic of numerous experimental researches over the past two decades due to the frequent failures of earthstructures associated with storms and floods. It has been widely recognized that the presence of silt particles may affect the mechanism of resistance of sands. Evidences of liquefaction case histories (Kishida, 1969; Tohno and Yasuda, 1981; Allen et al., 2010) show that soils containing a high portion of fines may liquefy. Whereas, Bolton Seed et al. (1985); Ohsaki (1970); Tokimatsu and Yoshimi (1983) report that the liquefaction potential increases for sands having a fine content less than 10%. Whether the presence of non-plastic silt in a granular soil affects the liquefaction potential and how to evaluate liquefaction resistance of sand containing different amounts of silt contents remain still controversial issue. Previous experimental programs carried out considering various types of sands and fines, fine contents, relative densities and confining pressures, show contradictory results in terms of liquefaction resistance. In fact, past experimental studies reveal that the liquefaction strength could increase (Kuerbis et al., 1988; Dezfulian and Marachi, 1984; Pitman et al., 1994; Amini and Qi, 2000) or decrease (Murthy et al., 2007; Belkhatir et al., 2010b; Stamatopoulos, 2010) with an increasing amount of fines. These discrepancies may depend on the parameter selected to characterize the soil mixture (e.g. initial relative density, global void ratio, intergranular void

ratio or interfine void ratio). Moreover, some studies show an increase in the liquefaction susceptibility with the addition of fines up to a limit fine content, followed by a decrease after this threshold value (Koester, 1994; Lade and Yamamuro, 1997; Xenaki and Athanasopoulos, 2003; Naeini and Baziar, 2004; Papadopoulou and Tika, 2008). Hence, the numerous experimental studies indicate that fines particles affect the intrinsic properties and the mechanical behavior of sand-silt mixtures including instability, critical state, strength and stress–dilatancy, but comparisons between clean sand and sand-fines mixtures are not easy to interpret due to the different parameters considered to reconstitute the mixtures in the various studies.

In the following sections, the mechanical behavior of sand-fines mixtures is analyzed from a microscopic (e.g. particle contacts, packing configuration) to macroscopic point of view.

Particle characteristics of mixtures

Natural sediments are granular mixtures made of particles of different sizes and shapes. To this regard, the macroscale behavior of the soil results from the packing patterns and interactions of the constituent particles (i.e. force chains) which are closely related to the characteristics of the particles. The particle characteristics include particle size, particle size distribution, particle shape and mineral composition of particles, and play a major role on the stress–strain response and volume change behavior of mixtures and in the governing particle-level forces and inter-particle packing (Cho et al., 2006). Particle shape affects also void ratios. Several experimental researches show how the maximum and minimum void ratios (e_{max} and e_{min}, respectively) and the difference between them increase with increasing angularity or decreasing roundness and sphericity (Graton and Fraser, 1935; De Graft-Johnson et al., 1969; Santamarina and Cho, 2004; Cubrinovski and Ishihara, 2002).

Furthermore, experimental results performed on sand mixtures indicate that platy particles decrease the packing density, stiffness and strength, the critical state friction angle and the intercept Γ of the critical state (Eq. 2.6), while irregular particles have an opposite effect (Cubrinovski and Ishihara, 2002; Cho et al., 2006). Cho et al. (2006) analyze the particle shape effects in a wide range of natural and crushed sands. Their results indicate that the critical state parameters decrease with increasing roundness, sphericity, and overall regularity. In particular, as shown in Fig. 2.23, both the critical state friction angle and the intercept of the critical state curve are strongly influenced by particle shape, while the slope is poorly affected by shape parameters.

Yang and Wei (2012) combine two types of non-plastic fines having different particle shapes with two uniformly graded quartz sands, in order to examine the role of the particle shape in the undrained shear behavior of sandy soils. They show that the addition of non-plastic fines increases the instability of the soil structure, regarding phase transformation, and they propose conceptual models to explain the various responses according to the particle shape, concluding that the round-to-round model represents the weakest structure. Whereas, the angular-to-angular model represents the strongest structure because angular particles favor sliding rather than rolling.
Recently, Yang and Luo (2015) further investigate the influence of the shape parameters on the critical state parameters through macro-scale and micro-scale laboratory experiments. Their results confirm that varying particle shape can significantly alter the overall mechanical response and shearing resistance of granular soils. Moreover, they show that for a given initial state, the liquefaction susceptibility is highly affected by its particle shape and increase with the particle regularity. Liu and Yang (2018) investigate the influence of particle size distribution on the shear modulus of sand-fine mixtures. They correlate stiffness parameters with particle shape.

Various researchers investigate the influence of particle gradation on the undrained shear strength of sands and silty sands under monotonic loading (Chang et al., 1982; Vaid et al., 1990b; Yilmaz et al., 2008; Belkhatir et al., 2011). Chang et al. (1982) and Vaid et al. (1990b) demonstrate that the undrained resistance of clean sands depends on both the mean size, D_{50}, and the uniformity coefficient, C_u, showing that the liquefaction resistance increases with increasing C_u at low relative density values and has an opposite tendency at high relative density values. Belkhatir et al. (2011) investigate the effect of grading characteristics on silty sands through a series of undrained monotonic triaxial tests, showing clearly relationships between the liquefaction resistance, D_{50} or D_{10} parameters and the coefficient of uniformity C_u. In particular, the results demonstrate that the peak and residual strength decrease linearly with the increase of C_u and with the decrease of the average diameter.

Variation of void ratios with fine content

The presence of fines mixed together with sand modifies the soil structure when compared to clean sand. Fig. 2.24 illustrates samples containing different percentage of fine content (FC) from a micromechanical point of view, which correspond to microstructures with different packing arrangements ranging from coarse grains skeleton (sand) to coarse grains separated by fines and to fines skeleton (silt). Three different types of intergranular

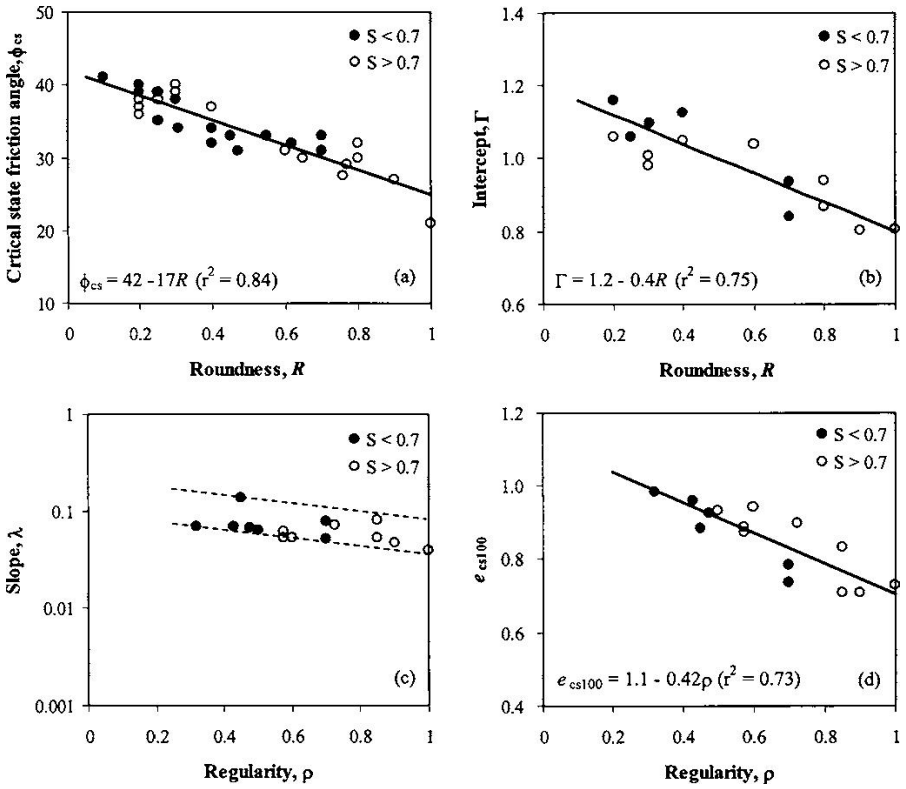

Figure 2.23: Effect of particle shape on critical state parameters (Cho et al., 2006)

contact influence the mechanical behavior of sand with fines: the contact between coarse particles of sand (CGS), the sand-fine-sand (SFS) contact and the sand-fine-fine-sand (SFFS) contact. The contact between the coarse particles is the strongest, while the sand-fine-fine-sand contact is the weakest. The type of contact in the soil structure is the main factor influencing the behavior of silty sands. Considering two mixtures with the same relative density, the one with the lower fine content presents a stronger structure than the one with the higher fine content, because it is mostly characterized by contacts between coarse particles. When the mixture has a higher fine content, the behavior becomes mostly characterized by sand-fine-sand contact and sand-fine-fine-sand contact ($FC > 25\%$ in Fig. 2.24).

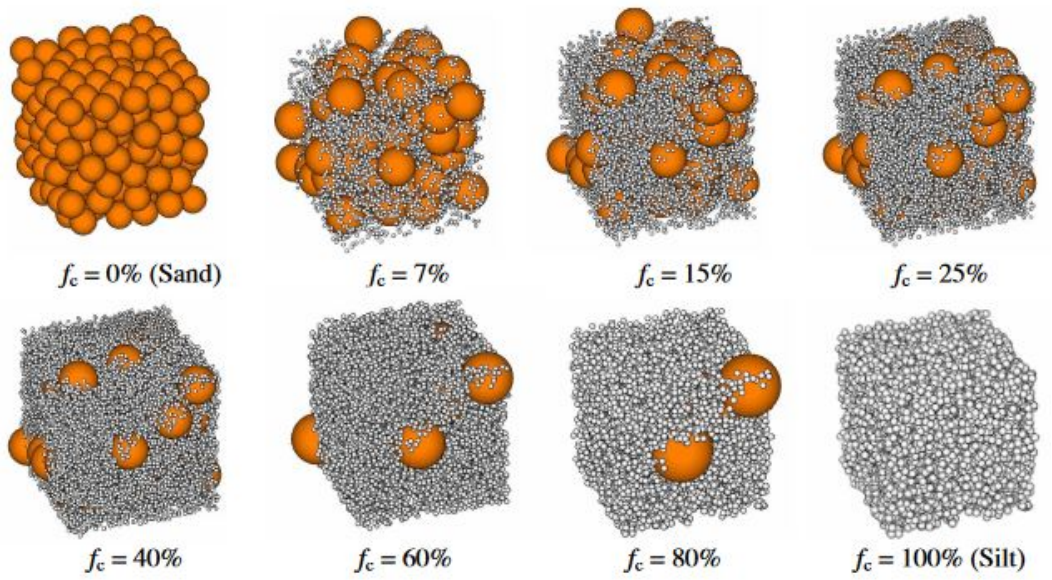

Figure 2.24: Sand-silt mixture packing with different fine content (Yin et al., 2014)

Over the past, many researchers has studied theoretical and experimental variation of binary packing (Graton and Fraser, 1935; White and Walton, 1937; McGeary, 1961; Lade et al., 1998).
Maximum and minimum void ratios are two intrinsic properties of granular soils describing the loosest and the densest states of the particles, respectively. The curves of maximum and minimum void ratios with respect to the fine content give information about the silty sand mixture characteristics. The variation of void ratio with volumetric fine content, illustrated in Fig. 2.25a, is theoretically derived by Lade et al. (1998) for a pair of idealized packings of spherical particles. According to this theory, the small filler particles have much smaller diameters than the large diameters of coarse grains. As shown in Fig. 2.25a, the increasing of fine content decreases the overall void ratio until the minimum void ratio is reached (Point B). The pont of minimum B represents the threshold fine content FC_{th} (Thevanayagam, 1998), which corresponds to the condition where the voids between the coarse grains are completely occupied by fine particles. The filling process is defined by the line from A to B. Then, as the amount of fines increases, the coarse grains are spread apart and thus, the void ratio increases linearly (from B to C). Thus, the void ratio versus fine content curve presents a V shape.

When particles of two different sizes are mixed, the packing is affected by the ratio between the large (D) and the small (d) size, which denotes

the gap in the grain size distributions (Lade et al., 1998; Cubrinovski and Ishihara, 2002). The experimental results on the binary packing of spherical balls obtained by McGeary (1961) shows that the void ratio decreases with an increase in fine content until the fine content reaches the threshold value, irrespective of the value of D/d, and then the trend is the opposite with a further increase in fine content (as already shown in the theroretical diagram of Lade et al. (1998)). The observed threshold fine content (FC_{th}) defines a point distinguishing between "fines in a sand matrix" to "coarse grains in a matrix of fines".

Lade et al. (1998) analyze the experimental data provided by McGeary (1961), showing the variation of void ratio with respect to the size ratio D/d (Fig. 2.25b). It can be observed that the void ratio sharply decreases as the size ratio increases up to the value of $D/d < 7$ because the smaller particles migrate into the voids. Beyond this value, the void ratio remains almost constant. In particular, the limiting value of 7 is consistent with the theoretical calculation of fitting a smaller sphere between larger spheres (Lade et al., 1998).

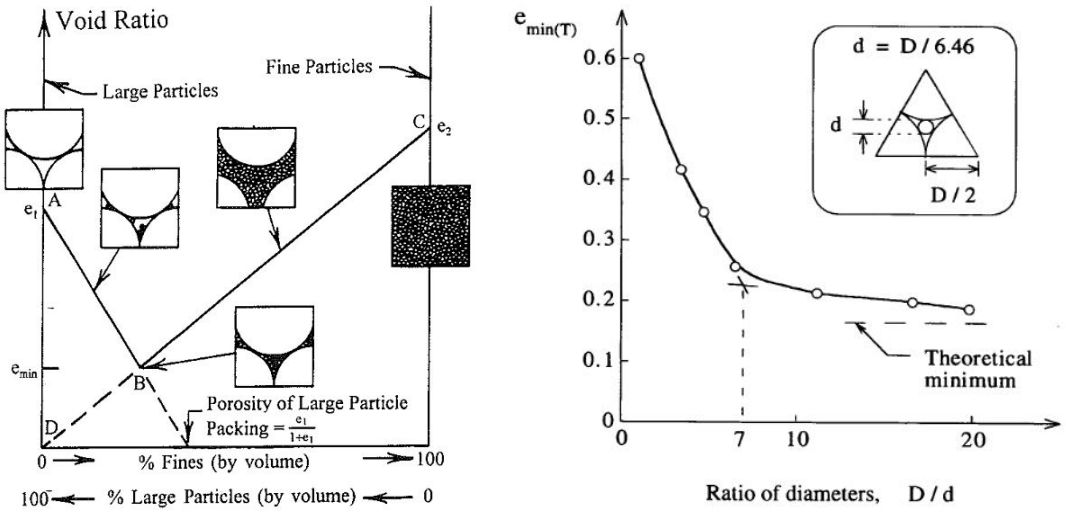

Figure 2.25: Schematic representation of theoretical variation of minimum void ratio in binary packings with fine content (a); effect of size ratio (D/d) on minimum void ratio of binary mix (after McGeary (1961); Lade et al. (1998))

Concept of equivalent intergranular void ratio

In a sand-fine mixture composed by non-plastic fine particles, the transfer force is characterized only by the intergranular mechanism, without the alteration observed in plastic soils (Yang and Wei, 2012). Fig. 2.26 depicts the effect of fine particles on soil graular mixtures, showing five different possible cases of packing density:

- **case i** → the structure consists completely of contacts between coarse grains of sand ($FC = 0\%$);
- **case ii** → the fine content is low, the fine particles are enclosed in the void spaces confined by coarse grains, thus they do not actively contribute to the mechanical resistance of the granular soil;
- **case iii and case iv** → due to the increase of the fine content, fine particles goes between the coarse grains and start to interact activelty affecting the stiffness of the packing mixture;
- **case v** → the amount of fine particles is high, thus the response of the granular soil is dominated by sand-fine-fine-sand contacts and the coarse grains are like reinforced elements among the fines particles.

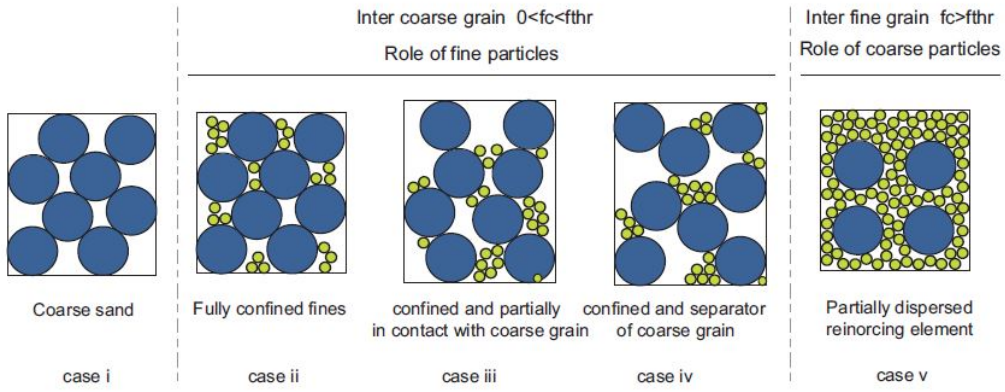

Figure 2.26: Active and inactive contacts in soil granular mixtures (after Thevanayagam (2007))

Different parameters are identified to characterize the shear behavior of sands in undrained conditions. The global void ratio e, defined as the void to solid volume ratio, is a parameter correlated to strength, stiffness and dilatancy of sands. This parameter cannot capture the influence of fine content on the liquefaction potential of sands. Indeed, silty sands having the same global void ratio show different responses. On the contrary, the intergranular void ratio e_g is identified in the literature as an adequate state parameter to characterize the global effect of fine particles (Thevanayagam, 1998; Rahman et al., 2008; Nguyen et al., 2017). In particular, it is dependent on the fine percentage that is more capable of characterizing silty sand mixtures, in terms of liquefaction triggering, than the global void ratio. As discussed by Mitchell et al. (2005), when the fine content is very low, the fines do not contribute to the transfer force. An equation to calculate the intergranular void ratio e_g is proposed by Thevanayagam (1998), defined as

$$e_g = \frac{e + FC}{1 - FC} \tag{2.8}$$

where FC is the fine content expressed in decimals and e is the global void ratio. Eq. 2.8 is based on the assumption that fines are all inside the void spaces between the coarse grains. Consequently, the fine content does not participate in the shear strength of the granular soil structure and the behavior of the mixture is associated to the sand particles only. The intergranular void ratio e_g is equal to the void ratio e, for clean sands having zero fine content ($FC = 0\%$).

The single fine content parameter FC is not sufficient to fully characterize the mechanical behavior of mixtures and their liquefaction resistance. In fact,

in the case of high fine content and high relative density, not all fine particles will fill the void spaces. Thus, the definition of equivalent intergranular void ratio has been updated by Thevanayagam et al. (2000) as

$$e_g^* = \frac{e + (1-b)FC}{1-(1-b)FC} \tag{2.9}$$

where b varies from 0 to 1 and represents the fine fraction participating to the force transfer. If $b = 1$, all the fine particles contribute to the force transfer with the sand and the equivalent intergranular void ratio corresponds to the global void ratio e. Similarly, for clean sand ($FC = 0\%$ and $e_g^* = e$). Eq. 2.9 is applicable only when the mechanical behavior of the mixture is sand-dominated and if fines are non-plastic. Soils are considered sand-dominated when the fine content FC is lower than the threshold FC_{th} (Thevanayagam et al., 2000).

Various attempts to define the active fine fraction b and equivalent intergranular void ratio e_g^* are reported in the literature. Several researchers assume the active fine fraction b as independent of the fine content and propose a single value of b using back analysis, for a given sand-fines mixture (Thevanayagam and Martin, 2002; Ni et al., 2004). On the other hand, according to Ni et al. (2004) and Rahman et al. (2008), the active fine fraction b strongly depends on the fine content FC. Rahman et al. (2008) propose a semi-empirical equation to estimate b as

$$b = \left\{1 - exp\left[-\mu \left(FC/FC_{th}\right)^n / k\right]\right\} \left(rFC/FC_{th}\right)^r \tag{2.10}$$

where $r = \chi^{-1}$, $k = 1 - r^{0.25}$ and $\chi = D_{10}/d_{50}$ is the particle size ratio. D and d are the diameter of the coarser matrix and fines, respectively. The subscript 10 and 50 denotes the 10% lower fractile and the median value, respectively. The suggestion of empirical constants $\mu = 0.3$ and $n = 1$ is obtained using back analysis applied to datasets reported in the literature.
Mohammadi and Qadimi (2015) investigate the efficiency of Eq. 2.10, proposed by Rahman et al. (2008), analyzing several sets of data described in the literature, using a wide variety of sand-fines mixtures. Accordingly, Eq. 2.10 is not accurate in several cases when the empirical constants suggested by Rahman et al. (2008) are used.
Another estimation of the active fine fraction based on the distribution of the coordination number is given by Nguyen et al. (2017). However, the application of this formula is difficult as the coordination number is often not available for a given mixture.

Influence of non-plastic fines on the static liquefaction

Over the decades, numerous experimental studies have been carried out in order to understand the effect of non-plastic fines on the response of sands to monotonic loading, providing an extensive database. Assembling the results, it is clear that the effect of the fine content FC depends upon the basis of comparison selected to discriminate soil having different fine content (e.g. initial relative density, global void ratio or intergranular void ratio). In fact, various criteria based on different parameters have been used to compare results. So the manner in which the presence of fines affects the soil structure with respect to clean sand is a matter of discussion until now.

At a constant global void ratio, several authors report an increase in the residual shear strength and in the dilatancy behavior with the increasing of the fine content (Pitman et al., 1994; Yamamuro and Lade, 1998), while others have shown an increase in the contractancy behavior leading to a decrease in the liquefaction resistance (Throncoso and Verdugo, 1985; Zlatović and Ishihara, 1995; Lade and Yamamuro, 1997; Thevanayagam, 1998; Naeini and Baziar, 2004; Belkhatir et al., 2010a; Benahmed et al., 2015). Furthermore, some studies showed an increase in liquefaction susceptibility with the addition of fines up to limiting fine content, followed by a decrease after this threshold value (Papadopoulou and Tika, 2008; Naeini and Ziaie-Moayed, 1994).

Sand skeleton void ratio is the void ratio that corresponds only to the sand grain voids that form the soil skeleton and the silt particles are considered as voids because completely confined by the coarse grains. At a constant sand skeleton void ratio, the residual shear strength and thus the dilatancy behavior increase with the amount of fines (Shen et al., 1997; Polito and Martin II, 2001; Dash and Sitharam, 2011; Dang, 2019). According to this approach, as long as there is space within the voids among the coarse grains to fully contain all of the silt particles without any interaction, liquefaction resistance is independent of fine content (Finn et al., 1994). Beyond this value of fine content, the fine particles will interact with the coarse grains leading to an increase in the dilatancy behavior (e.g. increase of the relative density).

At constant relative density approach, many researchers have observed that the undrained residual shear strength decreases linearly with increasing fine content up to the limiting silt content (Dash and Sitharam, 2011; Missoum et al., 2013; Sadrekarimi, 2013). The determination of the relative density of each mixture is based on the void ratio of the sample and the

maximum and minimum void ratios for that particular mixture of sand and silt.

Experimental studies indicate that both the approach based on the constant global void ratio and constant sand skeleton void ratio are not reliable parameters to characterize the mechanical behavior of silty sands because they cannot control and quantify the interactions between the particles.

Effects of fines on the critical state line

In soil mechanics, the critical state for a granular soil is an important aspect to count for in engineering practice for liquefaction analyses. The predicted resistance can be compared with expected stresses due to earthquake for liquefaction potential assessment. Experimental researches show that an increase in the fine content shifts the critical state curves downwards in the $(e - \log p')$ plane, up to a threshold fine content FC_{th}, as illustrated in Fig. 2.27a (Thevanayagam and Martin, 2002; Rahman et al., 2008; Papadopoulou and Tika, 2008). After the introduction of the equivalent granular void ratio concept (Thevanayagam et al., 2000), it is widely recognized that the global void ratio e is not a consistent state variable to describe the force chains in mixture. Therefore, over the last decades, the global void ratio has been replaced by the equivalent granular void ratio, which is able to capture the effect of fine particles on the mechanical behavior. In fact, as shown in Fig. 2.27b, the critical state points fall into a unique line in the $(e_g^* - \log p')$ plane, irrespective of FC. This trend is denoted as equivalent granular critical state line ($EGCSL$) and it is confirmed by many authors (Rahman et al., 2008; Mohammadi and Qadimi, 2015; Nguyen et al., 2017).

Recently, Rahman et al. (2011) and Rahman and Lo (2012) reconsider the state parameter proposed by Been and Jefferies (1985) to an equivalent granular state parameter (Ψ^*) in terms of equivalent intergranular void ratio (replacing e with e_g^* in Eq. 2.7) defined as (Fig. 2.28a)

$$\Psi^* = e_g^* - e_{cs}^* \tag{2.11}$$

Ψ^* is very useful for the prediction of undrained strength and instability of various sandy soils over a wide range of fine contents, densities, and stress levels. In fact, since (Ψ) is defined with respect to the CSL, then a separate CSL is needed for each fine content if the global void ratio is employed. Conversely, on the hypothesis that e is replaced by the equivalent granular

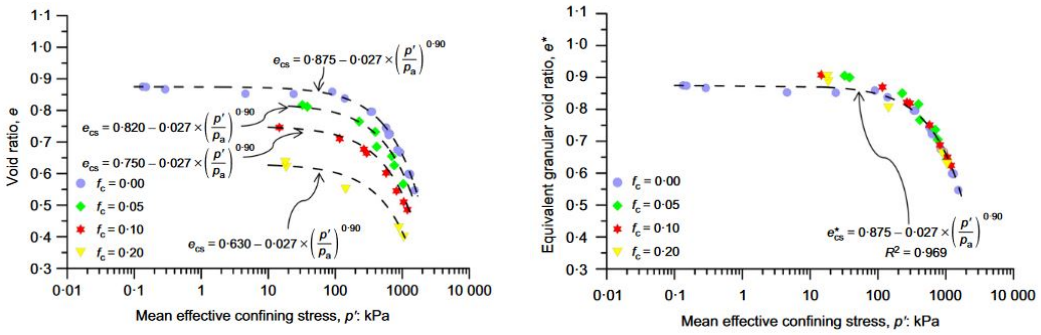

(a) (b)

Figure 2.27: Critical state lines (CSL) for soil granular mixtures in ($e - \log p'$) plane (a); and ($e_g^* - \log p'$) plane (after Barnett et al. (2020))

void ratio e_g^*, the equivalent state parameter (Ψ^*) will be defined only based on the unique line $EGCSL$. More recently, Ψ^* has been used in constitutive modelling of mixtures and to correlate mechanical behaviour independently of the value of fine content (Rahman et al., 2014b; Lashkari, 2016; Rahman et al., 2014a; Rahman and Sitharam, 2020) (Fig. 2.28b). The concept of (Ψ^*) is only applicable for a "sand-dominated" mixture ($FC < FC_{th}$), as in the case of e_g^*.

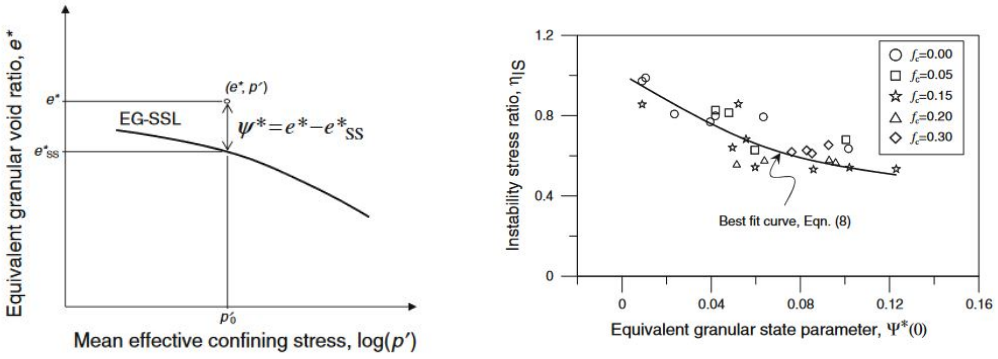

(a) (b)

Figure 2.28: Definition of equivalent granular state parameter Ψ^* (a); Relationship between instability stress ratio ($\eta_{IS} = q_{IS}/p'_0$), where the subscript IS denotes the onset of instability in the ($p' - q$) plane) and the equivalent granular state parameter for clean sand and sand with up to 30% fine contents (after Rahman et al. (2011))

2.3.2 Undrained cyclic loading

The undrained cyclic loading generally causes a progressive pore water pressure build-up that can develop large cyclic shear deformations. Two different mechanisms have been defined over the years, depending on the initial state of the granular soils (e.g. void ratio and effective confining stress), the stiffness, the cyclic energy dissipation and the characteristics of the loading: cyclic liquefaction and cyclic mobility (Castro, 1969; Vaid and Chern, 1985; Seed, 1979). For both mechanisms, the development of strains is due to the pore water pressure build-up and the associated decreasing of the mean effective stress. It is observed from experimental tests that deformations remain low until the pore water pressure reaches the 60% of the initial effective confining stress (Seed, 1979).

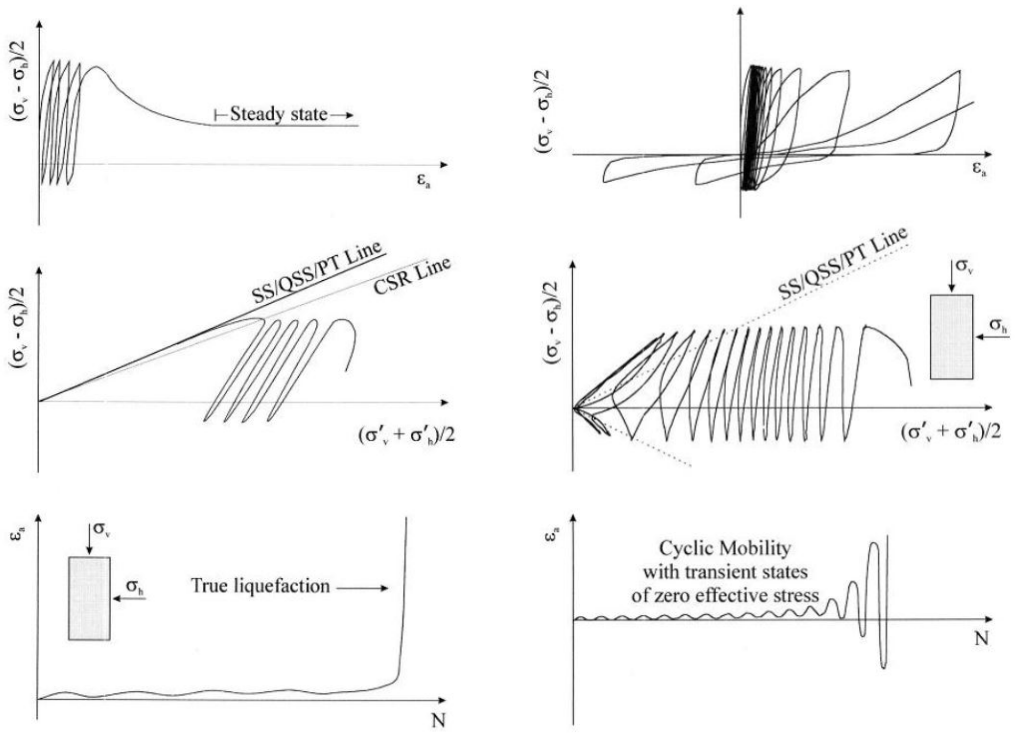

Figure 2.29: Mechanisms under cyclic loading: cyclic liquefaction (a); cyclic mobility (b) (after Vaid and Chern (1985))

The cyclic liquefaction, shown in Fig. 2.29a, is a phenomenon typical of loose to very loose sands that are only contracting and corresponds to a mechanism of instability quite similar to that already observed under

monotonic loading. It is characterized by a progressive and quasi-linear increase of the pore water pressure during the cyclic loading. During the first cycles, the axial strains are very low until reaching a particular cycle denoted as critical cycle, and then, after that cycle, the pore water pressure build-up is fast and tends towards a value close to or equal to the initial effective stress. The failure mechanism involves complete flow failure due to a significant loss of shear strength.

The cyclic mobility, illustrated in Figs 2.29b and 2.30, is a characteristic phenomenon of medium-dense to very dense sands whose volume variations under shear result in dilatation. It differs from flow liquefaction by the fact that it leads to failure through the accumulation of significant strains due to significant reduction in soil stiffness but it does not exhibit flow-type failures. In the $(q - p')$ plane, the effective stress path gradually migrates towards the origin of the axes with a reduction in the mean effective stress p' at each loading cycle. At low shear strains, the granular soil experiences a tendency for contraction, leading to development of excess pore water pressure and reduction in the mean effective stress. As the stress path moves towards the origin of the axes and crosses the phase transformation line, the soil dilates increasing the mean effective stress and consequently the shear stiffness. On the other hand, during the unloading phase, the soil contracts leading to an increase of pore pressure and thereby a decrease in the mean effective stress. The main feature of the stress path is the distinctive "butterfly" shape, which occurs to a transient zero effective stress state in a load cycle. This change in the shape of the stress-strain loop leads to the development of large cyclic strains. The transition from contractive to dilative behavior on loading, causes a change in the mechanism of pore water pressure generation and in particle arrangement and has a significant effect on the stress-strain behaviour of the soil. As shown in the $(q - \varepsilon_a)$ plane, the loading phase (dilation) leads to a rapid increase of stiffness and the opposite effect occurs during the unloading phase (contraction). Consequently, the stress-strain curve is characterized by alternate hardening and softening phases.

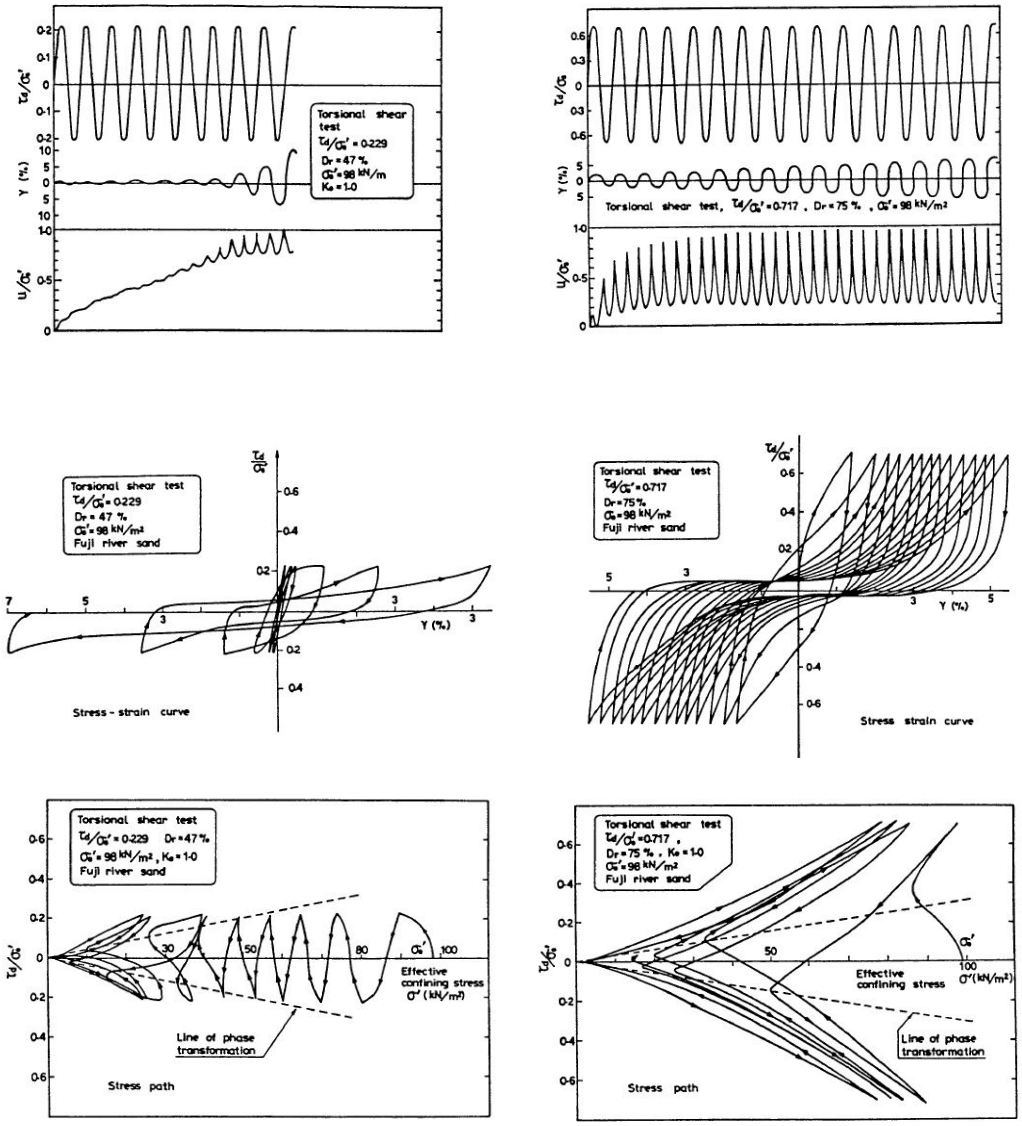

(a) (b)

Figure 2.30: Mechanisms of cyclic mobility: medium-dense sand (a); dense sand (b) (Ishihara, 1985)

2.3.2.1 Liquefaction resistance curves

The undrained cyclic stress ratio is defined by the magnitude of the cyclic shear stress required to cause liquefaction in the case of loose sand or a given strain in the case of dense sand. It is defined as

$$CSR = \frac{\tau_{cyc}}{\sigma'_c} \tag{2.12}$$

where $\tau_{cyc} = q_{cyc}/2$, σ'_c is the effective confining pressure, τ_{cyc} is the cyclic shear stress and q_{cyc} is the cyclic deviatoric stress.
It is well known that the soil state stress and density state control the number of cycles required to reach liquefaction N_L (Ishihara, 1993). This is typically determined by liquefaction resistance curves in the $(CSR - N)$ plane, which quantifies the number of cycles at a given uniform shear stress before liquefaction occurs. Hence, for each serie of tests characterized by a fixed value of relative density, a single curve is obtained, denoted as liquefaction resistance curve (Vaid et al., 1981; Benahmed, 2001), as shown in Fig. 2.31. The definition of N_L depends on the initial state of the soil. Generally, in the case of cyclic liquefaction, the critical cycle is the number of cycles necessary to achieve flow failure (Fig. 2.31a). However, in the case of cyclic mobility, N_L is defined by setting a peak-to-peak cumulative deformation level (Fig. 2.31b).The choice of the latter may be arbitrary or related to the maximum deformations eligible in the calculation of the structures. Some researchers have defined the initiation of liquefaction by a double-amplitude axial strain of 5% (Ishihara, 1985).

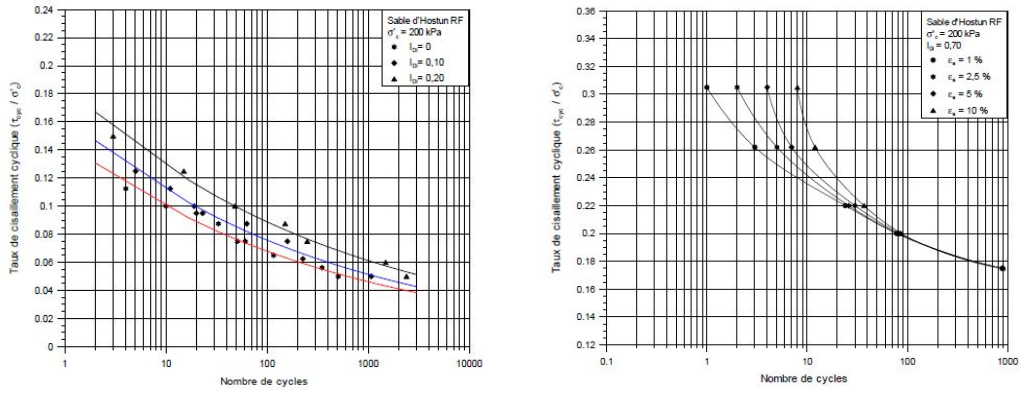

(a) (b)

Figure 2.31: Liquefaction resistance curves $(CSR - N)$: loose sand (a); dense sand (b) (Benahmed, 2001)

2.3.2.2 Influence of void ratio

The void ratio is one of the most affecting factor on the cyclic resistance of sands. In fact, the relative density controls both the type of soil reponse (cyclic liquefaction or cyclic mobility) and the shear resistance. From experimental studies, it is observed that liquefaction susceptibility increases with the increase of the void ratio (i.e. decrease of relative density) (Seed, 1979;

Vaid et al., 1981). This implies that also the cyclic stress ratio causing liquefaction failure increase with the relative density and thus, the liquefaction resistance curves for dense sands are above those of loose sands for the same type of granular soil, as illustrated in Fig. 2.31 (Ishihara et al., 1975; Vaid and Chern, 1985; Benahmed, 2001).

2.3.2.3 Influence of confining pressure

Cyclic laboratory test results indicate that liquefaction resistance increases with increasing confining stress (Seed and Lee, 1966; Peacock and Seed, 1968; Tokimatsu et al., 1986; Vaid and Chern, 1985; Chen and Lee, 1994). However, Vaid et al. (1985) show that the effect of overburden stress on the cyclic resistance ratio depends on the grains shape of the granular soil. They performed experiments on two medium sands with essentially identical gradation, but one having angular particle shapes and the other rounded. From the results, shown in Fig. 2.32, they find that the rounded Ottawa sand exhibits an extremely rapid build up of resistance with increasing density, regardless the level of confining pressure, while angular tailings sands, shows such rapid increase only at lower levels of confining pressure. To this regard, Fig. 2.32b shows that the liquefaction resistance curves in case of angular tailings become progressively flatter as the level of confining pressure increases. From Fig. 2.32, it is clear that in the range of higher relative densities, liquefaction resistance of both sands at a given value of relative density decreases with increasing confining pressure. The reason is that considerable densification, especially in case of angular sands, occurs under the application of higher confining pressure.
The combined effect of confining pressure and relative density can be observed in Fig. 2.33, where the liquefaction resistance is presented as a function of confining pressure at fixed initial relative densities for the two sands tested by Vaid et al. (1985). Fig. 2.33 indicates that a substantial decrease in resistance to liquefaction occurs with the increasing in confining pressure for both sands and that the observed decay increases with higher values of relative density and is larger for angular than for rounded sands.
In practice, this effect is accounted through the overburden correction factor K_σ, first introduced by Seed (1983) to extrapolate the simplified procedure to soil layers with overburden pressures, which is calculated as

$$K_\sigma = \frac{CRR_{\sigma'_c}}{CRR_{\sigma'_{c=100kPa}}} \tag{2.13}$$

where $CRR_{\sigma'_c}$ and $CRR_{\sigma'_{c=100kPa}}$ are the cyclic resistance ratio at a specific value of effective confining stress and at 100kPa effective confining stress,

respectively, for specimens having the same initial void ratio.

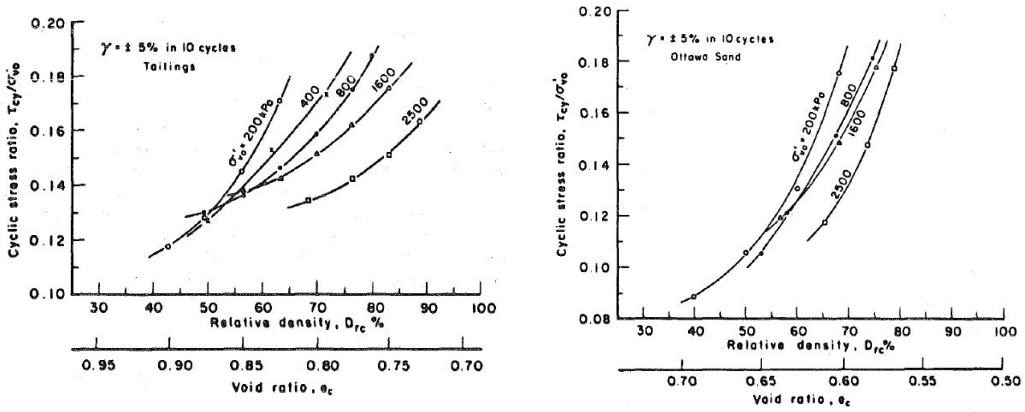

(a) (b)

Figure 2.32: Liquefaction resistance curves at various confining pressures: angular tailings sand (a); rounded sand (b) (Vaid et al., 1985)

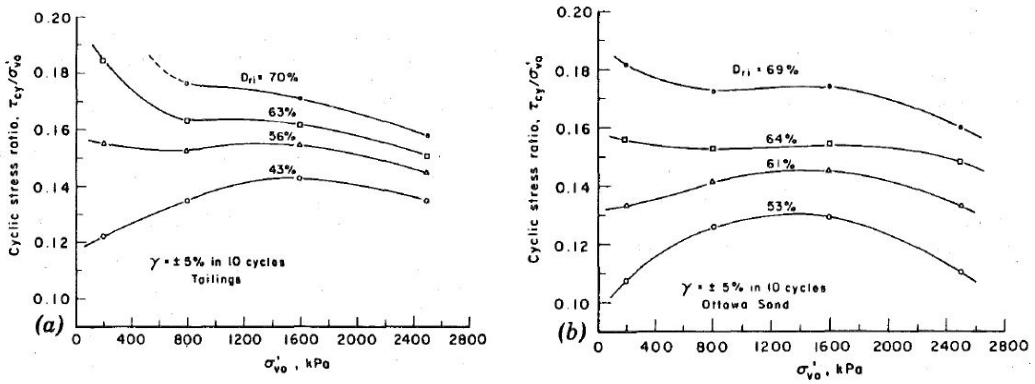

(a) (b)

Figure 2.33: Coupled effect of confining pressure and initial relative density on liquefaction resistance curves: angular tailings sand (a); rounded sand (b) (Vaid et al., 1985)

Numerous researchers have studied the influence of the overburden factor K_σ on liquefaction resistance showing that K_σ is affected by relative density, confining stress and liquefaction criterion used (Boulanger, 2003). Over the years, most K_σ relationships have been derived based upon laboratory test results (Harder Jr and Boulanger, 1997), while some other relationships have also been derived by theoretical considerations (Hynes et al., 1998; Boulanger,

2003).

In order to combine the coupled effect of relative density and confining stress on liquefaction resistance, Boulanger (2003) and Boulanger and Idriss (2004) revise the overburden factor using the critical state framework. The adopted relative state parameter index ξ_R is shown in Fig. 2.34a and is defined as the difference between the actual D_R and the critical state $D_{R,CS}$ for the same mean effective stress. Boulanger (2003) shows that the overburden factor K_σ can be expressed as a unique function of ξ_R. Thus, the recommended K_σ relationships proposed by Boulanger (2003) are then computed as (Fig. 2.34b):

$$K_\sigma = 1 - C_\sigma ln\left(\frac{\sigma'_c}{P_{atm}}\right) \tag{2.14}$$

where the coefficient C_σ can be expressed as a function of relative density (Boulanger and Idriss, 2004).

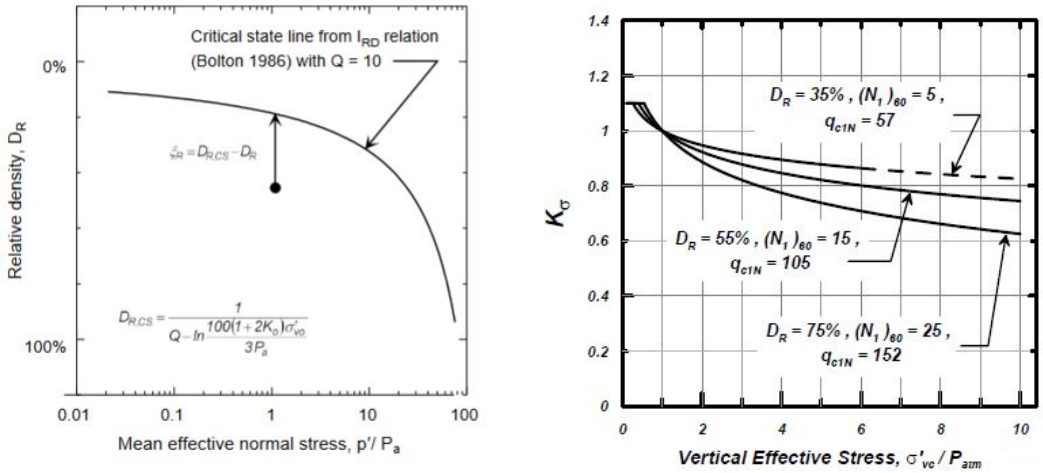

(a) (b)

Figure 2.34: Definition of the relative state parameter index ξ_R (a); K_σ relationships describing the effect that effective overburden stress has on cyclic resistance ratio CRR of sands (b) (after Boulanger and Idriss (2004))

2.3.2.4 Influence of non-plastic fines on cyclic liquefaction

Even if the effect of non-plastic fines on the liquefaction resistance of clean sand has been clearly identified in both the laboratory and the field, there is still a lack of agreement upon the factors that control the behavior of silty sand. In fact, past experimental studies reveal that the liquefaction resistance could increase (Chang et al., 1982; Dezfulian and Marachi, 1984; Kuerbis et al.,

1988; Amini and Qi, 2000) or decrease (Throncoso and Verdugo, 1985; Finn et al., 1994; Shen et al., 1997; Belkhatir et al., 2010b; Stamatopoulos, 2010) with an increasing amount of fines. While some other studies show an increase in the liquefaction susceptibility with the addition of fines up to a limit fine content, followed by a decrease after this threshold value (Cao and Law, 1991; Ling, 1992; Koester, 1994; Chien et al., 2002; Xenaki and Athanasopoulos, 2003; Papadopoulou and Tika, 2008). Polito and Martin (2003) show that these discrepancies depend on the parameter selected to characterize the soil mixture (e.g. initial relative density, global void ratio, intergranular void ratio or interfine void ratio) concluding that either the decrease or increase of cyclic resistance can be explained by the variation of the relative density with the introduction of the fine particles. In fact, as explained in Section 2.3.1.4, the maximum and minimum void ratios vary with fine content, and also control the variation of the relative density. Fig. 2.35 shows the variation of relative density with respect to the fine content keeping constant the value of the global void ratio. As the fine content increases, it is observed that the relative density of the specimens first decreases and then increases as a result of the corresponding changes in the maximum and minimum void ratios. Thus, a decrease in relative density produces a decrease in cyclic resistance and an increase in relative density causes an increase in cyclic resistance.

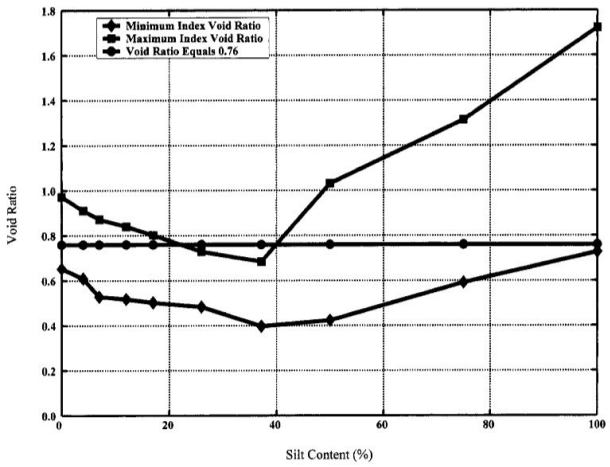

Figure 2.35: Variation in index void ratios with silt content for mixtures of Yatesville sand and silt (after Polito and Martin (2003))

The same problem is reported in practice for the field based methods for determining liquefaction susceptibility. Current simplified liquefaction evaluation procedures, such as methods based on SPT blow counts or CPT measurements, rely on extensive laboratory research and extrapolations of observed field data concerning past earthquakes and specify the cyclic resistance of a

sandy soil as a function of non-plastic fine content. Different fine content correction factors have been defined over the years to predict the liquefaction resistance concluding that the liquefaction resistance increases with increasing non/low-plastic fine content up to $FC = 35\%$ and remains constant thereafter (Seed, 1983; Kayen and Mitchell, 1997; Youd and Idriss, 2001; Cetin et al., 2004; Boulanger and Idriss, 2004). Whether this increase is caused by an actual increase of resistance or a decrease of penetration resistance is not clear. The experimental studies in literature show that the behavior of silty sand cannot be described by only the fine content parameter but the relative density is an important factor affecting the response. Hence, corrections based only on fine content should be used with engineering judgment and caution.

Influence of non-plastic fines on liquefaction resistance curves
As for the previous case of undrained monotonic loading, some researchers have attempted to apply the concept of equivalent intergranular void ratio e_g^* (Section 2.3.1.4) to predict cyclic liquefaction resistance of mixtures, irrespective of fine content, demonstrating consistent relationships between the cyclic strength and e_g^* (Thevanayagam and Martin, 2002; Rees, 2010; Hsiao and Phan, 2016; Porcino and Diano, 2017).

Rahman et al. (2008) investigate whether the cyclic resistance (defined in Ishihara (1993) as the cyclic stress ratio required to cause liquefaction in 15 cycles) can be correlated to e_g^*, independently of fine content, through the analysis of experimental results from the literature review. As shown in Fig. 2.36a, when the cyclic resistance is analyzed in terms of global void ratio e, multiple liquefaction resistance curves are identified and the effect of increased fine content on the cyclic response of sand-silt mixtures corresponds to a more contractive behavior and to a decrease in liquefaction resistance. However, when analyzing in terms of equivalent granular void ratio, the influence of fine content is significantly reduced and a unique curve is obtained (Fig. 2.36b).

Another approach that helps to interpret the results is based on the state parameter Ψ, which combines the effect of relative density and stress state to characterize the sand behavior (after Been and Jefferies (1985), Section 2.3.1.4), while the equivalent granular void ratio considers the density state only. Stamatopoulos (2010), Papadopoulou and Tika (2008) and Huang et al. (2004) show that the cyclic strength decreases as the state parameter increases at a rate that progressively decreases and that the relationship between the cyclic resistance and the state parameter is unique, independently of fine content. Moreover, many researchers indicate that the equivalent state parameter

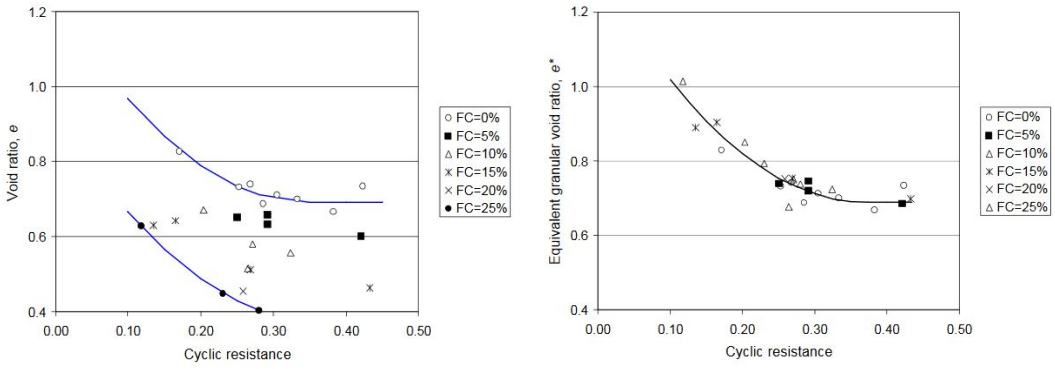

(a) (b)

Figure 2.36: Cyclic resistance for Sydney sand with different fine contents in terms of global void ratio (a) and equivalent granular void ratio (b) (after Rahman et al. (2008); source data after Polito and Martin II (2001))

Ψ^*, based on the definition of e_g^* and the unified critical state line, is better correlated to the cyclic resistance than Ψ, which is derived using e and separate critical state lines for each type of fine content (Huang and Chuang, 2011; Rahman et al., 2014a; Qadimi and Mohammadi, 2014), as presented in Fig. 2.37.

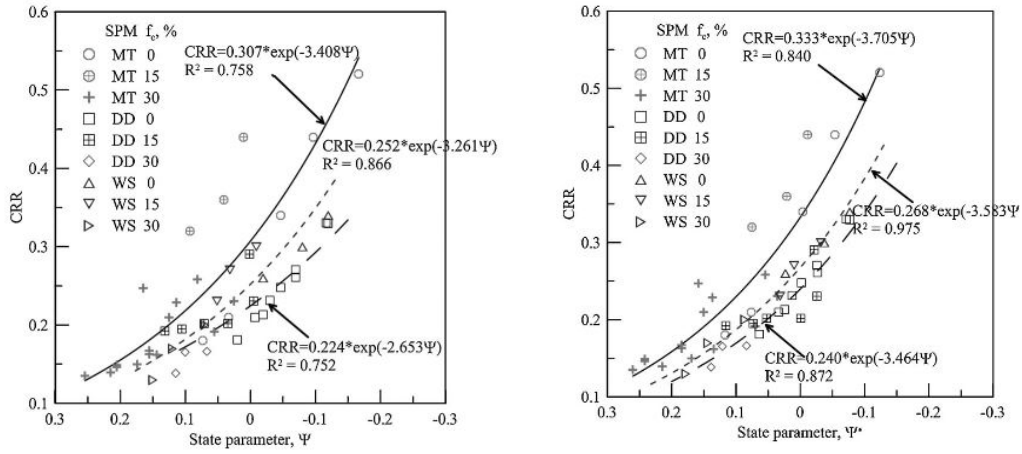

(a) (b)

Figure 2.37: Cyclic resistance for Mai Liao sand with different fine contents in terms of state parameter (a) and equivalent state parameter (b) prepared by water sedimentation (WS), dry deposition (DD) and moist tamping (MT) methods (Huang and Chuang, 2011)

Influence of non-plastic fines on the excess pore pressure generation

The rate and magnitude of pore water pressure generation is controlled mainly by the level of induced shear strains and may have important effects on liquefaction resistance, stability and settlement characteristics (Hazirbaba and Rathje, 2004; Chang et al., 2007). Generally, the excess pore pressure generation is quantified in terms of excess pore pressure ratio r_u defined as the ratio of the excess pore water pressure Δu to the initial effective mean confining stress p'_0. This ratio varies from zero to unity corresponding to the complete transfer of the load to the pore water pressure. In literature, two methods have been used to study the excess pore pressure response of granular soils.

Many researchers (Lee and Albaisa, 1974; Seed et al., 1975) show that there is a clear relationship between the pore water pressure ratio and the normalized cycles ratio, which is the ratio of cycles of loading to the loading cycle required to cause liquefaction. Based on experimental results from stress-controlled cyclic tests on clean sand, it is observed that all the curves fall within a relatively narrow band for a wide range of relative densities and consolidation pressures, suggesting that density may affect the number of cycles to reach liquefaction, but it only has a minor effect on the pore water pressure generation curve. To this regard, Konstadinou and Georgiannou (2014) show that despite the variation in type of sand, density and testing apparatus, the resulting curves from past published data fall into the narrow band proposed by Lee and Albaisa (1974) as shown in Fig. 2.38a.
Dash and Sitharam (2009) investigate the excess pore water pressure generation over a wide range of fine content, showing that the upper bound values proposed by Lee appears to be careless in case of sand-fines mixtures. Thus, they propose new pore pressure bands in order to integrate the upward deviations in upper bound values due to the presence of fines particles, presented in Fig. 2.39a. These finding are confirmed by other studies (Polito et al., 2008; Karim and Alam, 2014; Park et al., 2015; Porcino and Diano, 2017).

On the other hand, Dobry (1985) investigate the pore water pressure generation with respect to the shear strain and number of loading cycles for sands for a wide range of relative densities (Fig. 2.38b). The results from strain-controlled cyclic tests indicate the existence of a threshold shear strain ($\gamma = 0.01\%$) below which excess pore water pressure does not develop, while at large strains significant pore water pressure increase reaching the liquefaction ($r_u > 0.8$). Dobry (1985) boundary curves correspond to the specific case

in which r_u values are estimated at the end of the 10th cycle of loading.
As in the case of the stress-based method (Lee and Albaisa, 1974; Seed et al., 1975), also the applicability of strain-based models to non-plastic silty soils, has been investigated over the past decades. Many authors observe that experimental data for silty sands, at higher strains, have a tendency to fall on the right of the lower bound curves proposed by Dobry (1985) for clean sands, as shown in Fig. 2.39b (Erten and Maher, 1995; Dash and Sitharam, 2009; Porcino and Diano, 2017).

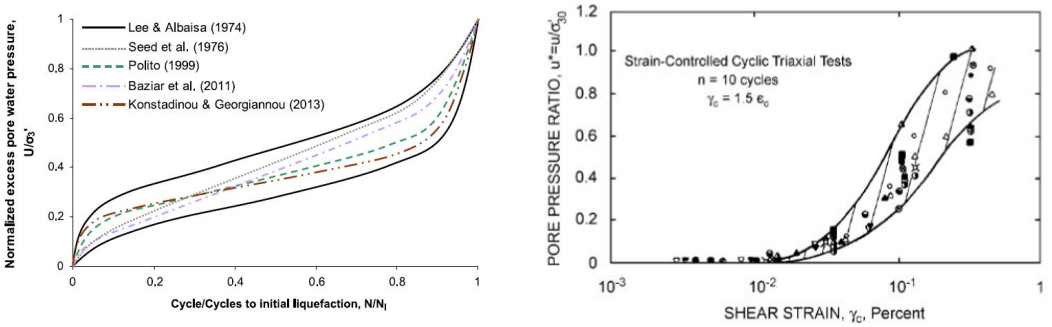

(a) (b)

Figure 2.38: Excess pore water pressure ratio data for clean sands reported in literature versus the cycle ratio (Konstadinou and Georgiannou, 2014) (a); excess pore water pressure generation versus shear strains (Dobry, 1985) (b)

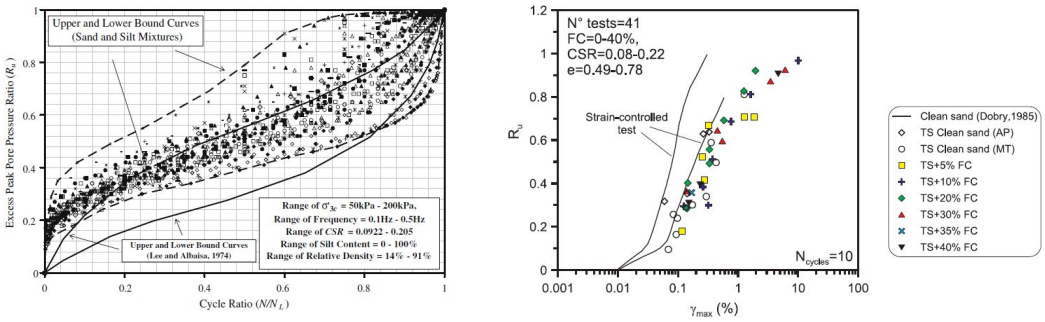

(a) (b)

Figure 2.39: Upper and lower bound curves of excess pore pressure ratio versus normalized cycles ratio proposed by Dash and Sitharam (2009) (a); trend of excess pore pressure ratios versus shear strains for silty sand compared with the upper and lower bound curves proposed by Dobry (1985) for clean sands (Porcino and Diano, 2017) (b)

2.3.3 Strain-dependent dynamic properties

It is well known that the evaluation of strain-dependent soil dynamic properties, such as shear modulus and damping ratio, varies significantly with the amplitude of shear strain under cyclic loading and is an important aspect for the prediction of the soil behavior. Shear modulus G represents the shear stiffness of soil and is defined as the slope of the $(\tau - \gamma)$ curve (Fig. 2.40a), where τ and γ denote the amplitude of shear stress and shear strain, respectively (Ishihara, 1996). According to Ishihara (1996), the material damping is calculated as the dissipated energy, ΔW, at a loading cyle over the total energy, W.

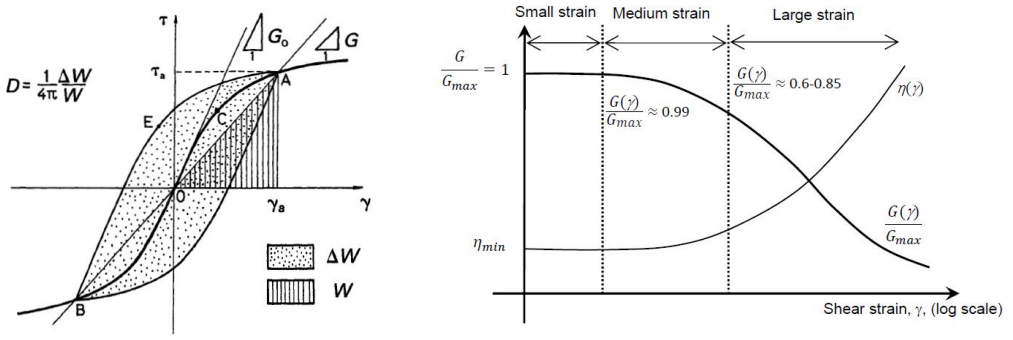

(a) (b)

Figure 2.40: Nonlinear hysteresis loop ($\tau - \gamma$ curve, Ishihara (1996)) (a); shear modulus and damping ratio curves versus amplitude of shear strain (b) (Wang and Santamarina, 2007)

Fig. 2.40b presents typical curves of damping and modulus ratio versus the amplitude of shear strain in a logarithmic scale. From this figure, it can be observed that the shear modulus decreases with respect to the shear strain, while the damping ratio increases with the increase of the amplitude of shear strain. In particular, many studies report that at very small levels of strains, shear modulus presents a maximum value which is denoted as maximum shear modulus, G_{max} or G_0, while damping ratio has a minimum value which is denoted as minimum damping ratio, D_{min} (Hardin and Drnevich, 1972; Drnevich, 1978; Seed et al., 1986). The ratio of G (calculated at a certain shear strain level) to G_{max} is denoted as shear modulus degradation or stiffness degradation and the curve expressing the ratio G/G_{max} versus the shear strain is denoted as shear modulus degradation curve or decay curve. Therefore, the shear modulus decay curve and the damping ratio are key parameters for evaluating soil response under dynamic loading, due to their strain dependency. In the laboratory, the most widely used procedure to de-

termine the shear modulus and damping is the resonant column test, but also the cyclic triaxial test procedure with precise monitoring of axial strains can be employed.

2.3.3.1 Influence of void ratio

It is widely recognized that the maximum shear modulus decreases, while the minimum damping ratio increases with the increase of void ratio because the number of contacts decreases significantly leading to a reduction of the soil stiffness (Hardin and Richart Jr, 1963; Hardin and Drnevich, 1972; Iwasaki and Tatsuoka, 1977). The effect of void ratio on G_{max} is shown in Fig. 2.41, for various granular soils collected from the literature (Bui, 2009).

Based on experimental studies, the effect of void ratio on G_{max} can be captured by using an empirical void ratio function, denoted as $f(e)$. Over the past, many void ratio function $f(e)$ have been proposed, with respect to the type of soil, which can be classified into hyperbolic and exponential functions (Hardin and Richart Jr, 1963; Drnevich, 1978; Jamiolkowski et al., 1995; Wichtmann and Triantafyllidis, 2004). However, the curves $G(\gamma)$ and $D(\gamma)$ are independent of void ratio, as presented in Fig. 2.42.

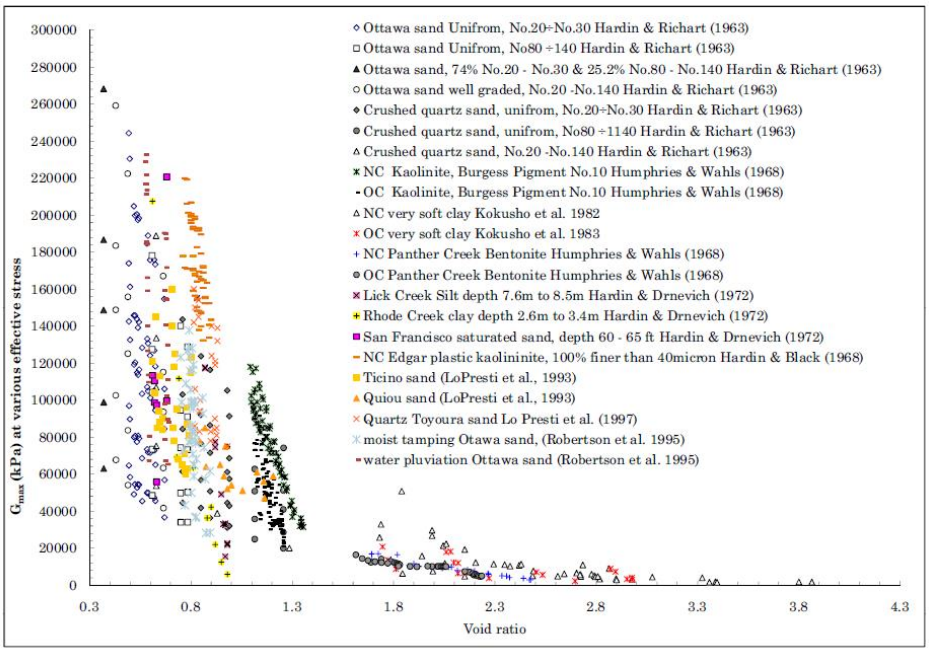

Figure 2.41: Maximum shear modulus versus void ratio for various materials (Bui, 2009)

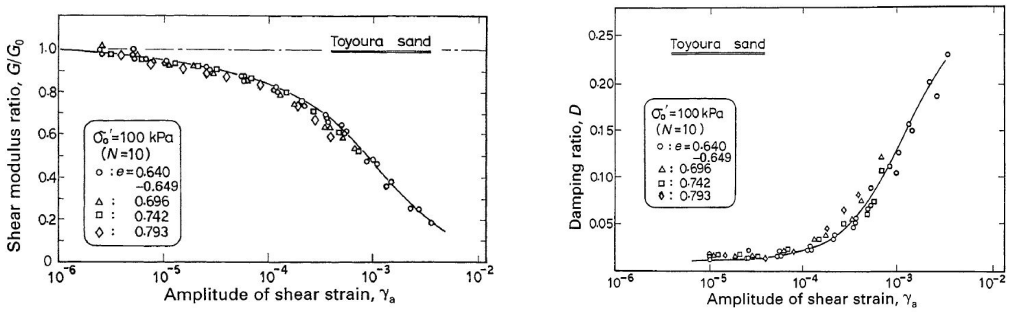

(a) (b)

Figure 2.42: (a); Normalized shear modulus (a) and damping ratio (b) versus shear strain with various void ratio conducted under a confining stress of 100kPa (Kokusho, 1980)

2.3.3.2 Influence of confining pressure

Many researchers show that the maximum shear modulus increases with the confining pressure p'_0 because at higher effective stress, the orientation of soil particles may rearrange leading to an increase of the density.
Hardin and Black (1966) propose the widely accepted empirical relation to predict G_{max} in soils, through the following general form:

$$G_{max} = Ap_a \left(\frac{p'_0}{p_a}\right)^n f(e) \tag{2.15}$$

where A is a material constant which depends on the type of soil, p_a is the atmospheric pressure (100 kPa), n is the stress exponent and $f(e)$ is the empirical void ratio function selected.
The value of the power n depends on the shear strain amplitude, at small shear strain (i.e. $\gamma < 10^{-4}$) it varies from 0.4 to 0.62, but the value of 0.5 is accepted by many researchers (Hardin and Richart Jr, 1963; Hardin and Black, 1966; Drnevich, 1978; Athanasopoulos and Richart Jr, 1983; Jamiolkowski et al., 1995; Shibuya et al., 1997).

Due to the dependency of the confining stress on the shear strength τ and initial shear modulus G_{max}, the rate of reduction in shear modulus with strain becomes greater as the confining stress decreases (Iwasaki et al., 1978; Kokusho, 1980; Ishihara, 1996), as shown in Fig. 2.43a. Consequently, the damping ratio versus the shear strains tends to increase with decreasing confining stress (Fig. 2.43b).

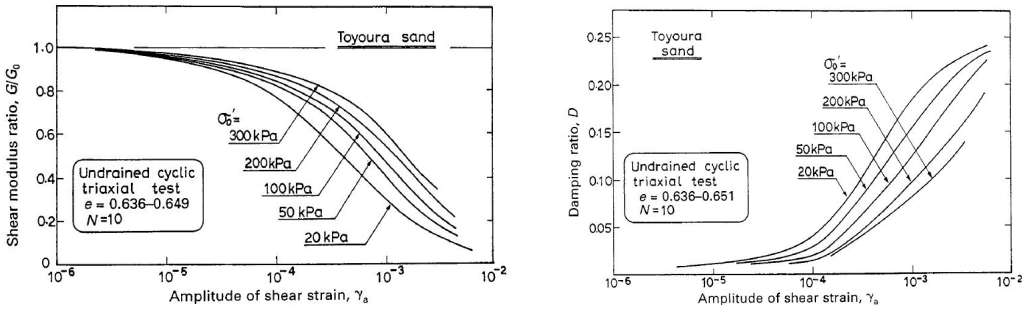

(a) (b)

Figure 2.43: Effects of confining stress on the strain-dependent shear modulus (a) and damping ratio (b) (Kokusho, 1980)

2.3.3.3 Influence of non-plastic fines

Since 1960's many experimental studies have been carried out to estimate the shear modulus for clean sands or gravels, while studies on sand containing fines are relatively limited. To this regard, some studies show that that G_{max} decreases with increasing fine content (Iwasaki and Tatsuoka, 1977; Salgado et al., 2000; Carraro et al., 2009; Wichtmann and Triantafyllidis, 2014; Goudarzy et al., 2016), while Tao et al. (2004) observes that G_{max} decreases with increasing non-plastic up a certain value of FC and then increases.
Several attempts have been made to refine Eq. 2.15 to capture the effect of fine content on maximum shear modulus by defining reduction factors (Iwasaki and Tatsuoka, 1977; Wichtmann and Triantafyllidis, 2014). Neverthless, these approaches rely on back-analysis, thus Rahman et al. (2012) propose an approach based to a single relationship between G_0 and the equivalent granular void ratio e_g^* (Section 2.3.1.4), irrespective of fine content. According to this approach, the global void ratio e is replaced by the equivalent granular void ratio e_g^* in order to predicte G_{max} with good accuracy. Goudarzy et al. (2016) confirm the existence of a unique relationship in the $(G_{max} - p'_0 - e_g^*)$ space defined for clean sand or sand with fines, as shown in Fig. 2.44b. Fig. 2.44a shows that G_{max} depends on FC and the surface is moved downward for increasing FC in the $(G_{max} - p'_0 - e)$ space, while when e is converted to e_g^*, a unique surface is obtained (Fig. 2.44b).

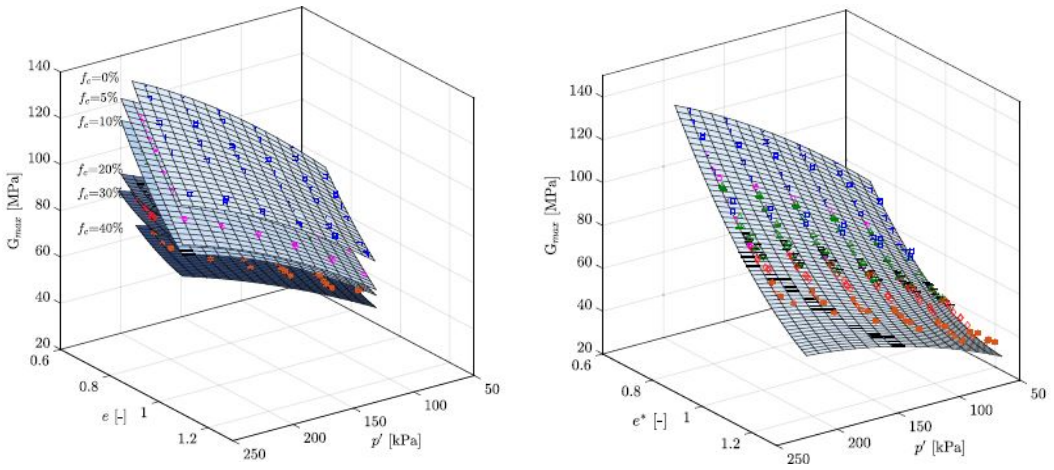

(a) (b)

Figure 2.44: The effect of fine content on maximum shear modulus in the $(G_{max} - p'_0 - e)$ space (a) and the $(G_{max} - p'_0 - e^*_g)$ space (b) (Goudarzy et al., 2016)

2.4 Constitutive models for soil rheology

The evaluation of liquefaction triggering and potential consequences are currently estimated through two types of approaches: empirically based simplified procedures and advanced numerical models based on the consideration of complex nonlinear soil behaviors. To this regard, several constitutive models for sand have been developed aiming to predict the progressive accumulation of plastic strains and the effective stress path for cyclic mobility under undrained cyclic loading conditions (Iwan, 1967; Dafalias, 1986; Prevost, 1985; Iai et al., 1990b; Manzari and Dafalias, 1997; Cubrinovski and Ishihara, 1998; Papadimitriou et al., 2001; Yang et al., 2003; Dafalias and Manzari, 2004; Byrne et al., 2004; Boulanger and Ziotopoulou, 2015; Fuentes and Triantafyllidis, 2015).

In order to understand the phenomenology of nonlinear soil response to dynamic loading, numerical models should be able to capture the essential physics of soil nonlinearity such as hysteretic behavior and pore pressure generation. Computational methods use the principles of mechanics and incorporate appropriate constitutive relations to properly characterize a given site and to describe the behavior of soils under different types of loading. The relevance of a computational method with respect to the soil behavior depends strongly on the accuracy of the calibration and on the numerical model parameters selected.

A constitutive model should be able to allow for different significant factors that affect the behavior of granular soils, such as soil density, confining stress, drainage conditions, loading conditions, among others, and reproducing salient aspects of the aforementioned contractive-dilative behavior (Kramer and Elgamal, 2001). Each constitutive model presents advantages and limitations, which may be prioritized with respect to the geotechnical engineering application and modelling purpose. However, in order to simulate pressure-dependent soil response under cyclic loading conditions, soil constitutive models typically include a large number of parameters. Thus, a reliable calibration of soil models is often difficult, especially if the constitutive parameters do not have a clear physical meaning. In fact, the calibration procedure is highly dependent upon the performance of constitutive model, and generally, a compromise, which involves considerable engineering judgment, must be made by choosing a reliable set of material parameters to properly characterize the response of granular soils.
In the 1990s, the VELACS project (VErification of Liquefaction Analysis by Centrifuge Studies) evidenced the need of validating the calibration of constitutive models in order to allow reliable predictions of excess pore pressure in numerical simulations and improve existing methods for the analysis of the consequences of soil liquefaction (Arulanandan et al., 1995). One of the major lessons learned from the VELACS project is that constitutive models play an essential role in dynamic soil modeling analysis, but yet there is still considerable ambiguity in the calibration procedure.
More recently, the LEAP-2017 project (Liquefaction Experiments and Analysis Projects) has produced reliable experimental data for the assessment, calibration, and validation of constitutive models for soil liquefaction (Kutter et al., 2018, 2020; Manzari et al., 2020). The results emphasize that it is necessary to improve calibration procedures, to assess the effects of experimental uncertainties on computed soil responses, to define the validity range of numerical predictions and to quantify the degree of replication of experiments.

2.4.1 Liquefaction front model

In this research, the extended 3D Iwan-Iai constitutive model (Iwan, 1967; Joyner, 1975; Joyner and Chen, 1975; Iai et al., 1990a,b; Santisi d'Avila et al., 2018) is adopted with the aim of modeling the nonlinear behavior of satured granular soils under cyclic loading taking into consideration the excess pore water pressure generation. This constitutive model is based on multiple inelastic shear springs, defined in the deviator strain space (Towhata and Ishihara, 1985), considering, furthermore, the effect of rotation of principal stress axis directions, which is an important aspect to take into account

in the cyclic soil behavior. According to this model, the excess pore water pressure generation is modelled by the liquefaction front concept. With the terminology "liquefaction front" we referred to the correlation between the cumulative shear work produced during cyclic loading and the excess pore water pressure at each state of shear stress, independent of the shear stress paths (Towhata and Ishihara, 1985). As shown in Fig. 2.45, the liquefaction front represents the envelope of stress points at equal shear work, and as the shear work is accumulated by cyclic shear, the liquefaction front moves towards the failure line.
Thus, the Iai et al. (1990a) constitutive model allows to estimate the effective mean stresses from the shear work using few parameters that can easily be obtained by fitting laboratory data, obtained from undrained stress controlled cyclic tests. In particular, the model is numerically controlled by five material parameters (S_1, w_1, p_1, p_2 and c_1) which characterize the liquefaction properties of the soil.

The extended 3D Iwan-Iai constitutive model is incorporated in the finite element SWAP_3C code (Santisi d'Avila et al., 2018), which is used in this study. For more detailed explanation of the model and its parameters, the reader is suggested to see Section 5.1.

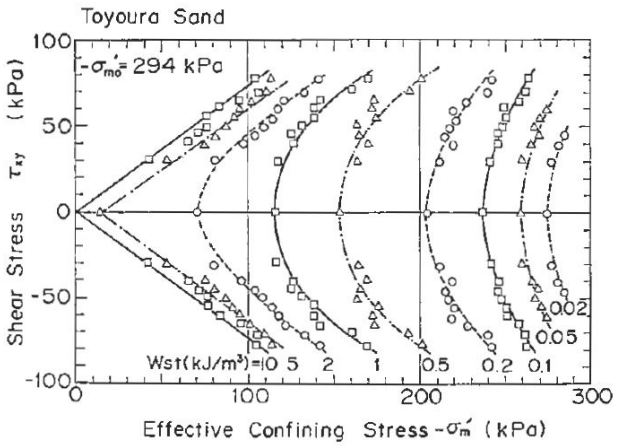

Figure 2.45: Envelope of stress points at equal shear work (after Towhata and Ishihara (1985))

2.4.2 Seismic site characterization

A proper measurement of dynamic soil properties is essential to predict the non-linear soil behavior under seismic loading conditions. Over the last

few decades, great progress has been achieved in predicting the onset of liquefaction and its consequences via field observations, laboratory tests, and advanced numerical modeling. Nevertheless, capturing the seismic response of a layered soil deposit in terms of settlements, accelerations, and excess pore pressures is still an important challenging issue, even under free-field conditions and 1D horizontal shaking. Additionally, seismic hazard is strongly affected by site response with reference to the amplification of the ground motion for the specific stratigraphic and topographic conditions and to instabilities due to ground shaking.

The propagation of seismic waves directly depends on the material properties of the medium through which they travel. Hence, uncertainty associated with the soil properties inevitably affects the seismic ground response.
Recent and past earthquakes, such as 1985 Mexico City, 1989 Loma Prieta, 1994 Northridge, 1995 Kobe events, among others, underline the need to characterize the effect of the local soil conditions on seismic site response prediction. It has been widely recognized that the seismic site effects are generally related to the stratigraphy, the surface topography, the impedance contrast and the rheology of the soils involved during the propagation of seismic waves (Semblat et al., 2005). Current seismic design codes consider the seismic site effects through a ground type classification solely based on the average shear velocity in the upper 30m of the soil profile, $v_{s,30}$, proposed by Borcherdt (1994), neglecting the depth of the bedrock and the property of the soil below 30m. Nevertheless, it has been recognized that $v_{s,30}$ is a useful parameter to capture some features of the local site amplification effects (Dickenson and Seed, 1996; Dobry et al., 2000; Seyhan et al., 2014; Seyhan and Stewart, 2014; Derras et al., 2016). However, several researches (Park and Hashash, 2004; Mucciarelli et al., 2006; Castellaro et al., 2008; Cadet et al., 2008; Luzi et al., 2011; Héloïse et al., 2012; Derras et al., 2017; Castelli et al., 2016) show that $v_{s,30}$ cannot be used as the single-site proxy to discriminate soils in terms of seismic amplification over the whole frequency range of interest. To this regard, Steidl (2000) and Park and Hashash (2004) recommended the introduction of a depth-to-bedrock parameter since they found that the previsions based on $v_{s,30}$ are over and under conservative for deep sediments at short and long periods, respectively. Many alternatives to $v_{s,30}$ are proposed to improve site soil characterization accounting for additional information on the shear wave velocity profile with depth, the site dominant frequency f_0, the impedance contrast between sediments and bedrock and the depth to the bedrock. Various studies (Cadet et al., 2008; Luzi et al., 2011; Kotha et al., 2018; Pitilakis et al., 2013; Castellaro and Mulargia, 2014; Zhao et al., 2006; Gallipoli and Mucciarelli, 2009) propose new site classification

based on a combination of these different proxies. Gallipoli and Mucciarelli (2009) and Cadet et al. (2008) propose a two-parameters site classification approach through the dominant frequency f_0 and the average shear wave velocity $v_s(\bar{Z})$ in the shallow soil up to the reference depth $\bar{Z}$. Kotha et al. (2018) introduce a new approach for the classification of sites characterized by the kernel density distributions of $v_{s,30}$, $v_{s,10}$, H_{800} and the predominant period. Recently, several researchers explore the performance of different site proxies in order to reduce the aleatory variability on the seismic prediction. Derras et al. (2017) investigate the performance of four site condition proxies, $v_{s,30}$, f_0, the topographical slope and the depth H_{800} (the depth where the shear wave velocity v_s reaches 800 m/s) using a neural networks approach, in order to assess their benefits to reduce the uncertainty of the site response. They conclude that the best single-proxy is $v_{s,30}$ for periods below 0.6s, and f_0 or H_{800} at longer periods and that the best pair is ($v_{s,30}$, H_{800}) at short periods and (f_0, H_{800}) at long periods. Stambouli et al. (2017) conduct a numerical investigation on 858 soil columns corresponding to real sites profiles from Japan, USA, and Europe. They show that the best performing site proxy is the impedance contrast between bedrock velocity and minimum surface velocity but even the pair ($v_{s,30}$, f_0) can reduce significantly the variability of the site response at least around 60%. Lately, Zhu et al. (2020) study the best performing site proxies for the linear characterization of the site response using 1840 ground-motion recordings from a KiK-net database. They focus their study on the dominant period of the site T_0, the site depths $Z_{0.8}$ and $T_{1.0}$, which are measured site depths to layers having shear-wave velocity 0.8 and 1.0 km/s, respectively. They demonstrate that predictions based on the configuration using T_0 as the primary and $v_{s,30}$ as the secondary proxy can induce a significant reduction in site-to-site amplification variability. Ciancimino et al. (2018) adopt some classical proxies for site characterization in the context of seismic site effect estimation. Their reliability is evaluated, under the assumption of linear regime, and compared to the ground type classification adopted in the Eurocode 8 (Eurocode, 2005), New Zealand Standard (NZS, 2004) and that suggested by Pitilakis et al. (2013). Following these recent reviews, the prediction of the seismic site response using only a single proxy over the whole period range does not seem satisfactory. Hence, to improve the site amplification estimation, it is advisable to use a combination of site proxies rather than a single site proxy.

2.5 Conclusions

The literature review presented in this chapter has provided a summary of the main existing works of experimental, theoretical and also numerical research on liquefaction phenomenon under monotonic and cyclic loading, with emphasis on the most recent studies such as the influence of non-plastic fine particles.
Literature research has shown that the presence of fines in the sand significantly affects its mechanical behaviour, particularly the initiation of liquefaction and the excess pore water generation. However, previous studies have also shown a discrepancy in terms of results, which may be due to the fact that the response of silty sand depends on various parameters such as type of sand, grains shape, range of fine content. Recently, it has been demonstrated that the concept of equivalent intergranular void ratio seems to be the most reliable parameter to understand the influence of fine content for soils presenting a sand dominant behavior.
The experimental program in the framework of this thesis is carried out on a clean sand and sand containing non-plastic fines covering a wide range of void ratios, confining pressures and fine contents in order to investigate the correlation between various factors and the liquefaction resistance and provide a robust and reliable dataset of laboratory tests.
The second objective is to assess the influence of these factors on the liquefaction model parameters characterizing the soil behavior according to constitutive models, and quantify and compare the accuracy of the selected constitutive model in simultaneously capturing the seismic response of 1D layered soil deposits seismic wave propagation.
The last objective is to investigate the influence of a proper site characterization on the seismic response of 1D layered soil profiles in terms of amplification factors.

Chapter 3

Materials and experimental procedures

This chapter presents the different soil samples, test devices and experimental procedures related to the present thesis. First, the characterisation of the tested material is presented and details pertaining to triaxial and resonant column testing systems with respect to mechanical components, data acquisition, and control system are described. Then, the experimental techniques used for clean sand and sand-fines specimens are also specified. Test repeatability of specimens prepared using the moist tamping undercompaction reconstitution method is demonstrated through duplicate testing under the same conditions for both monotonic and cyclic loading.

3.1 Materials tested

Soil samples are reconstituted in laboratory by mixing HN31 Hostun-RF sand and different amounts of commercial Silica C500. HN31 Hostun-RF sand is a quartz, medium-size sand with sub-angular particles ranging from 0.125 to 0.8 mm in average diameter (Fig. 3.1). Its color ranges from gray-white to rosy-beige and its chemical components consist of a large amount of silica ($SiO_2 > 99\%$). The physical properties of HN31 Hostun-RF sand are given in Table 3.1.
Silica C500 is a non-plastic fine silica flour ($SiO_2 > 99\%$), having a white color and a sub-angular grain shape.
The particle-size distribution curves of HN31 Hostun-RF sand, silica C500 and sand-fine mixtures for FC in the range $[0 - 20\%]$ are shown in Fig. 3.2.

In order to perform tests on mixtures with different relative densities, the maximum and minimum void ratio of the mixtures has to be determined, that represent the loosest and densest conditions for soil and can be used to assess the relative density of soil. The relative density $D_R = 100 \cdot (e_{max} - e)/(e_{max} - e_{min})$ depends on the global void ratio e and the maximum and minimum void ratios of the mixture, e_{max} and e_{min}, respectively. The presence of fines mixed together with sand modifies the soil structure when compared to clean sand.

To this regard, the curves of maximum and minimum void ratios as function of the fine content give information about the sand-fines mixture characteristics.

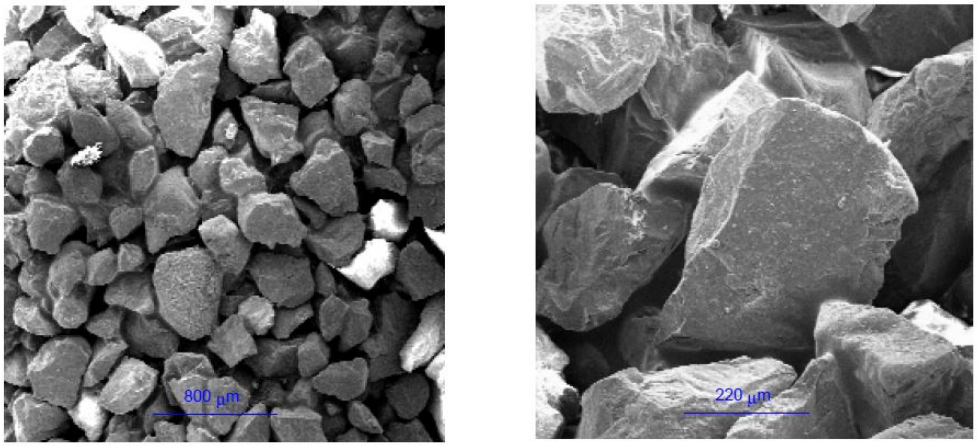

(a) (b)

Figure 3.1: Scanning electron microscope (SEM) image of Hostun sand (Benahmed, 2001)

Table 3.1: Properties of HN31 Hostun-RF sand

Sand	D_{50} (mm)	C_u	e_{min}	e_{max}	ρ (kg/m^3)
HN31 Hostun-RF Sand	0.32	1.57	0.67	1.00	2650

In this research, the variation of e_{max} and e_{min} with the increase of fine content is determined according to the French (NF-P94-059, 2000) and the Japanese Geotechnical Society (JGS-0111-2009, 2009) standards. The minimum void ratio is determined, according to both guidelines, producing the sample by pouring in a mold with a funnel, at a constant rate. Concerning the determination of the maximum void ratio, the Japanese standard (JGS-0111-2009, 2009) indicates to produce samples by pouring 10 layers in the mold and applying 100 impacts to the mold side, after each layer, to compact the sample. The French standard (NF-P94-059, 2000) prescribes to place the sample in the mold and compact using a small shaking table.

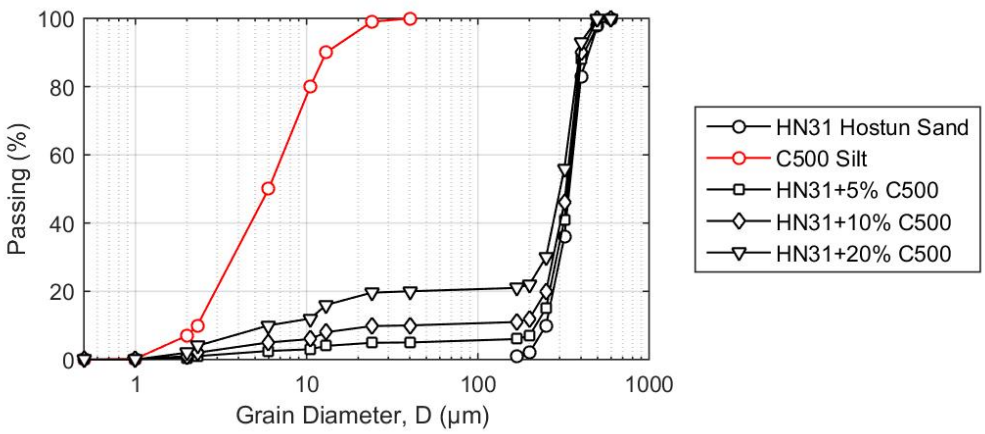

Figure 3.2: Grain size distribution of HN31 Hostun-RF sand, Silica C500 silt and various mixtures (5, 10 and 20%)

The maximum and minimum void ratio curves obtained for HN31 Hostun-RF sand with various fine contents are shown in Fig. 3.3. Even though the French procedure is suggested for sands presenting small fine fractions ($FC < 12\%$), it is also used for higher fine contents and then compared to the Japanese one. According to Fig. 3.3, the trend of e_{min} (densest mixtures) has first a decrease and then an increase, for larger fine content. In fact, for small fine content, some fine particles are included in the voids spaces between the coarse particles causing a decrease in void ratio. When the fine content increases and the maximum density is reached at the fine content threshold FC_{th} (Thevanayagam, 1998), the coarse particles are still in full contact with each other, but the void spaces are completely filled with fine particles. In this study, the threshold is $FC_{th} \cong 20\%$, as shown in Fig. 3.3. The fine content threshold FC_{th} represents the transition between sand dominant behavior and silt dominant behavior. When the fine content exceeds this threshold, the coarse particles are re-arranged and the void ratio increases. On the other hand, e_{max} (loosest mixtures) increases slowly with fine content, until the fine content threshold FC_{th}, but afterwards the slope changes and e_{max} increases quickly for higher fine content. French and Japanese standard procedures give similar results for the maximum void ratio. Whereas, they give different e_{min}, for fine content higher than the threshold $FC_{th} \cong 20\%$. The Japanese standard appears more accurate for high fine content because the achievement of lower minimum void ratios means that the procedure adopted for soil compaction is more adequate.
Fig. 3.3 also displays the void ratio curves obtained for loose, medium and dense state ($D_R = 30 - 50 - 80\%$). It can be observed that even if the relative density remains constant, the void ratio e changes with increasing fine content.

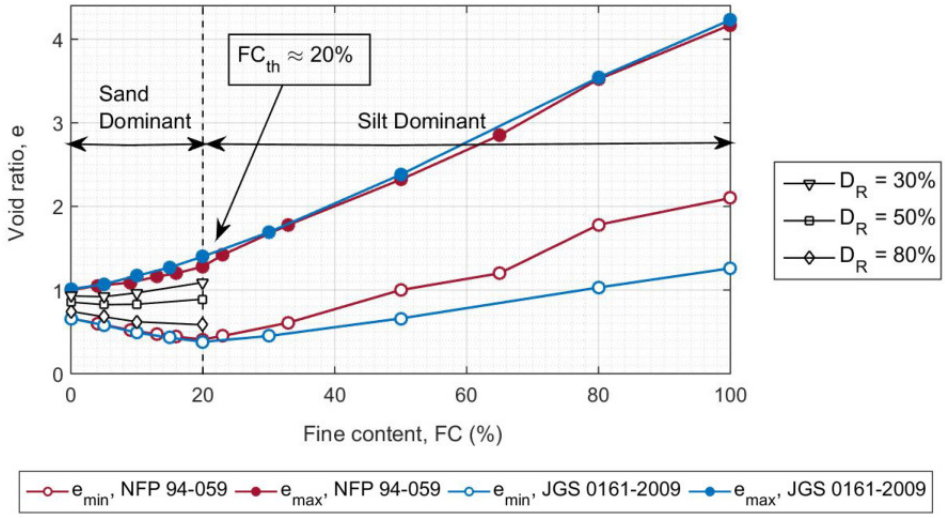

Figure 3.3: Maximum and minimum void ratios e_{max} and e_{min} versus fine content FC, for different relative density D_R

3.2 Testing Equipment

The measurement of soil properties is a critical aspect in the solution of geotechnical earthquake engineering problems. A wide variety of laboratory tests are available, presenting different advantages and limitations with respect to the problem analyzed. Hence, the selection of testing equipment and procedure for measurement of soil properties requires fully understanding of the specific geotechnical problem.
In this study, four different devices are used:

- Bishop and Wesley triaxial apparatus
- Advanced Dynamic Cyclic Simple Shear (ADVDCSS) apparatus
- Resonant column apparatus
- Piezoelectric elements (or bender elements)

3.2.1 Bishop and Wesley triaxial apparatus

The triaxial test is one of the most common geotechnical laboratory tests, which allows the characterization of soil by measuring their shear strength, stiffness and pore water pressure.
Fig.3.4a presents the triaxial apparatus, which is composed of a Bishop and Wesley type triaxial cell, an 8-channel data acquisition unit and three

(a)

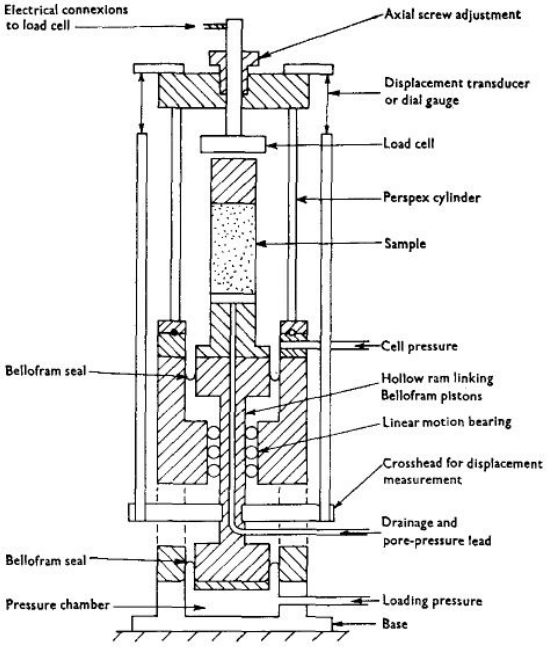

(b)

Figure 3.4: The Bishop and Wesley type triaxial testing system apparatus (Bishop and Wesley, 1975) with its pressure generators

pressure volume controllers. A pressure generator is designed to apply the pressure in the cell, one for the back pressure in the specimen and last one for the piston at the base of the lower support which can move vertically. The 8-channel data acquisition device, known as the "serial data pad", is used to transfer data from the displacement transducer, the pore pressure transducer, and the axial force transducer to the dedicated computer. The equipment is controlled by the GDSLAB Kernel software which allows to perform a wide variety of functions and tests automatically, including cell and back pressure control for saturation, consolidation (isotropic and anisotropic), drained and undrained, monotonic and cyclic, triaxial tests.

Fig. 3.4b shows the general set-up of the triaxial device (Bishop and Wesley, 1975). This triaxial apparatus is designed to test cylindrical specimens of 50 mm in diameter and 100 mm in height, with one way drainage provided through the base pedestal an the top-cap. The axial load is applied to the sample by increasing the pressure in the bottom pressure chamber. The loading system allows to perform monotonic loading under strain controlled conditions and cyclic loading, in a quasi-static configuration, under stress controlled conditions.

3.2.2 Advanced Dynamic Cyclic Simple Shear (ADVDCSS) apparatus

The GDS Advanced Dynamic Cyclic Simple Shear (ADVDCSS) testing system combines simple shear and triaxial testing using electro-mechanical force actuators. This system allows all types of triaxial tests (Fig. 3.5a) like the Bishop and Wesley device with the same specimen dimensions but also applying dynamic signals (with content up to 5 Hz) and not only in a quasi-static configuration. The device also allows cyclic simple shear tests, ranging from small strains (0.005%) to large strains, on 20 mm high specimens with a diameter of 50 mm. In addition, during simple shear tests, the cylindrical soil specimen is laterally confined by Teflon coated low friction retaining rings, which ensures a constant cross sectional area and the vertical displacement is kept constant, while shear force loading is applied (Fig. 3.5b).

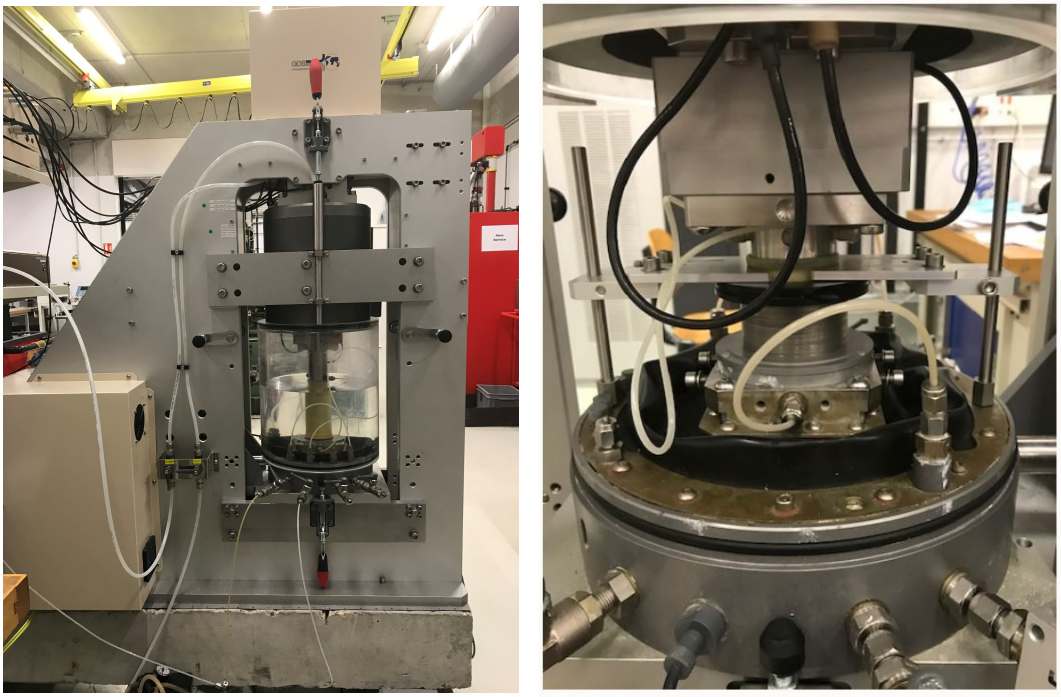

(a) (b)

Figure 3.5: GDS combined advanced dynamic cyclic simple shear (ADVDCSS) apparatus: triaxial testing system configuration (a) and simple shear testing system configuration (b)

3.2.3 Resonant column apparatus

The resonant column test allows to measure dynamic properties of soils from small to intermediate strains. The basic principle is to vibrate a cylindrical soil specimen in a foundamental mode of vibration. The most common type of resonant column is the fix-free configuration, where one side of the sample is constrained against rotation and the other side is free in rotation (Drnevich resonant column and Stokoe resonant column). The test is performed by applying a sinusoidal excitation via an electromagnetic drive system which consists of sets of coils and magnets (Fig. 3.6). The soil can be excited in torsional, flexural, and axial modes of vibration at different confinements and shear strain levels. During the test, the sample is excited in torsion at its fundamental frequency, the four pairs of coils are connected in series in order to apply a net torque to the sample and the response of the sample to torsional vibrations is monitored with an accelerometer mounted at the top of the drive system. Two parameters are obtained from the measured motion of the free part: resonant frequency and damping coefficient, which are then used to calculate the shear wave velocity and the shear modulus at the actual level strain.

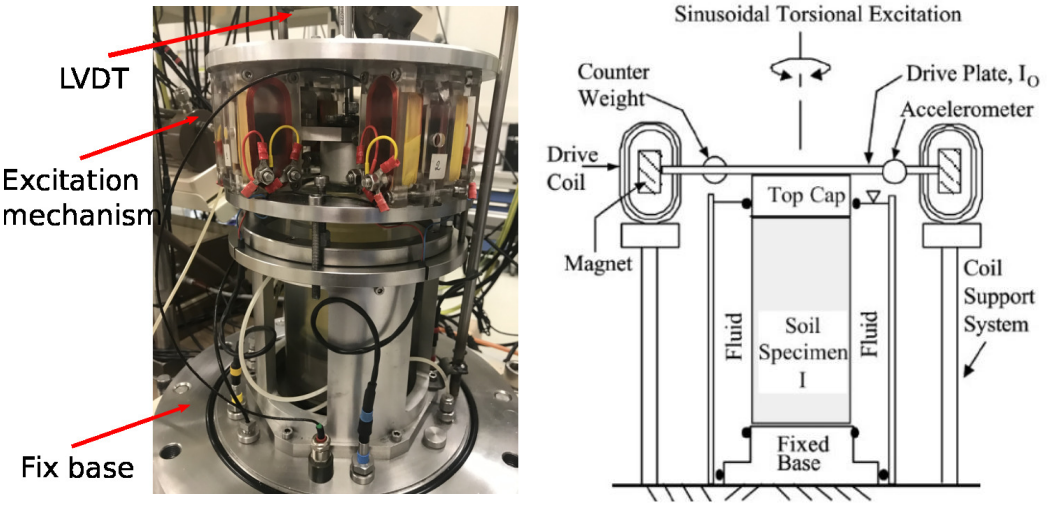

(a) (b)

Figure 3.6: Resonant column apparatus

3.2.4 Piezoelectric elements

The piezoelectric elements or bender elements can be mounted in different devices to measure the shear wave velocity at a low amplitude of vibration in laboratory conditions.

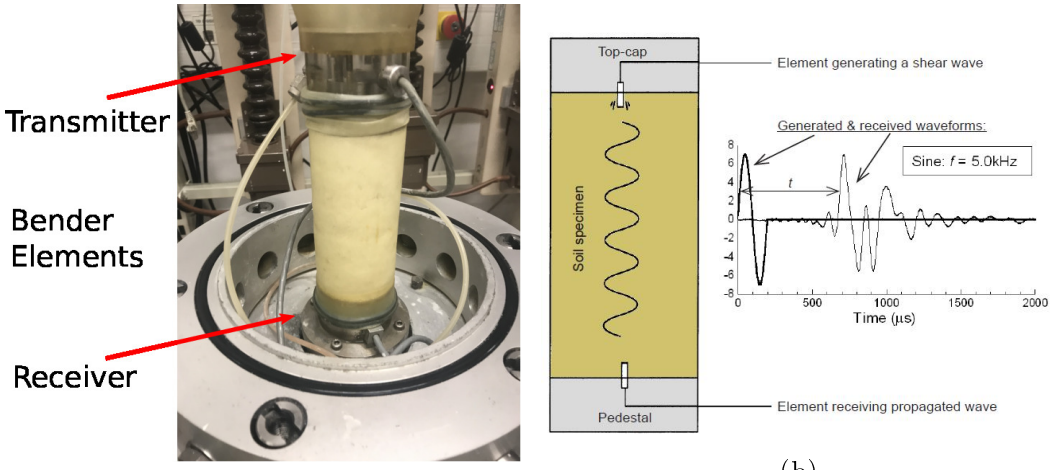

(a) (b)

Figure 3.7: Bender element set-up (a); Schematic of an S-wave bender element test, displaying generated and received waveforms (b)

Bender elements are made from piezoelectric ceramic bimorphs, which are encapsulated and mounted in the top-cap and base pedestal of the device (like those in Figure 3.7a). During the test, one element is supplied with an excitation voltage to generate either a P-wave or an S-wave in the specimen, while the other element receives the generated wave that propagates through the soil. A schematic detailing the configuration of a pair of vertical bender elements set in a specimen and the generated and received waveforms are shown in Figure 3.7b.
Thus, the bender element test is used to estimate the compression or shear waves velocity (P-wave or S-wave, respectively) by measuring the travel time through the soil specimen and dividing the distance between the elements by this travel time. Then, the maximum shear modulus can be calculated as follows:

$$G_0 = \rho V_s^2 \tag{3.1}$$

where ρ is the the density of the specimen also measured in laboratory.

3.3 Experimental procedure

The undrained consolidated laboratory tests generally consist of three common main phases: sample preparation, saturation and consolidation. Then, the fourth phase is the loading phase, which varies according to the apparatus used and the desired output.

3.3.1 Sample preparation

In this study, specimens are reconstituted by the moist tamping method (Castro, 1969), adding deaerated water (about 5% of the total sample dry weight) and using the under-compaction technique (Ladd, 1978) in order to minimize the tendency for particles segregation when using silty and well-graded sands, and to prepare uniform samples with a relative density ranging between very loose and very dense.
This procedure incorporates a tamping method of compacting moist mixture in layers, in which each layer is compacted to a selected percentage of the required dry unit weight of the specimen. In addition, in order to achieve uniform density of specimen, the soil is compacted applying the concept of under-compaction because when a soil is compacted with a constant compaction for each layer, the compaction of each succeeding layer may further densify the soil below it. Hence, this method implies that each layer is compacted to a lower density than the final desired value by a predetermined amount which is defined as undercompaction percentage (Fig. 3.8).
Each specimen, having 50 mm in diameter and 100 mm in height, is prepared with fixed initial relative density of the sand-fines mixture ($D_R = 30 - 50 - 80\%$). This means that when the amount of fines is increased, the amount of sand is reduced. This choice is made to have an easier comparison with natural sandy soils. In fact, natural soils are identified in day-to-day practice by means of relative density of the whole soil mixture and fine percentage.
Figure 3.9 shows the obtained mixtures with different fine content of 0, 5, 10 and 20%. It can be observed that the texture differs according to the amount of fine particles.

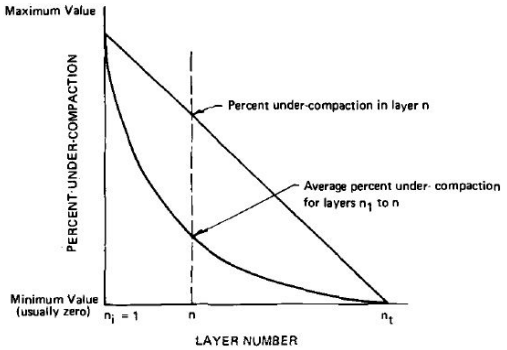

Where: A. Percent under-compaction in layer being considered, U_n

$$U_n = U_{ni} - \left[\frac{(U_{ni} - U_{nt})}{n_t - 1} \times (n - 1)\right]$$

B. Average percent under-compaction for layers compacted, $\overline{U}_n$

$$\overline{U}_n = \frac{U_n}{n}$$

U_{ni} = Percent under-compaction selected for first layer

U_{nt} = Percent under-compaction selected for final layer (usually zero)

n = Number of layer being considered

n_i = First (initial) layer

n_t = Total number of layers (final layer)

Figure 3.8: Concept of undercompaction procedure (Ladd, 1978)

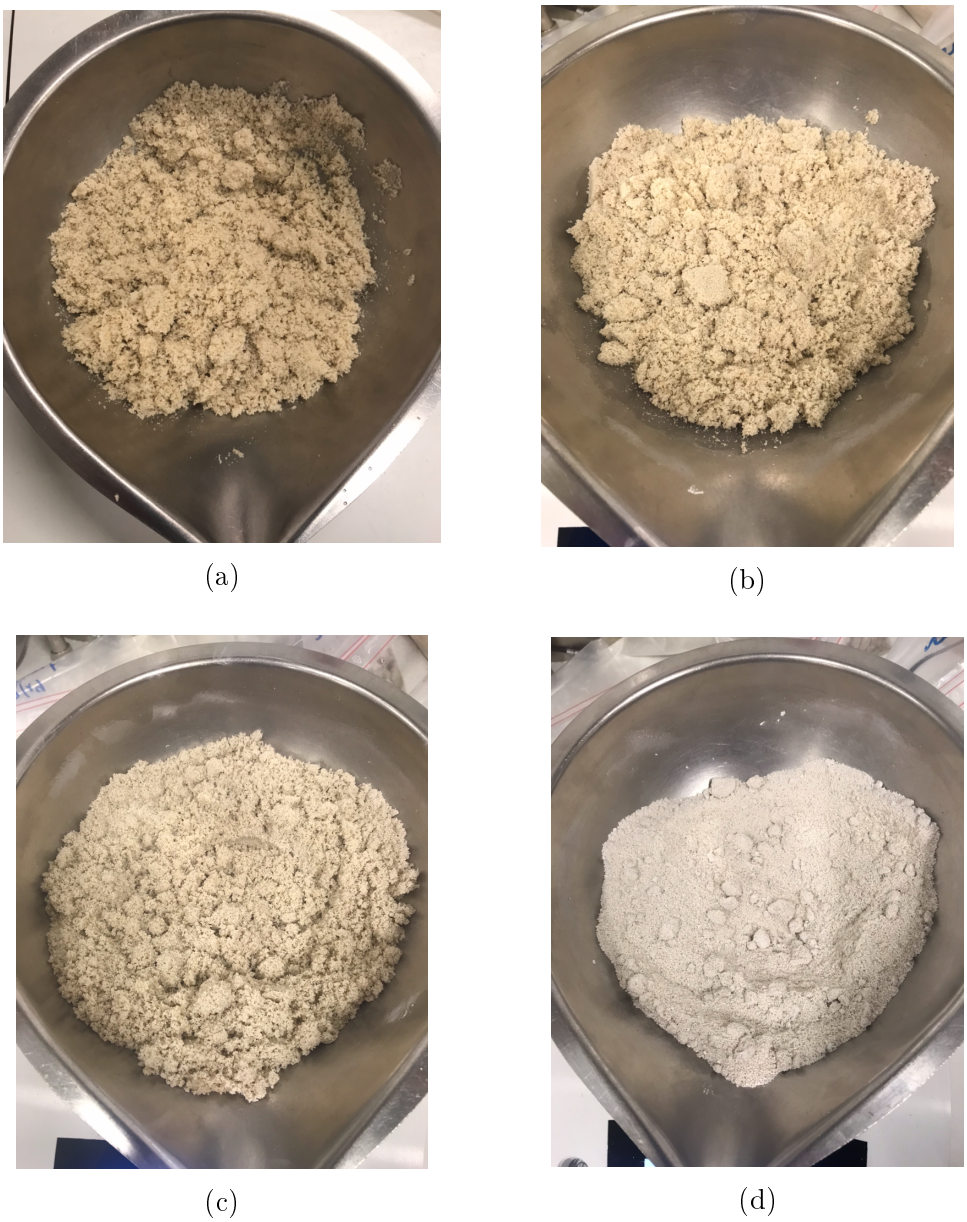

(a) (b)

(c) (d)

Figure 3.9: Sand-fines mixtures with different fine content of 0 (a), 5 (b), 10 (c) and 20% (d)

3.3.2 Specimen mould setup

First, a porous stone and a filter paper are placed on the pedestal in order to allow the drainage of water but prevent the migration of fines (Fig. 3.10a). Secondly, a latex membrane 0.3 mm thick is placed around the outside of the pedestal and fixed in place with two rubber O'ring (Fig. 3.10b). Thirdly, a metal split mould of diameter 50.5 mm is positioned around the base and secured in place with a metal split-ring (Fig. 3.10c). Finally, a small vacuum is applied to the internal mould space through a valve, holding the membrane against the mould wall during the sample preparation.
Once the mold is positionned, the soil material has to be prepared as follows. Dry material (clean sand or sand-fines mixtures) are thoroughly mixed before adding water until a good homogeneity of the material is reached. Then deaerated water, 5% of the total sample dry weight, is added to facilitate the capillarity and then the mixture is mixed carefully until it appears homogeneous. This operation requires extra care when the fine content is high because fine particles are very sensitive to segregation.
Then, the material mass calculated for each layer is meticulously deposited with a spoon at zero drop height inside the mould and it is compacted until the layer height of 2 cm. A tamper with a diameter of 3.5 cm is used to achieve the target density. This procedure is repeated until the mould is completely filled with the soil material (five layers, Fig. 3.11a).

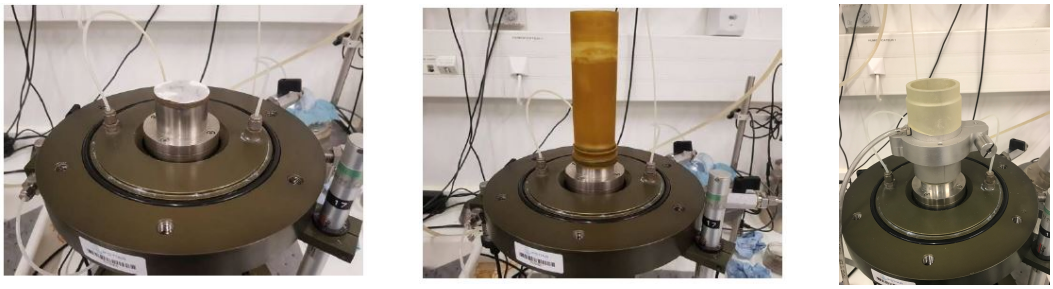

(a) (b) (c)

Figure 3.10: Preparation of the sample-placing (a) the porous stone, (b) the membrane, (c) and the metal mold

Once the sample is prepared, the second filter paper, the second porous stone and the top-cap are placed. Then, the membrane is flipped and fixed with two rubber O'rings. Before disassembling the mould, a slight vacuum, between -10 kPa and -20 kPa (lower than the consolidation stress), is applied in the specimen (Figs 3.11b and 3.11c). Then, the dimensions of the specimen are checked by measuring the height at three diametrically opposite points and

the circumference at three points. During the final step, the triaxial cell is assembled and filled with water and the two pressure sources (cell pressure and back pressure) are connected with the drainage lines (Fig. 3.11d).
A similar procedure is used for the preparation of the resonant column and the ADVDCSS system (Fig. 3.12).

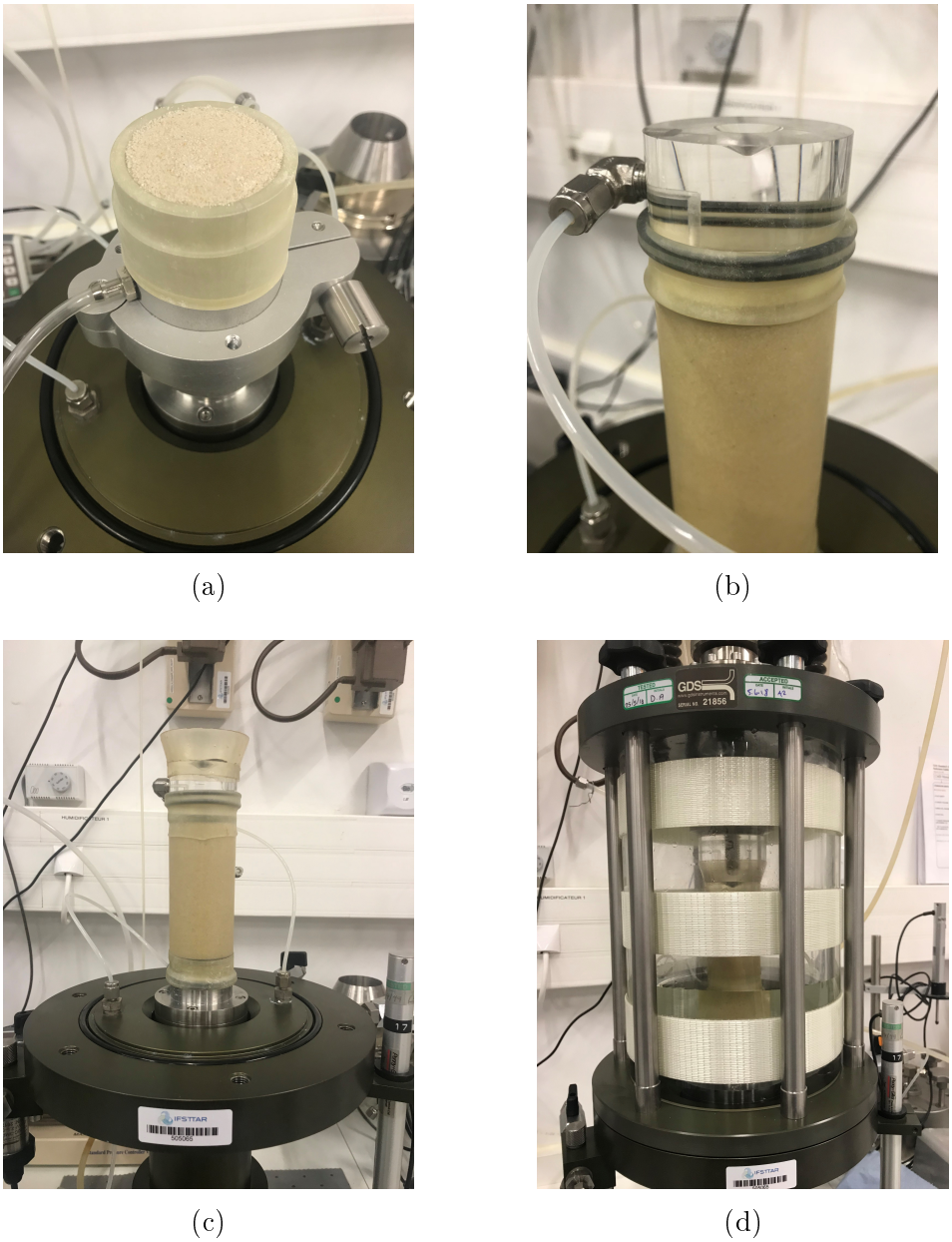

(a) (b)

(c) (d)

Figure 3.11: Sample preparation (a), placing the second porous stone and the upper base (b-c), assemblage and filling of the triaxial cell (d)

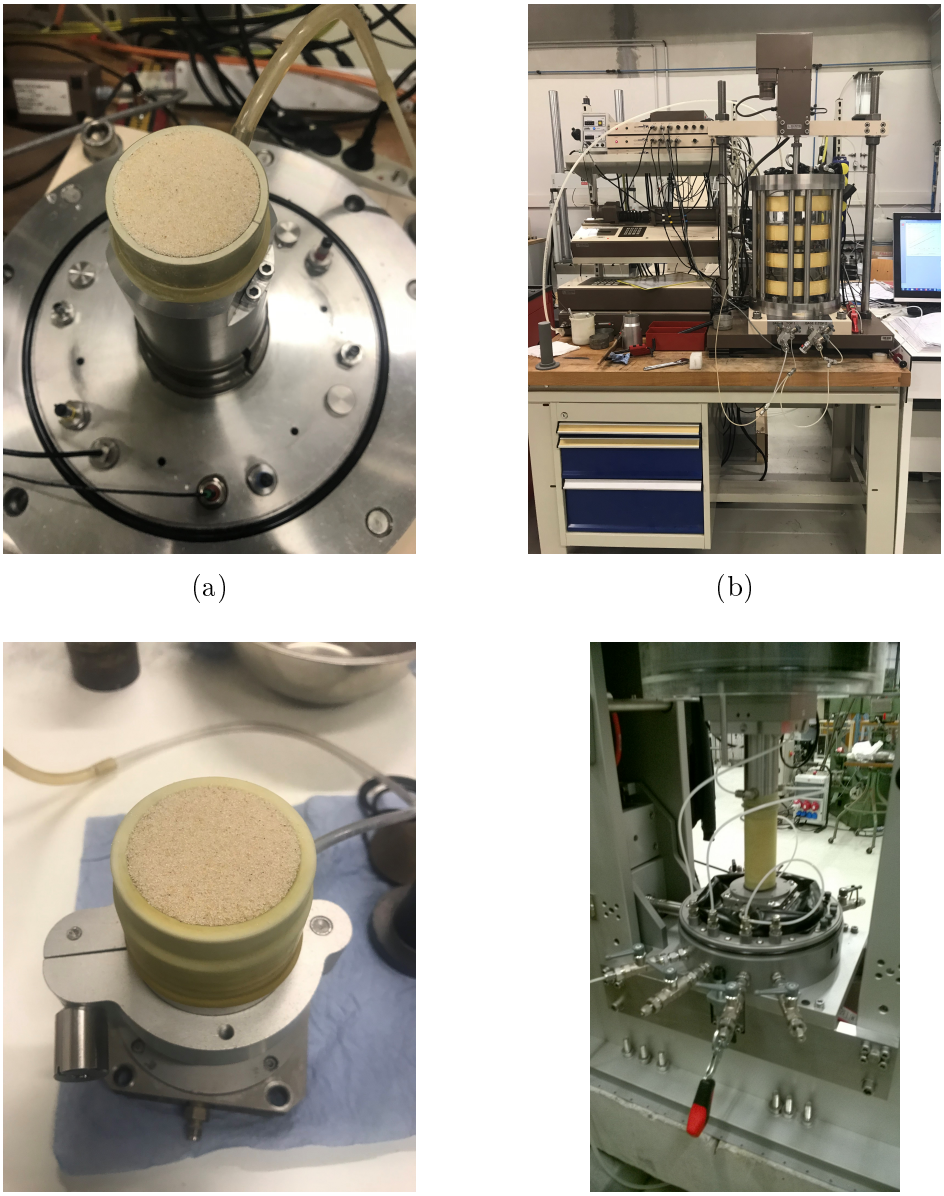

(a) (b)

(c) (d)

Figure 3.12: Sample preparation: resonant column (a-b), ADVDCSS system in triaxial configuation (c-d)

3.3.3 Saturation

The saturation process allows to ensure all voids within the test specimen are filled with water and it is achieved in three steps. First, carbon dioxide gas CO_2 is forced to circulate through-out the specimen for 10 minutes in order to remove the air and replace CO_2 at its place, more soluble in water. Then,

deaerated water is percolated through the specimen from the bottom to the top drainage line in order to increase the degree of saturation. A pressure gradient of less than 5 is used during this step in order to minimize specimen disturbance. Finally, the last phase consists of connecting the drainage lines to the pressure generator and then gradually applying a back pressure of minimum 200 kPa in order to improve the degree of saturation of the specimen by dissolution of the remained gas bubbles. The cell pressure is also simultaneously raised to a slightly higher value by ensuring that the difference between cell pressure and back pressure is minor than 2/3 of the desired confining pressure. In this research, a back pressure of 400 kPa is used to ensure full saturation. The time for this phase is at least 2 hours.
To check the degree of saturation, a B-check test is performed to determine the Skempton B-value (Skempton, 1954). During this phase, the drainage valves are closed and the cell pressure is raised by 50kPa. The B-value is computed as the ratio of the difference in pore pressure Δu to the difference in cell pressure Δp_{cell}. Thus, the Skempton coefficient B, indicating the percentage of saturation, is considered satisfactory when it is greater than 0.96. For all the performed tests, the B value reaches at least 0.98.

3.3.4 Consolidation

Once an acceptable B-value is obtained, the specimens are isotropically consolidated to a confining stress p'_0 (50-100-200 kPa). The consolidation phase allows to consolidate the specimen at the effective stress state required before shearing, by increasing the cell pressure to the desired value. Consolidation is considered complete when a change in volume of less than 5 mm^3 is observed over a period of 15 minutes for the sand and 20 minutes for the mixtures. These values are chosen according to standard NF-P94-059 (2000).
During the consolidation process, the drainage valves are open and the axial strain is continually monitored. Measurements of changes in the volume of the specimen are measured with the pressure volume controller in order to calculate the actual void ratio after consolidation and just before shearing.

3.3.5 Loading phase

The loading phase is the last phase and its characteristics depend on the device used and the desired outputs. During this phase, the drainage lines are closed and the specimen is loaded monotonically or cyclically.
In the monotonic CU triaxial tests, the specimens are sheared at a constant rate of axial displacement of 1mm/min. Cyclic CU triaxial tests are stress-controlled, using a sinusoidal signal having frequency $f = 0.5Hz$ and symmet-

ric alternating loading. In the resonant column tests, the harmonic excitation is applied at the top of the specimen by an electromagnetic driving system.

3.4 Repeatability

Evaluating the testing repeatability is a very important aspect to validate the experimental procedure and to assess the efficiency of the testing setup. To this regard, the degree to which the wet tamping technique is able to replicate specimens for identical initial conditions during undrained monotonic and cyclic loading is shown in Figs 3.13 and Fig. 3.14. Good repeatability is observed in these test results, confirming the homogeneity of the specimen reconstituted by the wet tamping with the under-compaction method.

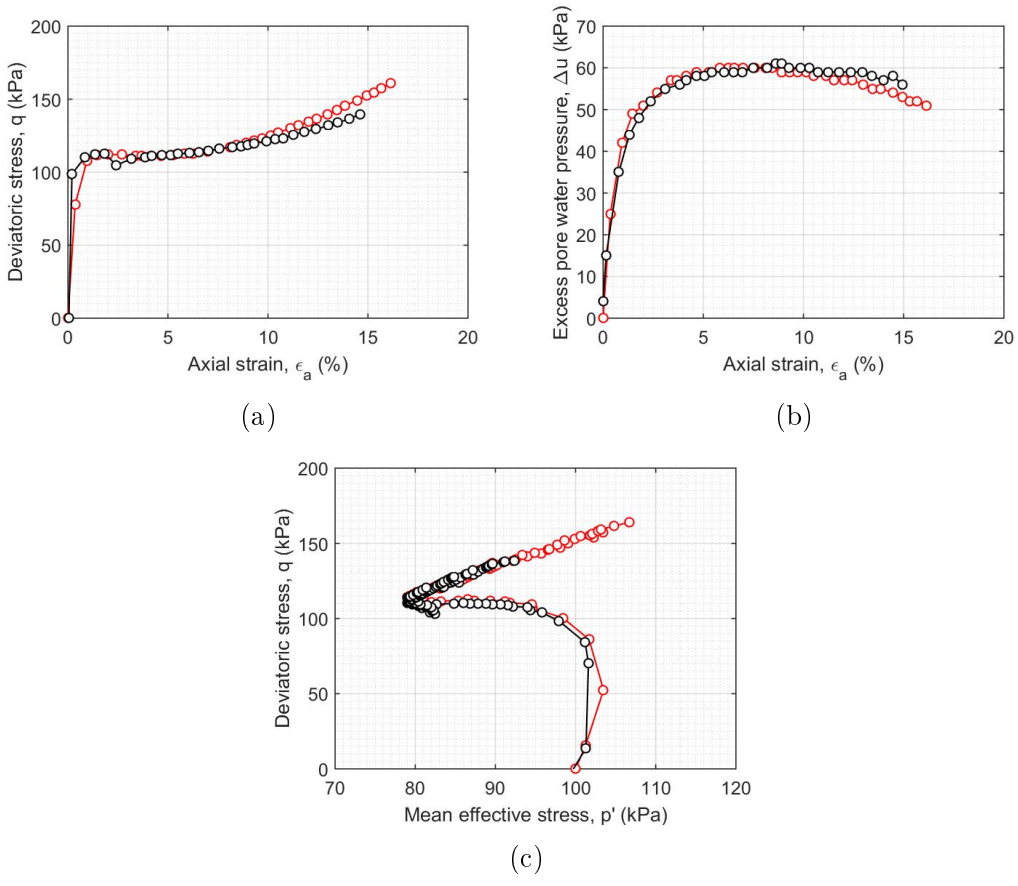

Figure 3.13: Repeatability of undrained monotonic test on Hostun sand-C500 mixtures ($D_R = 30\%$, $FC = 5\%$ and $p'_0 = 100$kPa): $(q - \varepsilon_a)$ curve (a) ; $(\Delta u - \varepsilon_a)$ curve (b); $(q - p')$ curve (c)

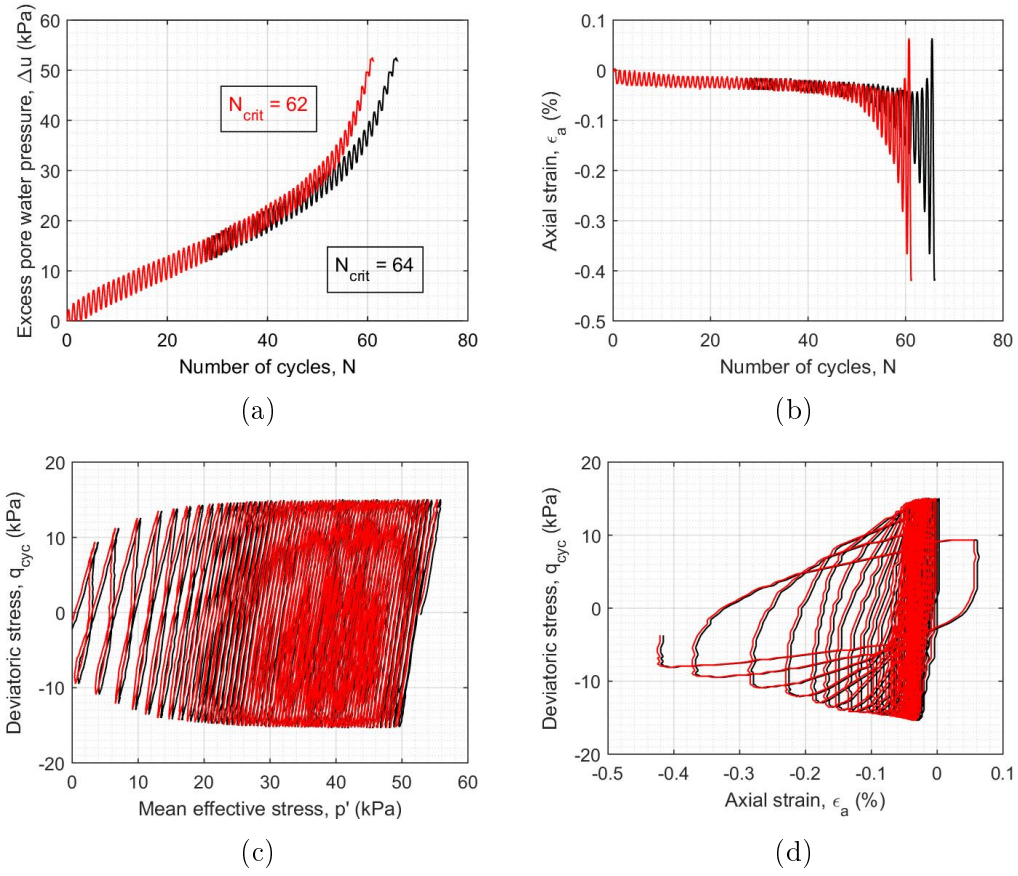

Figure 3.14: Repeatability of undrained cyclic test on Hostun sand ($D_R = 30\%$, $FC = 0\%$, $p'_0 = 100$kPa and $CSR = q_{cyc}/2p'_0 = 0.15$): $(\Delta u - N)$ curve (a) ; $(\varepsilon_a - N)$ curve (b); $(q - p')$ curve (c); $(q - \varepsilon_a)$ curve (d)

3.5 Conclusions

In this chapter, the experimental devices, the physical and mechanical properties of adopted materials, Hostun Sand and Silica C500, and the experimental procedures are discussed in the required details for the interpretation of the experimental results in the following chapters.
In this research, soil samples are specifically designed and reconstituted by the moist tamping method and the under-compaction technique, maintaining a given relative density. In particular, consolidated-undrained (CU) monotonic and cyclic triaxial tests as well as resonant column tests are performed on clean sand and silty sand mixtures to investigate the effect of non-plastic fines on liquefaction triggering in the case of loose, medium and dense mixtures.
The triaxial testing system is capable of conducting monotonic and stress, strain-controlled cyclic loading, therefore is used to determine the behavior and strength characteristics of soils and to investigate the cyclic stress-strain and excess pore water pressure response for large geometry specimens. The resonant column device is an accurate device to measure the low and mid strain shear modulus and damping ratio of soils.

Chapter 4

Liquefaction triggering in silty sands: effects of non-plastic fines and mixture-packing conditions

This chapter discusses procedure details and results of the laboratory testing program performed on silty sand to investigate the effect of fine content on soil liquefaction in terms of shear resistance, excess pore water pressure and shear modulus reduction. To this regard, the experimental program on clean sand and sand-silt mixtures under various conditions is first presented. Then, the experimental results are analyzed and discussed in terms of equivalent intergranular void ratio, which is identified in the literature as an adequate state parameter to characterize the global effect of fine particles. In particular, the undrained behavior of loose, medium and dense silty-sands is analyzed, using different fine contents and confining pressures.
The aim of this study is the assessment of the influence of non-plastic fines and mixture packing conditions on liquefaction triggering, and the creation of a robust laboratory test dataset in order to evaluate the predictive capabilities of the advanced soil constitutive model.

4.1 Experimental program

An experimental program is defined for a series of monotonic and cyclic consolidated undrained triaxial (CTU and CTX, respectively) as well as resonant column (RC) tests on reconstituted soil specimens of clean sand and sand-fines mixtures in order to characterize the undrained behavior and liquefaction susceptibility of sandy soils. In this experimental program, soil samples are specifically designed. Specimens with different fine contents are reconstituted maintaining a given initial relative density ($D_R = 30 - 50 - 80\%$) to assess the contribution of fine particles in the case of loose, medium and dense specimens. Four non-plastic fine contents ($FC = 0 - 5 - 10 - 20\%$), lower than the fine content threshold $FC_{th} \simeq 20\%$ (Fig. 3.3), are selected to investigate their effect on the sand-dominated mixtures. Three initial effective confining pressures ($p'_0 = 50 - 100 - 200kPa$) are imposed to consider the liquefaction

susceptibility at different depths. The experimental program corresponding to monotonic, cyclic and resonant column tests for clean sand and sand-fines mixtures is presented in Tables 4.1, 4.2, 4.3 and 4.4. A total of 42 CTU tests, 56 CTX tests and 39 RC tests are carried out in order to produce a robust set of test database.

The test name includes the type of test (CTU, CTX or RC), the value of relative density (DR00, DR20, DR30, DR50 or DR80), the fine content (FC00, FC05, FC10 or FC20) and the value of confining pressure (50, 100 or 200). In the case of cyclic triaxial tests, the value of the cyclic stress ratio (CSR) is also added at the end of the test name. For instance, the test name CTU_DR30_FC10_50 refers to a consolidated undrained monotonic triaxial test for a sample prepared at a relative density of 30%, a fine content of 10% and subjected to an initial isotropic confining pressure of 50 kPa. While the test name CTX_DR30_FC00_200_CSR0.125 refers to a consolidated undrained cyclic triaxial test for a sample prepared at a relative density of 30%, a fine content of 0%, subjected to an initial isotropic confining pressure of 200 kPa and a cyclic stress ratio of 0.125; and the test name RC_DR80_FC20_100 refers to a consolidated undrained resonant column test for a sample prepared at a relative density of 80%, a fine content of 20% and subjected to an initial isotropic confining pressure of 100 kPa.

Table 4.3 presents the cyclic triaxial test performed to investigate the influence of the frequency on the cyclic soil response. In particular, in this case the test name also includes the value of the frequency f used during the test.

Table 4.1: Consolidated undrained monotonic triaxial (CTU) testing program

N°	Test Reference	$FC(\%)$	$D_{Ri}(\%)$	p'_0 (kPa)	e_i	e_c
1	CTU_DR00_FC00_50	0	10	50	1.00	0.98
2	CTU_DR00_FC00_100	0	10	100	1.00	0.97
3	CTU_DR00_FC00_200	0	10	200	1.00	0.97
4	CTU_DR20_FC00_50	0	10	50	0.94	0.94
5	CTU_DR20_FC00_100	0	10	100	0.94	0.94
6	CTU_DR20_FC00_200	0	10	200	0.94	0.93
7	CTU_DR30_FC00_50	0	30	50	0.92	0.91
8	CTU_DR30_FC00_100	0	30	100	0.92	0.90
9	CTU_DR30_FC00_200	0	30	200	0.92	0.90
10	CTU_DR50_FC00_50	0	50	50	0.85	0.84
11	CTU_DR50_FC00_100	0	50	100	0.85	0.0.84
12	CTU_DR50_FC00_200	0	50	200	0.85	0.84
13	CTU_DR80_FC00_50	0	80	50	0.74	0.74
14	CTU_DR80_FC00_100	0	80	100	0.74	0.74
15	CTU_DR80_FC00_200	0	80	200	0.74	0.74
16	CTU_DR30_FC05_50	5	30	50	0.92	0.90
17	CTU_DR30_FC05_100	5	30	100	0.92	0.88
18	CTU_DR30_FC05_200	5	30	200	0.92	0.87
19	CTU_DR50_FC05_50	5	50	50	0.825	0.815
20	CTU_DR50_FC05_100	5	50	100	0.825	0.805
21	CTU_DR50_FC05_200	5	50	200	0.825	0.80
22	CTU_DR80_FC05_50	5	80	50	0.68	0.68
23	CTU_DR80_FC05_100	5	80	100	0.68	0.675
24	CTU_DR80_FC05_200	5	80	200	0.68	0.675
25	CTU_DR30_FC10_50	10	30	50	0.96	0.88
26	CTU_DR30_FC10_100	10	30	100	0.96	0.87
27	CTU_DR30_FC10_200	10	30	200	0.96	0.86
28	CTU_DR50_FC10_50	10	50	50	0.83	0.80
29	CTU_DR50_FC10_100	10	50	100	0.83	0.79
30	CTU_DR50_FC10_200	10	50	200	0.83	0.79
31	CTU_DR80_FC10_50	10	80	50	0.62	0.614
32	CTU_DR80_FC10_100	10	80	100	0.62	0.613
33	CTU_DR80_FC10_200	10	80	200	0.62	0.608
34	CTU_DR30_FC20_50	20	30	50	1.09	0.77
35	CTU_DR30_FC20_100	20	30	100	1.09	0.74
36	CTU_DR30_FC20_200	20	30	200	1.09	0.70
37	CTU_DR50_FC20_50	20	50	50	0.89	0.65
38	CTU_DR50_FC20_100	20	50	100	0.89	0.63
39	CTU_DR50_FC20_200	20	50	200	0.89	0.65
40	CTU_DR80_FC20_50	20	80	50	0.584	0.60
41	CTU_DR80_FC20_100	20	80	100	0.584	0.58
42	CTU_DR80_FC20_200	20	80	200	0.584	0.58

Table 4.2: Consolidated undrained cyclic triaxial (CTX) testing program

N°	Test Reference	$FC(\%)$	$D_{Ri}(\%)$	p'_0 (kPa)	CSR	f (Hz)	e_i	e_c
1	CTX_DR30_FC00_50_CSR0.1	0	30	50	0.1	0.5	0.92	0.91
2	CTX_DR30_FC00_50_CSR0.125	0	30	50	0.125	0.5	0.92	0.912
3	CTX_DR30_FC00_100_CSR0.075	0	30	100	0.075	0.5	0.92	0.91
4	CTX_DR30_FC00_100_CSR0.1	0	30	100	0.10	0.5	0.92	0.91
5	CTX_DR30_FC00_100_CSR0.125	0	30	100	0.125	0.5	0.92	0.906
6	CTX_DR30_FC00_200_CSR0.1	0	30	100	0.125	0.5	0.92	0.90
7	CTX_DR30_FC00_200_CSR0.125	0	30	100	0.125	0.5	0.92	0.904
8	CTX_DR50_FC00_50_CSR0.1	0	50	50	0.10	0.5	0.85	0.845
9	CTX_DR50_FC00_50_CSR0.125	0	50	50	0.10	0.5	0.85	0.845
10	CTX_DR50_FC00_100_CSR0.1	0	50	100	0.10	0.5	0.85	0.84
11	CTX_DR50_FC00_100_CSR0.125	0	50	100	0.125	0.5	0.85	0.83
12	CTX_DR50_FC00_100_CSR0.175	0	50	100	0.175	0.5	0.85	0.84
13	CTX_DR50_FC00_200_CSR0.1	0	50	200	0.10	0.5	0.85	0.85
14	CTX_DR50_FC00_200_CSR0.125	0	50	200	0.10	0.5	0.85	0.85
15	CTX_DR80_FC00_50_CSR0.1	0	80	50	0.20	0.5	0.74	0.745
16	CTX_DR80_FC00_50_CSR0.225	0	80	50	0.20	0.5	0.74	0.745
17	CTX_DR80_FC00_100_CSR0.1	0	80	100	0.10	0.5	0.74	0.736
18	CTX_DR80_FC00_100_CSR0.2	0	80	100	0.20	0.5	0.74	0.74
19	CTX_DR80_FC00_100_CSR0.225	0	80	100	0.225	0.5	0.74	0.73
20	CTX_DR80_FC00_200_CSR0.1	0	80	200	0.20	0.5	0.74	0.75
21	CTX_DR80_FC00_200_CSR0.225	0	80	200	0.20	0.5	0.74	0.75
22	CTX_DR80_FC00_50_CSR0.2_f_c	0	80	50	0.20	0.1	0.74	0.
23	CTX_DR80_FC00_100_CSR0.2_f_c	0	80	100	0.20	0.1	0.74	0.
24	CTX_DR30_FC05_100_CSR0.05	5	30	100	0.05	0.5	0.92	0.90
25	CTX_DR30_FC05_100_CSR0.1	5	30	100	0.10	0.5	0.92	0.89
26	CTX_DR30_FC05_100_CSR0.15	5	30	100	0.15	0.5	0.92	0.885
27	CTX_DR50_FC05_100_CSR0.075	5	50	100	0.075	0.5	0.825	0.81
28	CTX_DR50_FC05_100_CSR0.15	5	50	100	0.15	0.5	0.825	0.80
29	CTX_DR50_FC05_100_CSR0.175	5	50	100	0.175	0.5	0.825	0.80
30	CTX_DR80_FC05_100_CSR0.1	5	80	100	0.10	0.5	0.68	0.68
31	CTX_DR80_FC05_100_CSR0.2	5	80	100	0.20	0.5	0.68	0.68
32	CTX_DR80_FC05_100_CSR0.25	5	80	100	0.25	0.5	0.68	0.672
33	CTX_DR30_FC10_100_CSR0.075	10	30	100	0.075	0.5	0.96	0.88
34	CTX_DR30_FC10_100_CSR0.1	10	30	100	0.10	0.5	0.96	0.85
35	CTX_DR30_FC10_200_CSR0.125	10	30	100	0.125	0.5	0.96	0.84
36	CTX_DR50_FC10_100_CSR0.075	10	50	100	0.075	0.5	0.83	0.79
37	CTX_DR50_FC10_100_CSR0.125	10	50	100	0.125	0.5	0.83	0.78
38	CTX_DR50_FC10_100_CSR0.15	10	50	100	0.15	0.5	0.83	0.78
39	CTX_DR80_FC10_100_CSR0.1	10	80	100	0.10	0.5	0.62	0.612
40	CTX_DR80_FC10_100_CSR0.2	10	80	100	0.20	0.5	0.62	0.61
41	CTX_DR80_FC10_100_CSR0.25	10	80	100	0.25	0.5	0.62	0.606
42	CTX_DR30_FC20_100_CSR0.075	20	30	100	0.075	0.5	1.09	0.78
43	CTX_DR30_FC20_100_CSR0.1	20	30	100	0.10	0.5	1.09	0.75
44	CTX_DR30_FC20_100_CSR0.125	20	30	100	0.125	0.5	1.09	0.69
45	CTX_DR50_FC20_100_CSR0.075	20	50	100	0.075	0.5	0.89	0.67
46	CTX_DR50_FC20_100_CSR0.1	20	50	100	0.10	0.5	0.89	0.64

47	CTX_DR50_FC20_100_CSR0.125	20	50	100	0.125	0.5	0.89	0.64
48	CTX_DR80_FC20_100_CSR0.1	20	80	100	0.10	0.5	0.584	0.58
49	CTX_DR80_FC20_100_CSR0.15	20	80	100	0.15	0.5	0.584	0.60
50	CTX_DR80_FC20_100_CSR0.2	20	80	100	0.20	0.5	0.584	0.585

Table 4.3: Consolidated undrained cyclic triaxial (CTX) testing program for various frequencies f

N°	Test Reference	$FC(\%)$	$D_{Ri}(\%)$	p'_0 (kPa)	CSR	f (Hz)
1	CTX_DR30_FC00_100_CSR0.1_f0.0005	0	30	100	0.10	0.0005
2	CTX_DR30_FC00_100_CSR0.1_f0.001	0	30	100	0.10	0.001
3	CTX_DR30_FC00_100_CSR0.1_f0.1	0	30	100	0.10	0.1
4	CTX_DR30_FC00_100_CSR0.1_f0.5	0	30	100	0.10	0.5
5	CTX_DR30_FC00_100_CSR0.1_f1.0	0	30	100	0.10	1.0
6	CTX_DR30_FC00_100_CSR0.1_f2.0	0	30	100	0.10	2.0

Table 4.4: Resonant Column (RC) testing program

N°	Test Reference	$FC(\%)$	$D_{Ri}(\%)$	p'_0 (kPa)	e_i	e_c
1	RC_DR20_FC00_50	0	30	50	0.94	0.925
2	RC_DR20_FC00_100	0	30	100	0.94	0.92
3	RC_DR20_FC00_200	0	30	200	0.94	0.92
4	RC_DR30_FC00_50	0	30	50	0.92	0.91
5	RC_DR30_FC00_100	0	30	100	0.92	0.90
6	RC_DR30_FC00_200	0	30	200	0.92	0.90
7	RC_DR50_FC00_50	0	50	50	0.85	0.85
8	RC_DR50_FC00_100	0	50	100	0.85	0.83
9	RC_DR50_FC00_200	0	50	200	0.85	0.84
10	RC_DR80_FC00_50	0	80	50	0.74	0.73
11	RC_DR80_FC00_100	0	80	100	0.74	0.74
12	RC_DR80_FC00_200	0	80	200	0.74	0. 73
13	RC_DR30_FC05_50	5	30	50	0.92	0.91
14	RC_DR30_FC05_100	5	30	100	0.92	0.90
15	RC_DR30_FC05_200	5	30	200	0.92	0.90
16	RC_DR50_FC05_50	5	50	50	0.825	0.81
17	RC_DR50_FC05_100	5	50	100	0.825	0.81
18	RC_DR50_FC05_200	5	50	200	0.825	0.80
19	RC_DR80_FC05_50	5	80	50	0.68	0.68
20	RC_DR80_FC05_100	5	80	100	0.68	0.68
21	RC_DR80_FC05_200	5	80	200	0.68	0.67
22	RC_DR30_FC10_50	10	30	50	0.96	0.88
23	RC_DR30_FC10_100	10	30	100	0.96	0.86
24	RC_DR30_FC10_200	10	30	200	0.96	0.84
25	RC_DR50_FC10_50	10	50	50	0.83	0.80
26	RC_DR50_FC10_100	10	50	100	0.83	0.78
27	RC_DR50_FC10_200	10	50	200	0.83	0.77
28	RC_DR80_FC10_50	10	80	50	0.62	0.62
29	RC_DR80_FC10_100	10	80	100	0.62	0.60
30	RC_DR80_FC10_200	10	80	200	0.62	0.62
31	RC_DR30_FC20_50	20	30	50	1.09	0.76
32	RC_DR30_FC20_100	20	30	100	1.09	0.75
33	RC_DR30_FC20_200	20	30	200	1.09	0.73
34	RC_DR50_FC20_50	20	50	50	0.89	0.68
35	RC_DR50_FC20_100	20	50	100	0.89	0.66
36	RC_DR50_FC20_200	20	50	200	0.89	0.63
37	RC_DR80_FC20_50	20	80	50	0.584	0.59
38	RC_DR80_FC20_100	20	80	100	0.584	0.58
39	RC_DR80_FC20_200	20	80	200	0.584	0.58

4.2 Undrained monotonic behavior

4.2.1 Influence of relative density

The influence of relative density is investigated by carrying out tests on specimens consolidated at the same confining pressure p'_0 and having different initial relative densities.
The influence of relative density on the undrained behaviour of clean Hostun sand can be observed in Fig. 4.1. It shows a series of monotonic tests for specimens having different initial relative densities and consolidated under initial isotropic confining pressures of 100 kPa and 400 kPa. It is clear that the relative density strongly affects the mechanical response of sand. Figs 4.1a and 4.1b present the evolution of the deviatoric stress with respect to the axial strain and it can be observed that the deviatoric stress increases with the relative density. For the lowest relative density ($D_R = 0\%$), the undrained response presents a marked low strength peak at an axial deformation of about 0.5% followed by strong softening until a low constant ultimate strength is obtained (Fig. 4.1a). For the medium-loose relative density ($D_R = 20 - 30\%$), the peak of the deviatoric stress increases but less than in the case of loose sand with a slight decrease in average deformation (2 to 5%) followed by an increase in resistance beyond an axial deformation of 5% (Fig. 4.1a). This intermediate behavior, between contracting and dilatant, corresponds to limited liquefaction (Castro, 1969; Ishihara, 1993). On the other hand, in the case of dense sand ($D_R = 50 - 80\%$), the deviatoric stress increases continuously indicating a hardening behavior (Fig. 4.1b).

Figs 4.1c and 4.1d show the evolution of the excess pore water pressure, which decreases with the increase of the relative density. In fact, for loose sand, excess pore water pressure reaches the value of the confining pressure leading to liquefaction, while for the case of medium-loose, the pore pressure first increases and after reaching the peak of strength, it decreases (dilatation). Conversely, for dense sand, the pore water pressure presents a small increase at the very beginning of the loading and then it decreases reaching negative values that indicate dilatant and stable behavior.
Figs 4.1e and 4.1f illustrate the effective stress path of the loading showing the passage from a softening behavior (liquefaction) for very loose sand to a hardening behavior for denser sand. In the case of loose specimens, the mean effective stress migrates progressively towards the origin of the axes until reaching very low values of deviatoric stress indicating the collapse of the sample ($D_R = 0\%$), while for medium-loose sand, the effective stress initially decreases presenting a contractive behavior untilt it crosses the phase

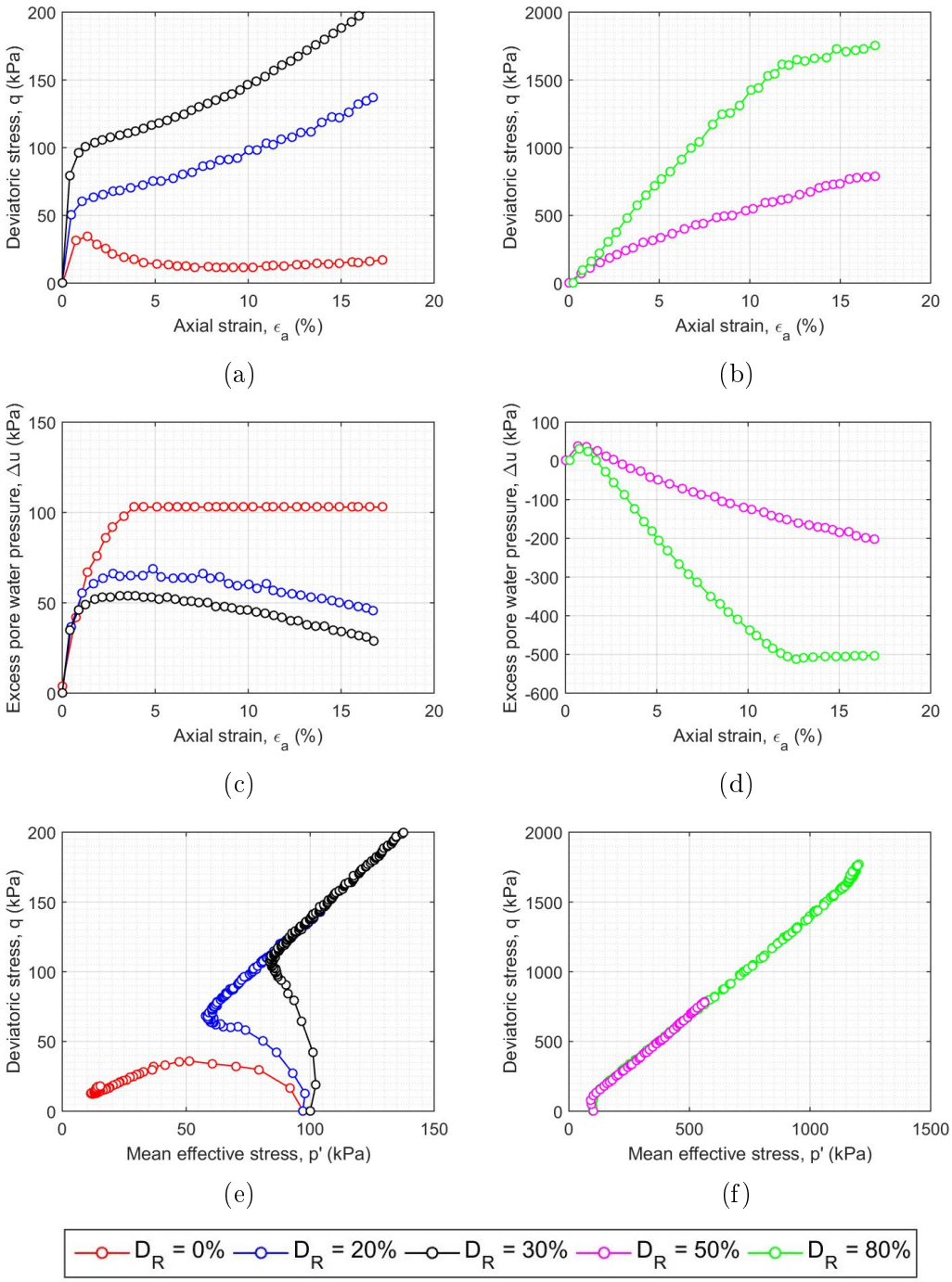

Figure 4.1: Influence of the relative density D_R on the undrained behavior of clean sand Hostun subjected to a confining pressure p'_0 of 100 kPa: curves $(q - \varepsilon_a)$ (a,b); $(\Delta u - \varepsilon_a)$ (c,d); $(q - p')$ (e,f)

transformation line, where it dilates and increases in strength to reach the critical state ($D_R = 20 - 30\%$). The dense material stress path increases to the right and exhibits a dilatant behavior during the overall loading phase ($D_R = 50 - 80\%$). The same effect of relative density is observed for all the confining pressures analyzed.

4.2.2 Influence of confining pressure

The influence of the isotropic consolidation pressure is investigated by carrying out tests on specimens with the same initial relative density and consolidated under different confining pressures p'_0 (50, 100, 200 kPa). To this regard, several series are performed on the Hostun clean sand and sand-fines mixtures by varying the initial relative density. Results of tests for loose, medium and dense specimens are shown in Figs 4.2, 4.3 and 4.4.

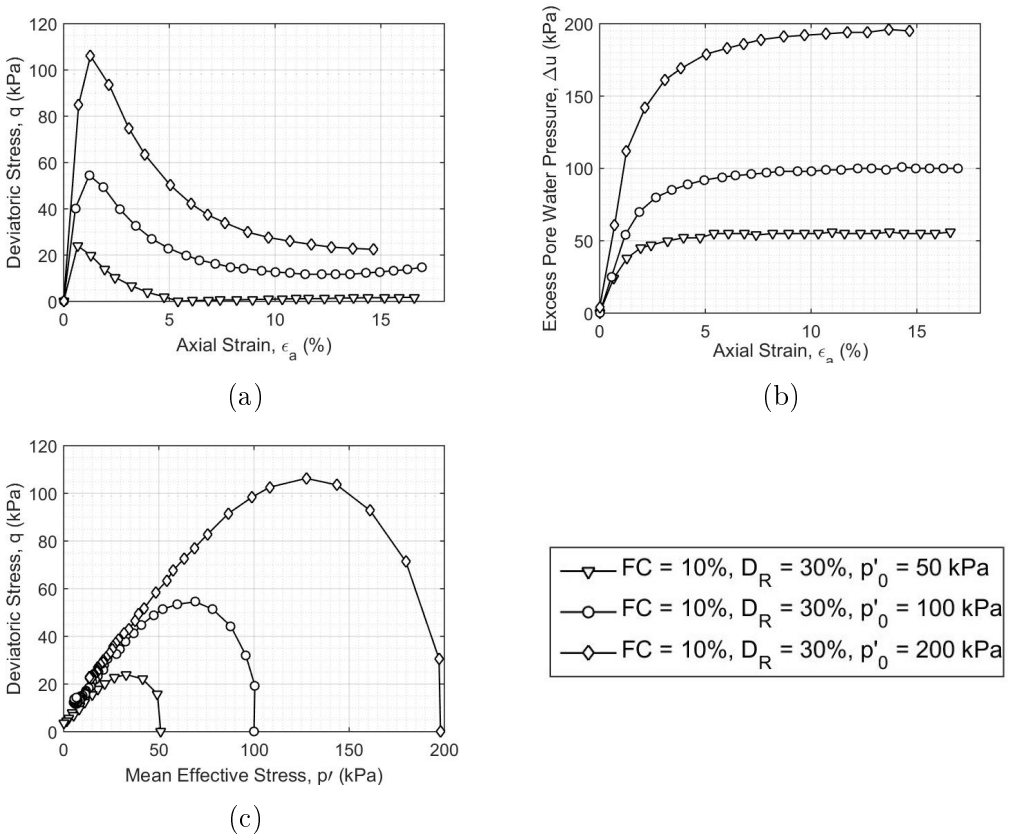

Figure 4.2: Influence of the confining pressure p'_0 on the undrained behavior of loose specimens: curves $(q - \varepsilon_a)$ (a); $(\Delta u - \varepsilon_a)$ (b); $(q - p')$ (c)

From these figures, it is observed that, for a given relative density, the confining pressure has a significant influence on the peak shear strength as

well as on the volume behaviour of the material. In particular, for specimens presenting either total contracting or contracting-dilating behavior (loose and medium soils), the peak resistance increases with the confining pressure, as shown in Figs 4.2 and 4.3. On the other hand, the ultimate resistance (at large deformation) increases with the confining pressure in both cases of loose and dense soils.
The generation rate of pore water pressure increases at higher confining stresses and the results show a similar general trend with respect to the confining pressure for both loose and dense soils.
Also the effective stress path in the $(q - p')$ plane presents a similar trend with respect to the confining pressure and the contracting behavior appears to increase with increasing initial confining stress.

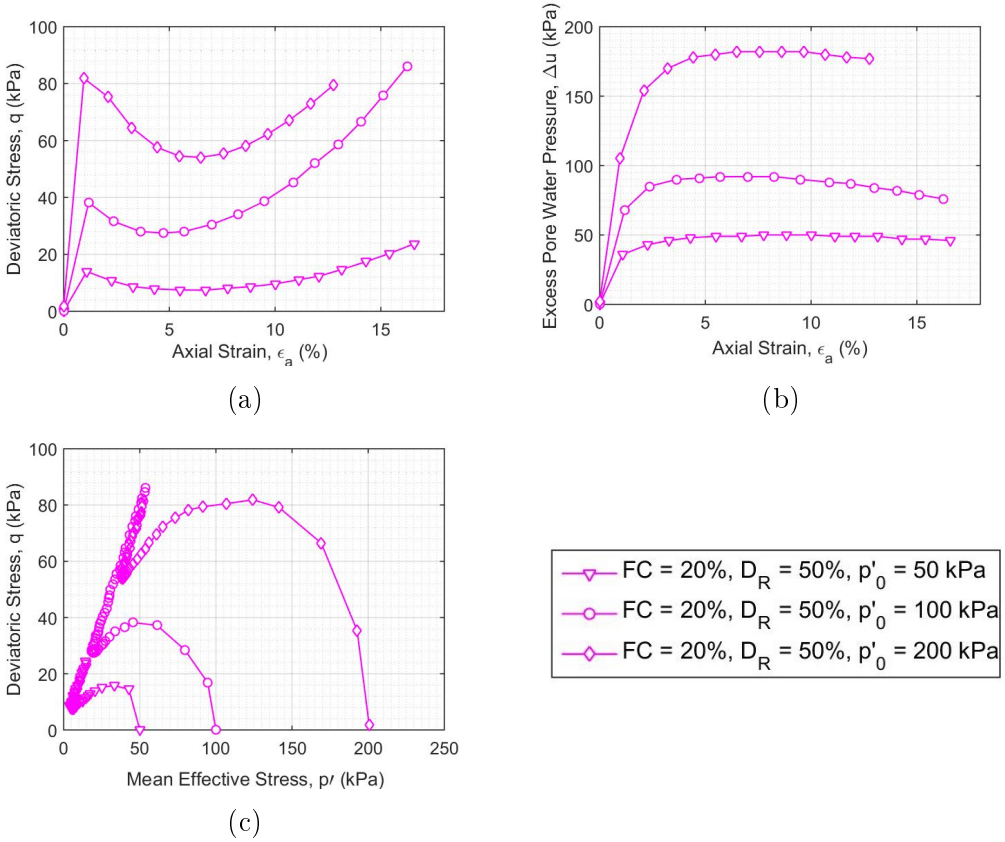

Figure 4.3: Influence of the confining pressure p'_0 on the undrained behavior of medium specimens: curves $(q - \varepsilon_a)$ (a); $(\Delta u - \varepsilon_a)$ (b); $(q - p')$ (c)

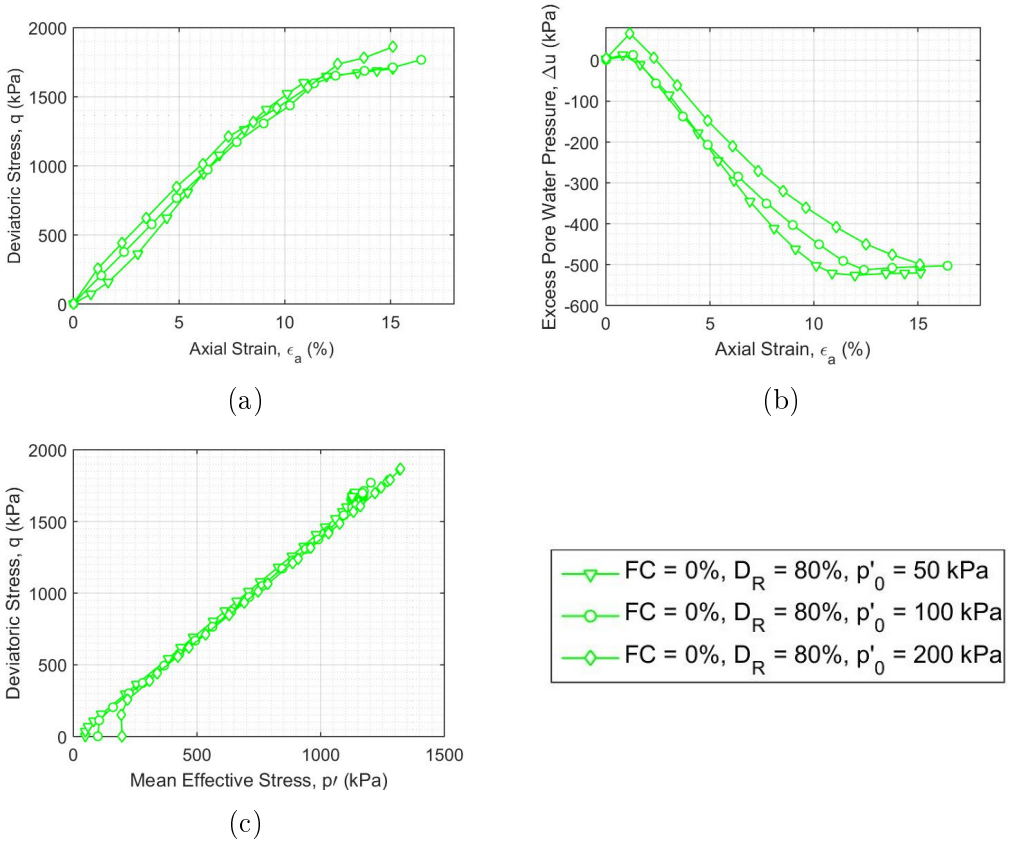

Figure 4.4: Influence of the confining pressure p'_0 on the undrained behavior of dense specimens: curves $(q - \varepsilon_a)$ (a); $(\Delta u - \varepsilon_a)$ (b); $(q - p')$ (c)

4.2.3 Influence of non-plastic fines

The effect of fine content on the intergranular mechanism is investigated analyzing the response of the mixture in undrained conditions. Figs 4.5, 4.6 and 4.7 present the influence of fine particles on the mechanical response of loose, medium and dense mixtures, respectively. From all the test results, it is concluded that the addition of fine particles implies a more contracting behavior of silty sand mixtures. Fine particles have a similar effect in the case of low and medium relative density (Figs 4.5 and 4.6). Below 5% of silt content, the peak shear strength is similar to clean sand and above, it remarkably decreases with increasing fine content, leading to complete static liquefaction in some cases. In the case of high relative density, shear strength is unaltered with fine content up to 10% and then decreases with increasing fine content (Fig. 4.7). The same effect is displayed in Fig. 4.8 through the ultimate deviatoric strength q_{cr} with respect to the fine content, which summarizes the results for confining pressures p'_0 of 50, 100 and 200 kPa.

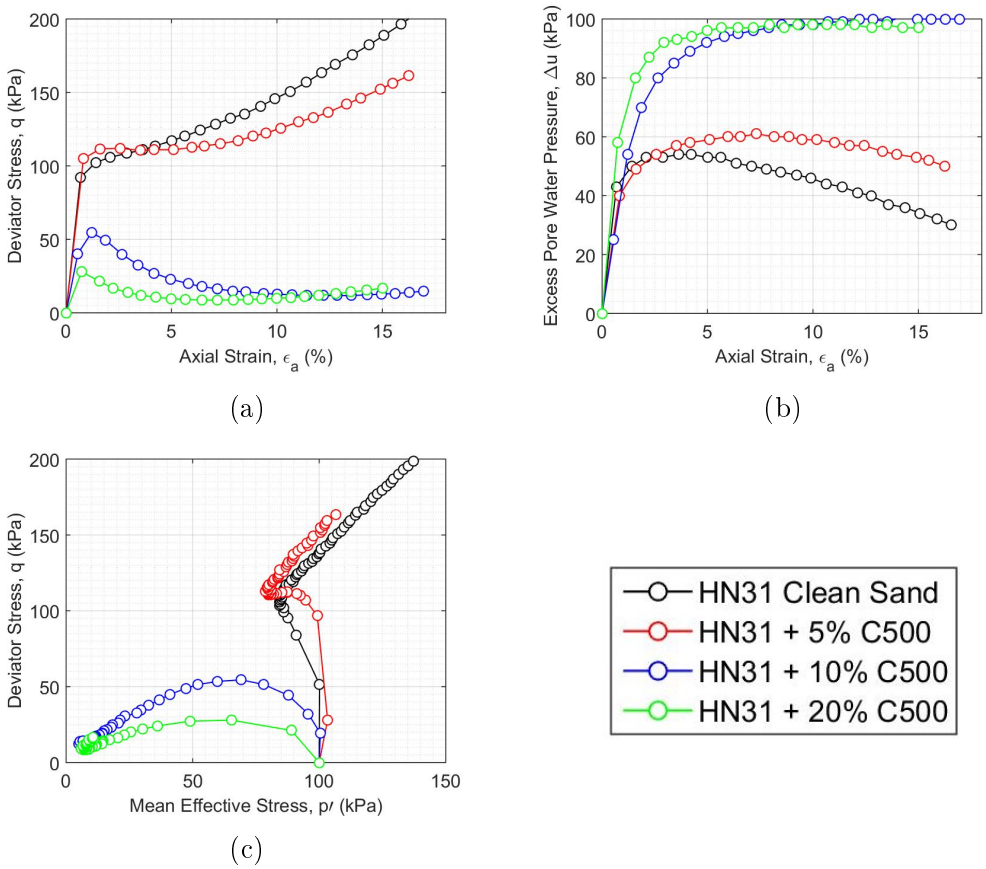

Figure 4.5: Influence of the fine content FC on the undrained behavior of loose mixtures ($D_R = 30\%$): curves $(q - \varepsilon_a)$ (a); $(\Delta u - \varepsilon_a)$ (b); $(q - p')$ (c)

The tests performed for mixtures having different relative densities are used to investigate the variation with fine content of the limit void ratio below which static liquefaction would no longer occur. Fig. 4.9 displays the static liquefaction envelope derived from the results of the monotonic CU triaxial tests. Each test result is plotted as a point defined by the global void ratio after consolidation e and the fine content FC. Filled circles indicate that static liquefaction occurred, whereas the empty circles denote that either temporary liquefaction or stable behavior is observed during the shear loading. In Fig. 4.9, the obtained static liquefaction line, indicates the limit between stable and unstable behavior with respect to liquefaction of the analyzed silty sand mixtures. The limit void ratio, at which static liquefaction occurs, decreases with increasing fine content. This result confirms that the global void ratio e is not an adequate parameter to capture the effect of fine particles on the liquefaction potential of silty sand mixtures because soils having the same

void ratio, present different behaviors.

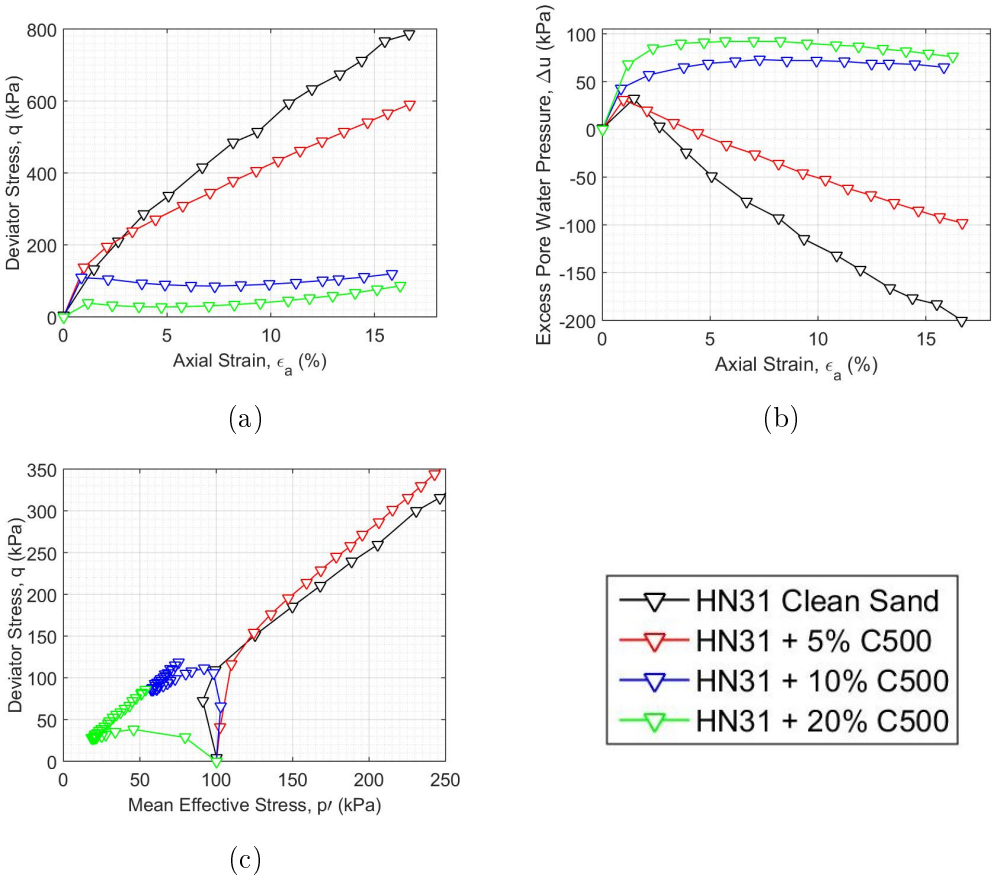

Figure 4.6: Influence of the fine content FC on the undrained behavior of medium mixtures ($D_R = 50\%$): curves $(q - \varepsilon_a)$ (a); $(\Delta u - \varepsilon_a)$ (b); $(q - p')$ (c)

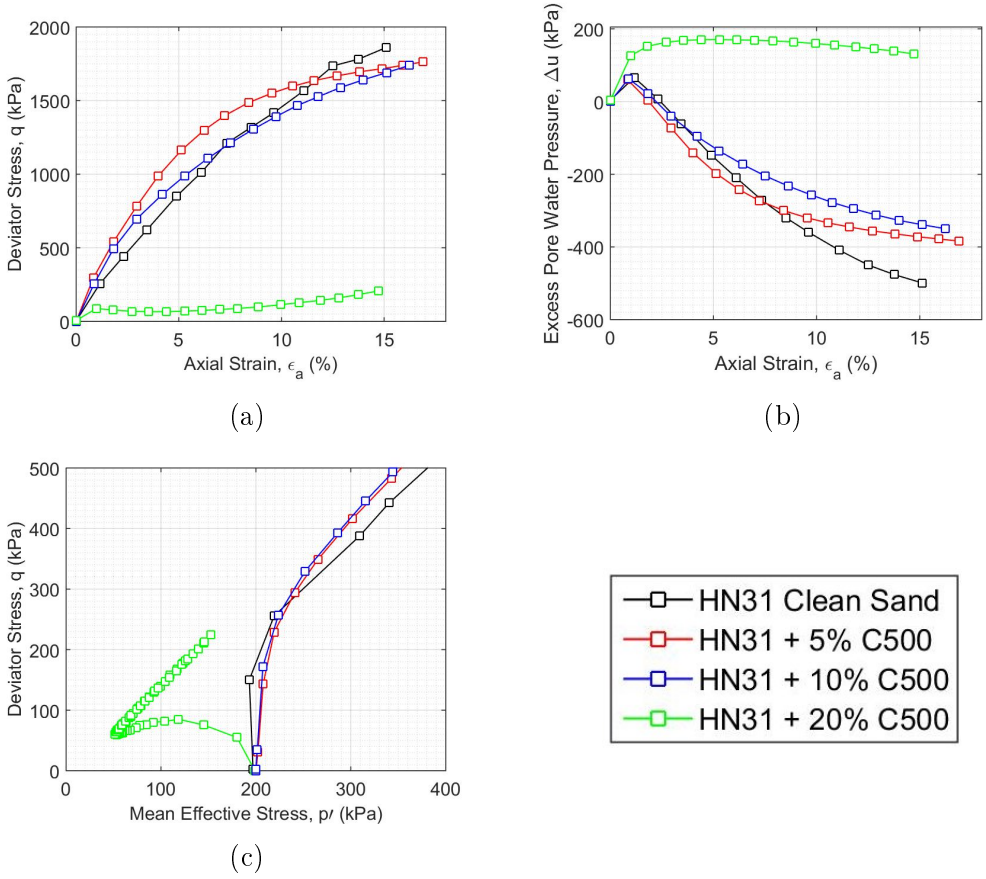

Figure 4.7: Influence of the fine content FC on the undrained behavior of dense mixtures ($D_R = 80\%$): curves $(q - \varepsilon_a)$ (a); $(\Delta u - \varepsilon_a)$ (b); $(q - p')$ (c)

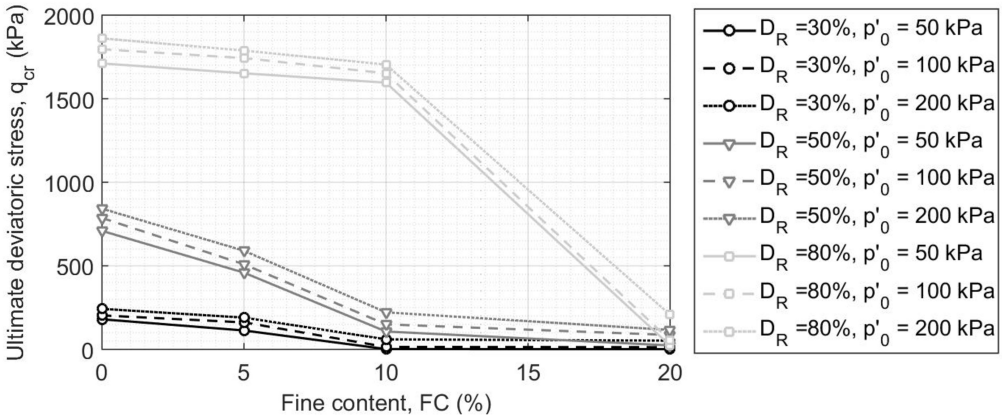

Figure 4.8: Ultimate deviatoric stress q_{cr} versus fine content FC in undrained conditions, for various relative densities $D_R = 30 - 50 - 80\%$ and confining pressure $p'_0 = 50 - 100 - 200kPa$

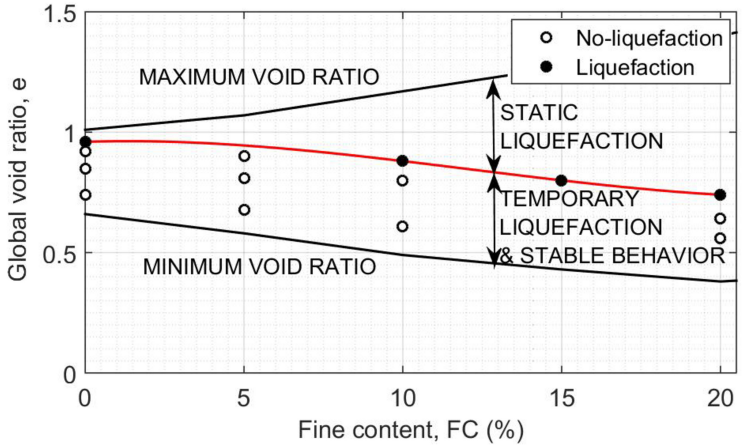

Figure 4.9: Ultimate deviatoric stress q_{cr} versus fine content FC in undrained conditions, for various relative densities $D_R = 30 - 50 - 80\%$ and confining pressure $p'_0 = 50 - 100 - 200kPa$

4.3 Undrained cyclic behavior

Stress-controlled cyclic CU triaxial tests are carried out at a frequency of 0.5 Hz. The intensity of the cyclic stress ratio is $CSR = q/2p'_0$, where q is the stationary amplitude of cyclic axial stress. The liquefaction strength curve is the cyclic stress ratio CSR required to attain liquefaction versus the number of uniform load cycles N. Liquefaction is deemed achieved for an excess pore water pressure reaching the initial confining pressure or single-amplitude shear strain equal to 3% (Ishihara, 1993). Liquefaction potential curves are obtained for different relative density ($D_R = 30-50-80\%$).

4.3.1 Case of loose soil

Figure 4.10 depicts a typical result of cyclic liquefaction for a loose specimen of Hostun sand characterized by a relative density of 30%, an isotropic confining stress of 100 kPa and subjected to a cyclic stress ratio CSR equal to 0.1, which corresponds to a cyclic stress q of 20 kPa (Fig. 4.10a).
Fig. 4.10b shows the excess pore water pressure Δu with respect to the number of cycles. Δu increases with the same slope until reaching a value of 60 kPa, which corresponds to a pore pressure ratio $\Delta u/p'_0 = 0.6$ and a cycle $N = 27$, and then, it increases with a higher slope reaching the consolidation pressure of 100 kPa at the critical cycle $N_L = 34$. Similarly, the value of the axial strain is very small throughout the test until the same cycle $N = 27$ when

it rapidly increases and develops large deformations ($\varepsilon_a = 10\%$) as shown in Fig. 4.10c. This increase is clearly confirmed in Fig. 4.10d, where the pore water pressure build-up is presented with respect to the axial strain. Finally, Fig. 4.10d illustrates the effective stress paths in the (q, p') plane showing the progressive migration of the path to the left until reaching the failure line at which the phenomenon of liquefaction is initiated in the extension phase.

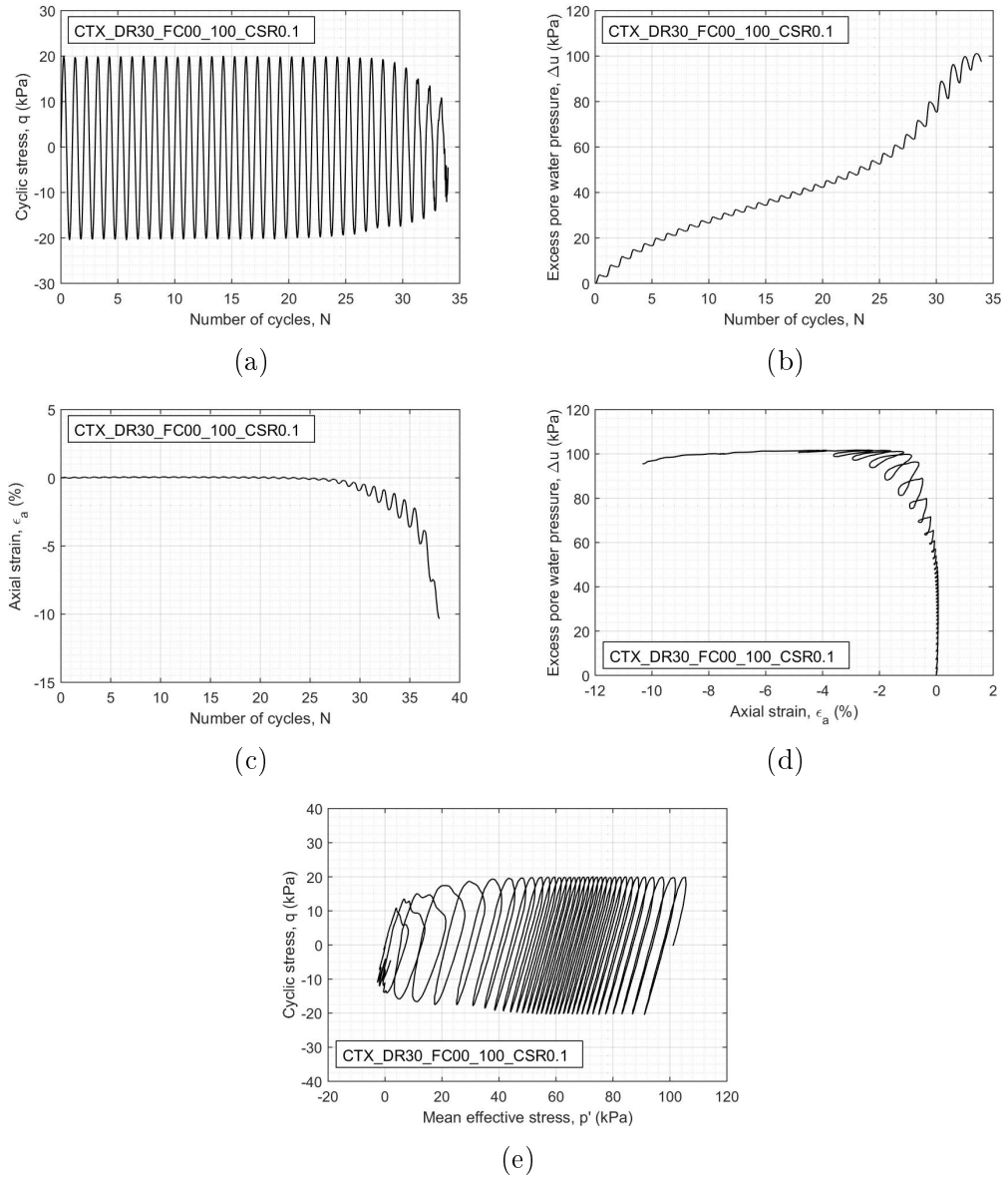

Figure 4.10: Phenomenon of cyclic liquefaction of Hostun sand loose specimen ($D_R = 30\%$, $p'_0 = 100kPa$, $CSR = 0.1$): curves $(N - q)$ (a); $(N - \Delta u)$ (b); $(N - \varepsilon_a)$ (c); $(\Delta u - \varepsilon_a)$ (d); $(q - p')$ (e)

4.3.2 Case of dense soil

Figure 4.11 depicts a typical result of cyclic mobility for a dense specimen of Hostun sand characterized by a relative density of 80%, an isotropic confining stress of 100 kPa and subjected to a CSR equal to 0.225, which corresponds to a cyclic stress q of 50 kPa (Fig. 4.11a).
Conversely to the case of loose specimen, the excess pore water pressure increases with almost the same slope until the value of 60 kPa, which corresponds to a pore pressure ratio $\Delta u/p'_0 = 0.6$ and a cycle number $N = 8$. Beyond this value, the pore water pressure build-up is characterized by the generation of a "two-peak" mechanism during which the excess pore water pressure reaches a peak twice per cycle as displayed in Fig. 4.11b. Moreover, the first phase (before reaching $\Delta u/p'_0 = 0.6$ and $N = 8$) is associated to small deformations qualitatively similar to those of loose sands and during the "two-peak" mechanism, strains increase to higher values (Fig. 4.11c). The same effect is observed in Fig. (Fig. 4.11d), where the curve presents the same value of Δu at two different values of axial strains per cycle after $\Delta u = 60kPa$. From this figure, it can be also noted the accumulation of strains due to the increasing of pore water pressure and the fact that strains are non-symmetrical and present higher values in the extension phase. Fig. 4.11e illustrates the effective stress paths in the (q, p') plane. Initially, the stress path gradually migrates towards the origin of the axes with a reduction in the effective mean stress p' at each loading cycle until it crosses the phase transformation line at $\Delta u = 60kPa$, which corresponds to $p' = 40kPa$. After that, the sample exhibits dilative behavior increasing the mean effective stress and regains strength, and then, during the unloading phase, the sample contracts again. This repeated mechanism of contractancy-dilatancy produces the so-called "butterfly" loops, which are characterized by a twice passage per cycle by a zero effective stress one corresponding to the end of unloading during compression and the other one corresponds to the end of unloading during extension phase. This feature is depicted in Fig. 4.11f in terms of deviatoric stress with respect to the axial strain forms very tight and concentrated loops at almost zero axial deformation up to the cycle at which the cyclic mobility mechanism begins ($\Delta u = 60kPa$, $N = 8$) and then the loops appear wider and characterized by cyclic stress q lower and lower in the $(q - \varepsilon_a)$ plane.

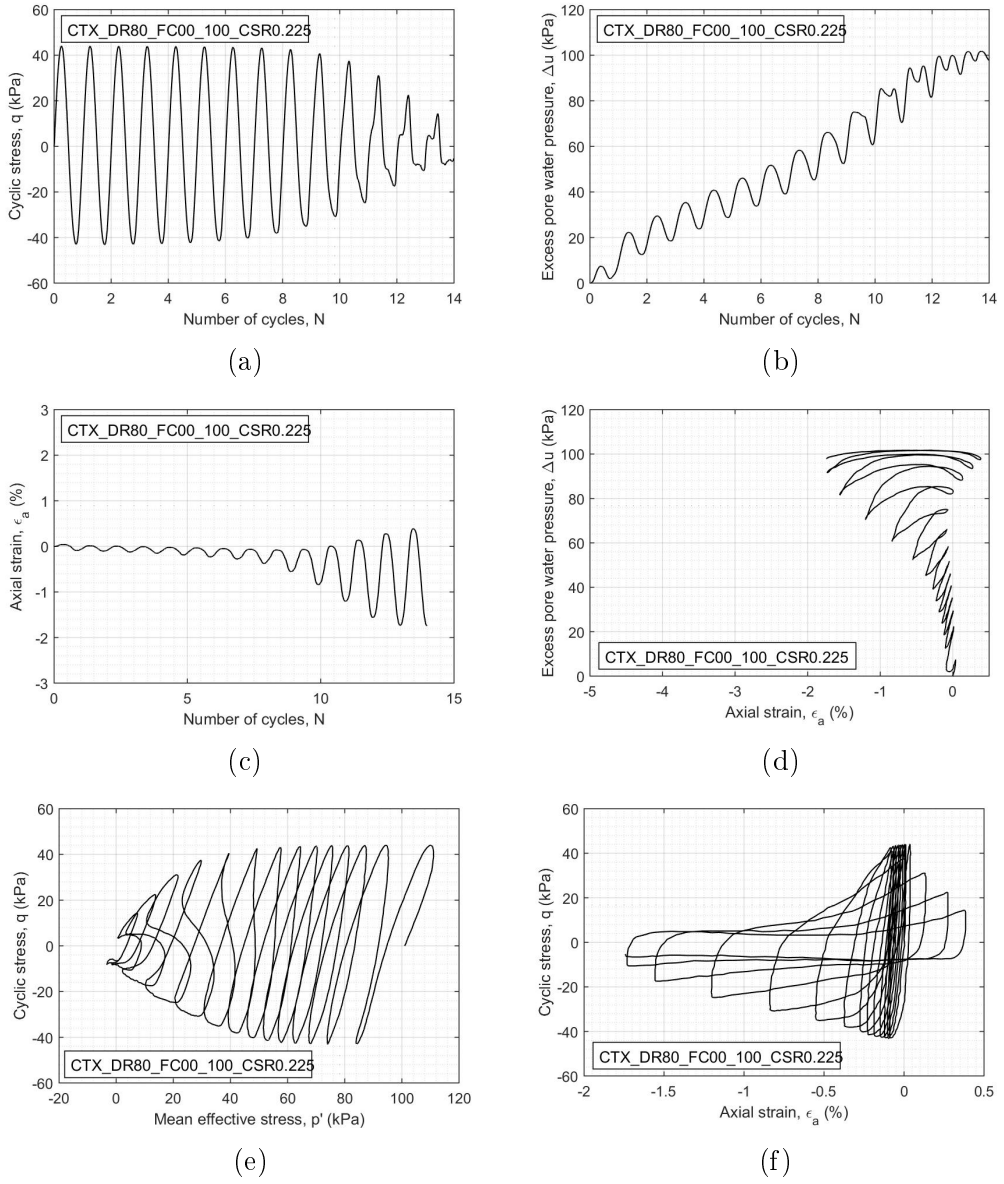

Figure 4.11: Phenomenon of cyclic liquefaction of Hostun sand dense specimen ($D_R = 80\%$, $p'_0 = 100kPa$, $CSR = 0.225$): curves $(N - q)$ (a); $(N - \Delta u)$ (b); $(N - \varepsilon_a)$ (c); $(\Delta u - \varepsilon_a)$ (d); $(q - p')$ (e); $(q - \varepsilon_a)$ (f)

4.3.3 Influence of relative density

Fig. 4.12 shows the influence of the relative density on cyclic resistance to liquefaction by varying the initial relative density and keeping the other parameters constant (loading amplitude and consolidation stress). This figure depicts two samples with relative densities of 30 and 50% consolidated at 100kPa and subjected to a CSR of 0.1. For the same given cyclic stress, the number of cycles to liquefaction increases with the increasing of the relative density. Hence, the resistance to liquefaction increases as the relative density increases. Moreover, as already seen in the previous sections, not only the number of cycles required to liquefaction varies with the relative density but also the nature of the cyclic response, which can be related to cyclic liquefaction for loose specimens and cyclic mobility for dense specimens. The medium specimens represent a behavior mixing the two phenomena.

The influence of relative density is confirmed from the liquefaction resistance curve reported in Fig 4.13 for the three relative density considerated and a confining pressure of 100 kPa. The experimental data are fitted adopting the following relationship between the CSR and N_L

$$CSR = a \cdot N_L^b \tag{4.1}$$

where a and b are material constant. The value of the b constant is the same for the three relative densities, while the value of a increases with respect to the latters.

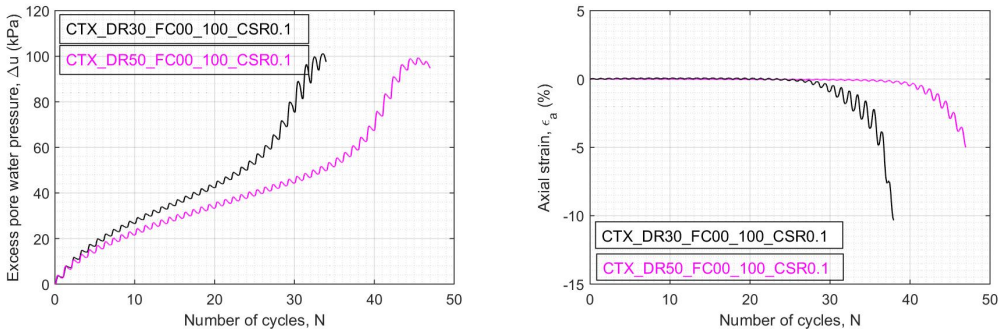

(a) (b)

Figure 4.12: Influence of the relative density on the cyclic resistance of Hostun RF sand ($D_R = 30$ and 50%, $p'_0 = 100kPa$, $CSR = 0.1$): curves $(N - \Delta u)$ (a); $(N - \varepsilon_a)$ (b)

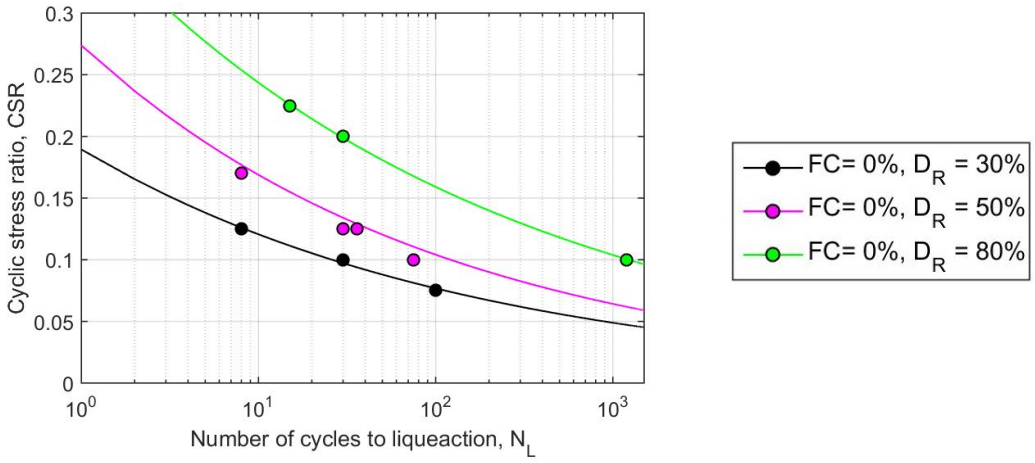

(a)

Figure 4.13: Liquefaction resistance curves of Hostun clean sand

4.3.4 Influence of confining pressure

Figs 4.14, 4.15 and 4.16 show the resistance to liquefaction of sand at several levels of mean confining pressure p'_0. The variation of the pore pressure ratio (i.e. the excess pore pressure normalized to effective consolidation pressure) versus the number of cycles of loading is shown in Figs 4.14a, 4.15a and 4.16a, while Figs 4.14b, 4.15b and 4.16b show the variation of the axial strain versus the number of loading cycles.
The results indicate that the influence of confining pressure on pore pressure buildup and development of axial strains depend on the relative density and the CSR value. For example, in medium and dense samples (Figs 4.15 and 4.16), the rate of pore pressure generation is almost similar for the consolidation pressures of 100 and 200 kPa. In particular, it is interesting to note that in case of medium soil ($D_R = 50\%$), the undrained behavior passes gradually from cyclic liquefaction to cyclic mobility from 50 to 200 kPa as shown from the "two-peak" mechanism in Fig. 4.15a for the sample consolidated at 200 kPa. The reason is due to the fact that the relative density of 50% corresponds to the transition from loose to dense material.
However, the liquefaction resistance, at a given value of relative density, decreases for all soils with an increase in consolidation pressures from 50 to 200kPa. This means that samples at low consolidation pressure, subjected to the same CSR value, need a large number of cycles to reach liquefaction.

Figure 4.17 summarizes liquefaction resistance obtained for each test series related to loose, medium and dense sand carried out at confining stresses of

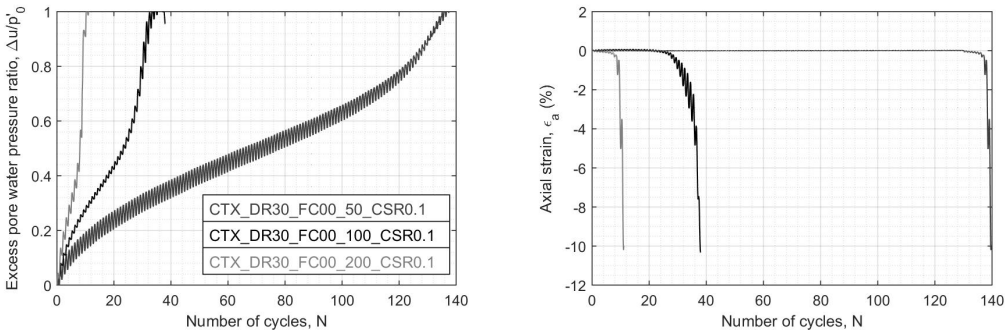

(a) (b)

Figure 4.14: Influence of the confining pressure on the cyclic resistance of loose specimens ($D_R = 30\%$, $FC = 0\%$, $CSR = 0.1$): curves ($N - \Delta u/p'_0$) (a); ($N - \varepsilon_a$) (b)

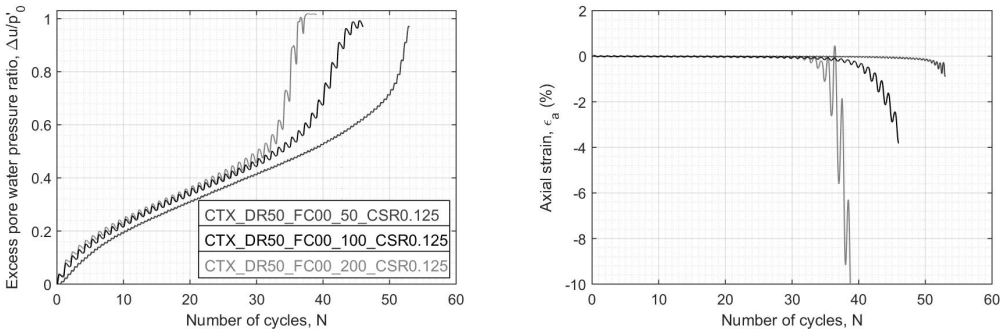

(a) (b)

Figure 4.15: Influence of the confining pressure on the cyclic resistance of medium specimens ($D_R = 50\%$, $FC = 0\%$, $CSR = 0.125$): curves ($N - \Delta u/p'_0$) (a); ($N - \varepsilon_a$) (b)

50 kPa, 100 kPa and 200 kPa. For all the densities, the liquefaction resistance decreases with the increasing of the consolidation pressure from 50 to 200 kPa. However, the effect of consolidation pressure on liquefaction resistance is less significant for the medium sand (Fig. 4.17b). From these figures, it can be also observed that the effect of consolidation pressure increases for higher CSR values. In fact, the effect of consolidation pressure is negligible at low cyclic stress ratios in all cases, while, conversely, there is a significant effect of the consolidation pressure on liquefaction resistance up to 100 cycles. In summary, from these tests, it can be concluded that the effect of the consolidation pressure on liquefaction resistance of soils mainly depends on the relative density. Soils consolidated at 50 kPa show high liquefaction resistance in all cases as a consequence of the low compressibility of sand at low consolidation

pressures.
Similar findings are reported by other authors (Vaid et al., 1985; Hyodo et al., 2002; Rangaswamy et al., 2010).

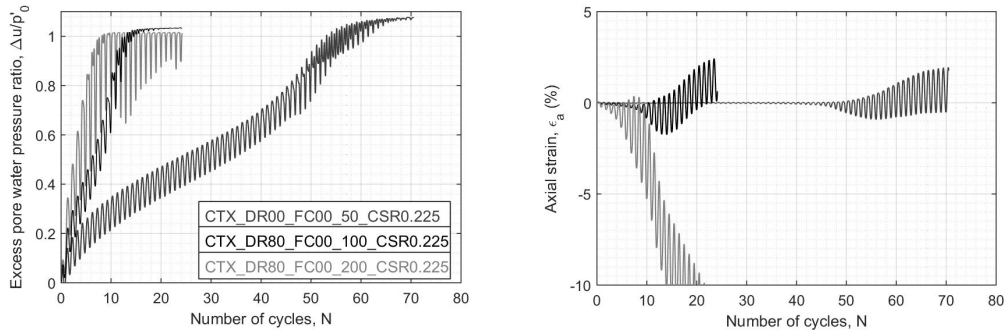

(a) (b)

Figure 4.16: Influence of the confining pressure on the cyclic resistance of dense specimens ($D_R = 80\%$, $FC = 0\%$, $CSR = 0.225$): curves ($N - \Delta u/p'_0$) (a); ($N - \varepsilon_a$) (b)

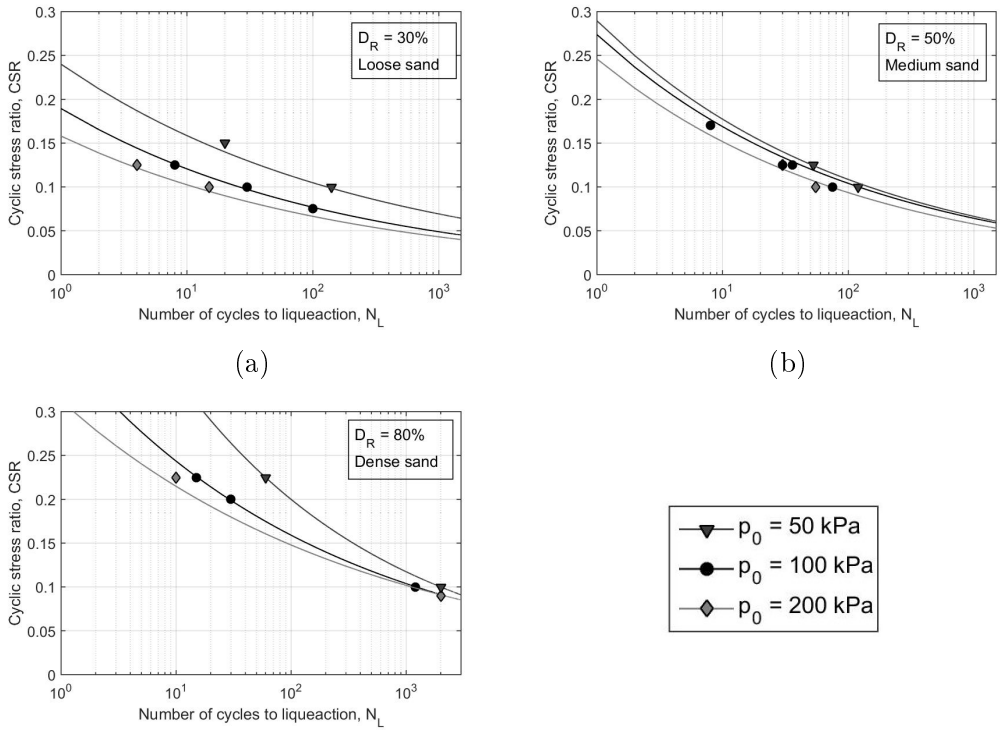

(a) (b)

(c)

Figure 4.17: Influence of the confining pressure on liquefaction resistance curves of Hostun clean sand

4.3.5 Influence of the frequency of cyclic loading

The frequency of cyclic loading is one of the major factors which influences both liquefaction and dynamic properties of saturated sands (Lin et al., 1996; Lombardi et al., 2013; Dash and Sitharam, 2016). In this section, the effect of frequency of cyclic loading on liquefaction resistance of Hostun sand is investigated. To this regard, test results concerning specimens prepared with a fixed relative density of 30%, consolidated at 100 kPa and cyclically loaded using sinusoidal loads at varied frequencies and for a given CSR value of 0.1 are presented therein. Frequency f of cyclic loading on the soil sample varies from 0.005 to 2.0 Hz.
Figs 4.18 and 4.19 show the effect of frequency of the loading on the pore water pressure generation and on the reduction of the mean effective stress at different frequencies.

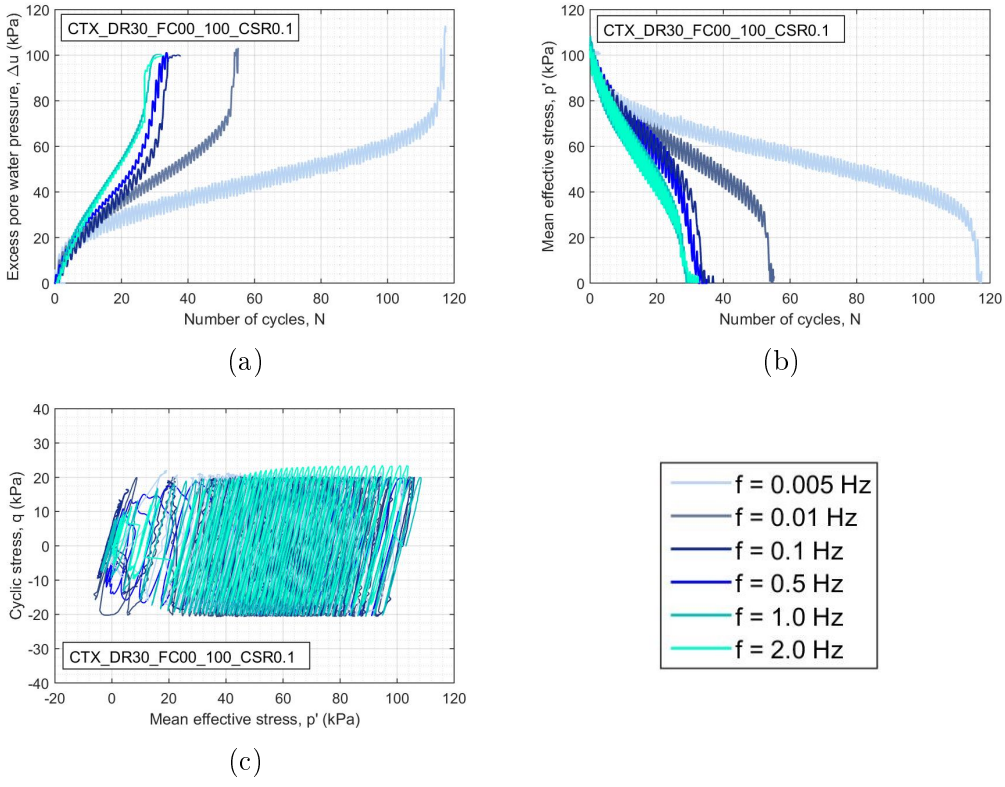

Figure 4.18: Influence of the frequency of cyclic loading: excess pore water pressure (a) and mean effective stress (b) versus cycles of loading and stress path in the $(p' - q)$ plane (c) for samples consolidated at given relative density $D_R = 30\%$ and confining pressure $p'_0 = 100kPa$, cyclically loaded at a cyclic stress ratio of 0.1

From Fig. 4.18a, the rate of generation of excess pore water pressure increases with the increasing of cyclic loading frequency and the cyclic liquefaction resistance decreases with the increasing of the loading frequency. Accordingly, as shown in Fig. 4.18b, the rate of decreasing of the mean effective stress also increases as the frequency increases. Moreover, the number of cycles required to initiate liquefaction differs greatly in the range from 0.005 to 0.1 Hz, while it is almost constant from 0.1 to 2.0 Hz. Fig. 4.18c depicts the stress paths in the $(p' - q)$ plane. The stress paths are similar until reaching the value of $p' = 30kPa$, independently from the frequency, and then they differ depending on the frequency.

The normalised pore water pressure and the variation of the mean effective stress versus the cycle ratio N/N_L are presented in Fig. 4.19. For the first cycles ($N/N_L < 0.4$), the rate of pore water pressure build-up and of the reduction of the mean effective stress increase with the decrease of the loading frequency. Conversely, for $N/N_L > 0.6$, the frequency causes an opposite effect on the pore pressure generation and the associated induced reduction of the mean effective stress.

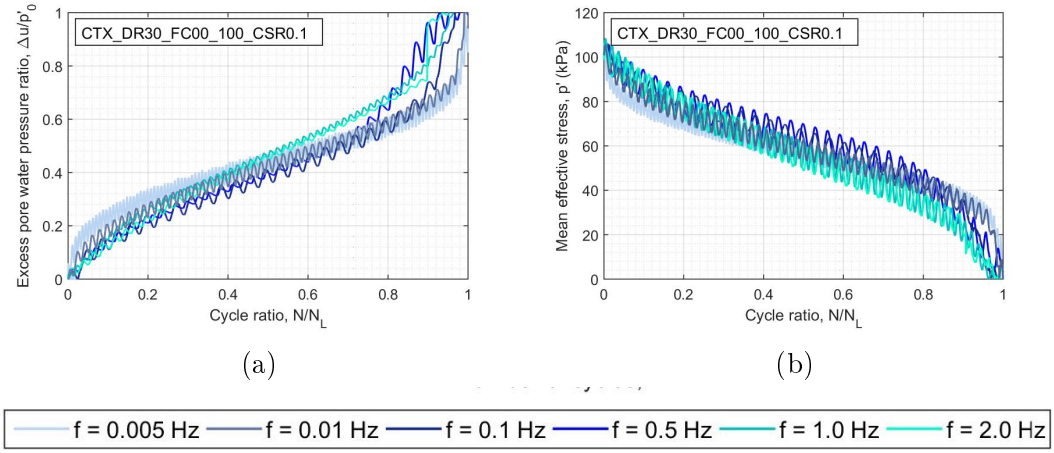

Figure 4.19: Influence of the frequency of cyclic loading: excess pore water pressure ratio (a) and reduction of mean effective stress (b) versus the cycle ratio N/N_L for samples consolidated at given relative density $D_R = 30\%$ and confining pressure $p'_0 = 100kPa$, cyclically loaded at a cyclic stress ratio of 0.1, and at various frequencies

The number of loading cycles required to cause initial liquefaction of specimens cyclically loaded at a cyclic stress ratio of 0.1, and at frequencies of

0.005, 0.01, 0.1, 0.5, 1.0 and 2.0 Hz is illustrated in Fig. 4.20. The number of cycles required to cause initial liquefaction, N_L, suddenly decreases when increasing the frequency of cyclic loading from 0.005 to 0.1 Hz and then it remains almost constant from 0.1 to 2.0 Hz at a given relative density and a cyclic stress ratio value, indicating that the cyclic resistance decreases when increasing the frequency of the cyclic loading in stress-controlled tests.

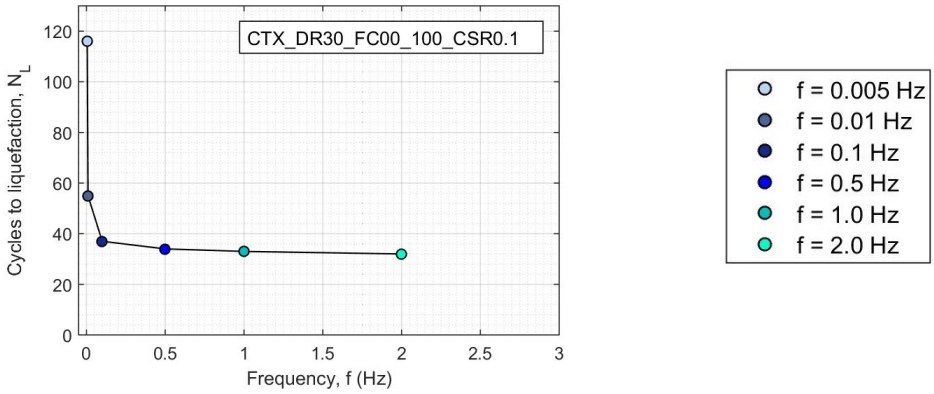

Figure 4.20: Cycles to initial liquefaction vs. frequency at constant $D_R = 30\%$, confining pressure $p'_0 = 100kPa$ and cyclic stress ratio of 0.1

4.3.6 Influence of fine content

Stress-controlled cyclic triaxial tests are carried out at a frequency of 0.5 Hz on sand-fines mixtures in order to investigate the influence of fine content on the cyclic liquefaction resistance of loose, medium and dense soils.
Figs 4.21 and 4.22 display the effect of fine content for low and high relative densities ($D_R = 30 - 80\%$) subjected to a cyclic stress equal to 0.1 and 0.2, respectively. As shown from these figures, the fine content affects significantly the liquefaction resistance. When the relative density is low ($D_R = 30\%$, Fig. 4.21), the liquefaction resistance, in terms of N_L , increases for increasing fine content up to 5% and then suddenly decreases for increasing fine content up to 20%. To this regard, it can be observed that the rate of pore water pressure generation and variation of the mean effective stress increase for $FC = 5\%$ and then decrease with further amount of fine particles. The same effect is found for medium mixtures ($D_R = 50\%$). Conversely, when the relative density is higher ($D_R = 80\%$, Fig. 4.22), the number of cycles to attain liquefaction, N_L, is greater than the one for clean sand up to a FC value of 10%. Then, a steep downward trend is observed for higher fine contents. In this case the rate of excess pore water pressure generation and

reduction of mean effective stress are higher for fine content up to 10% and then decrease, lower than clean sand, for $FC = 20\%$.

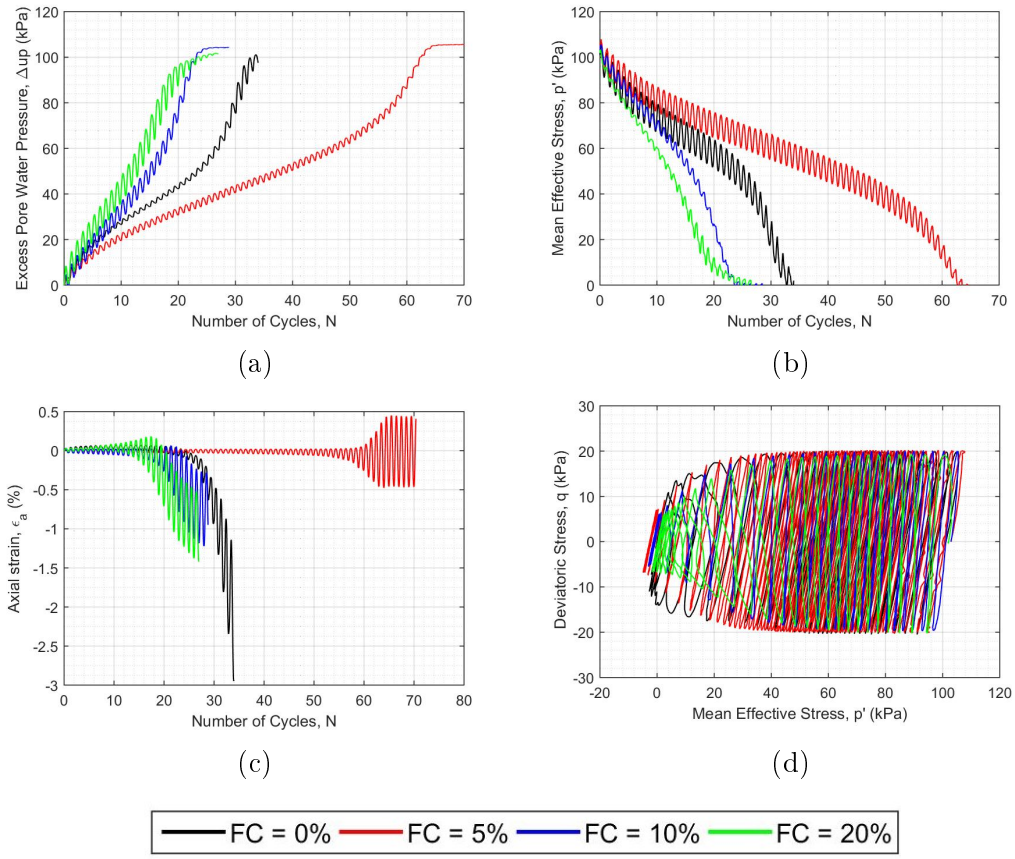

Figure 4.21: Influence of the fine content on loose mixtures ($D_R = 30\%$, $p'_0 = 100kPa$, $CSR = 0.1$) : excess pore water pressure (a), mean effective stress (b) and axial strain (c) versus cycles of loading and stress path in the $(p' - q)$ plane (d)

This same behavior is obtained for all the cyclic stress ratios investigated, as reported in Fig. 4.23, that presents liquefaction potential curves for loose, medium and dense mixtures ($D_R = 30 - 50 - 80\%$). Liquefaction potential curves display the CSR versus the number of cycles N_L required to trigger liquefaction. The mixtures with different fine contents show various mechanical behaviors even in the case of same relative density. The effect of fines can lead to an increase or decrease of the number of cycles N_L for a given value of CSR. The liquefaction resistance increases with the increasing of fine content up to 5% and then decreases with the increasing of fine content up to 20% for loose and medium relative densities. Soils with high relative

density show more remarkable variations with respect to the liquefaction resistance of clean sand, and the range of variation of N_L for a given value of CSR is larger. That means fine content and relative density can significantly affect the excess pore pressure build-up and the liquefaction resistance of silty sand mixtures.

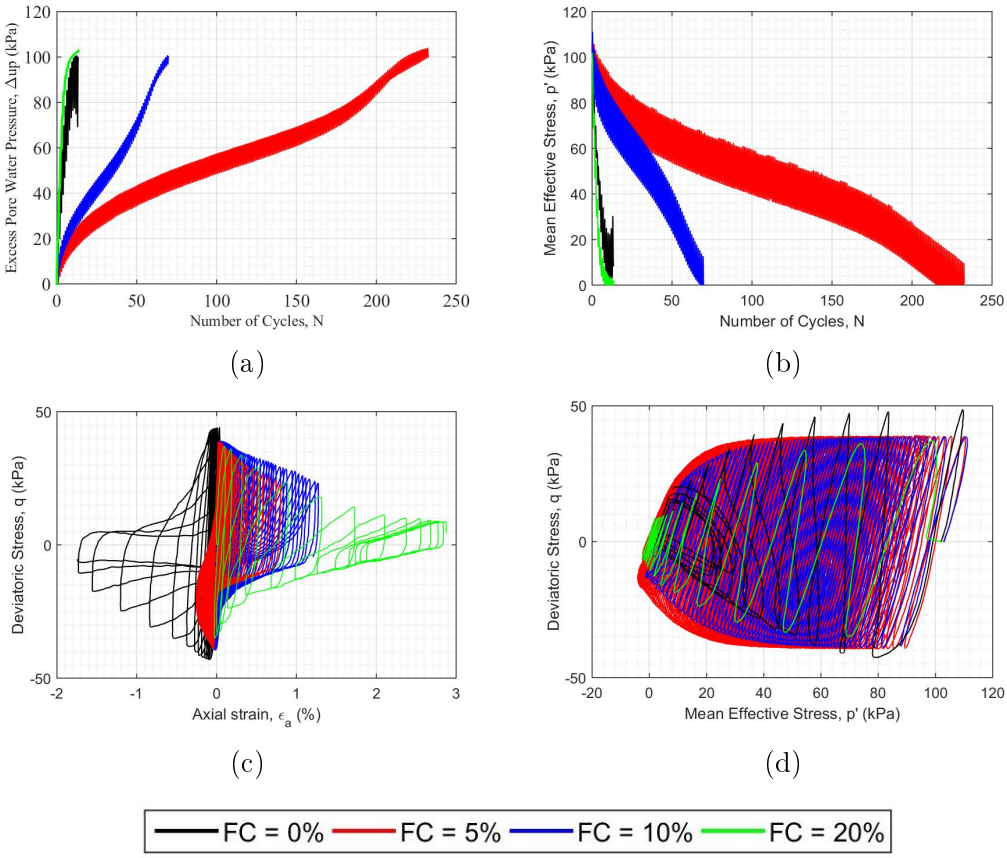

Figure 4.22: Influence of the fine content on dense mixtures ($D_R = 80\%$, $p'_0 = 100kPa$, $CSR = 0.2$) : excess pore water pressure (a) and mean effective stress (b) versus cycles of loading, hysteresis loops (c) and stress path in the $(p' - q)$ plane (d)

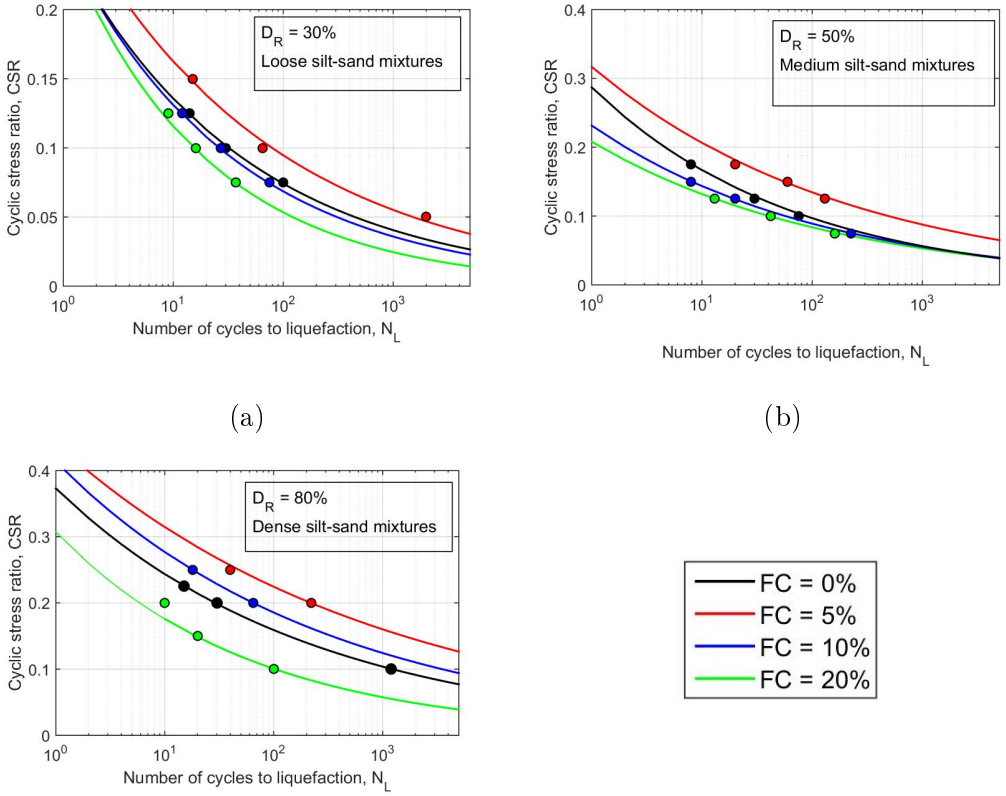

Figure 4.23: Liquefaction potential curves obtained for different fine contents and for loose (a), medium (b) and dense (c) silty sand mixtures at confining pressure $p'_0 = 100kPa$

More specifically, the influence of fine content on the pore water pressure build-up is presented in Fig. 4.24 by plotting the pore pressure ratio versus the corresponding cycle ratio for loose and dense soils (Figs 4.24a and 4.24b) and comparing these results to the lower and upper bounds suggested by Lee and Albaisa (1974).

Results show that for both loose and dense soils, the rate of pore pressure generation increases with the increase of the fine content, indicating their high potential to liquefaction and the fact that the upper bound values, proposed by Lee and Albaisa (1974), appear to be careless. Furthermore, this effect is more pronounced in the case of dense soils characterized by more fluctuations in the pore water pressure build-up since the start of the loading, while in the case of loose sand, this effect is more evident from $\Delta u/p'_0 > 0.6$.

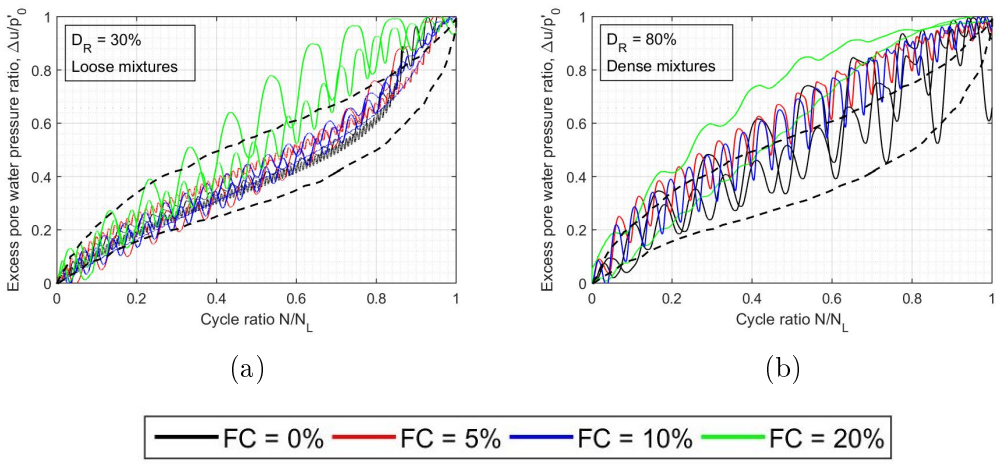

Figure 4.24: Influence of the fine content on the excess pore water pressure ratio for loose (a) and dense (b) mixtures compared with the bound curves suggested by Lee and Albaisa (1974)

4.4 Strain-dependent dynamic properties

4.4.1 Influence of relative density

Results from resonant column tests show that the shear modulus G and damping ratio D are strongly affected by the relative density. For instance, Fig. 4.25 presents the shear modulus, damping ratio, normalized shear modulus and excess pore water pressure ratio versus the shear strain for various relative densities at the same confining pressure of 100 kPa. From this figure, the shear modulus G increases as the relative density increases for a given value of the shear strain (Fig. 4.25a). Conversely, Figs 4.25b and 4.25d reveal that relative density has no significant effect on the damping ratio and the shear modulus reduction curve for samples consolidated at the same confining pressures, in agreement with the experimental results presented in literature (Kokusho, 1980; Iwasaki et al., 1978; Wichtmann and Triantafyllidis, 2014; Goudarzy et al., 2018). Finally, the excess pore water pressure ratio versus the shear strain is presented in Fig. 4.25b. The rate of excess pore water pressure gerneration increases with the relative density for a given value of the shear strain, confirming the fact that loose soils are more susceptible to liquefaction than dense soils.
The same observations ca be conducted for all the confining pressure values investigated.

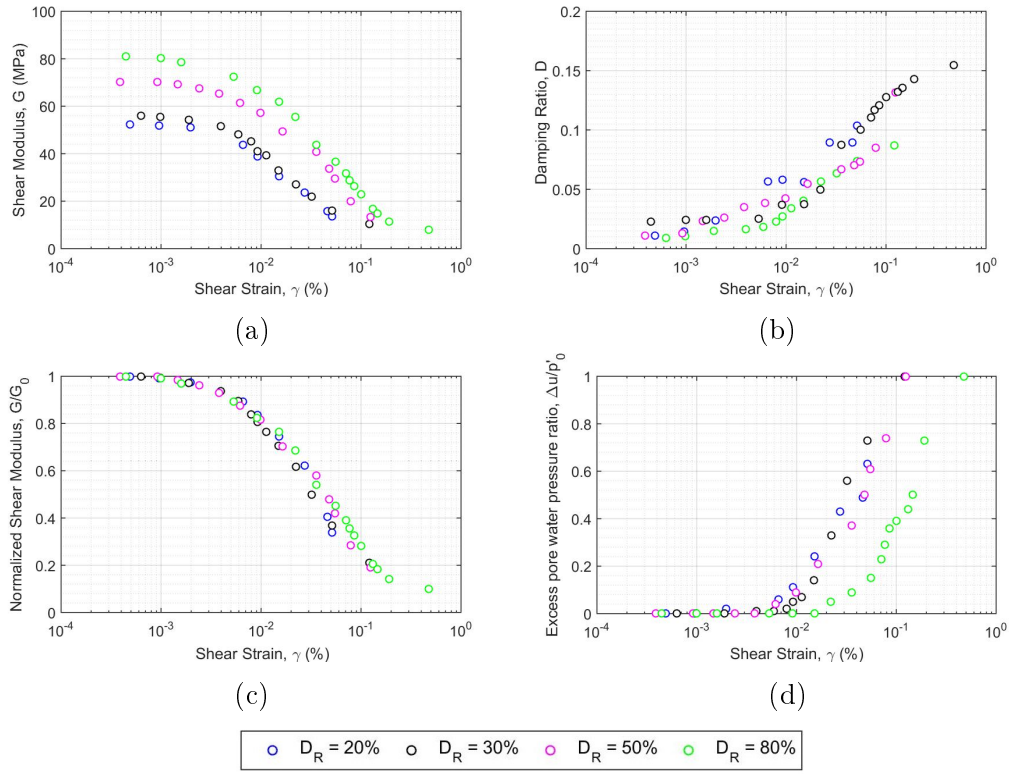

Figure 4.25: The effect of relative density on the shear modulus (a), damping ratio (b), normalized shear modulus (c) and excess pore water pressure ratio (d) versus shear strain for Hostun Sand ($FC = 0\%$, $p'_0 = 100kPa$)

4.4.2 Influence of confining pressure

Fig. 4.26 shows, as an example, the effect of the confining pressure p'_0 on the shear modulus, damping ratio, normalized shear modulus and excess pore water pressure ratio versus the shear strain for a sample of clean Hostun sand with relative density of 30%. From Fig. 4.26a, the shear modulus increases with the increasing of the confining pressure for a given value of the shear strain. Moreover, the confining pressure has no significant effect on the normalized shear modulus G/G_0 and on the damping ratio D in the small strain range ($\gamma < 1.0 \cdot 10^{-3}(\%)$), while at intermediate strain region, the effect on G/G_0 and D is the opposite. In fact after the small strain region, the ratio G/G_0 increases with an increase in the confining pressure (Fig. 4.26c) and the damping ratio D decreases as the confining pressure increases (Fig. 4.26b) for a given value of the shear strain. Also the excess pore water pressure ratio is is independent of the confining pressure at small shear strains and beyond this threshold, the rate of the excess pore water generation increases decreasing

the confining pressure.
The same conclusions are made for all the relative densities investigated.

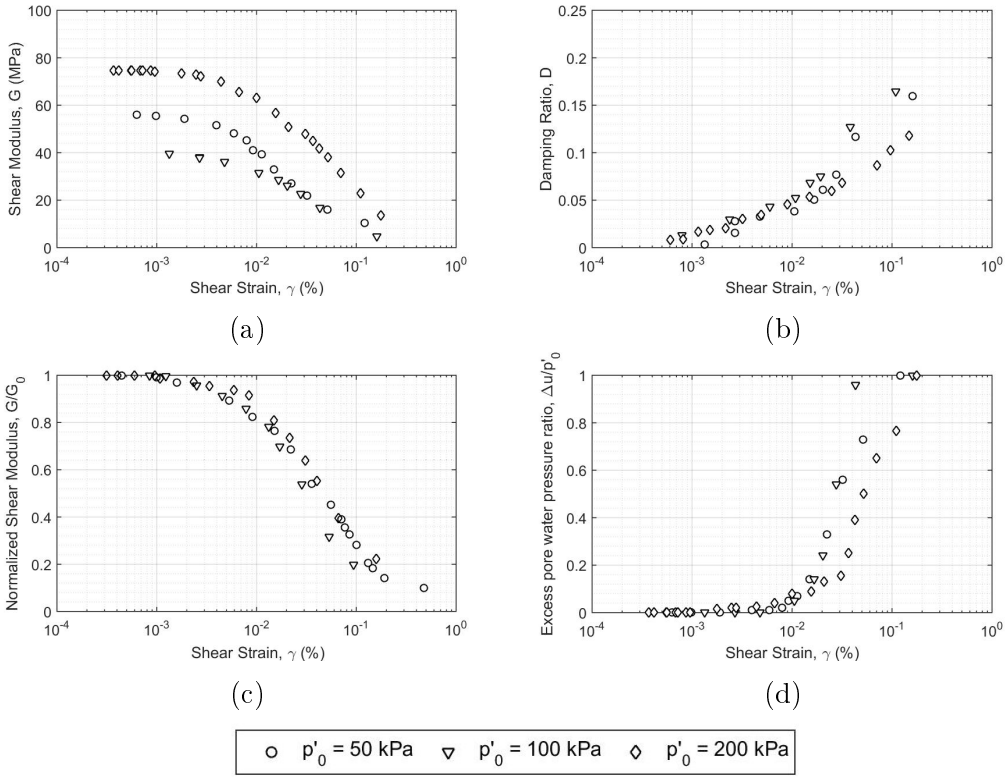

Figure 4.26: The effect of confining stress on the shear modulus (a), damping ratio (b), normalized shear modulus (c) and excess pore water pressure ratio (d) versus shear strain for Hostun sand ($FC = 0\%$, $D_R = 30\%$)

The coupling effect of effective initial confining pressure p'_0 and void ratio e on the maximum shear modulus G_0 of clean Hostun sand and sand containing fine particles is illustrated in Fig. 4.27, which summarizes the bender element results for all the mixtures tested. In these figures, clear and distinguished trends of $G_0 - e$ for various confining pressures can be observed. In particular, the value of G_0 increases with a decrease in the void ratio (i.e. increase of relative density) for all the mixtures. On the other hand, it is also shown that G_0 increases with the increasing of the confining pressure p'_0, irrespective of FC.

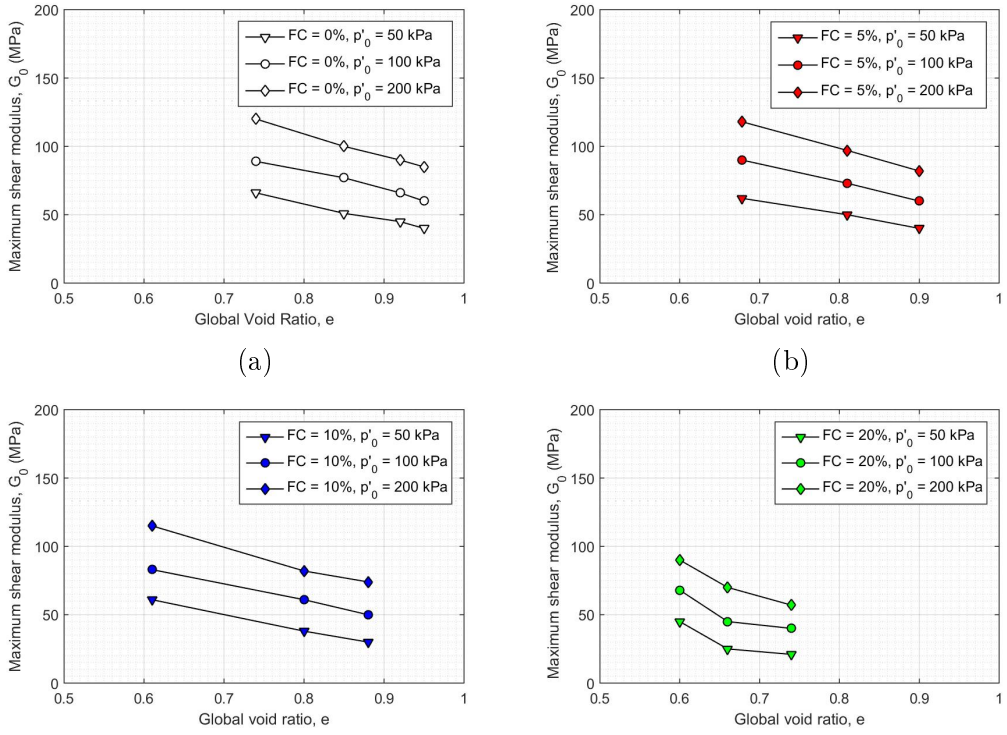

Figure 4.27: The effect of confining pressure and void ratio on the maximum shear modulus of mixtures measured by bender element technique: $FC = 0\%$ (a), $FC = 5\%$ (b), $FC = 10\%$ (c), $FC = 20\%$ (d)

4.4.3 Influence of fine content

In this section, the influence of the fine content on the behavior of analyzed silty sand mixtures under small and intermediate cyclic strains is investigated by resonant column tests.
Fig. 4.28 presents the effect of fine content FC on the maximum shear modulus versus global void ratio e for different confining pressures $p'_0 = 50 - 100 - 200kPa$. A significant decrease of G_0 with increasing fine particle amount is obtained for all the confining pressures, reaching up to a 40% reduction for $FC = 20\%$.

Fig. 4.29 displays the effect of fine content on the shear modulus decay curve, for loose and dense silty sand mixtures ($D_R = 30 - 80\%$) and confining pressure $p'_0 = 100kPa$. As for the monotonic and cyclic triaxial test, in the case of low and medium relative densities, the results obtained for clean sand and $FC = 5\%$ are similar. Instead, in the case of high relative densities, a

similar result is obtained up to $FC = 10\%$. Then, the stiffness decreases beyond these values of fine content.

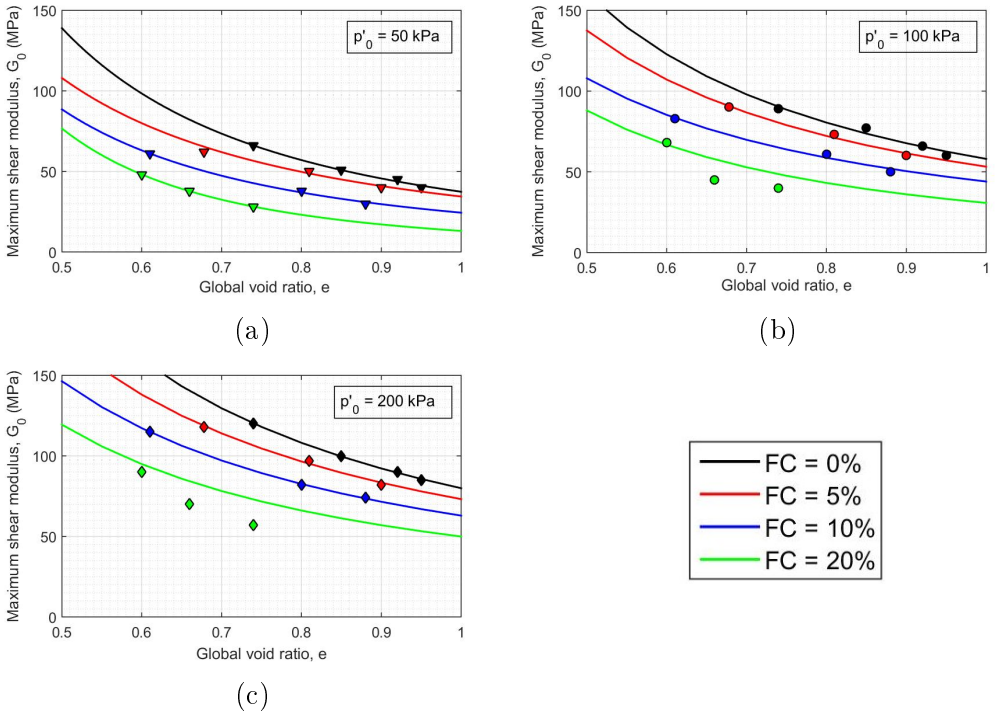

Figure 4.28: The effect of fine content on the maximum shear modulus of mixtures

The normalized shear modulus reduction G/G_0, damping ratio D and normalized excess pore water pressure ratio r_u with respect to the shear strain γ are shown in Fig. 4.30, for all the analyzed samples. Silty sands with high fine content FC demonstrate lower stiffness for a given level of shear strain (Fig. 4.30a). The experimental values are within the lower and upper bounds of the normalized shear modulus reduction curve proposed by Oztoprak and Bolton (2013) up to a shear strain $\gamma = 5 \cdot 10^{-2}\%$ and then they fall into the lower zone. Soils with high fine content FC show higher damping at a given level of shear strain (Fig. 4.30b). In addition, the higher damping is identified for lower confinement pressure. The bounds suggested by Rollins et al. (1998) for quartz soils describe reasonably well the response of Hostun sands without or with limited quantity of non-plastic fines ($FC < 20\%$). The pore water pressure build-up is faster for higher fine contents (Fig. 4.30c).

Fig. 4.31 illustrates the damping ratio D versus the normalized shear modulus G/G_0, for a confining pressure of 100 kPa, to better understand the effect of non-plastic fines on the damping capacity of silty sands. As FC increases,

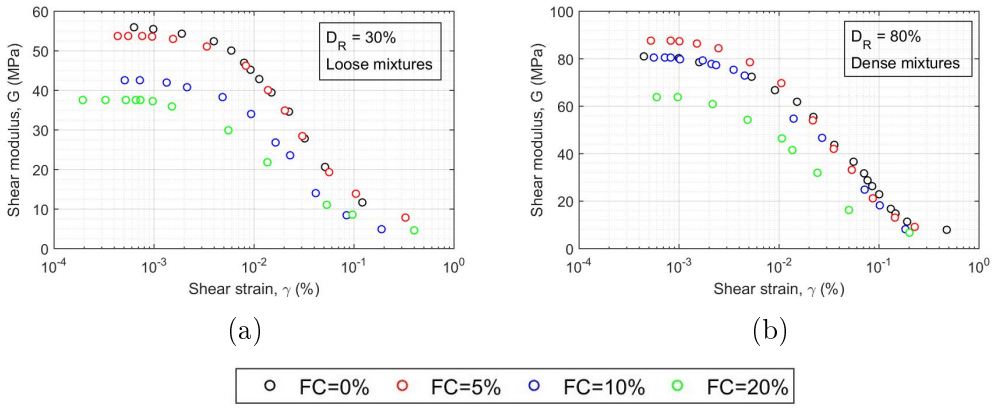

Figure 4.29: Shear modulus decay curve for HN31 Hostun sand with different fine percentages for loose (a) and dense (b) mixtures and confining pressure $p'_0 = 100kPa$

D tends to lower values for a given value of G/G_0. The same observation is valid for the other adopted confining pressures. This result is consistent with the trend observed from previous studies (Hardin and Drnevich, 1972; Iwasaki and Tatsuoka, 1977). The damping is reduced with high fine content until the shear modulus reaches 30% of the maximum one and then the trend is more uncertain.

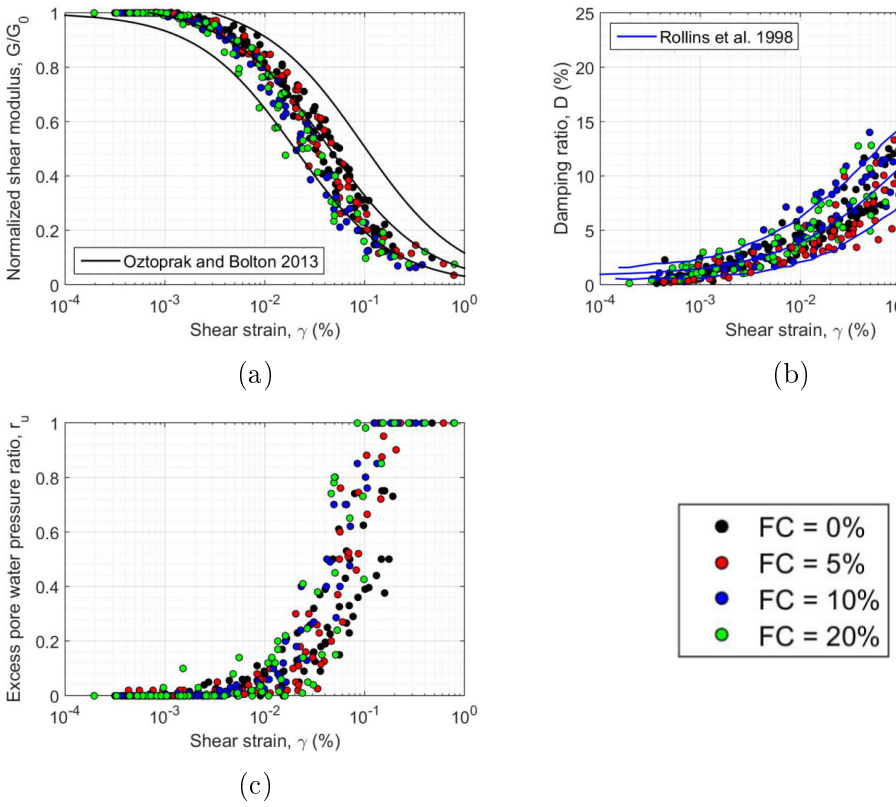

Figure 4.30: Mechanical behavior of fines-sand mixtures, considering all the analyzed relative densities ($D_R = 30 - 50 - 80\%$): normalized shear modulus G/G_0 (a), damping ratio D (b) and excess pore water pressure r_u (c) versus the shear strain γ

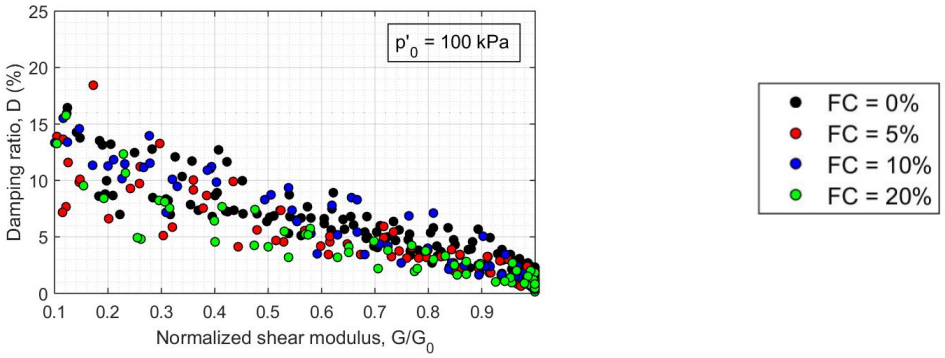

Figure 4.31: Damping ratio D with respect to the normalized shear modulus G/G_0, for fines-sand mixtures consolidated to a confining pressure $p'_0 = 100kPa$, considering all the analyzed relative densities ($D_R = 30 - 50 - 80\%$)

4.5 Evaluation of the liquefaction resistance in terms of intergranular void ratio

4.5.1 Proposed estimation of the active fine fraction

The presence of fine particles modifies the mechanical behavior of a silty sand mixture, compared to a clean sand. Experimental results show that fine content is not the only key parameter to evaluate the change in the mechanical response, but also grain-size distribution and particle shape (angularity) have a significant effect on the mixture behavior.
The active fine fraction b gives information about the participation of fine particles in the force transfer. It depends on grain-size distribution, particle shape and fine content with respect to the fine content threshold (Yang and Wei, 2012; Liu and Yang, 2018). Moreover, the same value of fine content yields different active fine fractions b according to the density of the mixture. The same amount of fine particles can be active in a dense packing rather than in a loose packing due to the different numbers of void spaces. In a loose packing, fine particles are included in the void spaces between the coarse particles, the contact between coarse particles of sand is dominant and fines do not participate in the force transfer. Instead, in a dense packing, the coarse particles are re-arranged, sand-fine-sand or sand-fine-fine-sand contacts are dominant and a considerable active fine fraction participates in the force transfer. Considering that the maximum and minimum void ratios e_{max} and e_{min}, respectively, combined with the global void ratio e of the mixture, control the soil response in undrained conditions, they are assumed as key parameters to assess the active fine fraction.
Based on these considerations, the following original formula is proposed to estimate the active fine fraction:

$$b = \frac{e_{max} - e_{min}}{1 + e/FC_{th}} \tag{4.2}$$

This expression incorporates the detected key parameters influencing the active fine fraction: the global void ratio of the mixture after consolidation e, the fine content threshold FC_{th} and the maximum and minimum void ratios e_{max} and e_{min}. In Eq. 4.2, FC_{th} is expressed in decimals.
The numerator $(e_{max} - e_{min})$ represents the influence of fine content. It is a function of particle size and shape (round or angular), strongly influencing the intergranular mechanism. The factor $(1 + e/FC_{th})$ expresses the state of the mixture, through the state variable e, and the effect of the fine content threshold FC_{th}.
The global void ratio e gives information about soil compaction influencing

the activation of the fine particles. In fact, the denser the material, the closer the fine and the sand particles, thus activating their contribution in the force transfer. Consequently, the active fine fraction b increases with the decreasing of global void ratio. FC_{th} represents the transitional value of fine content between sand-dominated behavior (i.e. $FC < FC_{th}$) and fines-dominated behavior (i.e. $FC > FC_{th}$), and denotes the range of applicability of the formula, which is valid for sand-dominant behavior. It is determined by the diagram of e_{max} and e_{min} versus FC (see Section 2.3.1.4). Its value depends on the particle shape and size for fines and sand particles that constitute the mixture.

The variation of active fine fraction b with the fine content is shown in Fig. 4.32, obtained using the analyzed mixtures having low, medium and high relative density ($D_R = 30 - 50 - 80\%$).

As shown in this figure, the active fine fraction b increases with increasing fine content and it reaches a significant value for higher fine content ($FC = 20\%$). This trend is consistent with the results of the literature (Rahman et al., 2008; Nguyen et al., 2017). Moreover, for a given fine content, a mixture with a high relative density has a higher active fine fraction b when compared to a loose mixture. It is expected that more fine particles are activated with a lower void volume.

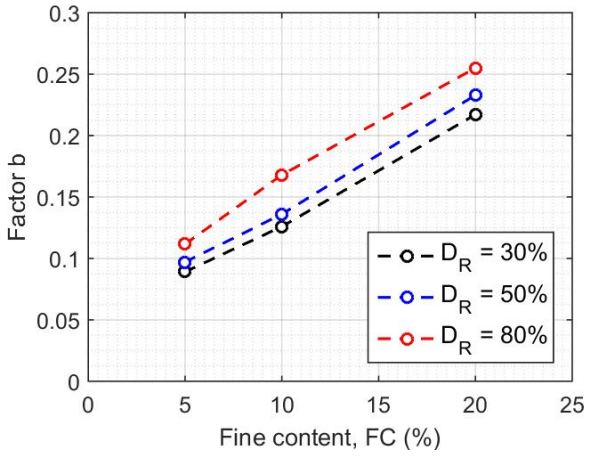

Figure 4.32: Active fine fraction b with respect to the fine percentage FC, for different relative densities ($D_R = 30 - 50 - 80\%$)

4.5.2 Validation by comparison with experimental data

In order to evaluate the applicability of the proposed formula, the validation of Eq. 4.2 is proposed using the experimental data of this research.
Afterwards, the same validation procedure is adopted using eight datasets reported in the literature (Yang et al., 2006; Stamatopoulos, 2010; Xenaki and Athanasopoulos, 2003; Papadopoulou and Tika, 2008; Nguyen et al., 2017; Askari et al., 2010; Carraro et al., 2005; Porcino and Diano, 2017). The datasets reported in the literature are selected because they provide the three parameters required in Eq. 4.2 to characterize the analyzed mixtures, for the estimation of the active fine fraction b: maximum and minimum void ratios e_{max} and e_{min}, respectively, and the global void ratio of the mixture after consolidation e. The fine content threshold FC_{th} is the same for a given sand-fine mixture, independently of the fine content FC in the mixture. It is determined by the diagram of e_{max} and e_{min} versus FC.
The steady state line SSL (ultimate value of p' under large strain with respect to the void ratio), cyclic liquefaction resistance and shear modulus are analyzed. According to experimental studies reported in the literature (Yang et al., 2006; Stamatopoulos, 2010; Xenaki and Athanasopoulos, 2003; Papadopoulou and Tika, 2008; Nguyen et al., 2017; Askari et al., 2010; Carraro et al., 2005; Porcino and Diano, 2017), the variation of these parameters with the global void ratio is strongly dependent on the fine content.
In order to obtain a single correlation curve for key mechanical parameters, independent of fine content, the efficiency of considering the equivalent intergranular void ratio e_g^*, instead of the global void ratio, is demonstrated. The root mean square deviation ($RMSD$) and the coefficient of determination R^2 (squared correlation coefficient) are calculated as a measure of data scattering.

4.5.2.1 Monotonic CU triaxial tests

In order to obtain a single curve correlating the equivalent intergranular void ratio e_g^* with the mean effective principal stress p' at the steady state, independent from fine content, the results of monotonic CU triaxial tests are analyzed.

The steady state line, represented by the global void ratio after consolidation e versus the mean effective stress p' at the steady state, is displayed in Fig. 4.33a, for different fine contents, various relative densities ($D_R = 30 - 50 - 80\%$) and confining pressures ($p'_0 = 50 - 100 - 200kPa$). The curves for silty sand mixtures with increasing fine content fall below the curve obtained for clean sand.

The experimental steady state lines in Fig. 4.33 are fitted using Eq. 2.6 proposed by Li and Wang (1998). In particular, the same value is obtained

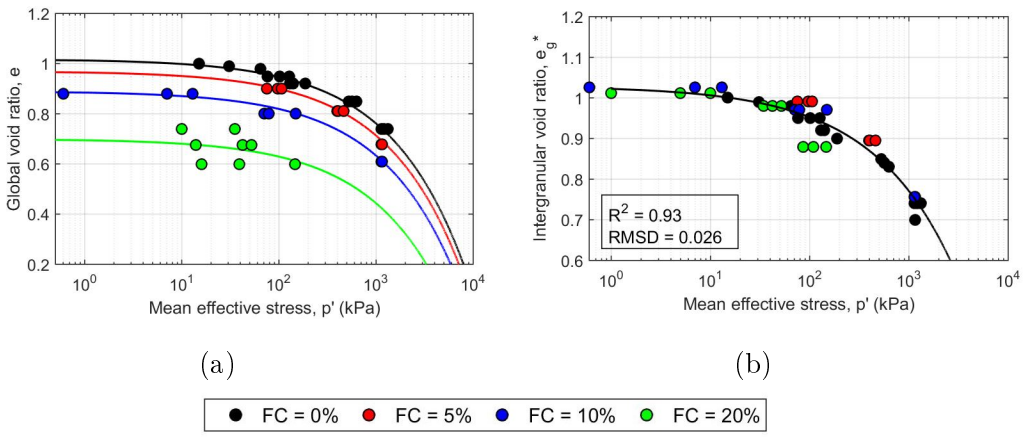

Figure 4.33: Steady state line SSL for HN31 Hostun sand with different percentages of Silica C500 non-plastic fine: global void ratio e versus the mean effective stress (a); proposed equivalent intergranular void ratio e_g^* versus the mean effective stress

for parameters λ and ξ, for the curves representing different fine contents, and only Γ changes (Cho et al., 2006). The steady-state lines obtained using, in Eq. 2.6, the global void ratio e and the proposed equivalent intergranular void ratio e_g^* are displayed in Figs 4.33a and 4.33b, respectively. The equivalent intergranular void ratio e_g^* is estimated using Eq. 2.9, where the active fine fraction b is calculated using the proposed formula in Eq. 4.2.
Considering the goal to obtain a single correlation curve independent of the fine content, Fig. 4.33a confirms that the common definition of the global void ratio e is not adequate to characterize the general behavior of silty sands. As observed by other researchers (Zlatović and Ishihara, 1995; Thevanayagam and Martin, 2002; Papadopoulou and Tika, 2008; Rahman et al., 2008; Stamatopoulos, 2010), the equivalent intergranular void ratio (Eq. 2.9) is a more suitable parameter to represent the steady state line. All data can thus be fitted by a single steady-state line which is independent of the fine content, as shown in Fig. 4.33b. The obtained $RMSD$ is 0.026 and the coefficient of determination is $R^2 = 0.93$.

4.5.2.2 Cyclic CU triaxial tests

In order to obtain a single curve correlating the equivalent intergranular void ratio e_g^* with the cyclic stress ratio CSR, independently of the fine content, the results of cyclic CU triaxial tests are analyzed. According to Bolton Seed et al. (1985), the cyclic stress ratio CSR_{15}, defined as the value of the cyclic stress ratio CSR triggering liquefaction in 15 cycles, is adopted for this

analysis.

The CSR_{15} versus the global void ratio after consolidation and the proposed equivalent intergranular void ratio are displayed in Figs 4.34a and 4.34b, respectively, for a confining pressure of 100kPa. The CSR_{15} decreases with the increasing of void ratio and, for a given global void ratio, the cyclic strength CSR_{15} decreases as fine content increases.
The experimental data are fitted adopting the following relationship between the CSR_{15} and the void ratio:

$$CSR_{15} = a \cdot exp(b \cdot e) \tag{4.3}$$

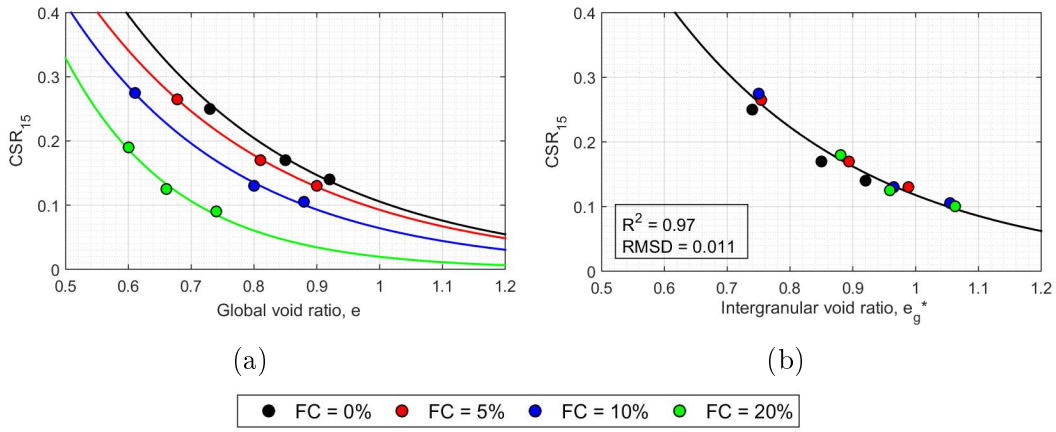

Figure 4.34: Cyclic strength CSR_{15} with respect to the global void ratio e (a) and the proposed equivalent intergranular void ratio e_g^* (b), for HN31 Hostun sand with different percentages of Silica C500 non-plastic fines. The confining pressure is $p_0' = 100kPa$

The parameters a and b are defined by numerical calibration using experimental data. The results obtained using, in Eq. 4.3, the global void ratio e and the proposed equivalent intergranular void ratio e_g^* are displayed in Figs 4.34a and 4.34b, respectively. The single correlation curve in Fig. 4.34b, is obtained with $RMSD = 0.011$ and $R^2 = 0.97$.
Using the proposed estimation of the equivalent intergranular void ratio, a strong correlation with CSR_{15} is obtained, independently of the fine content. Consequently, the liquefaction resistance of silty sands becomes independent of the fine content if correlated with the equivalent intergranular void ratio. In particular, when the global void ratio is considered, the value of b is the same for all the mixtures, while the value of a decreases with the increasing of the fine content, as shown in Table 4.5. On the other hand, if the equivalent

intergranular void ratio is used, a single value of $a = 2.365$ and $b = -3.13$ is found.

Table 4.5: Values of material constants for liquefaction resistance curves with respect to fine content

Soil type	a	b
$FC = 0\%$	2.304	-3.13
$FC = 5\%$	1.904	-3.13
$FC = 10\%$	1.601	-3.13
$FC = 20\%$	1.103	-3.13

4.5.2.3 Resonant column tests

The dependency of maximum shear modulus G_0 on the mean effective stress and void ratio is known. In Figs 4.35a and 4.35b, the maximum shear modulus is displayed with respect to the global void ratio after consolidation and the proposed equivalent intergranular void ratio respectively. The maximum shear modulus G_0 decreases with the increasing of void ratio and, for a given global void ratio, the maximum shear modulus G_0 decreases with increasing fine content. In Fig. 4.35a, the data are obtained for a confining pressure $p'_0 = 50kPa$ and, in Fig. 4.35b, the results are calculated for different confining pressures $p'_0 = 50 - 100 - 200kPa$, adopting the proposed estimation of the equivalent intergranular void ratio.

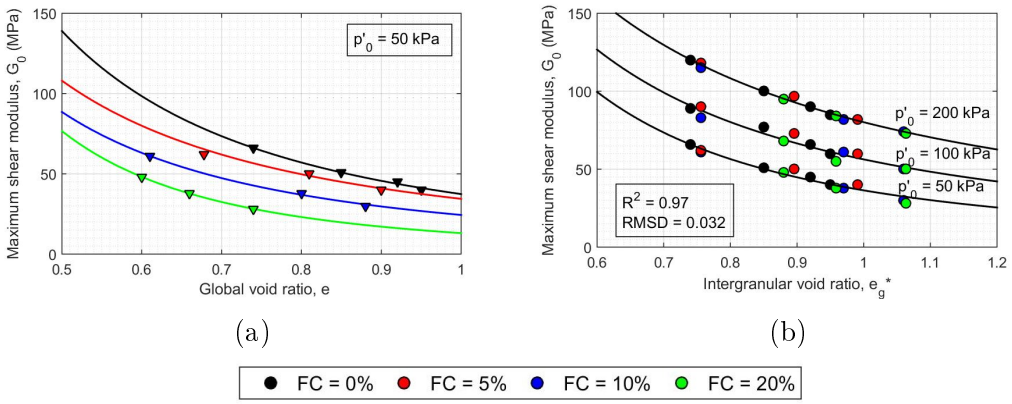

Figure 4.35: Maximum shear modulus G_0 with respect to the global void ratio e (a) and the proposed equivalent intergranular void ratio e_g^* (b), for HN31 Hostun sand with different percentages of Silica C500 non-plastic fines. The confining pressure is $p'_0 = 100kPa$

As shown in Fig. 4.36a, the value of G_0 decreases with increasing fine content at the same confining pressure and the surface moves downward in the $(e - p'_0 - G_0)$ space if the global void ratio is considered. On the contrary, when the global void ratio is replaced by the equivalent void ratio, a unique surface between G_0, p'_0 and e^*_g is provided (Fig. 4.36b), allowing to predict uknown G_0 for different FC.

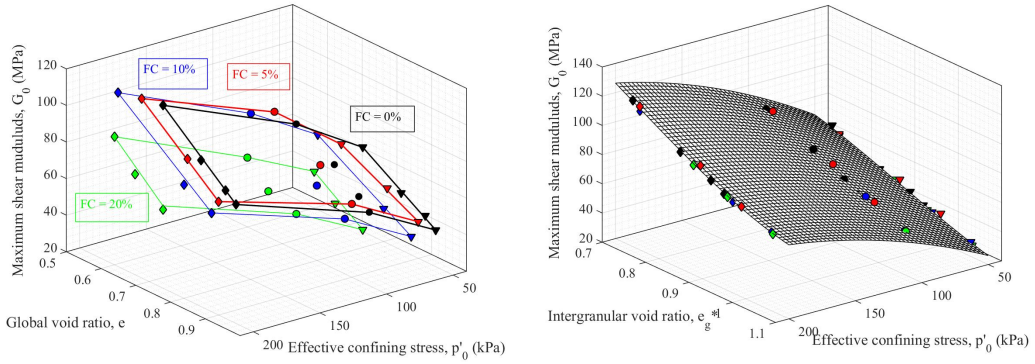

(a) (b)

Figure 4.36: Coupling effect of void ratio and confining pressure on the maximum shear modulus G_0, using the global void ratio e (a) and the proposed equivalent intergranular void ratio e^*_g (b), for HN31 Hostun sand with different percentages of Silica C500 non-plastic fine

The experimental data are fitted using the relationship proposed by Hardin and Drnevich (1972) to evaluate the variation of the maximum shear modulus G_0 with the mean effective stress and void ratio

$$G_0 = Ap_a \left(\frac{p'_0}{p_a}\right)^n f(e) \tag{4.4}$$

where A and n are constants depending on the soil type, p_a is the atmospheric pressure and $f(e)$ is a function of the void ratio. The parameters are defined by numerical calibration using experimental data.
Different functions $f(e)$ are proposed in the literature (Hardin and Drnevich, 1972; Jamiolkowski et al., 1995), depending on different parameters. In this research, the following expression is proposed to avoid the dependency of $f(e)$ on other constants:

$$f(e) = exp^{(-1+e)} \tag{4.5}$$

where e is the global void ratio.

The results obtained using, in Eqs 4.4 and 4.5, the global void ratio e and the proposed equivalent intergranular void ratio e^*_g are displayed in Figs 4.35a

and 4.35b, respectively. The correlation curves in Fig. 4.35b are obtained with $RMSD = 0.032$ and $R^2 = 0.97$. Using the proposed estimation of the equivalent intergranular void ratio, a strong correlation with the maximum shear modulus G_0 is obtained, only depending on the confining effective pressure p'_0 and independent of the fine content.

The maximum shear modulus normalized with respect to $f(e)p_a$ versus the normalized confining pressure p'_0/p_a is shown in Fig. 4.37. From Eqs 4.4 and 4.5, the global void ratio e and the proposed equivalent intergranular void ratio e^*_g are derived and displayed in Figs 4.37a and 4.37b, respectively. The normalized maximum shear modulus $G_0/(f(e)p_a)$ increases with the normalized confining pressure p'_0/p_a considering the dependency on the global or equivalent intergranular void ratio. When the dependency on the global void ratio is taken into account, the normalized maximum shear modulus $G_0/(f(e)p_a)$ decreases with the increasing of the fine content, for a given confining pressure. That means that parameters A and n in Hardin's equation (Eq. 4.4) are also affected by the fine content.
Using the proposed estimation of the equivalent intergranular void ratio, the correlation of the maximum shear modulus with the confining pressure is obtained, independently of the fine content. Consequently, a single value of fitting parameters A and n is adopted in Hardin's equation (Eq. 4.4).
In particular, when the global void ratio is considered, the value of n increases with the increasing of the fine content, while the value of A decreases, as shown in Table 4.6. On the other hand, if the equivalent intergranular void ratio is used, a single value of $A = 0.5493$ and $n = 0.5124$ is found.

Table 4.6: Values of material constants in Hardin's equation (Eq. 4.4) with respect to fine content

Soil type	A	n
$FC = 0\%$	0.5388	0.4716
$FC = 5\%$	0.472	0.4789
$FC = 10\%$	0.3814	0.5373
$FC = 20\%$	0.2865	0.5721

The correlation between measured and predicted maximum shear modulus G_0 is displayed in Fig. 4.38. The measured moduli are obtained by bender element tests. The calculated modulus is obtained using Eq. 4.4, where the dependency on the equivalent intergranular void ratio e^*_g is taken into account through the proposed function in Eq. 4.5 (by replacing the global void ratio e with e^*_g). The coefficient of determination is $R^2 = 0.99$.

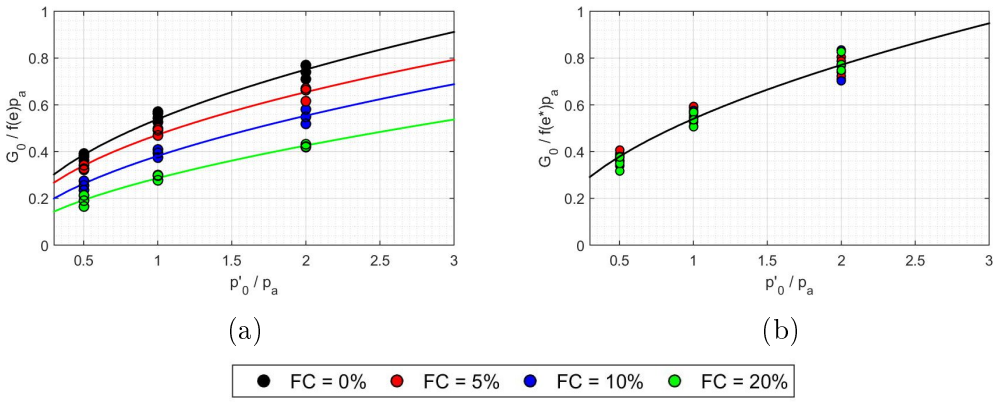

Figure 4.37: Normalized maximum shear modulus $G_0/(f(e)p_a)$ versus the normalized confining pressure p'_0/p_a, for HN31 Hostun sand with different percentages of Silica C500 non-plastic fines: the dependency of G_0 on the global void ratio e (a) and the proposed equivalent intergranular void ratio e^*_g (b) is considered. The results are shown for the analyzed confining pressures $p'0 = 50 - 100 - 200kPa$

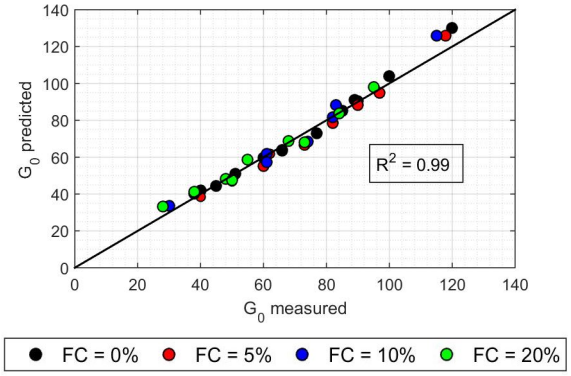

Figure 4.38: Correlation of measured and calculated maximum shear modulus G_0, for HN31 Hostun sand with different percentages of Silica C500 non-plastic fines. The calculated shear modulus is obtained using Hardin's equation (Hardin and Drnevich, 1972) and the dependency of G_0 on the proposed equivalent intergranular void ratio e^*_g. The results are shown for all the analyzed confining pressures $p'_0 = 50 - 100 - 200kPa$

4.5.2.4 Validation using databases reported in the literature

In this section, the relevance of Eq. 4.2 to predict the active fine fraction b is assessed using eight databases of experimental results reported in the literature (Yang et al., 2006; Stamatopoulos, 2010; Xenaki and Athanasopoulos,

2003; Papadopoulou and Tika, 2008; Nguyen et al., 2017; Askari et al., 2010; Carraro et al., 2005; Porcino and Diano, 2017) for a wide range of silty sand mixtures.

Fig. 4.39 displays the comparison of steady state line SSL when considering the global and equivalent intergranular void ratio, using the data provided by Yang et al. (2006).

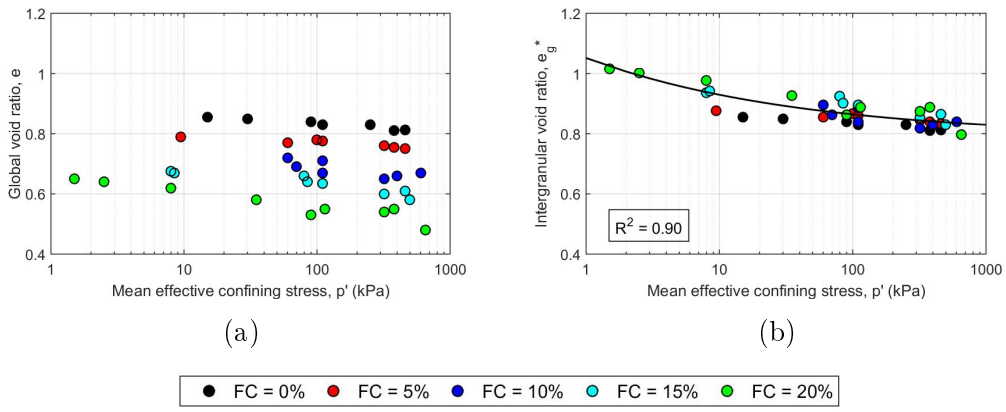

Figure 4.39: Steady state line SSL for Hokksund sand with Chengbei non-plastic fines (Yang et al., 2006), using the global void ratio (a) and the proposed equivalent intergranular void ratio (b)

Fig. 4.40 shows the CSR_{15} versus both the global void ratio and the proposed equivalent intergranular void ratio, using the datasets reported by Porcino and Diano (2017). Fig. 4.41 represents the maximum shear modulus with respect to both the global void ratio and the proposed equivalent intergranular void ratio, for the database of Askari et al. (2010).

A brief summary of the results obtained for the analyzed datasets is presented in Table 4.7. Accordingly, the coefficient R^2 is very high for all the fitted data.
Figs 4.39, 4.40 and 4.41 and Table 4.7 further validate the relevance of Eq. 4.2 to predict the active fine fraction b and provide a satisfactory intergranular void ratio. The proposed estimation approach of the equivalent intergranular void ratio is therefore validated for several types of silty sand mixtures, demonstrating it is an appropriate simple generalized method.

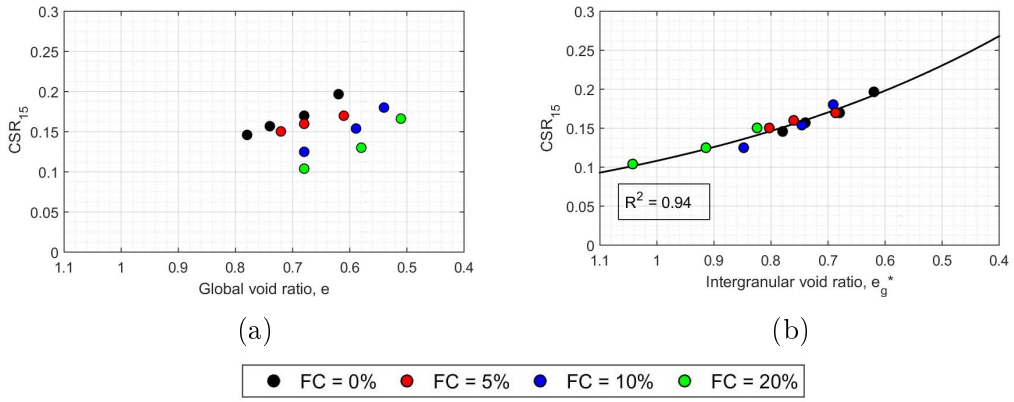

Figure 4.40: Cyclic stress ratio CSR_{15} for the Ticino sand with the natural non-plastic silt collected from Ticino river bank deposits (Porcino and Diano, 2017) with respect to the global void ratio (a) and the proposed equivalent intergranular void ratio (b)

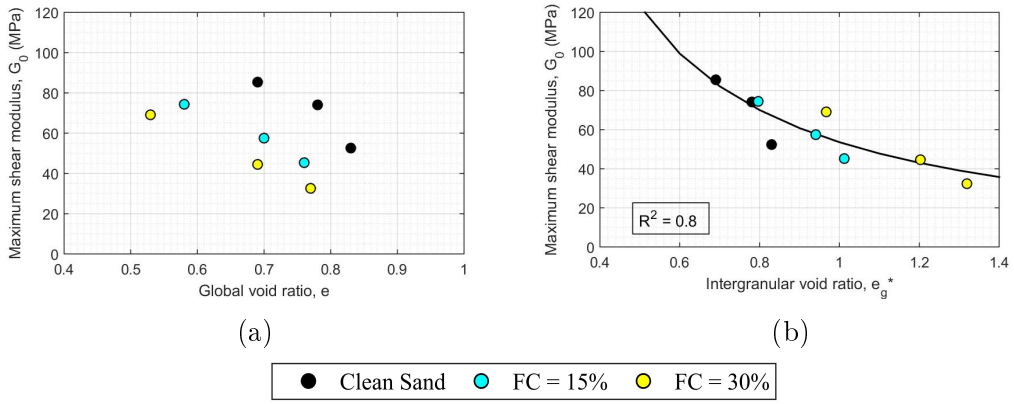

Figure 4.41: Maximum shear modulus for the Firoozkooh silty sand (Askari et al., 2010) with respect to the global void ratio (a) and the proposed equivalent intergranular void ratio (b)

Table 4.7: Summary of previous research for sand with fines

Source	FC (%)	FC_{th} (%)	D_{10}/D_{50}	Parameter	R^2
Yang et al. (2006)	0-20	30	7.05	SSL	0.90
Nguyen et al. (2017)	0-15	20	18.7	SSL	0.83
Stamatopoulos (2010)	0-25	30	9.6	SSL	0.83
Carraro et al. (2005)	0-25	35	9.0	SSL	0.80
Papadopoulou and Tika (2008)	0-15	20	11.8	CSR_{15}	0.92
Xenaki and Athanasopoulos (2003)	0-42	50	6.0	CSR_{15}	0.91
Porcino and Diano (2017)	0-20	25	16.0	CSR_{15}	0.94
Askari et al. (2010)	0-30	45	10.6	G_0	0.80

4.6 Conclusions

An experimental program is undertaken using reconstituted samples of silty sand mixtures to understand how fine particles contribute to the mixture strength in undrained conditions. Monotonic and cyclic triaxial tests and resonant column tests are carried out using HN31 Hostun sand and various amounts of commercial Silica C500 fines. Different relative densities are selected to investigate loose, medium and dense soils. Fine content is varied below a threshold of 20% to consider sand-dominated behavior. The initial confining pressure is modified to consider the liquefaction susceptibility at different depths. A detailed characterization of the static and dynamic properties of the analyzed mixtures is obtained considering the effect of relative density, confining pressure, frequency of the loading and fine content.

The response of silty sand mixtures is studied in terms of steady state line, liquefaction triggering and shear modulus. In order to obtain a single correlation curve for key mechanical parameters, independently of fine content, the efficiency of considering the equivalent intergranular void ratio, instead of the global void ratio, is demonstrated.
Based on the obtained experimental results, fine particles significantly affect the mixture packing configuration and play a major role in the mechanical behavior of sandy soils. When the dependency of steady state line, liquefaction resistance and shear modulus on the global void ratio is analyzed, experimental results confirm a strong variability with respect to the fine content. Whereas, when the equivalent intergranular void ratio is adopted as the key parameter to characterize the silty sand mixtures, a single correlation curve, independent of fine content, is found to represent the mean effective stress at the steady state, liquefaction resistance and shear modulus. It means that data obtained for clean sand are reliable for predicting the behavior of mixtures independently of the fine content. The adopted equivalent intergranular void ratio is function of the fine content and the active fine fraction b. An original formula is proposed to estimate the active fine fraction b, based on the mixture packing configuration (fine content, global void ratio of the mixture after consolidation, maximum and minimum void ratios). The reliability of this proposed formula is validated using the undertaken experimental program and eight experimental databases reported in the literature for non-plastic fines. The validation of the proposed expression of the active fine fraction b confirms its dependency on the nature of the sand and fine particles and the initial state of the mixture.

Chapter 5

Site response of liquefiable deposits: calibration of constitutive model and 1D numerical simulation

In this chapter, the laboratory test dataset described in the previous chapter, is used for the numerical calibration of a non-linear hysteretic model for saturated sands under triaxial cyclic loading and to identify the governing factors in the adopted constitutive model. First, the features of the extended Iwan-Iai constitutive model, adopted in this research, is presented and then the calibration process is illustrated for loose, medium and dense specimens of clean Hostun sand and mixtures of Hostun sand and various percentages of Silica C500 ($FC < 20\%$), consolidated at 50, 100 and 200 kPa and cyclically loaded at a wide range of cyclic stress ratio CSR. The correlation of liquefaction model parameters with the relative density, fine content and confining pressure is proposed. Further, calibration challenges are discussed and recommendations provided on calibration methodology with respect of soil type in order to better capture site response.
In the second part, the sets of calibrated parameters of each type of soil are subsequently employed in a finite element model simulating the vertical wave propagation in a horizontally layered soil, in free-field conditions, to predict the seismic response of liquefiable layers. To this regard, a parametric study is performed in order to understand how variations in the calibrated parameters could affect the accuracy of the constitutive model. The influence on the site response of relative density and fine content in the liquefiable layer is investigated with respect to depth and confining pressure. Lastly, the accuracy of numerical simulations of seismic wave propagation in layered soils is questioned using liquefaction parameters, obtained for soil samples at different depths. This aspect is of significant relevance to understand how to adequately implement the constitutive model when modelling potentially-liquefiable soils for current engineering practice, because the seismic response of soil deposits is generally predicted based on few laboratory tests obtained for soil samples at close locations and different depths.

5.1 Extended Iwan-Iai constitutive model

The Iwan's elasto-plastic model (Iwan, 1967; Joyner, 1975; Joyner and Chen, 1975; Santisi d'Avila et al., 2018) is adopted to represent the 3D nonlinear behavior of soils under cyclic loading. It is based on the knowledge of a small number of soil properties. The linear kinematic model approximates the hardening behavior with a constant hardening rate (Prager hardening rule). The plasticity model assumes an associated plastic flow rule, which allows for isotropic yielding. The energy dissipation in the soil is thus purely hysteretic. The nonlinear behavior is simply characterized through the shear modulus decay curve. A correction depending on the current average effective pressure is used during the dynamic process, to account for the effect of excess pore water pressure generation due to dilatancy. The correction $G = S \cdot G_0$ of the elastic shear modulus G_0 depends on the state variable $S = p'/p'_0$, representing the actual to initial average effective stress ratio. It is adopted the relationship proposed by Iai et al. (Iai et al., 1990a,b; Santisi d'Avila et al., 2018), named liquefaction front, between S and the deviatoric stress ratio $r = \tau/p'$ (Fig. 5.1), where $\tau = (\sigma_{max} - \sigma_{min})/2 = q/2 = \tau'$ is the shear stress, depending on the maximum and minimum principal stresses σ_{max} and σ_{min}, respectively, and q is the deviatoric stress.

Even if Iwan's plasticity model uses a von Mises yield surface that assumes a pressure independent behavior, Iai's correction for effective stress analysis is pressure-dependent. The extension of Iai's correction to three-components loadings is implemented in the framework of the finite element method, using SWAP_3C code (Santisi d'Avila et al., 2018).

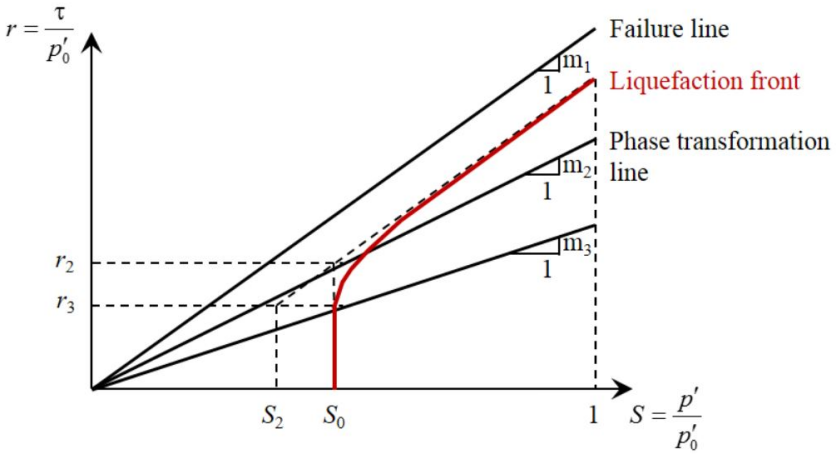

Figure 5.1: Liquefaction front: relationship between shear stress ratio r and state variable S

5.1.1 Liquefaction front equation

According to Iai et al. (1990a,b), the state variable S is expressed as

$$S = \begin{cases} S_0 & r \leq m_3 S_0 \\ S_2 + \sqrt{(S_0 - S_2)^2 + \left[(r - m_3 S_0)/m_1\right]^2} & r > m_3 S_0 \end{cases} \tag{5.1}$$

where m_1 is the failure line slope, m_2 is the phase transition line slope and $m = 0.67 m_2$ (Fig. 5.1). When the deviatoric stress ratio r is higher than $m_3 S_0$, the soil is affected by positive dilatancy.
The parameters in equation 5.1 are $S_2 = S_0(1 - (m_2 - m_3)/m_1)$ and

$$S_0 = \begin{cases} (0.4 - S_1)(w_1/w)^{p_2} + S_1 & w \geq w_1 \\ 1 - 0.6(w/w_1)^{p_1} & w < w_1, S_1 = 1 \end{cases} \tag{5.2}$$

where w is the normalized shear work. The relation between S_0 and w depends on four material parameters S_1, w_1, p_1 and p_2 that characterize the liquefaction properties of the cohesionless soil. It is observed that there is no pore water pressure build-up for cyclic strain or stress below a threshold in cyclic shear strain or shear stress. The shear work consumed to attain the threshold is $c_1 dW_{se}$, closely related to the elastic shear work dW_{se} ($c_1 \cong 1$).

The interested reader can refer to Santisi d'Avila et al. (2018) for more details about the formulation of the 3D Iwan-Iai constitutive model.

5.1.2 Liquefaction parameters

The 3D Iwan-Iai model requires the calibration of ten parameters, three to characterize the elasto-plasticity and seven to consider the effect of the excess pore water pressure build-up. Five of these parameters are directly measured in-situ or through laboratory tests, such as monotonic CU triaxial tests and resonant column tests. The others are calibrated fitting the curves obtained by cyclic CTX triaxial tests, using a trial-and-error procedure.

The elastic shear modulus G_0 and the reference shear strain γ_{ref}, corresponding to a secant shear modulus $G(\gamma)$ equivalent to 50% of the elastic shear modulus, are estimated by resonant column tests. The Poisson ratio is assumed $\nu = 0.5$ as in the laboratory test conditions.
Iai's correction of shear modulus for saturated soils needs the knowledge of the phase transition line slope $m_2 = \tan \alpha_P$ and failure line slope $m_1 = \tan \alpha$. These angles are estimated using the curves $(\tau - p')$ obtained by monotonic CU triaxial tests for three different confining pressure levels. The phase

transformation angle Φ'_P and friction angle Φ' can be derived through the relationships $\tan\alpha_P = \sin\Phi'_P$ and $\tan\alpha = \sin\Phi$, respectively.

The liquefaction parameters are S_1, w_1, p_1 and p_2 that appear in the liquefaction front equation and c_1 that corrects the elastic shear work.
According to Iai et al. (1990a,b), the numerical calibration of liquefaction parameters, characterizing liquefaction susceptibility, is undertaken fitting the curves obtained by cyclic CTX triaxial tests using a trial-and-error procedure. The deviatoric vertical stress q applied during the test is adopted as input of the numerical simulation. The axial strain amplitude ε_a and the normalized excess pore water pressure $\Delta u/p'_0$, with respect to the number of load cycles N, are obtained numerically and compared to the curves produced during the test. The generated excess pore pressure is $\Delta u = u - u_0$, where u is the measured total pore pressure and u_0 is the initial hydrostatic pore pressure.

The parameters w_1 and p_1 are determined to best reproduce the normalized excess pore water pressure curve for $\Delta u/p'_0 < 0.6$. The parameter w_1 is not greatly influenced by the variation of p_1, so it is determined at first for a given value of p_1. The appropriate value of p_1 is searched in the range $[0.4 - 0.7]$, according to Iai et al. (1990a,b). The greater w_1 and p_1, the lower the excess pore water pressure. The envelope of strain amplitude is also fitted, observing that the greater w_1, the lower the envelope of strain amplitude.

The parameter p_2 is determined to obtain the best fit for the normalized excess pore water pressure curve when $\Delta u/p'_0 > 0.6$.

The parameter c_1 is first imposed equal to one when w_1, p_1 and p_2 are determined and, if laboratory data are not well represented in the elastic range, c_1 can be increased. Parameter S_1 has a small positive value ($S_1 > 0.005$), introduced so that S_0 (Fig. 5.1) will never be zero.

Santisi d'Avila et al. (2018) validate the implementation of the Iai's constitutive model (Iai et al., 1990a,b) for different kinds of soil, loose and dense, following the laboratory work of Ishihara (1985). The cyclic tests are stress-controlled, the cyclic stress ratio are 0.717 for dense soil and 0.229 for loose soil, and the initial effective confining stress is equal to 98 kPa. Numerical curves are compared with experimental results in Figs 5.2 and 5.3, which show that numerical simulation results are quite coherent with the experimental results obtained for dense and loose soil types. The calibrated liquefaction parameters of the analyzed soil samples are listed in Table 5.1.

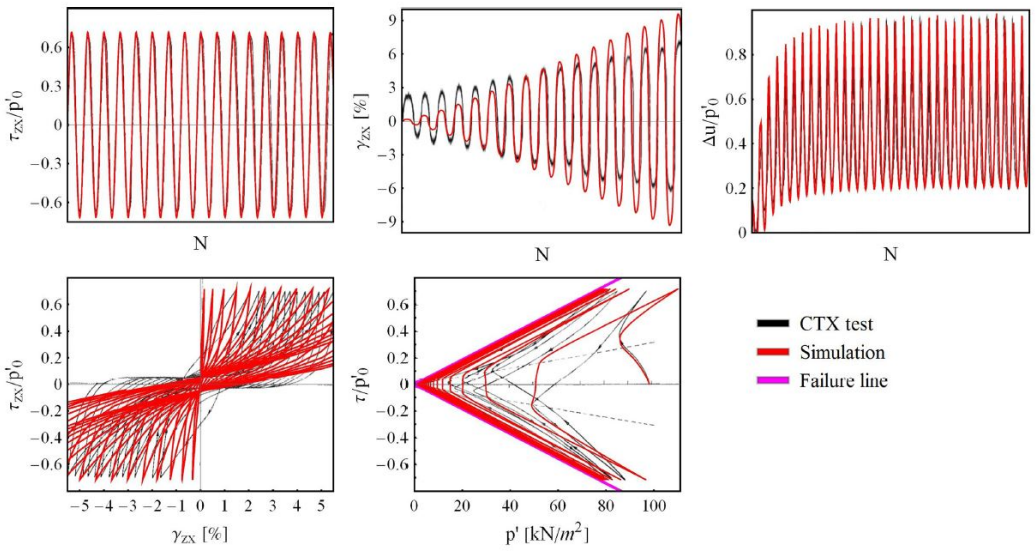

Figure 5.2: Fitting of cyclic consolidated undrained triaxial test curves obtained by Ishihara (1985) for dense sand, using the calibration parameters proposed by Iai et al. (1990a,b) (after Santisi d'Avila et al. (2018))

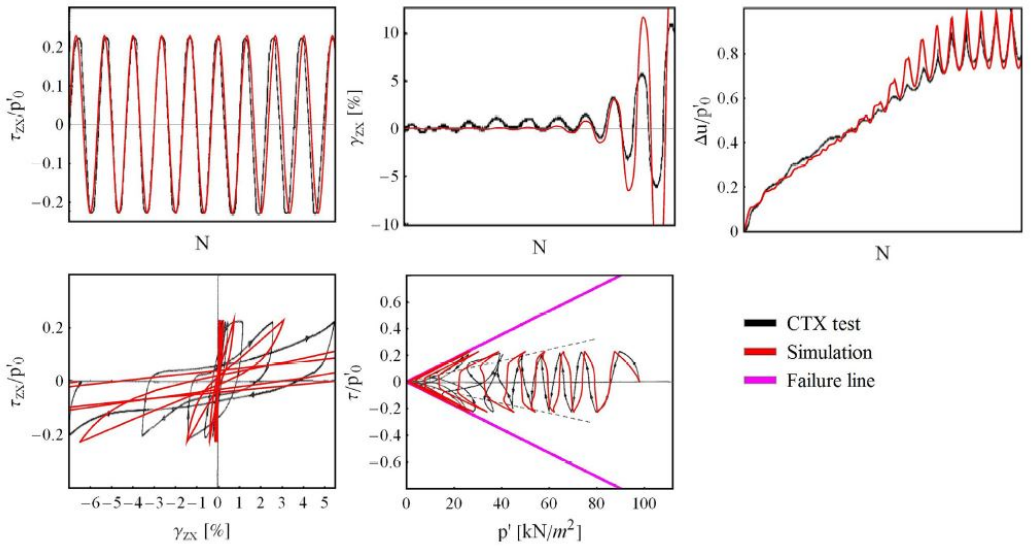

Figure 5.3: Fitting of cyclic consolidated undrained triaxial test curves obtained by Ishihara (1985) for loose sand, using the calibration parameters proposed by Iai et al. (1990a,b) (after Santisi d'Avila et al. (2018))

Table 5.1: Calibrated liquefaction parameters of soils samples used to validate the implementation of Iai's model (Iai et al., 1990a,b) by comparison with Ishihara's tests Ishihara (1985) (after Santisi d'Avila et al. (2018))

Soil sample	G_0 MPa	γ_{ref} ‰	w_1	p_1	p_2	c_1	S_1
Dense sand	140	0.6338	2.85	0.45	0.72	1	0.0050
Loose sand	103	0.8222	2.00	0.45	1.40	1	0.0035

5.2 Calibration of the constitutive model

The influence on liquefaction parameters of various factors affecting liquefaction, such as the relative density D_R, the fine content FC and the confining pressure p'_0 , is analyzed in this section. The liquefaction parameters are obtained calibrating the model for 18 silty-sand samples using 126 laboratory tests.

An example of the soil sample response and its numerical simulation is displayed in Fig. 5.4, for HN31 Hostun sand isotropically consolidated at a confining effective pressure $p'_0 = 100kPa$. The curves obtained by monotonic CU triaxial tests for three confining pressures (Fig. 5.4a) provide the friction angle Φ' and the phase transformation angle Φ'_P (as explained in Section 5.1.2). The curve obtained by the resonant column test is used to estimate the elastic shear modulus G_0 and the reference shear strain γ_{ref} (Fig. 5.4b).

The curves obtained by the cyclic CTX triaxial test are fitted to deduce the liquefaction parameters, applying the measured cyclic deviatoric stress q as the axial stress in the numerical simulation (Fig. 5.4c). Both experimental and numerical curves are plotted: normalized excess pore water pressure ratio $\Delta u/p'_0$ (Fig. 5.4d) and the axial strain amplitude ε_a (Fig. 5.4e) with respect to the number of load cycles N and the deviatoric stress ratio τ/p'_0 versus the actual average effective pressure p' (Fig. 5.4f).

The measured geotechnical properties and the five liquefaction parameters obtained by numerical calibration based on the laboratory tests for 18 silty-sand soil samples are listed in Table 5.2.

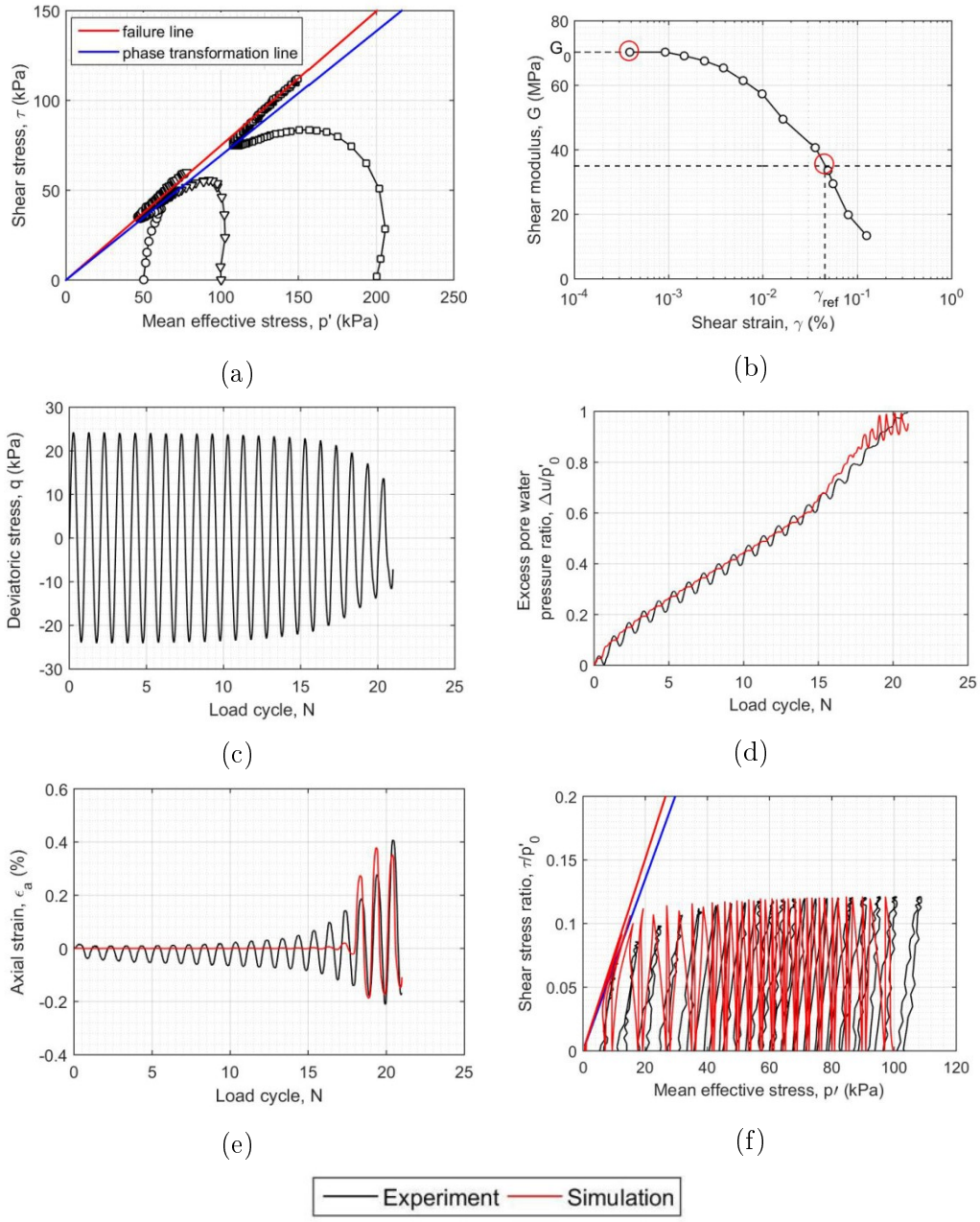

Figure 5.4: Experimental results and fitting for HN31 Hostun sand (relative density $D_R = 50\%$, fine content $FC = 10\%$ and confining pressure $p'_0 = 100kPa$: monotonic CU triaxial test (a), resonant column test (b) and cyclic CTX triaxial test (c, d, e, f)

Table 5.2: Geotechnical soil parameters for each soil sample. D_R: relative density; FC: fine content; p'_0: confining pressure; ρ: density; v_s: shear wave velocity; G_0: initial shear modulus; γ_{ref}: reference shear strain; Φ': friction angle; Φ'_P: phase transformation angle; w_1, p_1, p_2, c_1, S_1: parameters for saturated soil model (Eq. 5.2)

				Plasticity				Liquefaction						
Soil sample	D_R	FC	p'_0	ρ	v_s	G_0	γ_{ref}	Φ'_P	Φ'	w_1	p_1	p_2	c_1	S_1
	%	%	kPa	kg/m^3	m/s	MPa	‰	°	°					
DR30_FC00_50	30	0	50	1780	160	45	0.30	30.0	33.0	52.0	0.6	2.0	2.0	0.005
DR30_FC00_100	30	0	100	1780	193	66	0.35	30.0	33.0	10.0	0.6	3.5	2.0	0.005
DR30_FC00_200	30	0	200	1780	212	80	0.45	30.0	33.0	8.5	0.6	5.5	2.0	0.005
DR50_FC00_50	50	0	50	1840	170	50	0.34	28.0	34.5	53.0	0.6	1.8	2.0	0.005
DR50_FC00_100	50	0	100	1840	205	77	0.38	28.0	34.5	10.5	0.6	3.0	2.0	0.005
DR50_FC00_200	50	0	200	1840	228	95	0.54	28.0	34.5	12.0	0.6	4.5	2.0	0.005
DR80_FC00_50	80	0	50	1900	180	60	0.46	27.0	36.0	45.0	0.6	1.5	2.0	0.005
DR80_FC00_100	80	0	100	1900	220	92	0.51	27.0	36.0	9.0	0.6	2.5	2.0	0.005
DR80_FC00_200	80	0	200	1900	252	120	0.57	27.0	36.0	4.5	0.6	3.5	2.0	0.005
DR30_FC05_100	30	5	100	1845	195	63	0.52	34.0	37.0	8.5	0.6	3.5	2.0	0.005
DR30_FC10_100	30	10	100	1830	170	50	0.35	35.0	39.0	4.8	0.6	3.0	2.0	0.005
DR30_FC20_100	30	20	100	1700	150	35	0.33	30.5	35.0	3.3	0.6	2.5	2.0	0.005
DR50_FC05_100	50	5	100	1880	202	70	0.49	31.0	37.0	9.5	0.6	3.0	2.0	0.005
DR50_FC10_100	50	10	100	1840	182	61	0.40	34.0	37.0	7.0	0.6	2.5	2.0	0.005
DR50_FC20_100	50	20	100	1800	158	42	0.35	35.0	36.0	6.0	0.6	2.0	2.0	0.005
DR80_FC05_100	80	5	100	1920	215	90	0.58	33.0	37.0	8.5	0.6	2.5	2.0	0.005
DR80_FC10_100	80	10	100	2000	206	85	0.48	33.0	37.0	8.0	0.6	2.0	2.0	0.005
DR80_FC20_100	80	20	100	2000	185	68	0.40	32.0	37.0	4.5	0.6	1.5	2.0	0.005

Fig. 5.5 shows experimental and numerical results in the cases of cyclic liquefaction in loose sand and cyclic mobility in dense sand, for the same confining pressure $p'_0 = 100kPa$. The shear stress amplitude q is different because dependent on the relative density.
In the case of cylic liquefaction, the normalized excess pore water pressure $\Delta u/p'_0$ increases with the same slope for $\Delta u/p'_0 < 0.6$ and then, it increases with a higher slope reaching the consolidation pressure.
On the other hand, in the case of cyclic mobility, the normalized excess pore water pressure $\Delta u/p'_0$ increases with almost the same slope for $\Delta u/p'_0 > 0.6$. The cyclic mobility is characterized by the generation of a "two-peak" mechanism where the excess pore water pressure reaches a peak twice per cycle.

The results in Fig. 5.5 show that the 3D Iwan-Iai model is able to simulate the onset of liquefaction in both cases of cyclic liquefaction and cyclic mobility in triaxial conditions.

The liquefaction strength curve is the cyclic stress ratio CSR required to attain liquefaction versus the number of uniform load cycles N. Liquefaction is deemed achieved for an excess pore pressure ratio $\Delta u/p'_0 = 1$ or single-

amplitude shear strain equal to 3% (Ishihara, 1993).
Fig. 5.6 shows experimental (solid line) and numerical (dashed line) liquefaction strength curves obtained for three CSR, in the case of various relative densities and fine percentages, at an average effective stress $p'_0 = 100kPa$. Numerical curves are in good agreement with the experimental ones.

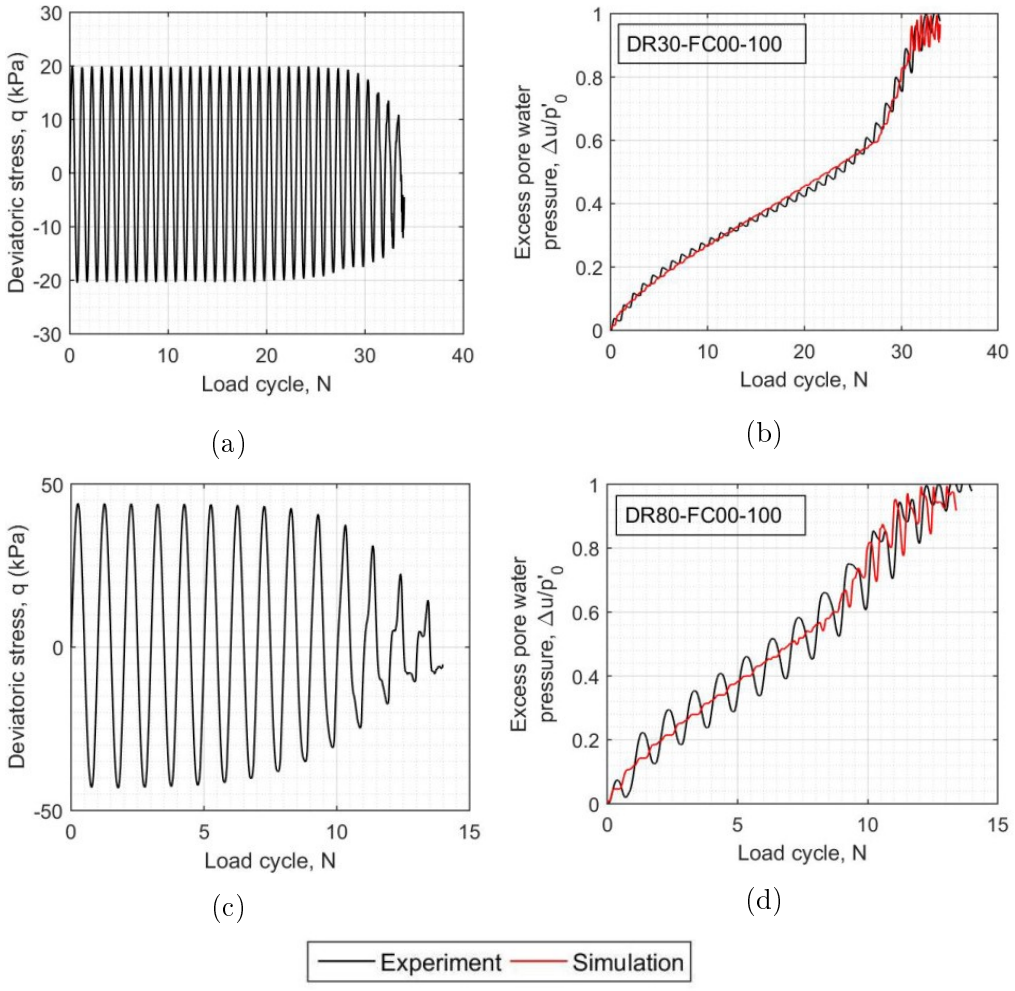

Figure 5.5: Experimental results and fitting for clean HN31 Hostun sand in case of cyclic liquefaction (a, b) of loose sand ($D_R = 30\%$) and cyclic mobility (c, d) of dense sand ($D_R = 80\%$), for confining pressure $p'_0 = 100kPa$

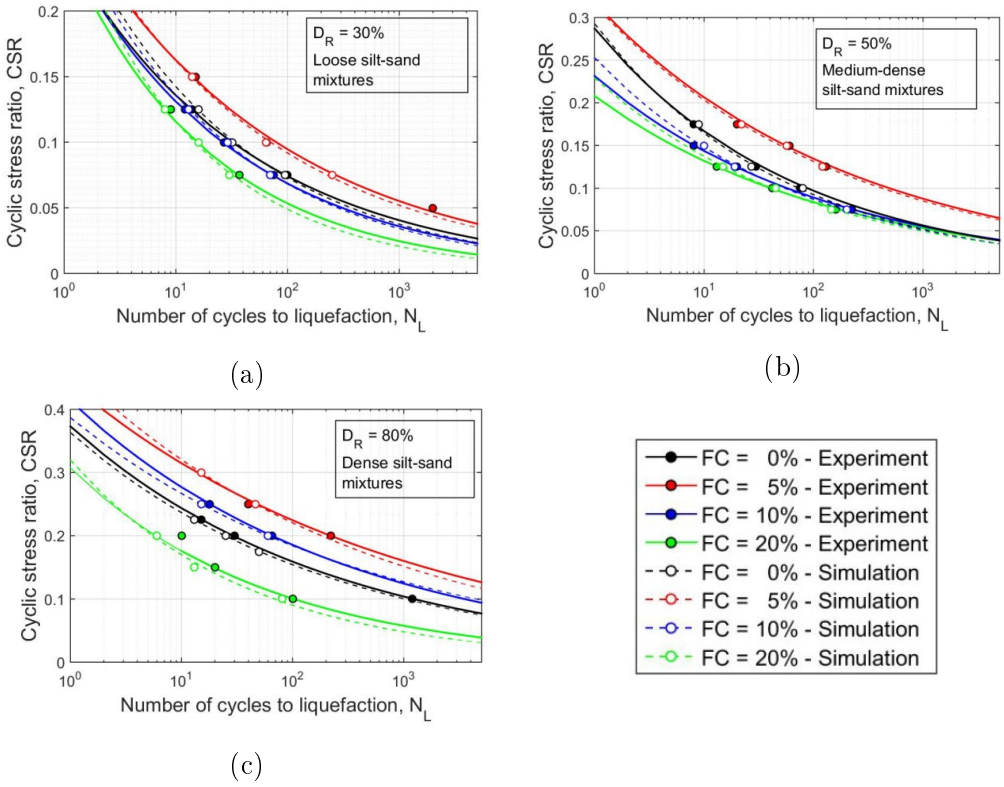

Figure 5.6: Experimental and numerical $CSR - N_L$ liquefaction strength curves for HN31 Hostun sand having relative density $D_R = 30 - 50 - 80\%$, fine content $FC = 0 - 5 - 10 - 20\%$ and confining pressure $p'_0 = 100kPa$

5.2.1 Liquefaction parameters vs mixture and depth

The trend of liquefaction parameters with relative density, fine content and confinement pressure is discussed in this section. According to Table 5.2, the parameters $S_1 = 0.005$, $p_1 = 0.6$ and $c_1 = 2$ are fixed for all the samples. The only parameters varying with mixtures characteristics and depth are p_2 and w_1.

5.2.1.1 Influence of relative density

As shown by Castro (1969), soil liquefaction mostly depends on the relative density. Fig. 5.7 illustrates the trend of liquefaction parameters p_2 and w_1 with respect to the relative density, for clean HN31 Hostun sand. The value p_2 increases with decreasing relative density. On the other hand, the value of w_1 does not seem affected by the relative density. In the case of dense sand $D_R = 80\%$, the value of w_1 appears slightly reduced.

Iai et al. (1990a,b) suggested that the appropriate value of p_2 should be searched in the range $[0.6 - 1.5]$. This is not the case for all soil samples used in this analysis (Table 5.2).
The parameter p_2 is related to the build-up of the excess pore water pressure for $\Delta u/p'_0 > 0.6$. Fig. 5.8 shows the normalized excess pore water pressure for three samples of clean HN31 Hostun sand, during a stress-controlled cyclic CTX triaxial test and the obtained value of p_2. In the case of loose to medium sand (Figs 5.8a and 5.8b), the excess pore water pressure steadily increases at the beginning of the test. Then, it follows a relatively linear accumulation phase in the middle of the test and finally a sudden increase in the excess pore water pressure is observed. The slope variation is much less significant for high relative density ($D_R = 80\%$).

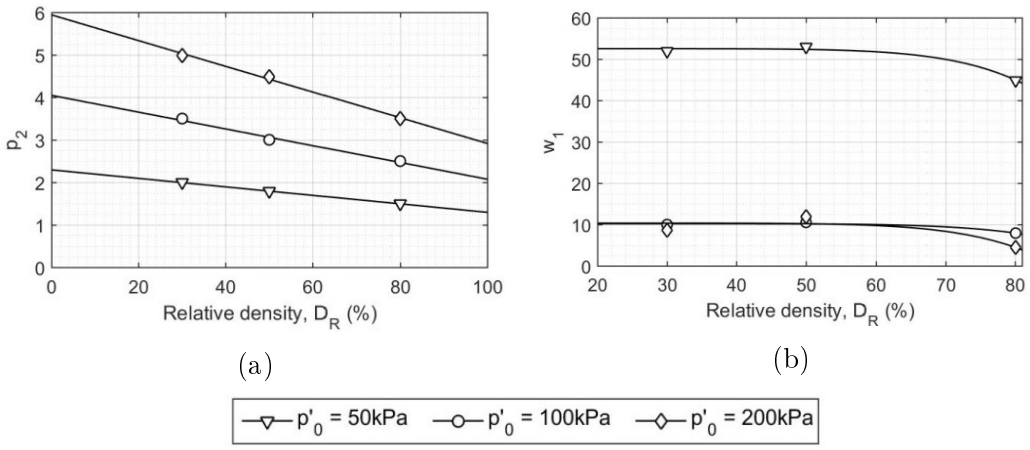

Figure 5.7: Liquefaction parameters p_2 (a) and w_1 (b) versus relative density D_R for clean HN31 Hostun sand at various confining pressures $p'_0 = 50 - 100 - 200kPa$

The increase of p_2 is related to the rate of excess pore water pressure build-up for $\Delta u/p'_0 > 0.6$. In the case of loose to medium sand (Figs 5.8a and 5.8b) $\Delta u/p'_0$ increases significantly faster than in dense sand (Fig. 5.8c). Accordingly, the value of p_2 is high for loose to medium sand and decreases for high relative density D_R.

5.2.1.2 Influence of fine content

Recent liquefaction case histories evidenced the sensitivity of soils containing fines to liquefaction, lateral spreading and flow failure (Cubrinovski and Taylor, 2011). For sand samples with various percentages of silty fines, below

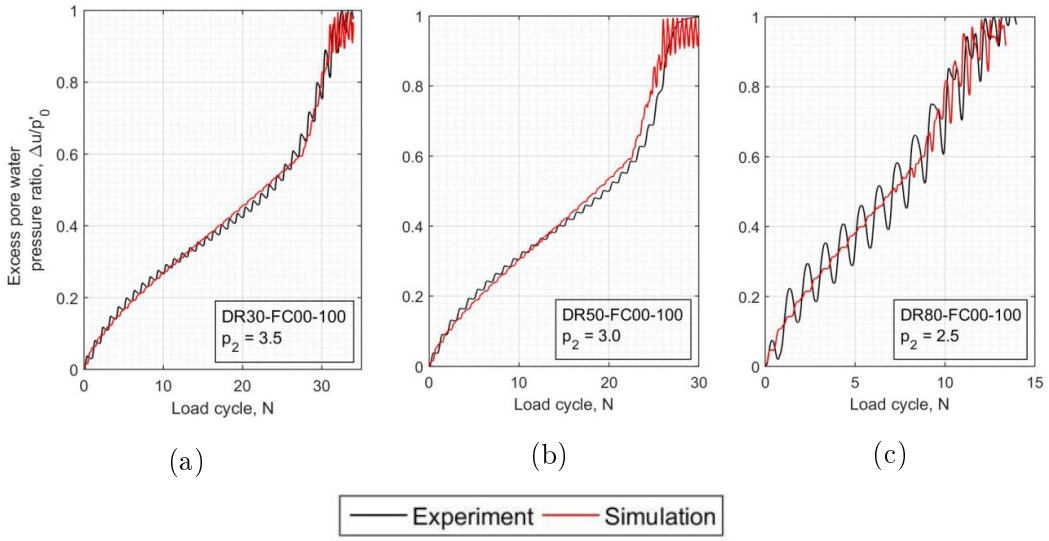

Figure 5.8: Experimental and numerical curves of excess pore water pressure versus the number of load cycles for clean HN31 Hostun sand having relative density $D_R = 30\%$ (a), 50% (b) and 80% (c), during a stress-controlled cyclic CTX triaxial test isotropically consolidated at $p'_0 = 100kPa$

the fine content threshold $FC_{th} = 20\%$, prepared at the same relative density D_R, the test data are analyzed. The variation of liquefaction parameters p_2 and w_1, obtained by numerical calibration, is plotted in Fig. 5.9 versus the fine content FC.

Fig. 5.9a shows a clear relation between p_2 and FC, for a given relative density D_R. The parameter p_2 decreases with increasing fine content. This is due to the trend of excess pore water pressure build-up in the final part of the test, for samples of sand mixed with non-plastic fines. Fig. 5.10 displays the normalized excess pore water pressure versus the load cycle ratio N/N_L, where N_L is the number of load cycles to reach liquefaction. The trend of normalized excess pore water pressure deviates for $\Delta u/p'_0 > 0.6$. The slope variation is much less significant for higher fine contents, as discussed by Dash and Sitharam (2011) and Karim and Alam (2014).

On the other hand, there is no clear correlation between w_1 and the fine content FC (Fig. 5.9b). In fact, the fine content is not the only key parameter to evaluate changes in the mechanical response as already observed in Chapter 4. In the case of loose to medium mixtures ($D_R = 30 - 50\%$), the value of w_1 is independent of fine content for percentages lower than 5% and w_1 decreases rapidly with increasing fine contents. In the case of dense mixtures

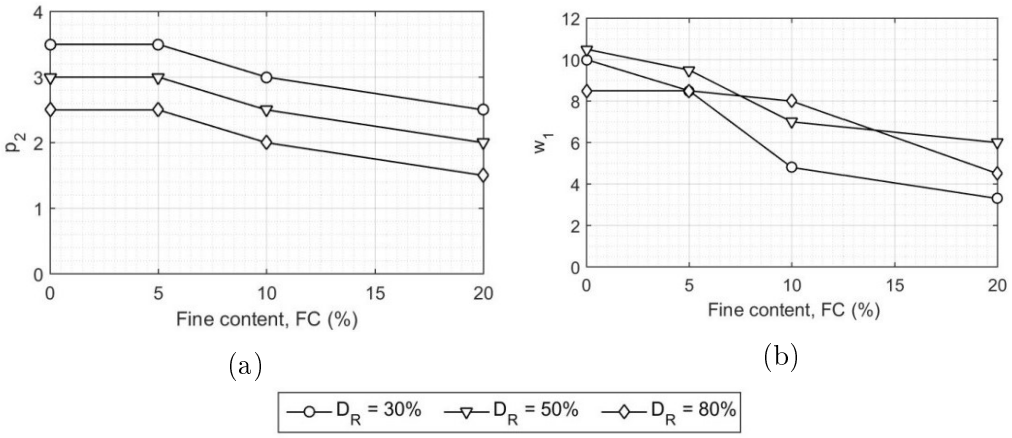

Figure 5.9: Liquefaction parameters p_2 (a) and w_1 (b) versus fine content FC for clean HN31 Hostun sand and non-plastic fines for given relative density D_R

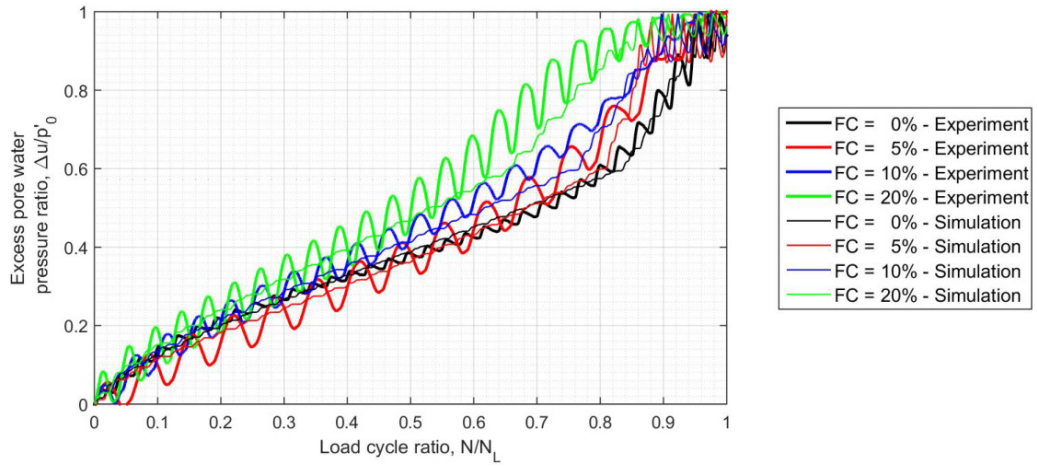

Figure 5.10: Experimental and numerical normalized excess pore water pressure ratio versus load cycle ratio, for silty-sand mixtures with various fine contents FC

($D_R = 80\%$), w_1 is independent of fine content for percentages up to 10% and then decreases with increasing fine contents.
The influence of relative density and fine content on the liquefaction parameters p_2 and w_1 is combined in Fig. 5.11. The trend of p_2 with respect to the relative density shown in Fig. 5.11a is confirmed. The value of p_2 depends on the fine content but its variation with the relative density maintains the slope for different fine contents. The parameter w_1 is also affected by the fine content and the relative density but the relationship is less obvious.

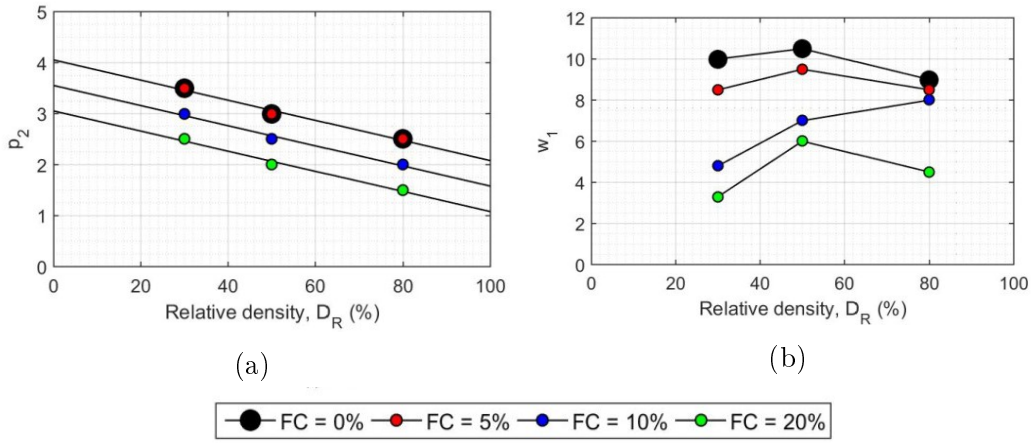

Figure 5.11: Liquefaction parameters p_2 (a) and w_1 (b) versus relative density D_R for HN31 Hostun sand containing non-plastic fines (confining pressure $p'_0 = 100kPa$)

5.2.1.3 Influence of confining pressure

The cyclic strength of saturated sands depends on depth. This means that it is affected by the average effective stress. Generally, the cyclic resistance of soils decreases with increasing confining pressure, if all other factors are kept constant (Seed, 1983; Montgomery et al., 2014).

In the performed laboratory tests, the average effective stress p'_0, at the consolidation phase, is modified to understand its influence on liquefaction parameters. The variation of parameters p_2 and w_1 with the confining pressure is illustrated in Fig. 5.12. With increasing confining pressure, p_2 increases and w_1 decreases. In particular, p_2 is less affected by the confining pressure than w_1. The consequence of these results is that using the same calibration parameters for the same soil layer located at different depths, in relatively close soil profiles, does not seem appropriate.

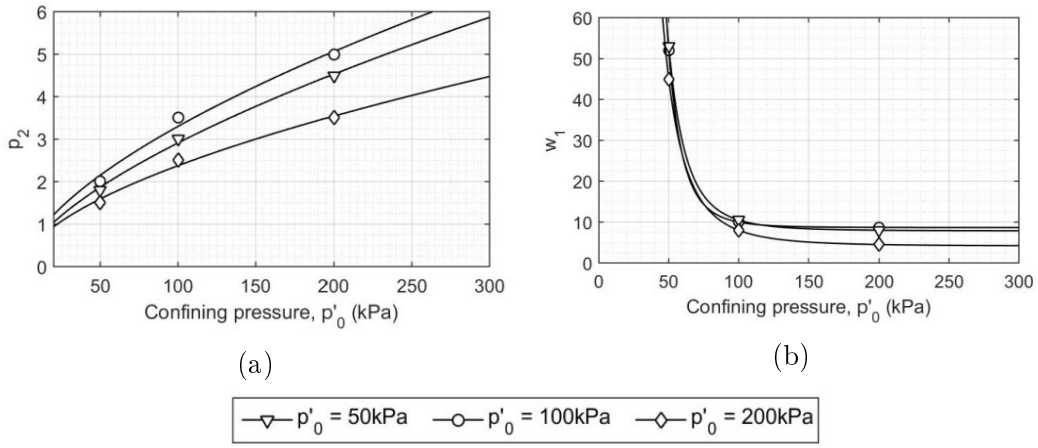

Figure 5.12: Liquefaction parameters p_2 (a) and w_1 (b) versus versus confining pressure p'_0 for samples of clean HN31 Hostun sand prepared at the same relative density D_R

5.3 Application to liquefaction triggering in layered soil profiles

In order to investigate the influence of liquefaction parameters in the seismic response of a soil profile, numerical simulations of the one-directional (1D) propagation of seismic waves in saturated soil profiles are carried out.
Two stratigraphies are considered, having a 5m thick liquefiable layer at different depth z, such as, in geostatic conditions, the middle of the layer has an effective average stress $p'_0 = 50kPa$ ($z = 6.25m$) and $p'_0 = 100kPa$ ($z = 12.5m$), respectively (Fig. 5.13). The depth of soil-bedrock interface and water table are assumed 30m and 1m, respectively.
The soil properties in the non-liquefiable soil layers of C1 and C2 profiles are listed in Table 5.3. The reference shear strain in non-liquefiable soils is assumed equal to that adopted for the liquefiable layer (Table 5.2). The adopted soil properties for the liquefiable layer are listed in Table 5.2.

A one-component signal is imposed as incident shear wave at the top of the underlying elastic bedrock and propagated vertically along both soil profiles. The one-component input load is the North-South component of a corrected signal of the 20 May 2012 Mw 5.9 Emilia earthquake (Santisi d'Avila et al., 2019), scaled to reach liquefaction in each analyzed soil profile (Fig. 5.14).

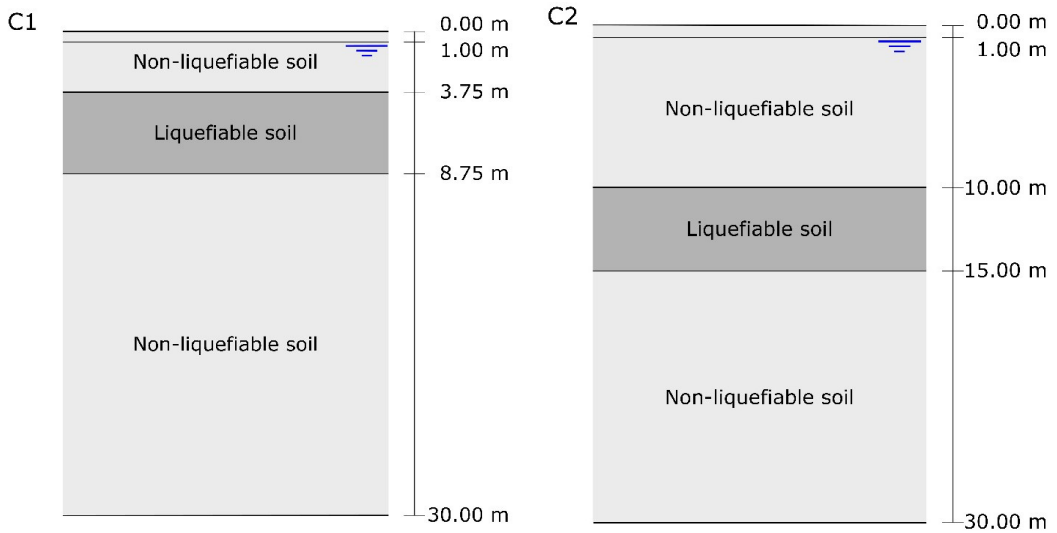

Figure 5.13: Stratigraphy of analyzed soil profiles C1 and C2, chosen to have confining pressure $p'_0 = 50kPa$ ($z = 6.25m$) and $p'_0 = 100kPa$ ($z = 12.5m$), respectively, in the middle of the liquefiable layer

Table 5.3: Stratigraphy and geotechnical parameters of soil profiles C1 and C2. NLS: non-liquefiable soil; LQ: liquefiable soil; v_s: shear wave velocity; v_p: compressional wave velocity; ρ: density

Layer	Soil type	Thickness m		v_s m/s	v_p m/s	ρ kg/m^3
		C1	C2			
1	NLS1	3.75	10.00	200	1335	1800
2	LS	5.00	5.00	-	-	-
3	NLS2	21.25	15.00	700	2091	1800
4	Bedrock	>30	>30	1000	2450	2200

5.3.1 1D seismic wave propagation model

The seismic wave propagation is computed by the finite element method using quadratic 3-noded line elements and the 3D Iwan-Iai constitutive model involving both elasto-plasticity and liquefaction front formulation (Santisi d'Avila et al., 2018; Santisi d'Avila et al., 2019).

The soil column is bounded at the bottom by an elastic semi-infinite bedrock. An absorbing boundary condition is imposed at the soil-bedrock interface (as adopted by Joyner and Chen (1975)), to account for the finite

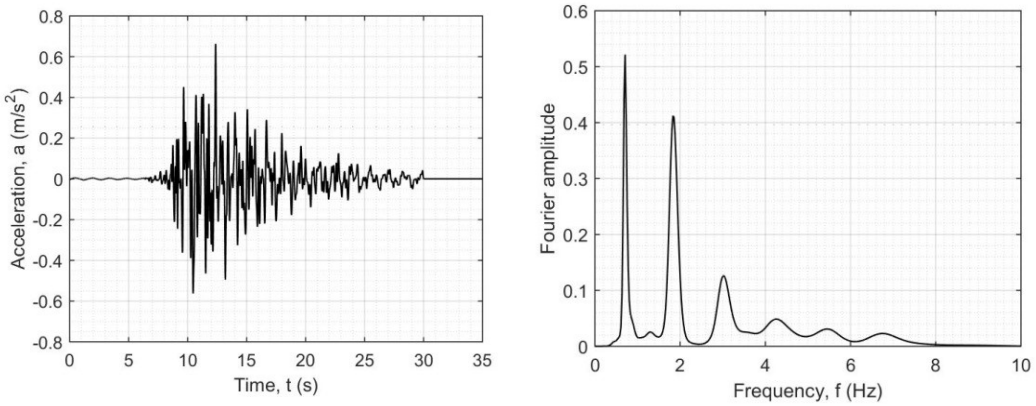

(a) (b)

Figure 5.14: The one-component signal of the incident motion, in terms of horizontal acceleration, applied at the soil–bedrock interface (a) and its Fourier spectrum (b)

rigidity of the bedrock and allow energy radiation into the underlying medium. At this regard, the interested reader can refer to Santisi d'Avila et al. (2012) for more details.
The minimum number of quadratic line elements per layer is defined as $pf_{max}h_i/(2v_{si})$, where h_i is the thickness of the i-th layer and v_{si} is the shear wave velocity in the medium. The maximum frequency, above which the spectral content of the input signal can be considered negligible, is fixed as $f_{max} = 15Hz$. The minimum number of nodes per wavelength accurately representing the seismic signal, is assumed as the maximum between $p = v_{si}/f_{max}$ (almost one node every meter) and $p = 10$. The number of finite elements per layer is checked according to the reduction of the shear wave velocity v_s observed during the dynamic process, that modifies the wavelength v_s/f_{max}.
The time integration is performed through Newmark's algorithm (Hughes, 1987). The two parameters $b = 0.3025$ and $g = 0.6$ guarantee an unconditionally numerical stability of the time integration scheme and some numerical damping to reduce spurious high frequency content, without having any significant effect on the meaningful, lower frequency response.
The dynamic equilibrium equation is directly solved using a time step $dt = 10^{-4}s$.

5.3.1.1 Influence of relative density

Fig. 5.15 shows the seismic response of C1 and C2 profiles in the case of a liquefiable layer composed by clean HN31 Hostun sand at different relative

densities ($D_R = 30 - 50 - 80\%$). The confining pressure in the middle of the liquefiable layer is $p'_0 = 50kPa$ and $p'_0 = 100kPa$ for C1 and C2 profiles, respectively. The adopted soil properties for the liquefiable layer are listed in Table 5.2.
The input signal, imposed in the horizontal x -direction at the soil-bedrock interface as incident motion, is scaled to a peak acceleration equal to 1.05m/s^2 and 0.66m/s^2, to reach liquefaction in C1 and C2 profiles, respectively.
Liquefaction occurs in both profiles, in the case of loose sand ($D_R = 30\%$) and does not occur for medium and dense sand ($D_R = 50 - 80\%$). The maximum excess pore water pressure ratio $\Delta u/p'_0$, shear strain γ_{xz} and shear modulus reduction G/G_0 increase with decreasing relative density (Fig. 5.15). The decay shear modulus G/G_0 may even be very close to zero for $D_R = 30\%$.

5.3.1.2 Influence of fine content

Both experimental and field investigations evidence the influence of fine particles on the liquefaction resistance of sands. In this research, the variation of the seismic response of C2 soil profile is analyzed using the soil properties for the liquefiable soil (Table 5.2), obtained by numerical calibration, for various fine contents ($FC = 0 - 5 - 10 - 20\%$) and relative densities ($D_R = 30 - 50 - 80\%$). The confining pressure in the middle of the liquefiable soil is $p'_0 = 100kPa$. The input signal is scaled to a peak acceleration equal to 0.66m/s^2, to reach liquefaction in C2 profile.

Fig. 5.16 displays the response of C2 profile in terms of vertical profiles of the maximum normalized excess pore water pressure $\Delta u/p'_0$ (a), maximum shear strain γ_{xz} (b), maximum shear stress τ_{xz} (c) and maximum shear modulus reduction G/G_0 (d).
The presence of fine particles can lead to either an increase or decrease of the liquefaction resistance. In fact, for loose to medium mixtures ($D_R = 30-50\%$), the seismic response of sand with fine content up to 5% is similar to that of clean sand. Whereas, the excess pore water pressure and shear strain increase for higher fine contents. Dense soils ($D_R = 80\%$) show results similar to those of clean sand for fine contents up to $FC = 10\%$ and then, for higher fine contents, the excess pore water pressure and shear strain increase.
Thus, the variations of the seismic response for various fine contents, in different liquefiable soil profiles, confirms the results of cyclic laboratory tests discussed in Chapter 4, showing that the fine content, as single parameter, cannot fully characterize the behavior of mixtures. It is proved by the cyclic laboratory tests and by these seismic computations that fine content and relative density significantly affect the liquefaction resistance of silty sandy soils.

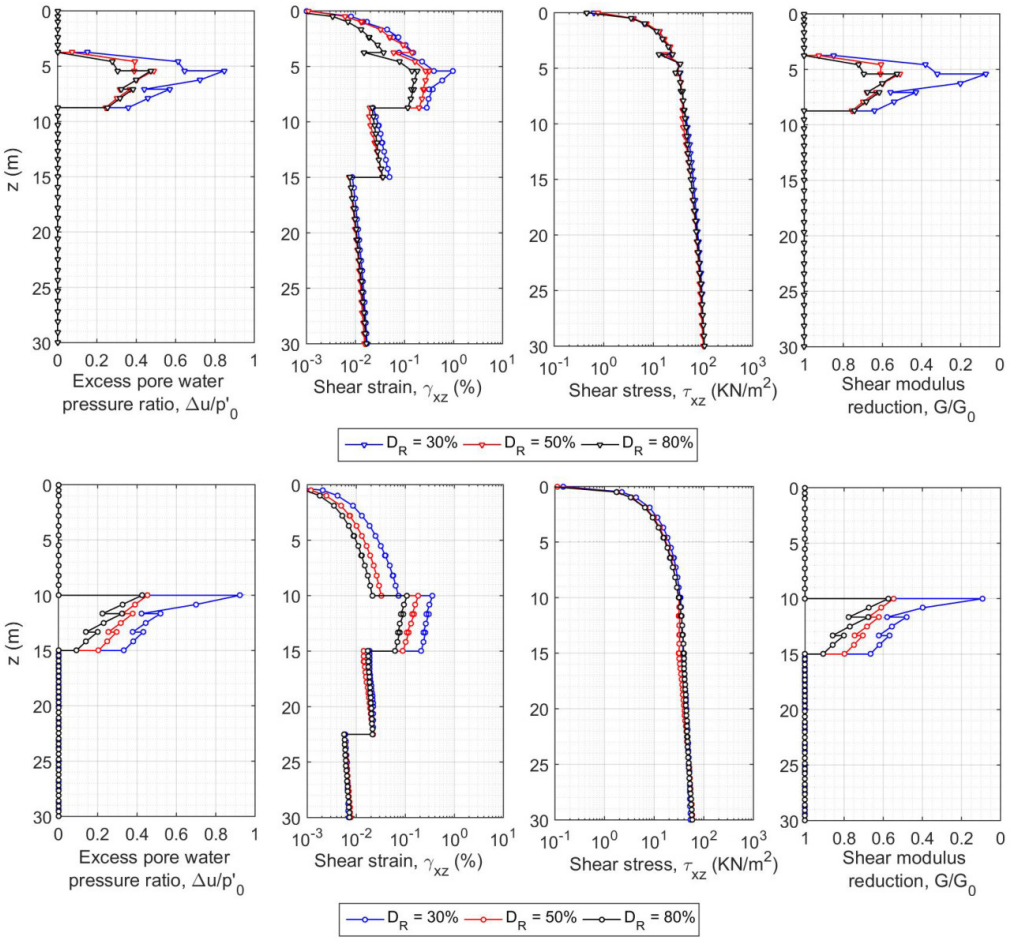

Figure 5.15: Influence of relative density ($D_R = 30 - 50 - 80\%$) on the seismic response of soil profiles C1 (top) and C2 (bottom), in the case of clean sand: vertical profiles of maximum normalized excess pore water pressure ratio (a), maximum shear strain (b), maximum shear stress (c) and maximum shear modulus reduction (d). In profile C1 (top), the confining pressure in the middle of the liquefiable layer is $p'_0 = 50kPa$ and 1.05m/s^2 is the peak acceleration of the input signal. In profile C2 (bottom), the confining pressure in the middle of the liquefiable layer is $p'_0 = 100kPa$ and the peak acceleration of the input signal is 0.66m/s^2

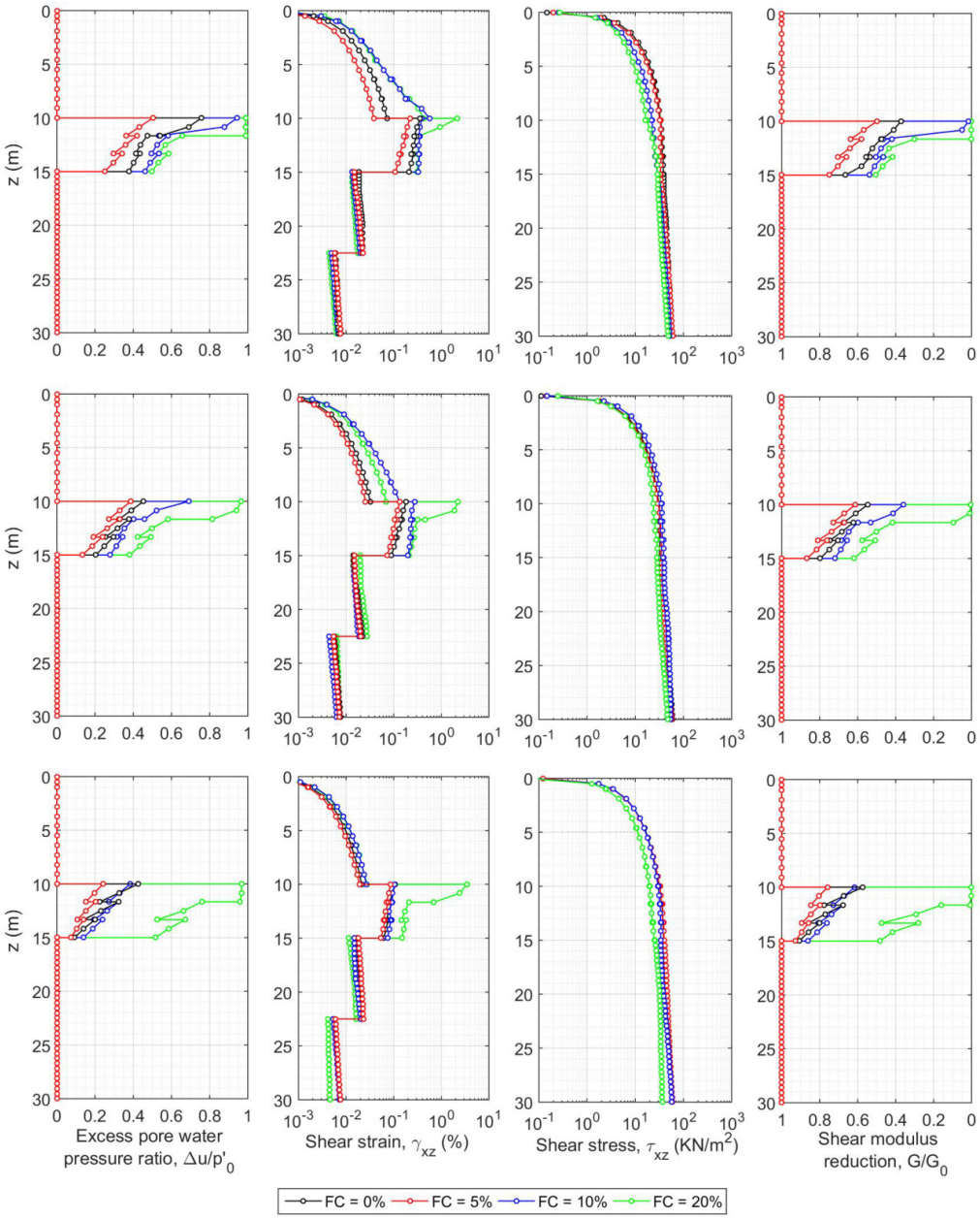

Figure 5.16: Influence of fine content ($FC = 0 - 5 - 10 - 20\%$) on the seismic response of C2 soil profile, in the case of relative density $D_R = 30\%$ (top), 50% (middle) and 80% (bottom): vertical profiles of maximum excess pore water pressure ratio (a), maximum shear strain (b), maximum shear stress (c) and maximum shear modulus reduction (d). The confining pressure in the middle of the liquefiable layer is $p'_0 = 100kPa$ and the peak acceleration of the input signal is 0.66m/s^2

5.3.1.3 Influence of confining pressure

The effect of confining pressure on the calibration of liquefaction parameters in the seismic response of soil profiles is now investigated.
The confining pressure in the middle of the liquefiable layer in C1 profile is $p'_0 = 50kPa$. Whereas, the confining pressure in the middle of the liquefiable layer in C2 profile is $p'_0 = 100kPa$. The seismic response of C1 and C2 soil profiles is computed in the cases of the liquefiable layer having liquefaction parameters calibrated for various confining pressures ($p'_0 = 50 - 100 - 200kPa$). The input signal is scaled to a peak acceleration equal to 0.66m/s^2.
The vertical profiles of the maximum normalized excess pore water pressure $\Delta u/p'_0$ (a), maximum shear strain γ_{xz} (b), maximum shear stress τ_{xz} (c) and maximum shear modulus reduction G/G_0 (d) are displayed in Figs 5.17 and 5.18 for C1 and C2 soil profiles, respectively, and various relative densities ($D_R = 30 - 50 - 80\%$).

The results in Fig. 5.17 highlight that using liquefaction parameters calibrated for higher confining pressure ($p'_0 = 100 - 200kPa$) is a safe choice. The computed results are inaccurate but conservative. In fact, C1 soil profile does not reach liquefaction ($\Delta u/p'_0 \simeq 0.2$, $\gamma_{xz} = 0.1\%$) if the assumed liquefaction parameters are those calibrated for the correct confining pressure $p'_0 = 50kPa$. Instead, liquefaction occurs if the liquefaction parameters calibrated for higher confining pressures are adopted.
Conversely, the results in Fig. 5.18 point out that using liquefaction parameters calibrated for lower confining pressure ($p'_0 = 50kPa$) is not at all a safe choice. In fact, C2 soil profile reaches liquefaction if the assumed liquefaction parameters are those calibrated for the correct confining pressure ($p'_0 = 100kPa$) or a higher one ($p'_0 = 200kPa$). Instead, liquefaction is not predicted by the numerical simulations carried out using liquefaction parameters calibrated for a lower confining pressure ($p'_0 = 50kPa$).

It can be concluded that, in numerical simulations, the use of liquefaction parameters calibrated using soil samples taken at a lower depth or by means of laboratory tests at a lower confining pressure, may lead to an important overestimation of the cyclic liquefaction resistance of the soil layer.
The same conclusions are drawn for the various relative densities selected for the analyses ($D_R = 30 - 50 - 80\%$).

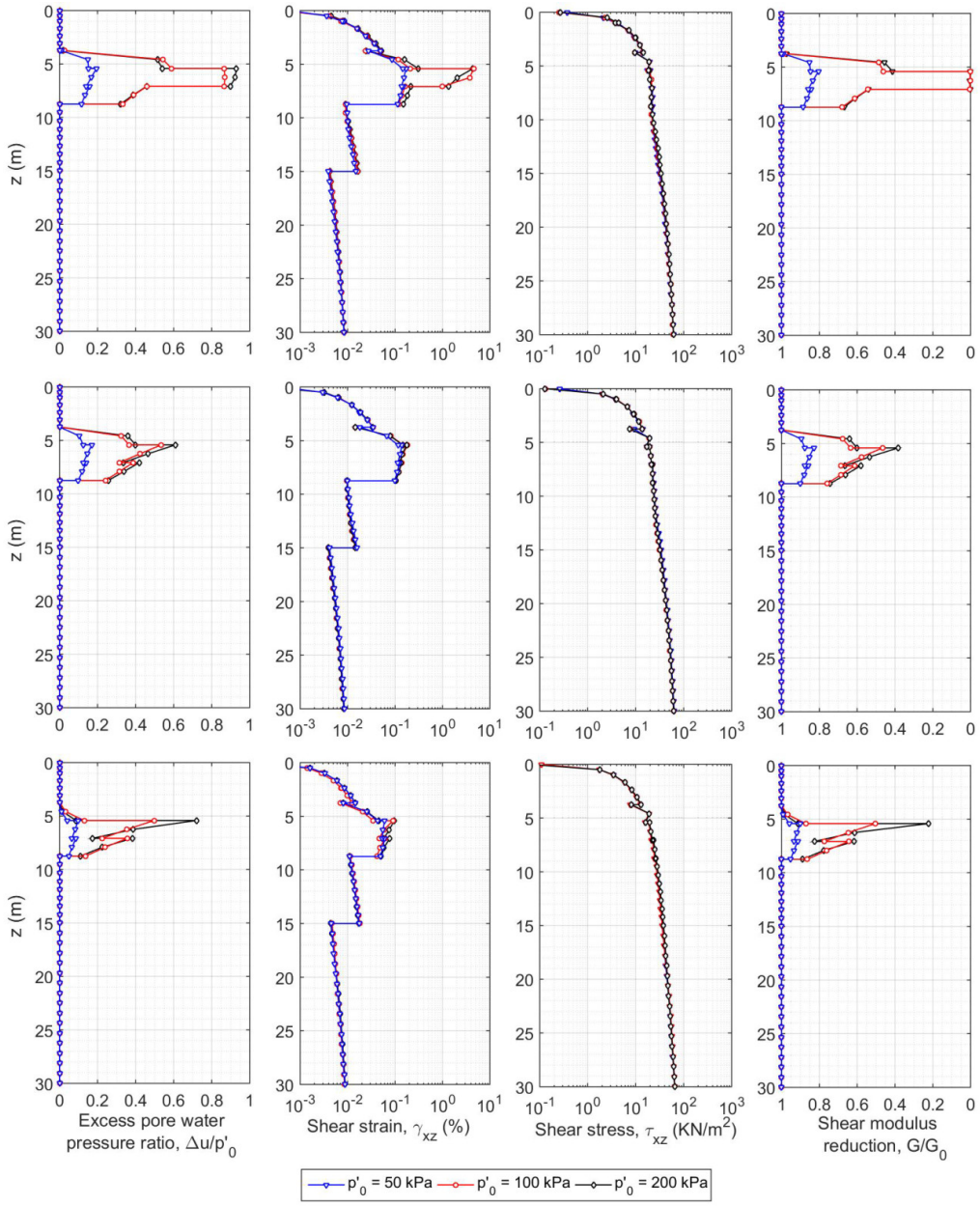

Figure 5.17: Influence on the seismic response of C1 soil profile of using liquefaction parameters calibrated for various confining pressures ($p'_0 = 50-100-200kPa$), in the case of clean sand having relative density $D_R = 30\%$ (top), 50% (middle) and 80% (bottom): vertical profiles of maximum excess pore water pressure ratio (a), maximum shear strain (b), maximum shear stress (c) and maximum shear modulus reduction (d). The confining pressure in the middle of the liquefiable layer is $p'_0 = 50kPa$ and the peak acceleration of the input signal is 0.66m/s^2

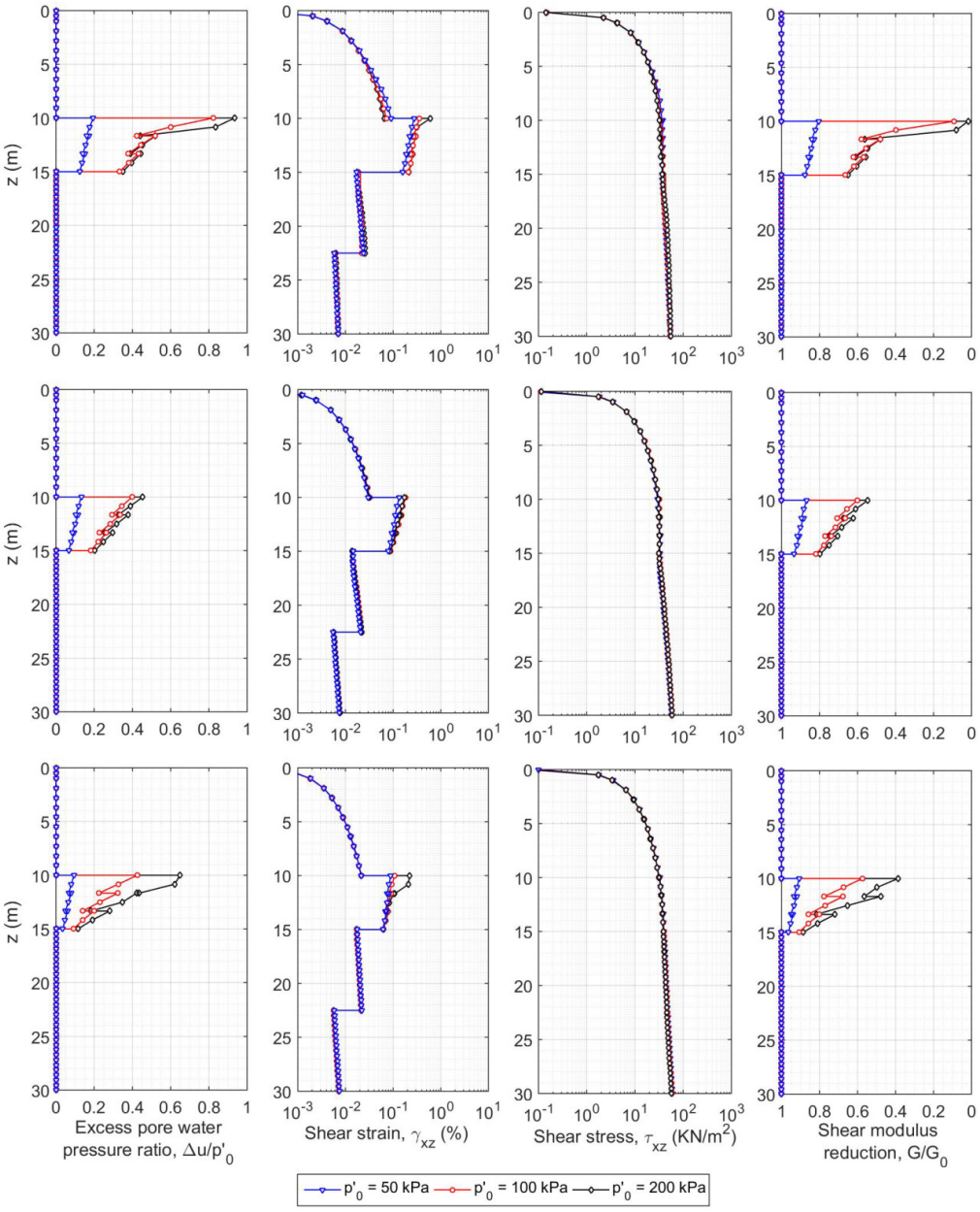

Figure 5.18: Influence on the seismic response of C2 soil profile of using liquefaction parameters calibrated for various confining pressures ($p'_0 = 50-100-200kPa$), in the case of clean sand having relative density $D_R = 30\%$ (top), 50% (middle) and 80% (bottom): vertical profiles of maximum excess pore water pressure ratio (a), maximum shear strain (b), maximum shear stress (c) and maximum shear modulus reduction (d). The confining pressure in the middle of the liquefiable layer is $p'_0 = 100kPa$ and the peak acceleration of the input signal is 0.66m/s^2

5.4 Conclusions

In this chapter, the set of laboratory tests carried out for each type of soil (different initial conditions D_R, FC, p'_0) is used to calibrate the 3D Iwan-Iai constitutive model. This elasto-plastic constitutive model with hardening, pressure-dependent through Iai's correction of the shear modulus, is able to model the cyclic behavior of saturated soils and to predict both cyclic mobility and cyclic liquefaction of sands. In particular, it is observed that the 3D Iwan-Iai model simulates the cyclic behaviour of dense sands better, in terms of strain evolution, compared to loose samples. While, in terms of pore pressure generation, results show that the 3D Iwan-Iai model is able to well simulate the triggering of liquefaction in both cases of cyclic mobility and cyclic liquefaction.

After the evaluation of the calibration characteristics based on the laboratory tests, trends for liquefaction front parameters p_2 and w_1, which control the evolution of pore water pressure and strains, are found with varying relative density, fine content and confining pressure. To this regard, it is not possible to reproduce cyclic undrained behavior at different initial states conditions (D_R, FC, p'_0) while only using a single model parameter set. In fact, a different material parameter set has to be derived for each specified initial state condition applied to the soil sample.
The value of p_2 increases for higher confining pressures and decreasing of relative density and fine content. The value of p_2 is high for loose to medium sand and decreases for high relative density.
The value of w_1 does not seem affected by the relative density. On the other hand, w_1 is strongly affected by the confining pressure. With increasing confining pressure, w_1 quickly decreases. In the case of loose to medium mixtures, the value of w_1 is independent of fine content for percentages lower than 5% and decreases rapidly with increasing fine content. In the case of dense mixtures, w_1 is independent of fine content for percentages up to 10% and then decreases with increasing fine content, confirming that the fine content cannot be the only factor to characterize the behavior of silty sand mixtures, but the relative density also has an important effect in the mixture behavior.

During the calibration process for all soil samples, it has been also observed that the 3D Iwan-Iai constitutive model can adequately reproduce cyclic undrained behaviour in terms of pore water pressure and strain evolution and stress path, but is not able to fully simulate the hysteresis loops of soils samples, as shown in Fig. 5.19. Differences between the predicted

and measured shear-strain responses are associated with limitations in the numerical model. The explanation is the fact that the Iai model has been formulated based on cyclic shear simple tests and thus the axial components are not associated with the shear components. For this reason, the numerical hysteresis loops appears more tightened than the experimental ones (Fig. 5.19e). To this regard, direct cyclic simple shear tests rather than triaxial tests, would be more relevant and are recommended.

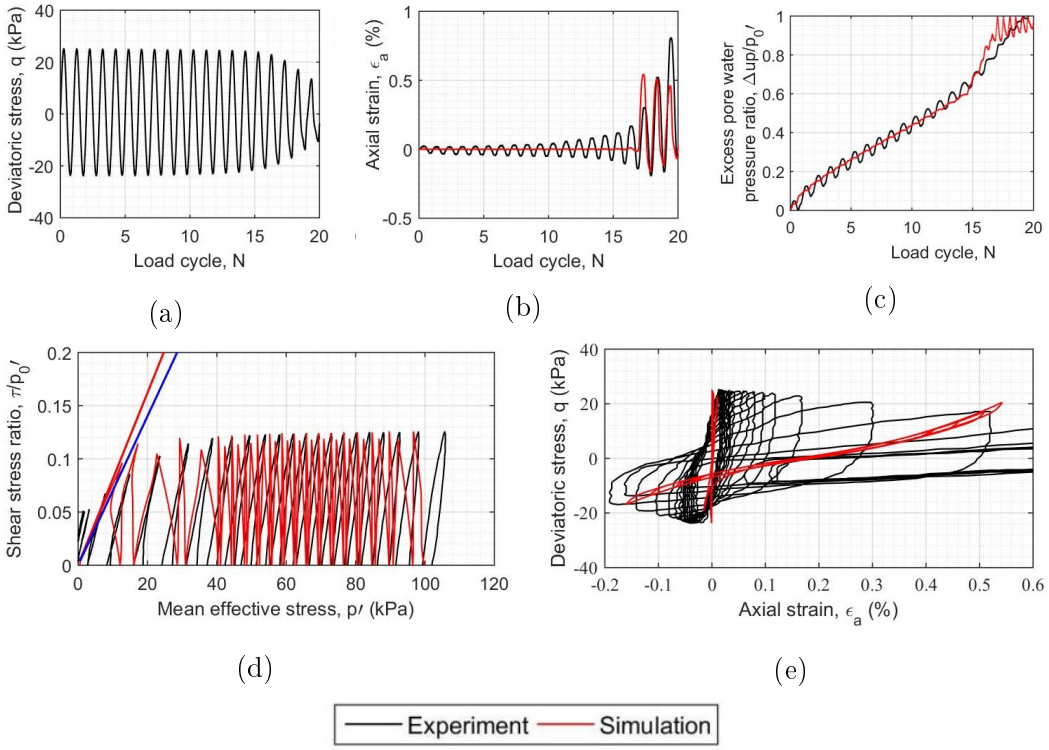

Figure 5.19: Experimental results and fitting for clean HN31 Hostun mixture (relative density $D_R = 30\%$, fine content $FC = 10\%$ and confining pressure $p'_0 = 100kPa$: deviatoric stress (a), axial strain (b) and excess pore water pressure ratio (c) versus the number of load cycle, deviatoric stress versus effective stress (stress path, d) and hysteresis loops (e)

In the second part of the chapter, the seismic response of soil profiles with a liquefiable layer is numerically simulated using the liquefaction parameters obtained for the 18 soil samples in order to evaluate their influence for practical case studies. These laboratory tests as well as the seismic computations evidence that fine content and relative density significantly affect the liquefaction resistance of silty sand soils. In the case of loose to medium mixtures, the response of sand with fine content up to 5% is similar to that of clean

sand. Whereas, the excess pore water pressure and shear strain increase for higher fine contents. Dense soils show results similar to those for clean sand for fine content up to 10% and then, for higher fine content, the excess pore water pressure and shear strain increase.
The experimental and numerical results highlight the variation of liquefaction parameters with depth. In numerical simulations, the use of liquefaction parameters calibrated using soil samples taken at a lower depth or by means of laboratory tests at lower confining pressures, may lead to an important overestimation of the liquefaction resistance of the soil layer, independently of its relative density.

Chapter 6

Influence of the variability of soil profile properties on weak and strong seismic response

Advanced constitutive models require a number of parameters to characterize the response of granular soils undergoing elastic or elastoplastic deformations as well as common features in soils susceptible to liquefaction. On this subject, in this chapter, a stochastic analysis is carried on in order to further investigate the influence of numerical soil parameters on seismic site response simulations in layered soil profiles.

A dataset of 300 one-dimensional soil profiles with a given $v_{s,30}$ are generated through a Monte Carlo method with the aim of evaluating the reliability and the limit of using the average shear wave velocity in the upper 30m of the soil profile $v_{s,30}$, as single proxy, to characterize seismic site effects for weak and strong events. Soil profile responses are computed for a set of 40 real accelerograms, with different seismic features. The vertical propagation from the bottom of the generated columns is modeled using a finite element spatial discretization, accounting for both linear and nonlinear soil behavior.

The site dominant frequency f_0 and the shear wave velocity gradient B_{30} are proposed as complementary proxies, in addition to $v_{s,30}$, to characterize seismic site effects and the variability of the response spectra for the numerical signals, at the free surface of the set of columns. The two proposed proxies have been selected because they can be estimated, without excessive cost, by geophysical methods applied to ambient vibrations or seismic motions, recorded using temporary instruments located at the soil surface (Brûlé and Javelaud, 2014). Correlations between site-specific amplification factors deduced using the numerical response spectra and the proposed site proxies are analyzed for different sub-ranges of periods. The obtained amplification factors are then compared to those proposed by different international and national design codes.

The results, obtained under assumption of linear and nonlinear behavior of soil, emphasize the need to introduce complementary site parameters proxies, in addition to $v_{s,30}$ to characterize the expected site effects in design response spectra.

Moreover, according to recent reviews (see Section 2.4.2), the prediction of the seismic site response using only a single proxy over the whole period range does not seem satisfactory. Hence, to improve the site amplification estimation, it is advisable to use a combination of site proxies rather than a single site proxy. Based on this idea, the goal of this chapter is to assess the correlation between site amplification factors and soil parameters used to characterize the site condition, with the aim of improving the expected ground motion prediction.
Then, since the nonlinear behavior of soils has been recognized as an important factor in site response (Régnier et al., 2013, 2016b), the second aim is to explore how these site proxies allow to capture and account for the nonlinear component of site response.

6.1 Methodology

The stratigraphy of a set of soil profiles with a given average shear wave velocity in the upper 30m $v_{s,30}$ is randomly generated, using the Monte Carlo method. Consequently, all the generated profiles belong to the same ground type in the Eurocode classification (Eurocode, 2005). The seismic wavefield along these soil profiles has been computed using the finite element method (FEM) for spatial discretization and the Newmark algorithm for time discretization, implemented in the SWAP_3C FEM package (Santisi d'Avila et al., 2012; Santisi d'Avila et al., 2013). The highest-amplitude horizontal component of a wide variety of recorded earthquakes, representative of regions of low to moderate intensity, is applied as input motion at the base of each soil profile. These recorded signals are propagated along each soil profile and the ground response at the surface is evaluated in both cases of linear and nonlinear soil behavior. Results are presented with respect to the amplification factors adopted by Ciancimino et al. (2018), in different period ranges, in order to distinguish short-, mid- and long-period amplification factors. Differences between the response spectra of numerical signals at the soil surface and the reference spectrum proposed by European buildings codes (Eurocode, 2005) are then quantified and discussed.

6.1.1 Set of generated soil profiles for the statistical analysis

The parameters chosen for the set of soil profiles are the average shear wave velocity $v_{s,30} = 270m/s$, corresponding to the ground type C according to the Eurocode 8 (Eurocode, 2005), the soil depth of 30m, the number of layers equal to 4 and the density $\rho = 1850kg/m^3$. The geotechnical properties assumed for the bedrock are the density $\rho_b = 2200kg/m^3$ and the shear wave velocity $v_{sb} = 1000m/s$. The properties of each layer are generated considering each stochastic parameter uniformly distributed in a given range. The soil layer thickness ranges in [1 - 15 m], the shear wave velocity in [100 - 800 m/s] and 4 soil types can be randomly targeted. Each soil type from 1 to 4 is associated to a plasticity index $PI = 0, 5, 10$ and 20%, respectively. Yokota et al. (1981) have shown that normalized shear modulus reduction curve for different types of soils can be expressed by a set of formulas in the absence of available test data. To this regard, a normalized shear modulus reduction curve, as a function of the shear strain γ, is derived using the four-parameter model proposed by Darendeli (2001) to characterize normalized modulus reduction

formulation:

$$G(\gamma)/G_0 = 1/[1 + (\gamma/\gamma_r)^{\alpha}] \tag{6.1}$$

assuming a normal consolidated soil (over-consolidation ratio $OCR = 1$). The reference shear strain is defined as $\gamma_r = (\Phi_1 + \Phi_2 PI \cdot OCR^{\Phi_3}) \cdot {p'_0}^{\Phi_4}$, where Φ_1, Φ_2, Φ_3 and Φ_4 are parameters relating the normalized modulus reduction curve to soil type and loading conditions estimated on the basis of statistical analysis ($\Phi_1 = 0.0352$, $\Phi_2 = 0.001$, $\Phi_3 = 0.3246$, $\Phi_4 = 0.3483$) and $\alpha = 0.92$. The vertical effective stress p' is calculated each $5m$ using the chosen soil density $\rho = 1850kg/m^3$, to account for the variation of the shear modulus decay curve with depth. The normalized shear modulus reduction curves employed for the four soil types, associated to a different plasticity indices PI are shown in Fig. 6.1a, for a given depth $z = 5m$. The $G(\gamma)/G_0$ curves at various depths, associated to a related vertical effective stress p', for the soil type 1 having plasticity index $PI = 0$, are shown in Fig. 6.1b.

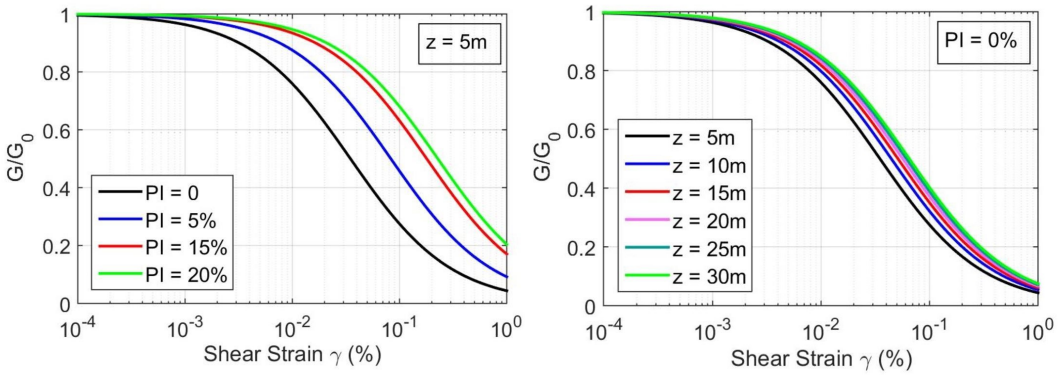

(a) (b)

Figure 6.1: Normalized shear modulus reduction curves obtained by Darendeli (2001) (a) for the four soil types associated to different plasticity index PI and a given depth $z = 5m$, (b) and for increasing depth z and a given plasticity index $PI = 0$

A set of 300 soil profiles is randomly generated with different layer thicknesses and impedance contrasts, in order to represent various site conditions and estimate the influence of their uncertainty on the amplification process. Among these 300 soil profiles, for 200 of them, the shear wave velocity profile increases with depth to consider the effect of increasing confining stresses. In the other 100 soil profiles, there is an inversion of the shear wave velocity profile in one of the middle layers. The position and the thickness of the layer with the shear wave velocity inversion are selected randomly. The generated

shear wave velocity profiles with depth $v_s(z)$ are shown in Fig. 6.2, in the cases of increasing v_s and of inversions in the profile (a and b, respectively). It can be noted that the variability in the shear wave velocity profile, according to the same $v_{s,30} = 270m/s$, can be very large.

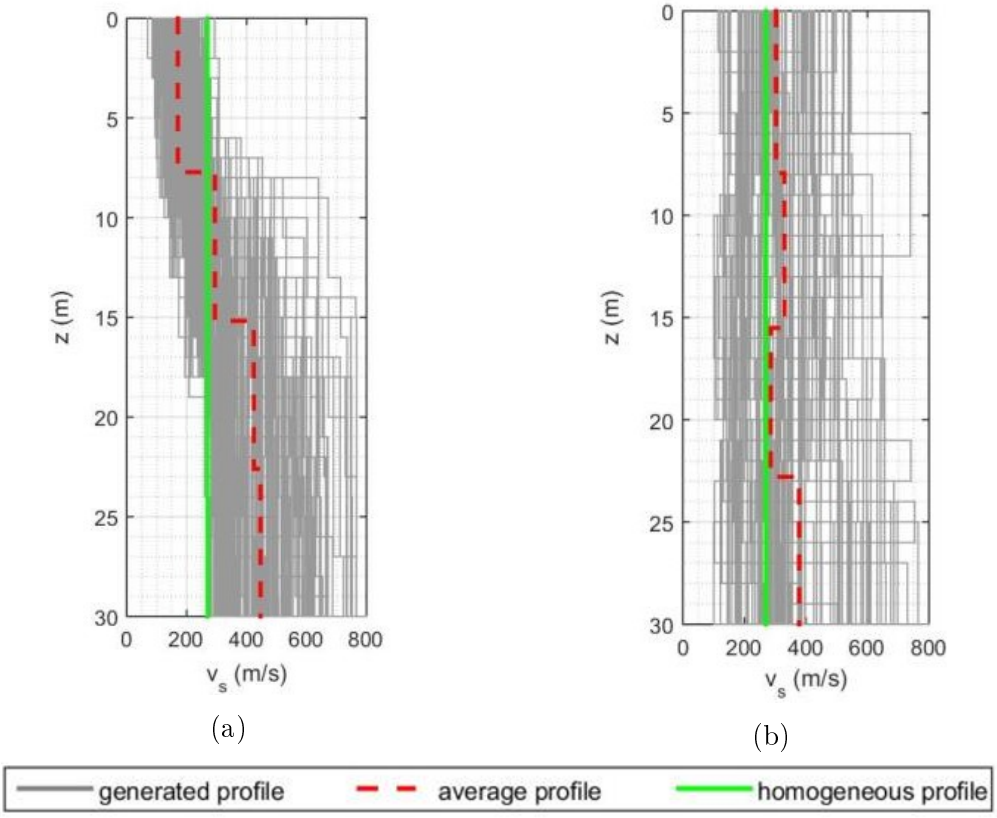

Figure 6.2: Generated shear wave velocity profiles with depth $v_s(z)$ in the cases of (a) increasing v_s and (b) shear wave velocity inversion. All the generated soil profiles have the same average shear wave velocity $v_{s,30} = 270m/s$

6.1.2 Set of recorded seismic motions

A set of 40 signals, recorded at rock outcrops, is selected as input for the computation of the seismic wave propagation along the 300 generated soil profiles. These seismic motions originate from ITACA, the Italian Strong Motion Database (Massa et al., 2010), ISESD, European Strong Motion Database (Ambraseys et al., 2004) or PEER, Pacific Earthquake Engineering Research Center Database (PEER, 2014). In the adopted set of seismic signals, 20 of them are representative of low to moderate intensity with magnitudes ranging from 3 to 5.5 (associated to the type 2 response spectrum of Eurocode 8 (Eurocode, 2005)) and the other 20 are representative of moderate to high

seismicity with magnitude ranging from 5.6 to 7.5 (type 1 response spectrum). Taking into account the influence of the frequency content on the free-field (FF) ground motion, the selected seismic records are representative of a wide variety of dominant frequencies. The set of recorded seismic motions is sorted in terms of frequency content using the equivalent period T_{VA}, parameter proposed by Cameron and Green (2004), defined as

$$T_{VA} = 2\pi \frac{\alpha_V(\varepsilon = 5\%)}{\alpha_A(\varepsilon = 5\%)} \frac{v_{gR}}{a_{gR}} \tag{6.2}$$

where a_{gR} and v_{gR} are the peak ground acceleration and velocity at the outcrop, respectively. The median spectrum amplification factors for horizontal motion are estimated by Newmark and Hall (1982) as $\alpha_A(\varepsilon = 5\%) = 2.12$ and $\alpha_V(\varepsilon = 5\%) = 1.65$, for the constant acceleration and constant velocity regions of 5% damped response spectra, respectively. Fig. 6.3 shows the equivalent predominant frequency $1/T_{VA}$ related to the peak ground acceleration on rock outcrop a_{gR} for the set of 40 seismic motions. The oblique lines represent uniform values of v_{gR}. The severity of seismic motions increases according to the direction of increasing velocity (from the bottom-right corner toward the top-left one, where the values of a_{gR} and v_{gR} are both higher). Based on the observations in Kobe (Kawase, 2011), the values $a_{gR} = 0.8g$ and $v_{gR} = 100cm/s$ are considered as risk limits, meaning that the input motions above these values are considered as the most severe ones (Fig. 6.3). Then the set of the selected seismic motions is made up of a wide variety of frequency content, peak acceleration and peak velocity.

6.1.3 Wave propagation model

Assuming a vertical propagation in a horizontally layered medium, the numerical analysis is undertaken as a one-dimensional approach. The soil is assumed homogeneous and both assumptions of linear and nonlinear constitutive behavior are analyzed. Quadratic line finite elements are adopted for spatial discretization and the Newmark algorithm for time discretization, with some numerical damping. The SWAP_3C finite element software (Santisi d'Avila et al., 2012; Santisi d'Avila et al., 2013; Régnier et al., 2016a, 2018) is used for the numerical simulations. At the soil-bedrock interface, an absorbing boundary condition adopted by Joyner and Chen (1975) is applied in order to take into account the elasticity of the underlying bedrock and allow energy to be radiated back. The mechanical properties characterizing the bedrock are the density ρ_b and the shear wave velocity v_{sb}. The largest horizontal component of the signal recorded at the reference outcrop is halved and imposed as the incident wave at the soil-bedrock interface. The finite element size in each soil

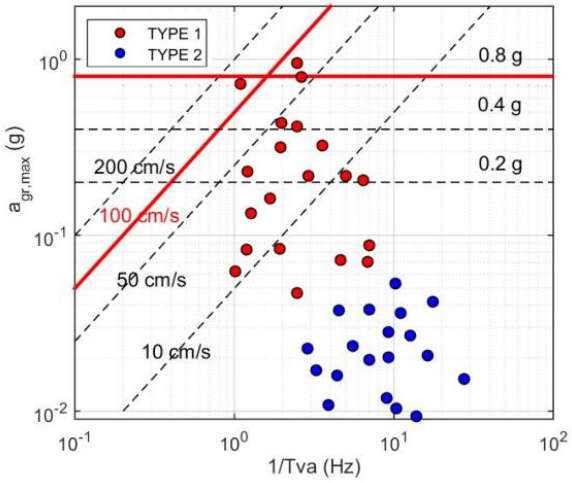

Figure 6.3: Equivalent predominant frequency T_{VA} related to the peak ground acceleration at the outcrop a_{gR} for the set of 40 seismic motions. The oblique lines represent uniform values of v_{gR}. The horizontal lines represent constant values of a_{gR}

layer is defined as the minimum between 1m and one tenth of the minimum wavelength, related to shear wave velocity in the layer and the maximum frequency assumed equal to $15Hz$, above which the spectral content of the input signal is considered negligible.
Details of the finite element model employed in this research are completely described by Santisi d'Avila et al. (2012) and Santisi d'Avila et al. (2013).

6.1.4 Hysteretic model for soil

The so-called Masing-Prandtl-Ishlinskii-Iwan (MPII) nonlinear constitutive model (Iwan, 1967) is used for the soil in a total stress analysis. Its main feature is the satisfactory reproduction of nonlinear and hysteretic behavior of soils under cyclic loadings (Régnier et al., 2016a, 2018), starting from the knowledge of a small number of parameters characterizing the soil properties, such as elastic parameters and the shear modulus reduction curve. The MPII model is elasto-plastic with linear kinematic hardening. The plasticity model assumes an associated plastic flow, which allows for isotropic yielding. This rheological model has no viscous damping and the dissipation is purely hysteretic and frequency independent. The size of the Von Mises yield surface is imposed by the backbone curve in the uniaxial stress case. The tangent constitutive matrix is deduced from the actual strain level and the strain and stress values at the previous time step (Iwan, 1967; Joyner, 1975). This means

that the stress level depends on the strain increment and strain history but not on the strain rate.

6.1.5 Data analysis

An optimal selection of site parameters is an important tool for the prediction of the expected ground motion. Based on recent results (Derras et al., 2017; Stambouli et al., 2017; Zhu et al., 2020; Ciancimino et al., 2018), the site dominant frequency f_0 and the shear wave velocity gradient B_{30} are chosen as complementary proxies in this study. As proposed by Régnier et al. (2014), the shear wave velocity gradient B_{30} is defined as the slope of the linear regression of the relation between the logarithm of the shear wave velocity profile $v_s(z)$ and the depth z. Thus, it is computed as:

$$log(v_s(z)) = B_{30}log(z) + A_{30} \pm \sigma_{30} \tag{6.3}$$

where A_{30} is the vertical intercept of the regression, σ_{30} is the standard deviation associated to the linear regression. The shear wave velocity gradient B_{30}, estimated by Eq. 6.3 for all the generated $30m$ deep soil profiles, quantifies the variation of the shear wave velocity $v_s(z)$ contrast in the superficial layers. Its value is close to zero if the velocity is nearly constant with depth and it is larger if the shear wave velocity v_s increases rapidly with depth (Régnier et al., 2014). The results of the numerical simulations of seismic wave propagation in the set of generated soil profiles, are first analyzed in terms of amplification factors, according to Ciancimino et al. (2018), in both cases of linear and nonlinear soil behavior. The soil amplification factor S_s is a local indicator of the site amplification, providing an estimate of the site effect on the free field (FF) motion. It is defined as the ratio of the peak ground acceleration at the surface a_g to the peak acceleration at the outcrop a_{gR}:

$$S_s = a_g/a_{gR} \tag{6.4}$$

The spectral amplification factor SA and the spectral velocity factor SV are used to quantify the ground motion intensity in a given period range. These parameters are proposed by Rey et al. (2002). They are defined as the ratio of I_{soil} to I_{rock}. These are the intensity of the spectrum estimated using the signal at the ground surface and at the outcrop, respectively. The intensities used in the amplification factors SA and SV are calculated by Housner (1952) using the spectrum in terms of acceleration $PSA(T)$ and velocity $PSV(T)$, respectively, as follows:

$$SA = \frac{I_{soil}}{I_{rock}} \quad \text{with} \quad I = \int_{T_1}^{T_2} PSA(T)dT \tag{6.5}$$

$$SV = \frac{I_{soil}}{I_{rock}} \quad \text{with} \quad I = \int_{T_1}^{T_2} PSV(T)dT \tag{6.6}$$

In Eqs. 6.5 and 6.6, $[T_1 - T_2]$ is the fixed range of vibration period. In this research, the spectra $PSA(T)$ and $PSV(T)$ are normalized with respect to the peak acceleration at the outcrop a_{gR}. The period range $[0.05 - 2.5s]$, representative of the fundamental vibration period for more common structures, is divided into three sub-ranges in order to analyze the results for short, middle and long periods of vibration. Spectral amplification factors for short $[0.05 - 0.5s]$, middle $[0.5 - 1s]$ and long $[1 - 2.5s]$ periods of vibration are indicated as (SA_S, SV_S), (SA_M, SV_M) and (SA_L, SV_L), respectively. In a second phase, the response spectra of numerical FF motions are compared to those suggested by Eurocode 8 (Eurocode, 2005). Finally, the results in terms of site amplification factors are compared to the Eurocode 8 (Eurocode, 2005), the New Zealand Standard (NZS, 2004) building codes, and those evaluated by Pitilakis et al. (2013) and Ciancimino et al. (2018).

6.2 Results and discussion

The variability of the shear wave velocity profiles with depth $v_s(z)$ for the set of generated soil profiles, having the same average $v_{s,30} = 270m/s$, is shown in Fig. 6.2. The FF motion obtained by numerical simulation, propagating the set of recorded seismic signals along the generated soil profiles is analyzed. In the following, the influence on site amplification of complementary parameters as the shear wave velocity profiles with depth $v_s(z)$, the site dominant frequency f_0 and the shear wave velocity gradient B_{30} is assessed. The fluctuation of amplification factors with the site parameters f_0 and B_{30} is also analyzed.

6.2.1 Site parameter variability

The dominant frequency of the site f_0 is obtained by evaluating the FF to bedrock transfer function (TF) that is the ratio of the Fourier spectrum of the accelerograms at the FF soil surface and at the outcropping bedrock surface. A low-amplitude signal is used so that the soil remains in the elastic regime. The frequency corresponding to the peak of this TF corresponds to the fundamental frequency of the soil column, considered as the dominant frequency of the site f_0. In the case of a homogeneous soil, the fundamental frequency of a $30m$ deep soil profile, having a shear wave velocity $v_s = 270m/s$, is also deduced (Kramer, 1996) as $f_0 = v_s/(4H) = 2.25Hz$. The homogeneous soil profile is adopted in the following comparisons as canonical case. Fig. 6.4

displays the TF obtained for the soil profile with a homogeneous soil, the generated soil profiles with increasing shear wave velocity with depth $v_s(z)$ and those with an inversion in the $v_s(z)$ profile. The dominant frequency of the site f_0, obtained for the set of all the generated soil profiles ranges from 1.5 to 3.5Hz. For increasing $v_s(z)$ profiles (Fig. 6.4a), the dominant frequency of the site is mostly higher than the frequency for the homogeneous case. Whereas the natural frequencies obtained for soil profiles with an inversion in $v_s(z)$ are distributed in a frequency range (Fig. 6.4b). The peaks of the TF obtained for the generated soil profiles show a higher amplification compared to the homogeneous soil profile in most cases. In particular, the amplification estimated for the soil profiles having increasing $v_s(z)$ is larger for higher f_0 (Fig. 6.4a). According to Fig. 6.4, the site amplification changes depending on the stratigraphy (i.e. shear wave profile with depth, $v_s(z)$) and the fundamental frequency of the site f_0. The frequency content of the surface motion varies accordingly.

Fig. 6.5 illustrates the linear correlation between the shear wave velocity gradient B_{30} and the fundamental frequency of the site f_0 for the set of generated soil profiles with given $v_{s,30}$. This correlation is high, with a correlation coefficient $r^2 = 0.85$, for the whole set of 300 soil profiles. The amplification factors in Eqs. 6.4, 6.5 and 6.6 are calculated using the computed FF motion and the related response spectrum for all the 24000 samples (set of 40 recorded seismic signals applied to 300 generated soil profiles, for linear and nonlinear soil behaviors). The estimated amplification factors S_s, SA and SV, SA_S, SA_M and SA_L, SV_M and SV_L, are shown in Figs 6.6, 6.7, 6.8 and 6.9 as functions of the dominant period of the site $T_0 = 1/f_0$ and of the shear wave velocity gradient B_{30}, respectively, for both linear (a) and nonlinear (b) cases. The trend of mean and standard deviation is also displayed by the thick and dashed lines, respectively.

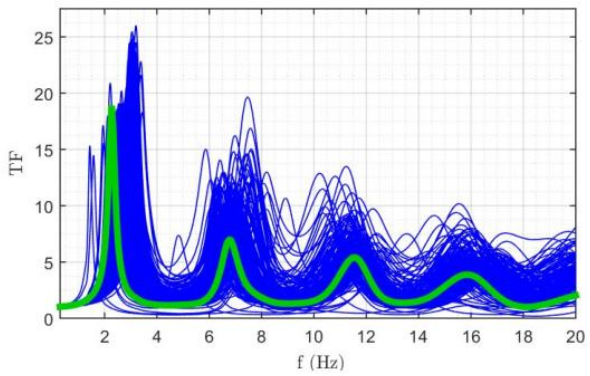

(a)

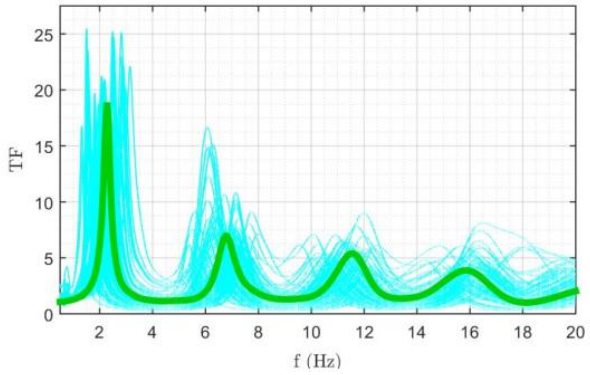

(b)

Figure 6.4: Free-field to bedrock transfer function for the generated deep soil profiles having increasing shear wave velocity profile (a) and a velocity inversion (b). The thick line is the transfer function for the homogeneous soil profile

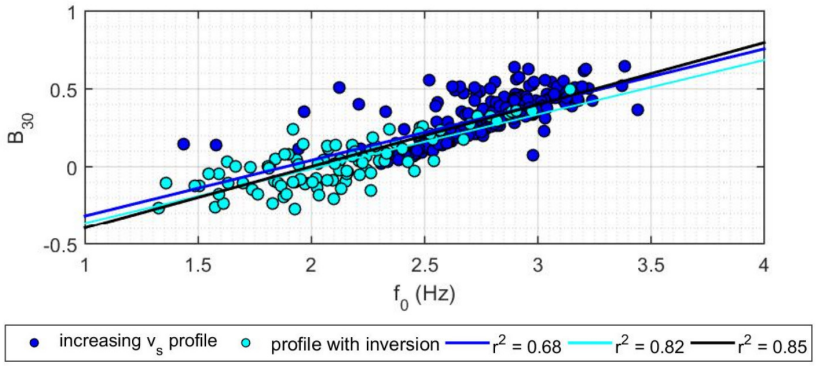

Figure 6.5: Linear regression of the shear wave velocity gradient B_{30} with reference to the fundamental frequency of the site f_0, for the generated deep soil profiles. The thick line is for the set of all 300 generated soil profiles

Figs. 6.6, 6.7, 6.8 and 6.9 illustrate the amplification factors in the three fixed period ranges in order to understand if their variation is modified for different periods. It appears that the largest amplifications are reached for short vibration periods (lower than $0.5s$). Figs. 6.6 and 6.8 evidence that site amplification is strongly dependent on the site predominant period T_0, for short vibration periods of the FF motion (SA_S, SV_S) and independent from it for long periods (SA_L, SV_L). Moreover, site amplification is much more pronounced in soil profiles having T_0 lower than that of the homogeneous profile, for short vibration periods of the FF motion (SA_S, SV_S). Whereas, for middle periods of vibrations (SA_M, SV_M), site amplification is more pronounced in soil profiles having predominant period T_0 higher than that of the homogeneous profile.

Figs. 6.7 and 6.9 show that the largest values of amplification factors are reached for short vibration periods of the FF motion (SA_S, SV_S), lower than $0.5s$, in soil profiles having a high shear wave velocity gradient B_{30}, which corresponds to sites with a large impedance contrast in the first $30m$ or with a steep slope in shear wave velocity profile.

The nonlinear soil behavior on the site response induces a reduced amplification effect. Similarly to the case of linear soil behavior, the site amplification is more pronounced in the case of short vibration periods of the FF motion and it is strongly dependent on the proposed site parameters. On the contrary, the site amplification is less pronounced and independent from the proposed site parameters, for longer vibration periods of the FF motion.

6.2.2 Influence on site effects of the nonlinear soil behavior

In this section, the effects of soil nonlinearities on site response are investigated with reference to the proposed site proxies (predominant period T_0 and shear wave velocity gradient B_{30}). The main goal is to verify the reliability of T_0 and B_{30} even in the range of soil nonlinear behavior. The impact of nonlinearities on the site response is characterized in terms of amplification factor SV. The SV factor is estimated in both cases of linear and nonlinear soil response, in the three adopted period ranges. The amplification factor NL/L is computed as the ratio of spectral velocity factors SV_S, SV_M and SV_L in the ranges of short, middle and long period, for nonlinear soil behavior with respect to the linear soil behavior.

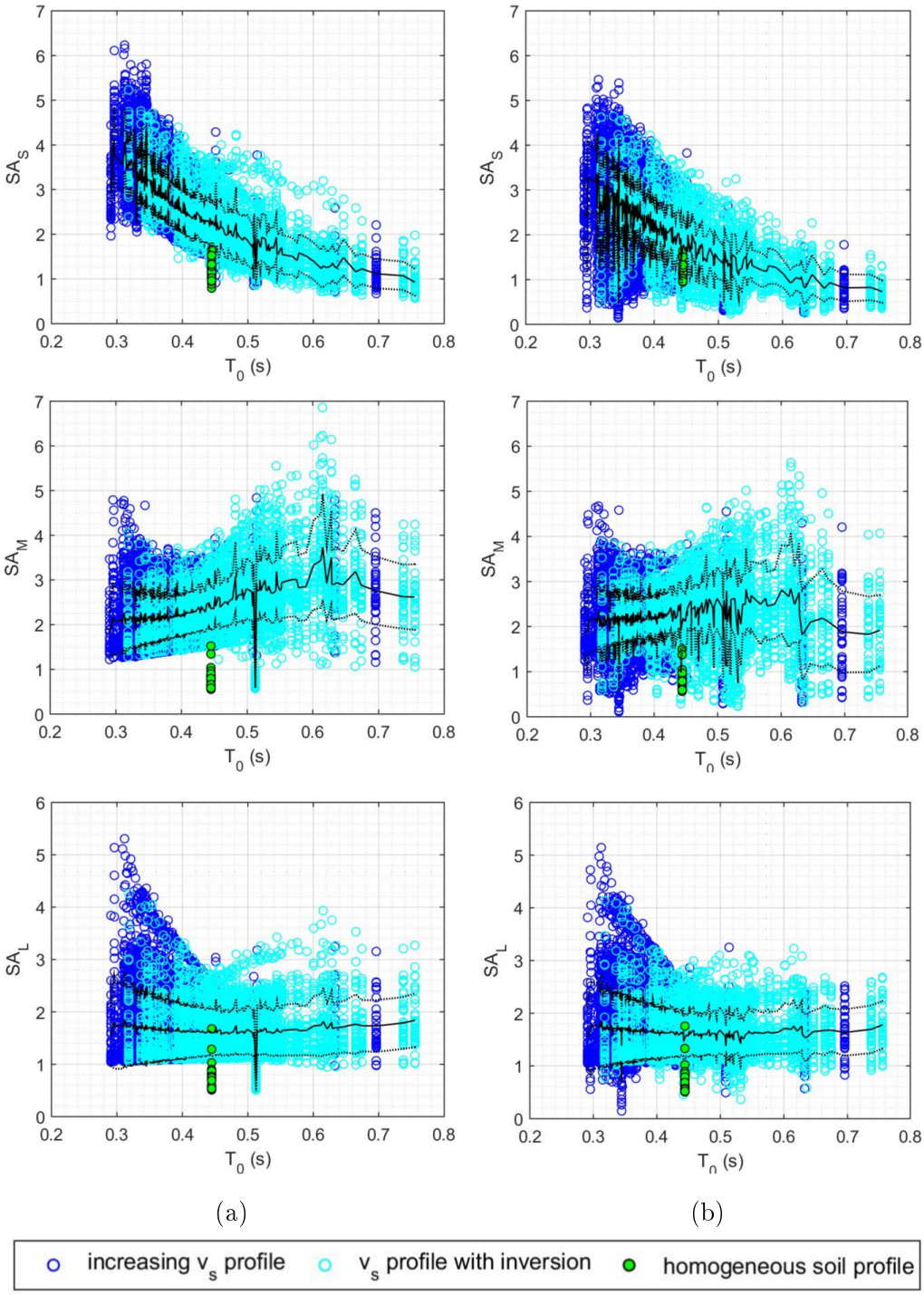

Figure 6.6: Amplification factors SA_S, SA_M and SA_L as a function of the dominant period of the site T_0, for both linear (a) and nonlinear (b) cases. The thick and dashed lines represent the mean and means plus one standard deviation (SD) trend

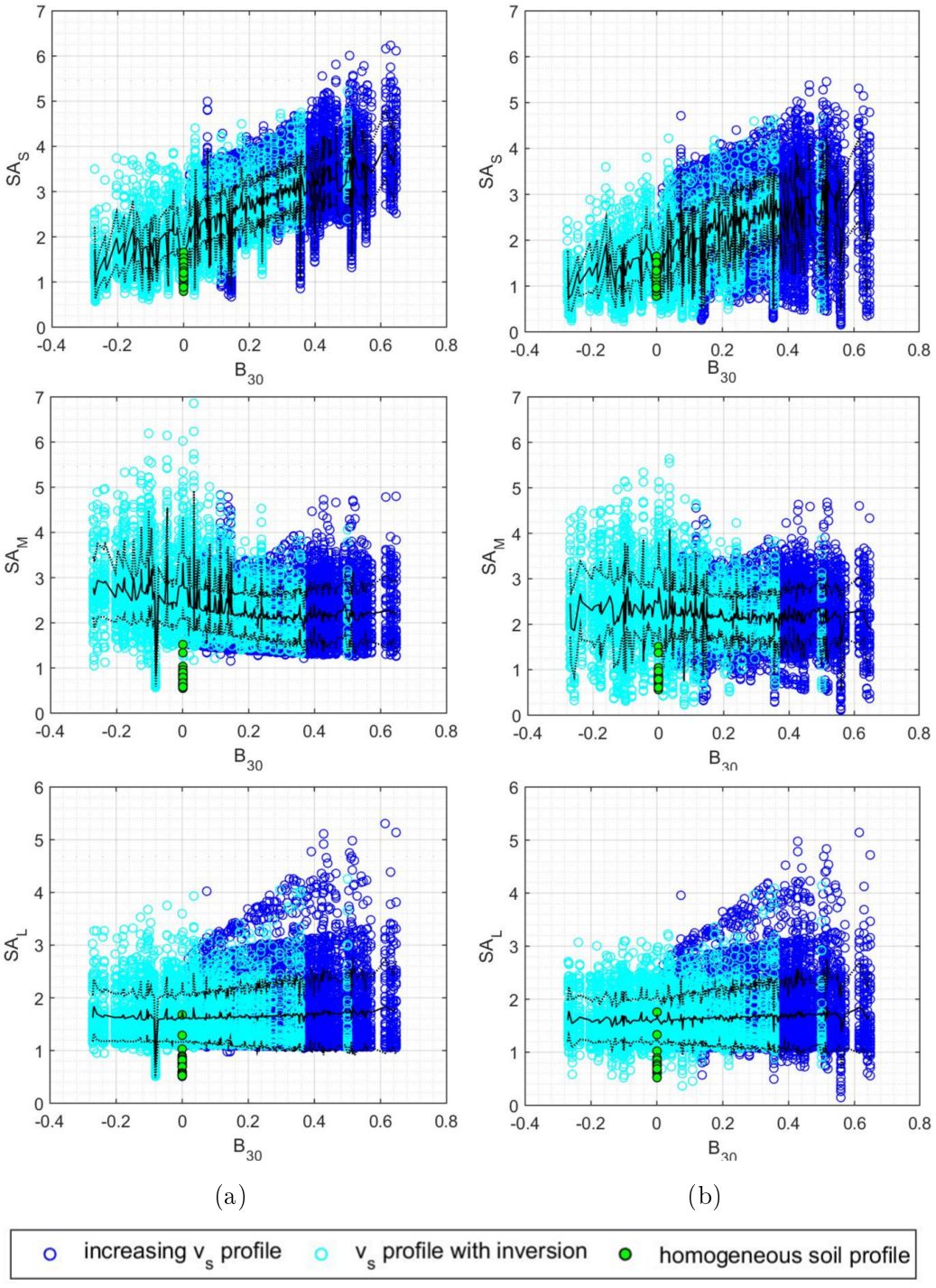

Figure 6.7: Amplification factors SA_S, SA_M and SA_L as a function of the shear wave velocity gradient B_{30}, for both linear (a) and nonlinear (b) cases. The thick and dashed lines represent the mean and means plus one standard deviation (SD) trend

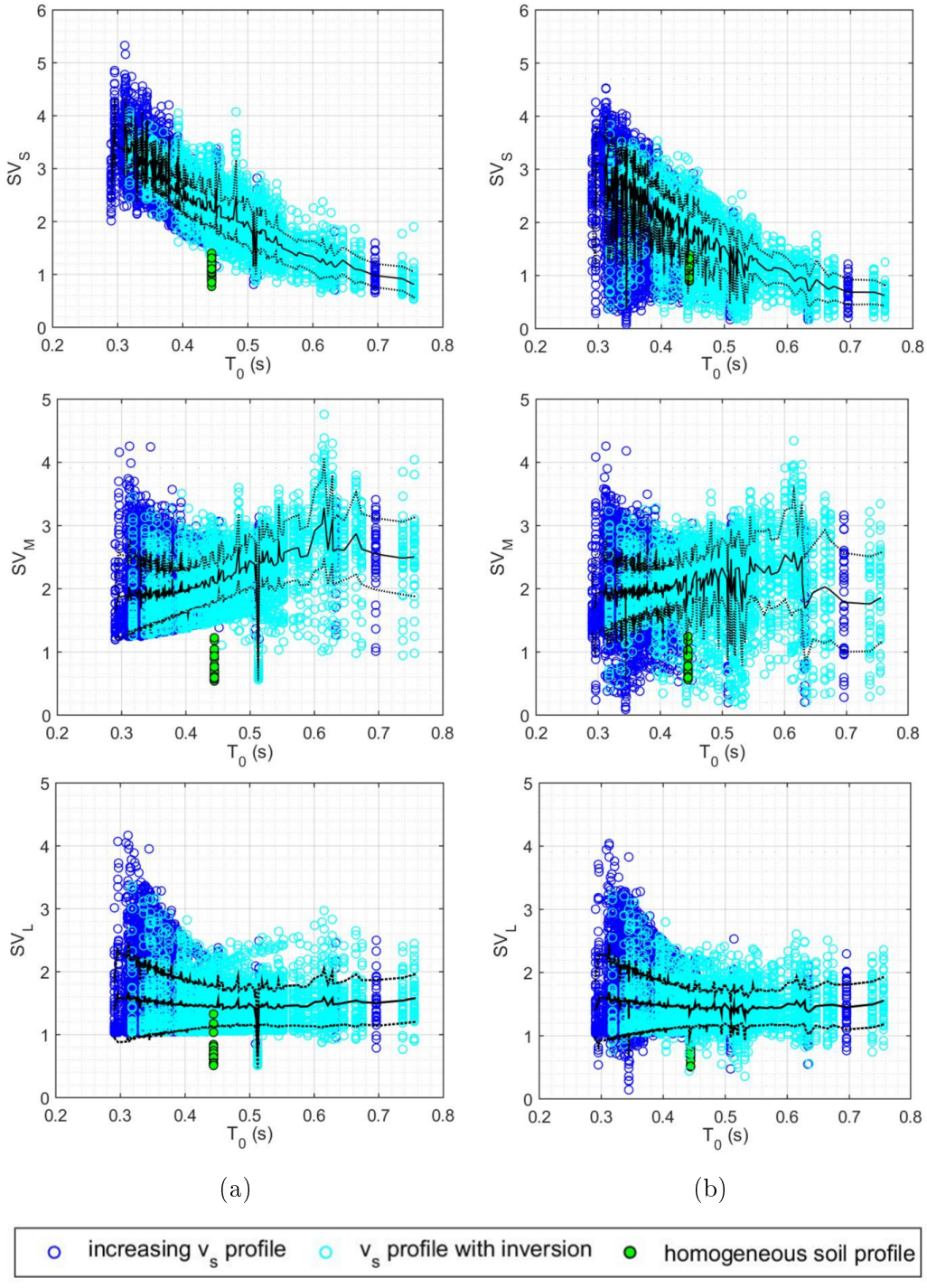

Figure 6.8: Amplification factors SV_S, SV_M and SV_L as a function of the dominant period of the site T_0, for both linear (a) and nonlinear (b) cases. The thick and dashed lines represent the mean and means plus one standard deviation (SD) trend

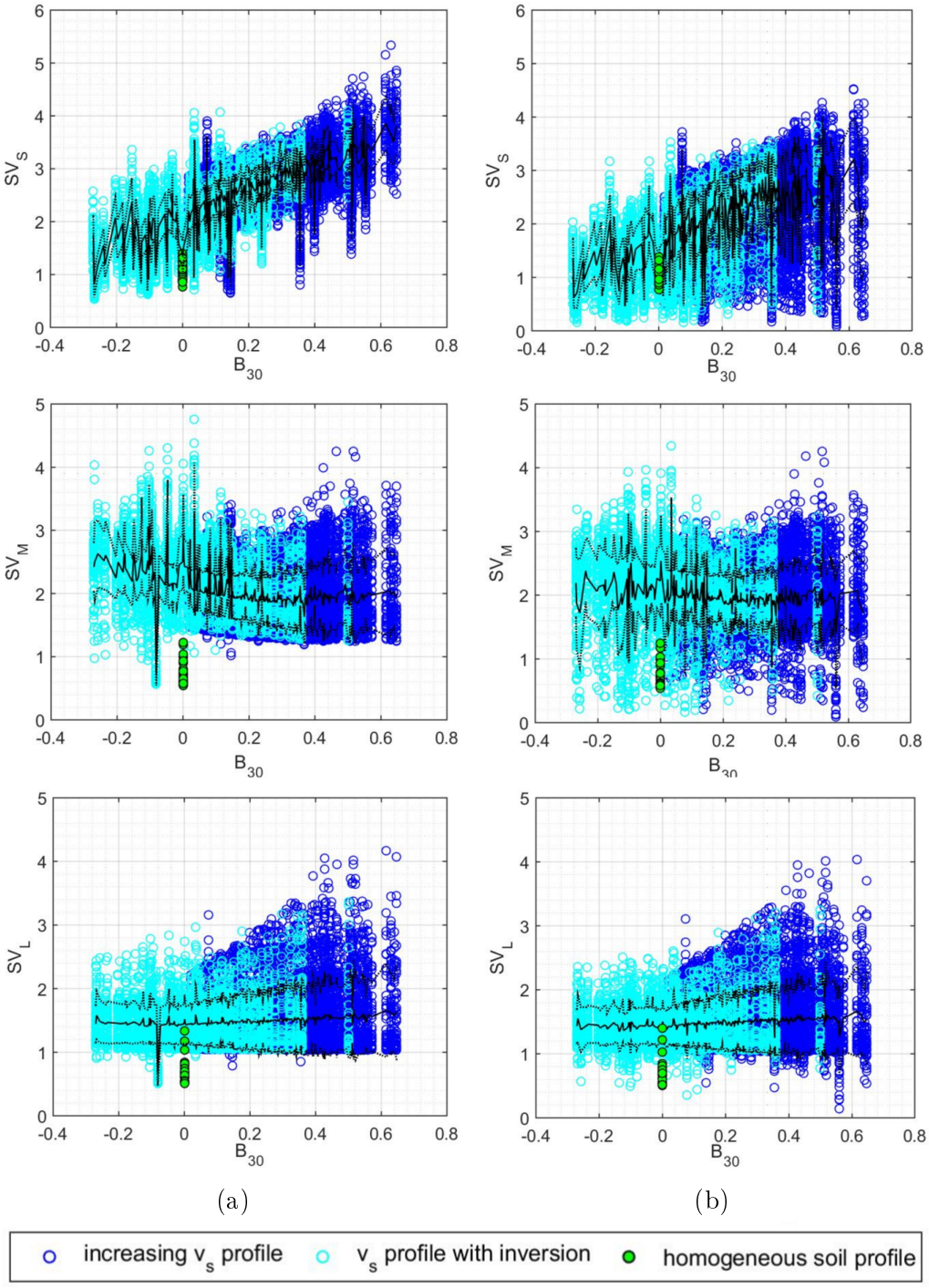

Figure 6.9: Amplification factors SV_S, SV_M and SV_L as a function of the shear wave velocity gradient B_{30}, for both linear (a) and nonlinear (b) cases. The thick and dashed lines represent the mean and means plus one standard deviation (SD) trend

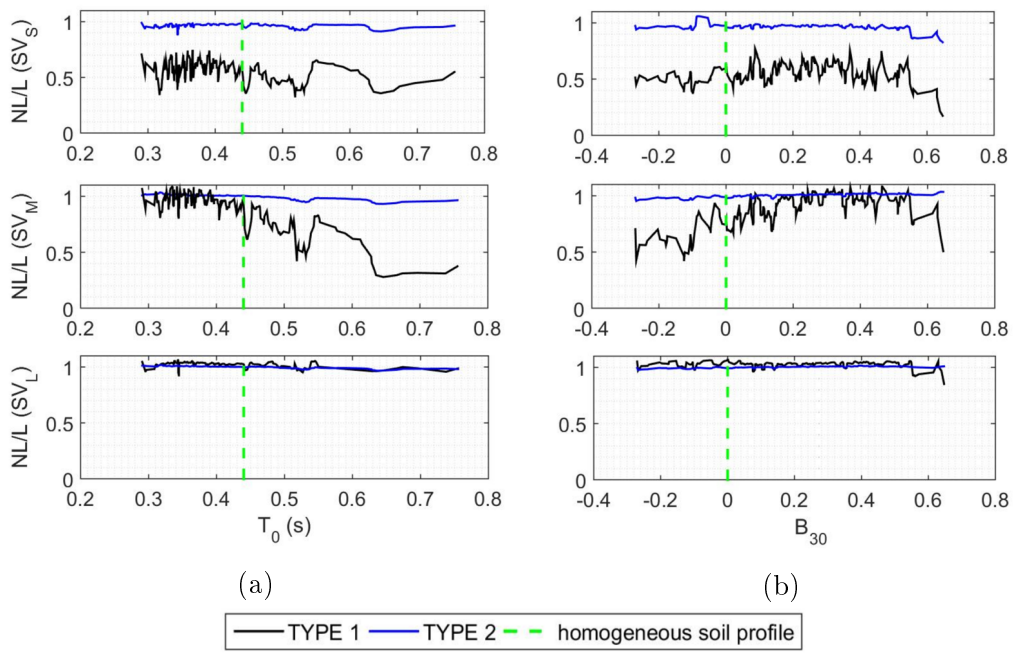

Figure 6.10: Computed ratio of spectral velocity factors SV_S, SV_M and SV_L (short, intermediate and long periods of vibration) for nonlinear soil behavior to that for linear soil behavior (NL/L) as a function of the dominant period of the site T_0 (a) and the shear wave velocity gradient B_{30} (b), for the whole set of generated soil profiles. The curves are distinguished between those for small earthquakes (associated to the type 2 response spectrum of Eurocode 8) and strong earthquakes (type 1 response spectrum)

Fig. 6.10 illustrates the average amplification factor as a function of the site dominant period T_0 (Fig. 6.10a) and shear wave velocity gradient B_{30} (Fig. 6.10b). Results are distinguished for weak earthquakes (associated to the type 2 response spectrum of Eurocode 8 (Eurocode, 2005)) and for strong earthquakes (type 1 response spectrum). As expected, the effect of nonlinear soil behavior is negligible for small earthquakes (type 2 response spectrum of Eurocode 8 (Eurocode, 2005)) for the whole range of periods of vibration. In fact, the NL/L ratio is close to one. In the case of stronger earthquakes (type 1 response spectrum), the modification in the site response depends on the stratigraphy and varies with the vibration period of the FF motion. According to Fig. 6.10, for vibration periods of the strong motion over 1s, the effect of nonlinear soil behavior is negligible (see SV_L). On the contrary, in the range of short periods (see SV_S), the amplitude reduction due to nonlinear effects is up to 60%. Moreover, the amplification factor in the range of middle periods (see SV_M) shows a remarkable amplitude reduction for a site predominant period T_0 higher than $0.44s$ (period of vibration of the homogeneous soil profile)

and a reduction up to 10% for lower values of T_0 (Fig. 6.10a). An important amplitude reduction is obtained for a shear wave velocity gradient B_{30} outside the range $[0-0.5]$, that correspond to soil profiles with significant impedance contrast (high B_{30}) and velocity inversions (negative B_{30}).

6.2.3 Comparison with building codes

Fig. 6.11 displays the comparison of the average pseudo-acceleration response spectrum normalized with respect to the peak acceleration of the outcropping motion, using a damping ratio of 5%.

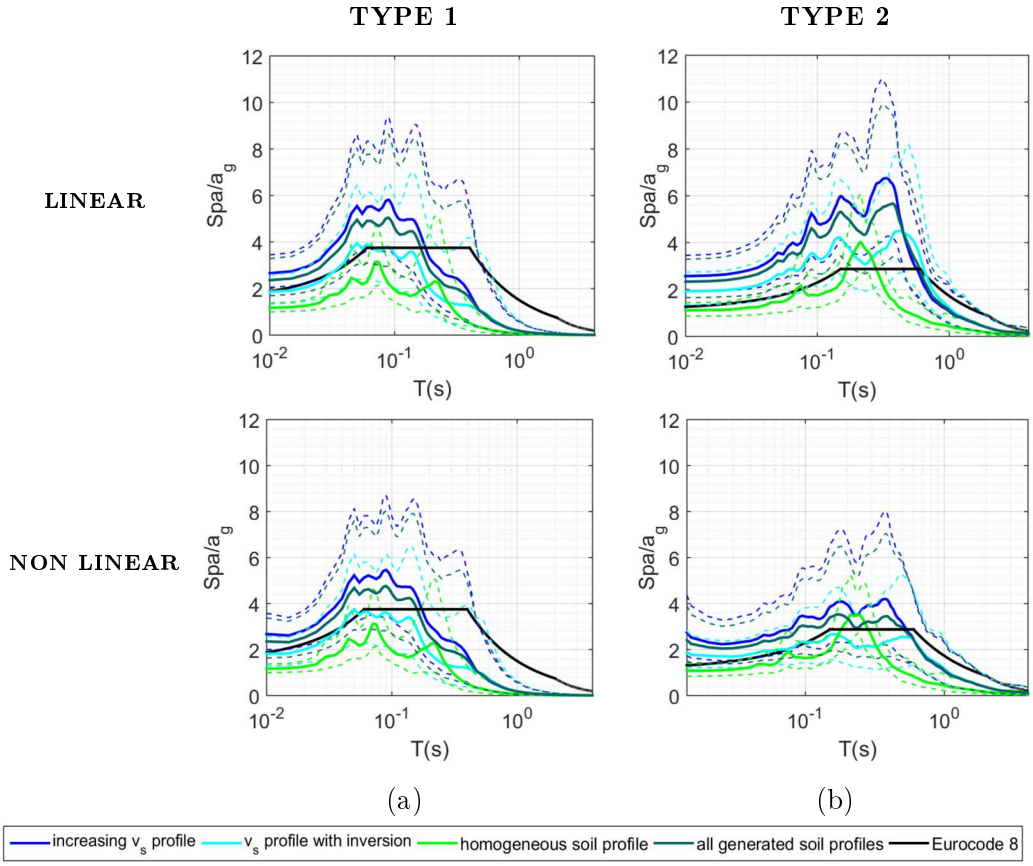

Figure 6.11: Mean (solid line) acceleration response spectra (damping ratio of 5%) and mean plus/minus one standard deviation (dashed line), evaluated for the free-field motion of the generated multilayered soil profiles, compared to the homogeneous case and the elastic response spectrum proposed by Eurocode 8 (Eurocode, 2005). The cases are distinguished as follows: assumption of linear and nonlinear soil behavior; weak earthquakes (a) and strong earthquakes (b)

The linear and nonlinear computations are separated and, for both, the cases of weak earthquakes (associated to the type 2 response spectrum of the Eurocode 8 (Eurocode, 2005)) and strong earthquakes (type 1 response spectrum) are distinguished. In each of these combinations, the average pseudo-acceleration response spectra are estimated for the FF motion in the case of increasing shear wave velocity and for profiles with a velocity inversion. The elastic response spectra proposed by Eurocode 8 is conservative, compared to the obtained average response spectra, for higher periods (higher than $0.2s$ for type 2 and $0.6s$ for type 1). Conversely, for lower periods, the average response spectrum, obtained for all the generated soil profiles, gives higher acceleration peaks. If the elastic response spectrum proposed by Eurocode 8 (Eurocode, 2005) is compared to average soil properties for the spectrum in the homogeneous case, it is conservative for all period ranges for weak earthquakes (type 2) and in most cases for strong earthquakes (type 1). The reduction of the site response for the nonlinear soil behavior is negligible for weak earthquakes (type 2) and significant for strong earthquakes (type 1).

Following the approach adopted by Ciancimino et al. (2018) for the linear regime, the site amplification factors are evaluated for the samples of the present statistical analysis, in the case of linear and nonlinear soil behavior. The computed amplification factors are compared with those suggested by Eurocode 8 (Eurocode, 2005) and New Zealand Standard (NZS, 2004) building codes, with those proposed by Pitilakis et al. (2013) and with those obtained by Ciancimino et al. (2018). The ground type classification used in the Eurocode 8 (Eurocode, 2005) is only based on the $v_{s,30}$ parameter. In the New Zealand Standard (NZS, 2004), the fundamental site period is included as a proxy of site effects. In addition, Pitilakis et al. (2013) classify the ground type using the fundamental period of the site, the depth of the seismic bedrock and the average soil column shear wave velocity. The 300 generated soil profiles are identified as ground type C according to Eurocode 8 (Eurocode, 2005) and as C2 according to Pitilakis et al. (2013). Among them, 286 are identified as ground type C according to the New Zealand Standard (NZS, 2004) building codes ($T_0 > 0.6s$).

The comparison between the mean value of site amplification factors S_s (Eq. 6.4) and SA (Eq. 6.5), and the values within one standard deviation of the mean are represented in Fig. 6.12 for weak earthquakes and in Fig. 6.13 for strong earthquakes. These values are compared to those obtained according to the building codes to analyze their reliability. The coefficient of variation CV of S_s and SA is also calculated. In each figure, the simulations under the assumption of linear and nonlinear soil behavior are separated. The

amplification factors are estimated, for both soil behaviors, using only the FF motions of multilayered soil profiles with increasing shear wave velocity with depth, only the FF motions of soil profiles with a velocity inversion, the FF motions of all the generated soil profiles and the FF motion of the homogeneous soil profile.

The numerical results obtained under the assumption of linear soil behavior are also compared to those obtained by Ciancimino et al. (2018), performing analyses on a database of seismic responses of one-dimensional soil profiles having equivalent linear behavior. We can observe that our results under the assumption of linear behavior are in good agreement with those obtained by Ciancimino et al. (2018). According to Figs. 6.12 and 6.13, only the amplification factors obtained for the case of homogeneous soil profiles are smaller than those suggested by Eurocode 8 (Eurocode, 2005) and the same consideration is made comparing with the New Zealand Standard (NZS, 2004) building codes (Fig. 6.14). It is interesting to note that the values proposed by Pitilakis et al. (2013) for the site amplification factor SA are close to those computed using the set of generated samples in the present analysis. Conversely, the values proposed by Pitilakis et al. (2013) for the site amplification factor S_s are lower than those obtained in the present research. This means that ground classification based on complementary site proxies instead on a single proxy is more adequate. But also it is important to understand the best complementary proxies that allow predicting the site response for different ranges of periods. Moreover, the nonlinear effects are negligible in terms of mean values and CV of the amplification factors, for weak earthquakes (Fig. 6.12) and they are significant for strong earthquakes (Fig. 6.13). The average amplification factors obtained for soil profiles with a velocity inversion are lower than the ones associated to other soil profiles. Lastly, Fig. 6.14 shows that the comparison between the computed amplification factors and those deduced by New Zealand Standard (NZS, 2004). The difference observed could be justified by a higher seismicity expected in New Zealand that could increase the effect of nonlinear soil behavior and thus reduce the peak acceleration.

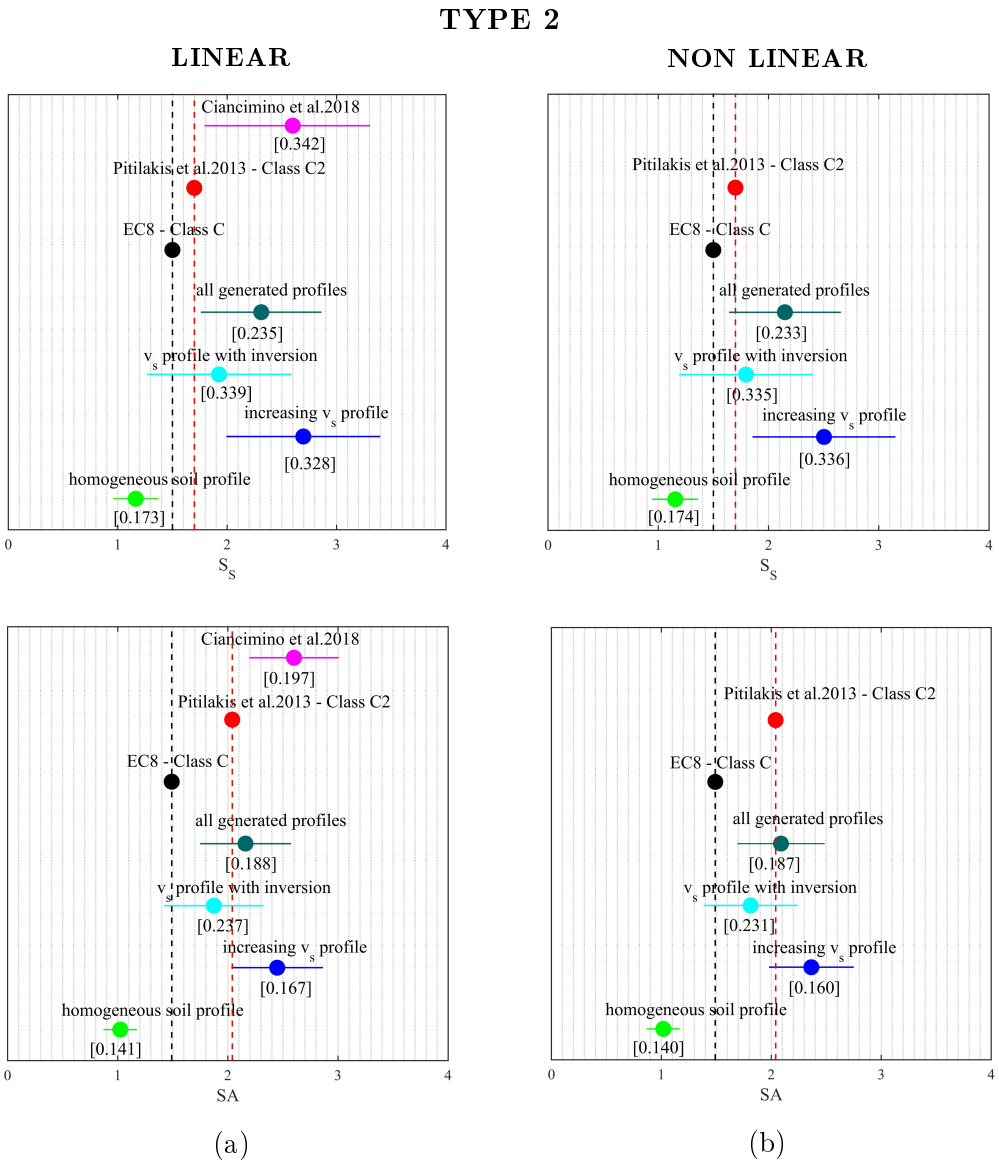

Figure 6.12: Mean value of site amplification factors S_s (top) and SA (bottom), the values within one standard deviation of the mean and the coefficient of variation CV (value between brackets) in the case of small earthquakes (type 2 response spectrum of Eurocode 8 (Eurocode, 2005)), for numerical simulations under the assumption of linear (a) and nonlinear (b) soil behavior. The values suggested by Eurocode 8 (Eurocode, 2005), Pitilakis et al. (2013) and Ciancimino et al. (2018) are indicated

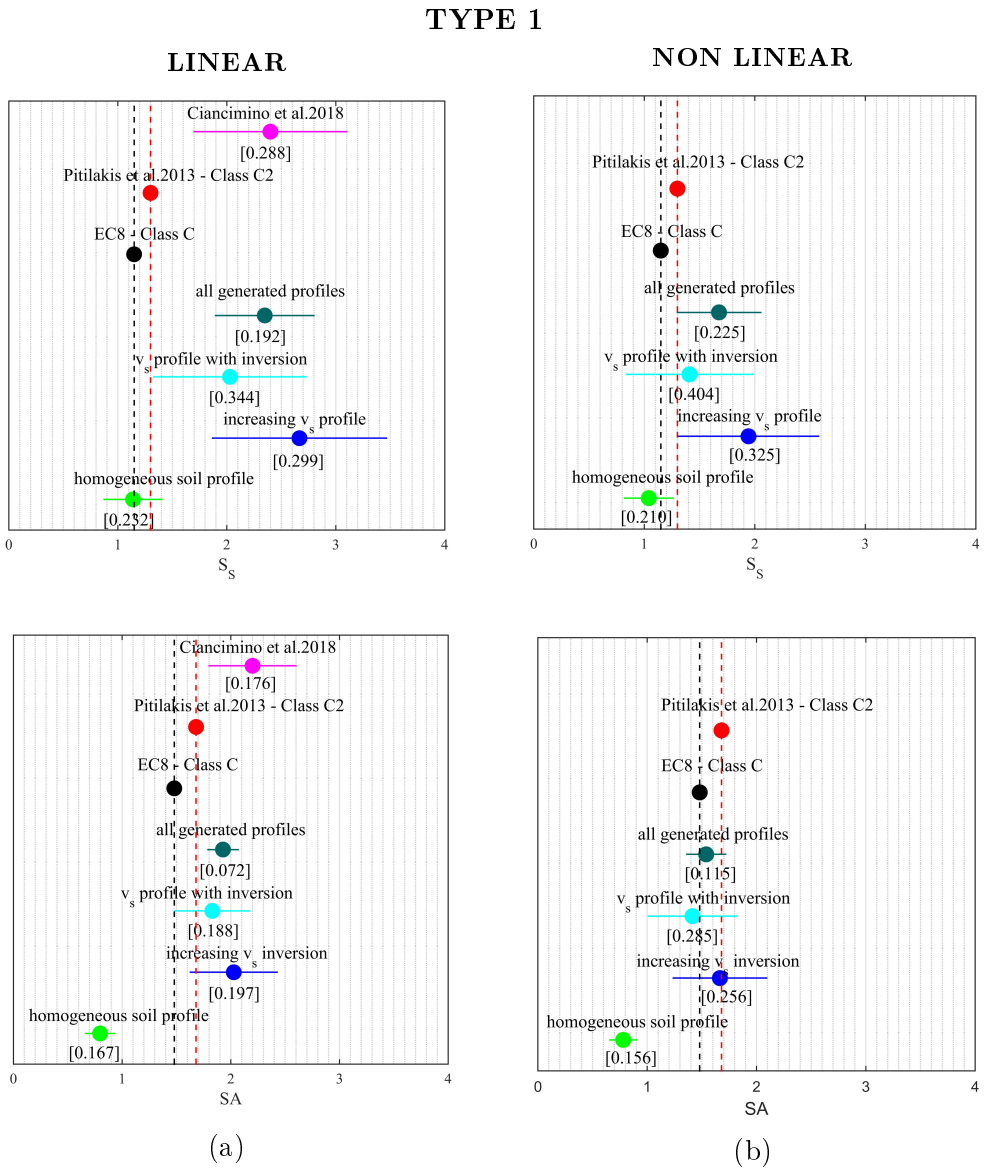

Figure 6.13: Mean value of site amplification factors S_s (top) and SA (bottom), the values within one standard deviation of the mean and the coefficient of variation CV (value between brackets) in the case of small earthquakes (type 1 response spectrum of Eurocode 8 (Eurocode, 2005)), for numerical simulations under the assumption of linear (a) and nonlinear (b) soil behavior. The values suggested by Eurocode 8 (Eurocode, 2005), Pitilakis et al. (2013) and Ciancimino et al. (2018) are indicated

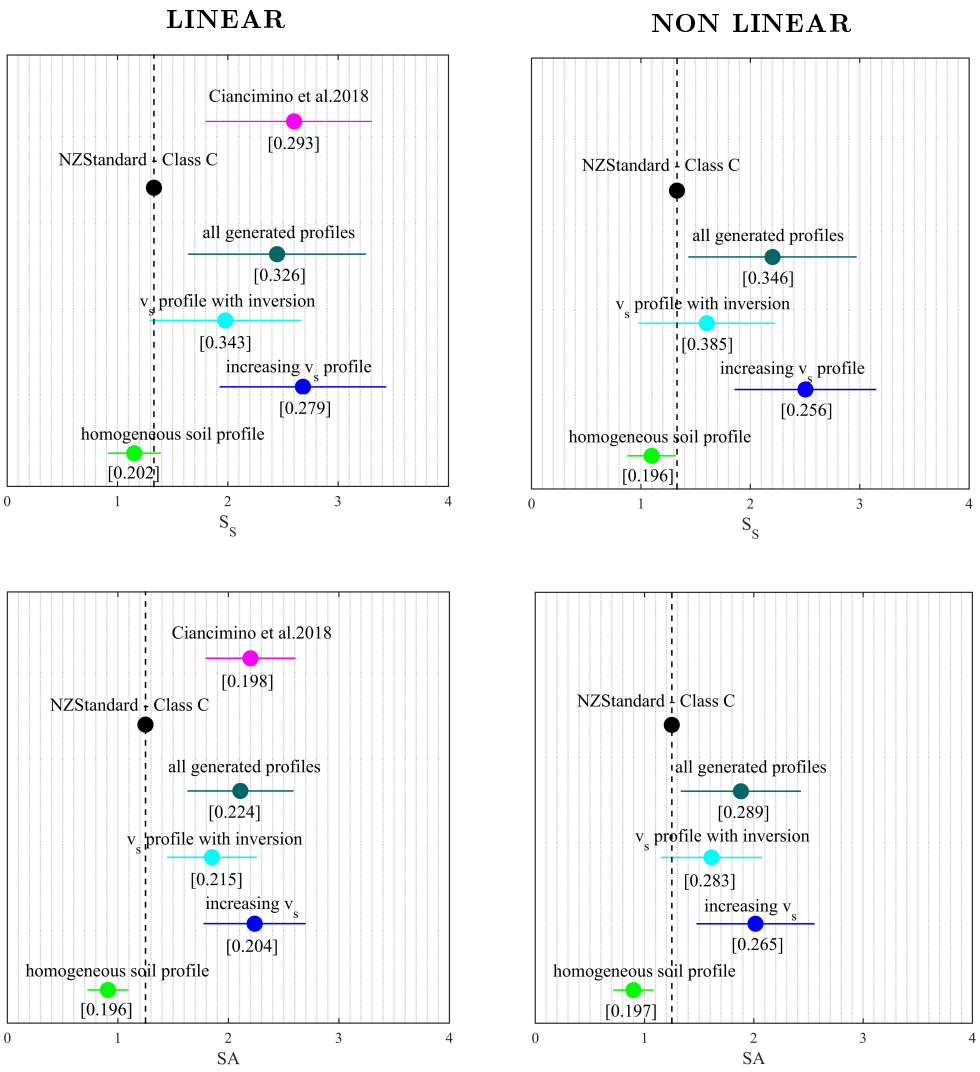

(a) (b)

Figure 6.14: Mean value of site amplification factors S_s (top) and SA (bottom), the values within one standard deviation of the mean and the coefficient of variation CV (value between brackets) for the whole set of recorded seismic signals. Numerical simulations under the assumption of linear (a) and nonlinear (b) soil behavior are separated. The values suggested by the New Zealand Standard (NZS, 2004) building codes are indicated

6.3 Conclusions

The vertical propagation of various recorded seismic signals along stochastically generated soil profiles is numerically simulated to obtain the FF motion,

in both cases of linear and nonlinear soil behavior. The average shear wave velocity in the upper $30m$ of soil profiles $v_{s,30}$ is fixed and corresponds to the ground type C, according to the Eurocode 8. The soil-bedrock interface depth is selected as $H_{800} = 30m$.

Two site proxies, complementary to $v_{s,30}$, are proposd such as the dominant frequency of the site f_0 and the shear wave velocity gradient B_{30}. The site response is represented in terms of site amplification factors, deduced using the response spectrum of the FF motion, for the 24000 performed simulations (set of 40 recorded seismic signals applied to 300 generated soil profiles, for linear and nonlinear soil behaviors). The influence on site amplification of the shear wave velocity profile, site dominant frequency and shear wave velocity gradient are analyzed independently from H_{800}.

The obtained amplification factors are functions of both site conditions and intensity of rock motions and the values could decrease due to soil nonlinearity. The amplification factors increase with decreasing site dominant period T_0 and increasing shear wave velocity gradient B_{30}, when they are evaluated over a wide period $[0.05 - 2.5s]$. Nevertheless, site amplification appears strongly dependent on the site predominant period T_0, for short vibration periods of the FF motion and independent from it for long periods. Moreover, site amplification is much more pronounced in soil profiles having T_0 lower than that of the homogeneous profile, for short vibration periods of the FF motion. The largest values of amplification factors are reached for short vibration periods of the FF motion, lower than $0.5s$, in soil profiles having a high shear wave velocity gradient B_{30}, which corresponds to sites with a large impedance contrast in the first 30m or with a steep slope in the shear wave velocity profiles.

The site response is modified when the nonlinear soil behavior is taken into account in the numerical simulations. The nonlinear soil behavior on the site response induces a reduced amplification effect. Similarly to the case of linear soil behavior, the site amplification is more pronounced in the case of short vibration periods of the FF motion and it is strongly dependent on the proposed site parameters. On the contrary, the site amplification is less pronounced and independent from the proposed site parameters, for vibration periods of the FF motion higher than $1s$. Nonlinear effects are negligible for small earthquakes and for vibration periods of strong ground motions longer than $1s$. Whereas, they are significant for short- and middle-periods of strong earthquakes. In particular, soil profiles having dominant period T_0 higher than that of the homogeneous profile exhibit significant nonlinear effects. In

addition, soil profiles with negative value of B_{30} (i.e. velocity inversion) and profiles with high value of B_{30} lead to pronounced nonlinear site effects.

In the last part of the chapter, average amplification factors are compared to those suggested by Eurocode 8 (Eurocode, 2005) and New Zealand Standard (NZS, 2004) building codes, and by Pitilakis et al. (2013). The obtained results demonstrate that the ground type classification proposed by Eurocode 8 (Eurocode, 2005), based on $v_{s,30}$ only, is not suitable. The comparison to the amplification factors proposed by Pitilakis et al. (2013) shows that the introduction of complementary site proxies makes the ground type classification more adequate. In fact, the computed average spectral amplification factors SA are comparable to those estimated by Pitilakis et al. (2013). The average amplification factors computed for soil profiles with a velocity inversion are lower than for the profiles having monotonic shear wave velocity profiles.

Further work should be done to simulating seismic site response in layered saturated level liquefiable soil profiles based on the the results of laboratory tests, to compare the predictive capabilities of advanced soil constitutive capturing the seismic response in terms of settlements, accelerations, and excess pore pressures under 1D horizontal earthquake shaking.

Chapter 7
Conclusions

Seismic soil site response strongly depend on variability of soil properties, stratigraphy, surface topography, impedance contrast and rheology of the soils involved during the propagation of seismic waves. Site characterization include measurements related to dynamic response characteristics of the soil and the liquefaction resistance of various deposits and thus, it is an essential aspect of geotechnical earthquake engineering to predict the non-linear soil behavior under seismic loading conditions. To this regard, laboratory tests are essential to improve the knowledge of the liquefaction phenomena in terms of their induced effects because they underpin the ongoing development, calibration, and validation of advancend constitutive models for liquefaction predction.

In this thesis, a testing campaign is carried out on fines-sand mixtures using clean HN31 Hostun sand and different fine percentages, remaining in the range of sand dominant behavior, with the aim of showing the influence of the main factors affecting liquefaction on the undrained behavior of silty sand via experimental and numerical analyses. In particular, the experimental response of each silty sand mixture is obtained for monotonic and cyclic triaxial tests and resonant column tests using a standardized experimental protocol. Effects of the characteristics of the mixture (relative density and fine content) and depth (confining pressure) are observed analyzing the results of laboratory tests.
The experimenal database is then used to calibrate the 3D Iwan-Iai constitutive model to capture the cyclic behavior of the tested soils under undained conditions and evaluate the variabiliy of the numerical liquefaction parameters on the seismic response of a layered saturated level liquefiable soil deposit under 1D horizontal earthquake shaking.
Lastly, a stochastic analysis is performed to further investigate the effect of soil parameters variability on the seismic site response of layered soil profiles for weak and strong events.

Findings presented in this work highlight the need to improve research on liquefaction related phenomena, both theoretical and experimental, to advance the state of the art and practice, and to improve current empirical

and advanced methods used for liquefaction assessment by more and better data, by standardized laboratory tests and by quantification of uncertainties.

7.1 General Conclusions

The conclusions drawn from this study and recommendations with respect to implementing these findings into engineering practice are summarized below.

- Based on our experimental results, fine particles significantly affect the mixture packing configuration of coarse and fine particles and play a major role in the mechanical behavior of sandy soils. It is concluded that fine content affects significantly the liquefaction resistance and the addition of fine particles implies a more contracting behavior of silty sand mixtures, in undrained conditions. In particular, it is observed that fine content and relative density can significantly affect the excess pore pressure build-up and the liquefaction resistance of silty sand mixtures.

  When the dependency of steady state line, cyclic liquefaction resistance and shear modulus on the global void ratio is analyzed, the present experimental results confirm a strong variability with respect to the fine content. Whereas, when the equivalent intergranular void ratio is adopted as key parameter to characterize the silty sand mixtures, a single correlation curve, independent of fine content, is found to represent the mean effective stress at the steady state, cyclic liquefaction resistance and shear modulus. It means that data obtained for clean sand are reliable for predicting the behavior of mixtures independently of the fine content.

  The adopted equivalent intergranular void ratio is function of the fine content and the active fine fraction b. An original formula is proposed to estimate the active fine fraction b, based on the mixture packing configuration (fine content, global void ratio of the mixture after consolidation, maximum and minimum void ratios). The reliability of this proposed formula is validated through our experimental program and seven experimental databases reported in the literature for non-plastic fines. The validation of the proposed expression of the active fine fraction b confirms its dependency on the fine content and the state of the mixture.

- The parameters of the 3D Iwan-Iai constitutive model, including the liquefaction front approach, are calibrated with the set of laboratory

tests carried out on the 18 silty sand mixtures. It is demonstrated that the 3D Iwan-Iai model is able to simulate the onset of liquefaction in both cases of cyclic mobility and cyclic liquefaction and the influence of relative density, confining pressure and fine content on the calibration process is investigated.
It is observed that liquefaction front parameters p_2 and w_1, which control the evolution of the pore water pressure and strain, are strongly dependent on relative density, fine content and confining pressure and that the fine content cannot be the only factor to characterize silty sand mixtures, but the relative density also has an important effect in the mixture behavior (as already noted from experimental results).

- The 1D seismic response of soil profiles with a liquefiable layer is numerically simulated using the liquefaction parameters obtained for the 18 soil samples and the coupling effect of relative density and fine content is confirmed from the simulation of nonlinear 1D wave propagation.
  Moreover, the experimental and numerical results highlight the importance of the variation of liquefaction parameters with depth. In numerical simulations, it is observed that the use of numerical parameters calibrated using soil samples taken at a lower depth or by means of laboratory tests on reconstituted samples at lower confining pressures, may lead to an important overestimation of the liquefaction resistance of the soil layer, independently of its relative density.

- In the last chapter, an important aspect of the soil characterization is pointed out: the influence of the layering uncertainty on the site response for weak and strong motions under linear and non-linear behavior. It is demonstrated that the average shear wave velocity $v_{s,30}$ is not able, as single proxy, to characterize the soil profiles in terms of expected amplification level over the whole frequency range of interest in engineering practice. To this regard, two site parameters are proposed as proxies, complementary to $v_{s,30}$, the dominant frequency of the site f_0 and the shear wave velocity gradient B_{30}.
  The site response is represented in terms of site amplification factors, deduced using the response spectrum of the FF motion, for the 24000 performed simulations (set of 40 recorded seismic signals applied to 300 generated soil profiles, for linear and nonlinear soil behaviors). It is found that amplification factors increase with decreasing site dominant period T_0 and increasing shear wave velocity gradient B_{30}, when they are evaluated over a wide range of vibration periods [0.05 - 2.5 s], while site amplification appears strongly dependent on T_0 for short vibration periods.

The site response is reduced when the nonlinear soil behavior is taken into account in the numerical simulations. Nonlinear effects are negligible for small earthquakes and for vibration periods of strong ground motions longer than 1 s. Whereas, they are significant for short- and middle-periods of strong earthquakes.
Lastly, average amplification factors are compared to those suggested by Eurocode 8 (Eurocode, 2005) and New Zealand Standard (NZS, 2004) building codes, and by Pitilakis et al. (2013). The obtained results demonstrate that the ground type classification proposed by Eurocode 8 (Eurocode, 2005), based on $v_{s,30}$ only, is not suitable, while the introduction of complementary site proxies makes the ground type classification more adequate.
This statistical study confirms that it is possible to improve the current ground type classification taking into account simple and accessible site parameters complementary to $v_{s,30}$, allowing a better prediction of the expected amplification, in particular for short vibration up to 1s.

7.2 Further research

- The results of this work are referred to fines-sand mixtures remaining in the range of sand dominant behavior. Therefore, further research is required for non-plastic fines and fine content higher than the threshold, in the fines dominant behavior, in order to determine the effect of particle characteristics (e.g. size and shape of fine particles) on the mechanical behavior of granular materials.

- Furthermore, the program of this research examines the effect of non-plastic fines on the liquefaction resistance of mixtures, thus the effects of plasticity on the estimation of the active fine fraction also need to be assessed.

- Additional research should be undertaken with the objective of comparing laboratory sample behavior with data obtained from different devices such as direct simple shear testing or hollow cylinder testing to further investigate the influence of mode of shear on the cyclic liquefaction resistance.

- The findings of this work show that relevant laboratory tests can provide high-quality databases and can help to improve prediction models for conditions not adequately constrained by case history data. Hence, strict protocols for laboratory tests need to be standardized and followed to

ensure consistency of quality of the databases and comparisons of results related to them. Moreover, field case histories need to be complemented with laboratory test data, particularly for overburden pressures and fine content, in order to better characterize the depth dependent distribution and properties of soil profile, and thus develop more reliable methods for liquefaction assessment and overcome current limitations in their predictive capabilities.

- Liquefaction phenomena are associated to large deformations and potential instabilities, due to particle rearrangement and reconsolidation. These mechanisms should be further investigated through discrete element method (DEM), which could be a promising tool for modeling contact mechanisms at the grain level.

- Further study should be done to simulating seismic site response in layered saturated level liquefiable soil profiles based on the the results of laboratory tests, to compare the predictive capabilities of advanced soil constitutive capturing the seismic response in terms of settlements, accelerations, and excess pore pressures under 1D and 2D assumptions.

Bibliography

Alarcon-Guzman, A., Leonards, G., and Chameau, J. (1988). Undrained monotonic and cyclic strength of sands. *Journal of Geotechnical Engineering*, 114(10):1089–1109.

Allen, J., Bradley, B., Green, R., Orense, R., Wotherspoon, L., Ashford, S., Cox, B., Hutchinson, T., Pender, M., Bowman, E., et al. (2010). Geotechnical reconnaissance of the 2010 darfield (canterbury) earthquake. *Bulletin of the New Zealand Society for Earthquake Engineering*, 43(4):243.

Ambraseys, N., Smit, P., Douglas, J., Margaris, B., Sigbjörnsson, R., Olafsson, S., Suhadolc, P., and Costa, G. (2004). Internet site for european strong-motion data. *Bollettino di geofisica teorica ed applicata*, 45(3):113–129.

Amini, F. and Qi, G. (2000). Liquefaction testing of stratified silty sands. *Journal of geotechnical and geoenvironmental engineering*, 126(3):208–217.

Arulanandan, K., Manzari, M., Zeng, X., Fagan, M., Scott, R., and Tan, T. (1995). Significance of the velacs project to the solution of boundary value problems in geotechnical engineering.

Askari, F., Dabiri, R., Shafiee, A., and Jafari, M. (2010). Effects of non-plastic fines content on cyclic resistance and post liquefaction of sand-silt mixtures based on shear wave velocity.

Athanasopoulos, G. and Richart Jr, F. (1983). Correlation between g_0 and τ max for kaolinite clay. *Journal of Geotechnical Engineering*, 109(5):719–723.

Barnett, N., Rahman, M. M., Karim, M. R., Nguyen, H. K., and Carraro, J. A. H. (2020). Equivalent state theory for mixtures of sand with non-plastic fines: A dem investigation. *Géotechnique*, pages 1–18.

Bedin, J., Schnaid, F., Da Fonseca, A., and Costa Filho, L. D. M. (2012). Gold tailings liquefaction under critical state soil mechanics. *Géotechnique*, 62(3):263–267.

Been, K. and Jefferies, M. G. (1985). A state parameter for sands. *Géotechnique*, 35(2):99–112.

Belkhatir, M., Arab, A., Della, N., Missoum, H., and Schanz, T. (2010a). Influence of inter-granular void ratio on monotonic and cyclic undrained shear response of sandy soils. *Comptes Rendus Mecanique*, 338(5):290–303.

Belkhatir, M., Arab, A., Della, N., Missoum, H., and Schanz, T. (2010b). Liquefaction resistance of chlef river silty sand: effect of low plastic fines and other parameters. *Acta Polytechnica Hungarica*, 7(2):119–137.

Belkhatir, M., Arab, A., Schanz, T., Missoum, H., and Della, N. (2011). Laboratory study on the liquefaction resistance of sand-silt mixtures: effect of grading characteristics. *Granular Matter*, 13(5):599–609.

Benahmed, N. (2001). *Comportement mécanique d'un sable sous cisaillement monotone et cyclique: application aux phénomènes de liquéfaction et mobilité cyclique*. PhD thesis, Marne-la-vallée, ENPC.

Benahmed, N., Nguyen, T. K., Hicher, P. Y., and Nicolas, M. (2015). An experimental investigation into the effects of low plastic fines content on the behaviour of sand/silt mixtures. *European Journal of environmental and civil engineering*, 19(1):109–128.

Bishop, A. and Wesley, L. (1975). A hydraulic triaxial apparatus for controlled stress path testing. *Geotechnique*, 25(4):657–670.

Bobei, D. and Lo, S. (2005). Reverse behaviour and critical state of sand with small amount of fines. In *Proceedings of the international conference on soil mechanics and geotechnical engineering*, volume 16, page 475. AA Balkema publishers.

Bolton Seed, H., Tokimatsu, K., Harder, L., and Chung, R. M. (1985). Influence of spt procedures in soil liquefaction resistance evaluations. *Journal of Geotechnical Engineering*, 111(12):1425–1445.

Borcherdt, R. D. (1994). Estimates of site-dependent response spectra for design (methodology and justification). *Earthquake spectra*, 10(4):617–653.

Boulanger, R. and Idriss, I. (2004). State normalization of penetration resistance and the effect of overburden stress on liquefaction resistance. In *Proc., 11th International Conference on Soil Dynamics and Earthquake Engineering, and 3rd International Conference on Earthquake Geotechnical Engineering, D. Doolin et al., eds., Stallion Press*, volume 2, pages 484–491.

Boulanger, R. and Ziotopoulou, K. (2015). Pm4sand (version 3): A sand plasticity model for earthquake engineering applications. *Center for Geotechnical Modeling Report No. UCD/CGM-15/01, Department of Civil and Environmental Engineering, University of California, Davis, Calif.*

Boulanger, R. W. (2003). High overburden stress effects in liquefaction analyses. *Journal of geotechnical and geoenvironmental engineering*, 129(12):1071–1082.

Bray, J. D., Sancio, R. B., Riemer, M., and Durgunoglu, T. (2004). Liquefaction susceptibility of fine-grained soils. In *Proc., 11th Int. Conf. on Soil Dynamics and Earthquake Engineering and 3rd Int. Conf. on Earthquake Geotechnical Engineering*, volume 1, pages 655–662. Stallion Press, Singapore.

Brûlé, S. and Javelaud, E. (2014). H/v method in geotechnical engineering. application to a two layers model. *Revue Française de Géotechnique*, (142).

Bui, M. T. (2009). *Influence of some particle characteristics on the small strain response of granular materials*. PhD thesis, University of Southampton.

Byrne, P. M., Park, S.-S., Beaty, M., Sharp, M., Gonzalez, L., and Abdoun, T. (2004). Numerical modeling of liquefaction and comparison with centrifuge tests. *Canadian Geotechnical Journal*, 41(2):193–211.

Cadet, H., Bard, P. Y., and Duval, A. M. (2008). A new proposal for site classification based on ambient vibration measurements and the kiknet strong motion data set. In *Proceedings of the 14th World Conference on Earthquake Engineering*, pages 12–17.

Cameron, W. I. and Green, R. A. (2004). Soil nonlinearity versus frequency effects. In *International Workshop on the Uncertainties in Nonlinear Soil Properties and their Impact on Modeling Dynamic Response*.

Canou, J. (1989). Contribution a l'etude et a l'evaluation des proprietes de liquefaction d'un sable. *Ph. D. Thesis, ENPC*.

Cao, Y. and Law, K. (1991). Energy approach for liquefaction of sandy and clayey silts.

Carraro, J., Bandini, P., and Salgado, R. (2005). Liquefaction resistance of clean and silty sands from cone penetration resistance. In *Earthquake Engineering and Soil Dynamics*, pages 1–15.

Carraro, J. A. H., Prezzi, M., and Salgado, R. (2009). Shear strength and stiffness of sands containing plastic or nonplastic fines. *Journal of geotechnical and geoenvironmental engineering*, 135(9):1167–1178.

Carrera, A., Coop, M., and Lancellotta, R. (2011). Influence of grading on the mechanical behaviour of stava tailings. *Géotechnique*, 61(11):935–946.

Casagrande, A. (1936). Characteristics of cohesionless soils affecting the stability of slopes and earth fills. *J. Boston Society of Civil Engineers*, 23(1):13–32.

Casagrande, A. (1975). Liquefaction and cyclic deformation of sands. In *A Critical Review, Lecture at 5th Panamerican Conference on Soil Mechanics and Foundation Engineering, Buenos Aires*, volume 5, pages 80–133.

Castellaro, S. and Mulargia, F. (2014). Simplified seismic soil classification: the vfz matrix. *Bulletin of earthquake engineering*, 12(2):735–754.

Castellaro, S., Mulargia, F., and Rossi, P. L. (2008). Vs30: Proxy for seismic amplification? *seismological research letters*, 79(4):540–543.

Castelli, F., Cavallaro, A., Grasso, S., and Lentini, V. (2016). Seismic microzoning from synthetic ground motion earthquake scenarios parameters: the case study of the city of catania (italy). *Soil Dynamics and Earthquake Engineering*, 88:307–327.

Castro, G. (1969). Liquefaction of sands. *ph. D. Thesis, Harvard Soil Mech.*

Cetin, K. O., Seed, R. B., Der Kiureghian, A., Tokimatsu, K., Harder Jr, L. F., Kayen, R. E., and Moss, R. E. (2004). Standard penetration test-based probabilistic and deterministic assessment of seismic soil liquefaction potential. *Journal of geotechnical and geoenvironmental engineering*, 130(12):1314–1340.

Chang, N., Yeh, S., and Kaufman, L. (1982). Liquefaction potential of clean and silty sands. In *proceedings of the third international earthquake microzonation conference*, volume 2, pages 1017–1032.

Chang, W.-J., Rathje, E. M., Stokoe, K. H., and Hazirbaba, K. (2007). In situ pore-pressure generation behavior of liquefiable sand. *Journal of geotechnical and geoenvironmental engineering*, 133(8):921–931.

Chen, Y.-C. and Lee, C.-G. (1994). Evaluation of liquefaction resistance of sand by maximum shear modulus. *Journal of the Chinese Institute of Engineers*, 17(5):689–699.

Chern, J.-C. (1985). *Undrained response of saturated sands with emphasis on liquefaction and cyclic mobility*. PhD thesis, University of British Columbia.

Chien, L.-K., Oh, Y.-N., and Chang, C.-H. (2002). Effects of fines content on liquefaction strength and dynamic settlement of reclaimed soil. *Canadian Geotechnical Journal*, 39(1):254–265.

Cho, G.-C., Dodds, J., and Santamarina, J. C. (2006). Particle shape effects on packing density, stiffness, and strength: natural and crushed sands. *Journal of geotechnical and geoenvironmental engineering*, 132(5):591–602.

Chu, J., Lo, S.-C., and Lee, I. K. (1993). Instability of granular soils under strain path testing. *Journal of Geotechnical Engineering*, 119(5):874–892.

Ciancimino, A., Foti, S., and Lanzo, G. (2018). Stochastic analysis of seismic ground response for site classification methods verification. *Soil Dynamics and Earthquake Engineering*, 111:169–183.

Cubrinovski, M. and Ishihara, K. (1998). State concept and modified elastoplasticity for sand modelling. *Soils and foundations*, 38(4):213–225.

Cubrinovski, M. and Ishihara, K. (2002). Maximum and minimum void ratio characteristics of sands. *Soils and foundations*, 42(6):65–78.

Cubrinovski, M., Rhodes, A., Ntritsos, N., and Van Ballegooy, S. (2019). System response of liquefiable deposits. *Soil Dynamics and Earthquake Engineering*, 124:212–229.

Cubrinovski, M. and Taylor, M. (2011). Liquefaction map of christchurch based on drive-through reconnaissance after the 22 february 2011 earthquake. *University of Canterbury*.

Dafalias, Y. F. (1986). Bounding surface plasticity. i: Mathematical foundation and hypoplasticity. *Journal of engineering mechanics*, 112(9):966–987.

Dafalias, Y. F. and Manzari, M. T. (2004). Simple plasticity sand model accounting for fabric change effects. *Journal of Engineering mechanics*, 130(6):622–634.

Dang, Q.-H. (2019). *Comportement des sols sous liquéfaction artificielle, amélioration des sols à risques liquéfiables*. PhD thesis, University Paris Est.

Darendeli, M. B. (2001). Development of a new family of normalized modulus reduction and material damping curves.

Dash, H. and Sitharam, T. (2009). Undrained cyclic pore pressure response of sand–silt mixtures: effect of nonplastic fines and other parameters. *Geotechnical and Geological Engineering*, 27(4):501–517.

Dash, H. and Sitharam, T. (2011). Undrained monotonic response of sand–silt mixtures: effect of nonplastic fines. *Geomechanics and Geoengineering: An International Journal*, 6(1):47–58.

Dash, H. and Sitharam, T. (2016). Effect of frequency of cyclic loading on liquefaction and dynamic properties of saturated sand. *International Journal of Geotechnical Engineering*, 10(5):487–492.

De Graft-Johnson, J., Bhatia, H., and Gidigasu, D. (1969). The strength characteristics of residual micaceous soils and their application to stability problems. In *Intl Conf Soil Mech & Fdn Eng Proc*, volume 2.

Derras, B., Bard, P.-Y., and Cotton, F. (2016). Site-condition proxies, ground motion variability, and data-driven gmpes: Insights from the nga-west2 and resorce data sets. *Earthquake spectra*, 32(4):2027–2056.

Derras, B., Bard, P.-Y., and Cotton, F. (2017). of various site-condition proxies in reducing ground-motion aleatory variability and predicting nonlinear site response.

Dezfulian, H. and Marachi, N. (1984). Liquefaction potential of silty sand site.

Dickenson, S. and Seed, R. (1996). Nonlinear dynamic response of soft and deep cohesive soil deposits. In *Proceedings of the international workshop on site response subjected to strong earthquake motions*, volume 2, pages 67–81.

Dobry, R. (1985). Liquefaction of soils during earthquakes, national research council (nrc), committee on earthquake engineering. Technical report, Report No. CETS-EE-001. Washington, DC, USA: National Academy Press.

Dobry, R., Borcherdt, R., Crouse, C., Idriss, I., Joyner, W., Martin, G. R., Power, M., Rinne, E., and Seed, R. (2000). New site coefficients and site classification system used in recent building seismic code provisions. *Earthquake spectra*, 16(1):41–67.

Drnevich, V. (1978). Resonant-column testing-problems and solutions. In *Dynamic geotechnical testing*. ASTM International.

Erten, D. and Maher, M. (1995). Cyclic undrained behavior of silty sand. *Soil Dynamics and Earthquake Engineering*, 14(2):115–123.

Eurocode (2005). Eurocode 8: Design of structures for earthquake resistance-part 1: general rules, seismic actions and rules for buildings. *Brussels: European Committee for Standardization*.

Finn, W., Ledbetter, R., and Wu, G. (1994). Liquefaction in silty soils: design and analysis. In *Ground failures under seismic conditions*, pages 51–76. ASCE.

Fuentes, W. and Triantafyllidis, T. (2015). Isa model: a constitutive model for soils with yield surface in the intergranular strain space. *International Journal for Numerical and Analytical Methods in Geomechanics*, 39(11):1235–1254.

Gallipoli, M. R. and Mucciarelli, M. (2009). Comparison of site classification from vs 30, vs 10, and hvsr in italy. *Bulletin of the Seismological Society of America*, 99(1):340–351.

Goudarzy, M., König, D., and Schanz, T. (2018). Small and intermediate strain properties of sands containing fines. *Soil Dynamics and Earthquake Engineering*, 110:110–120.

Goudarzy, M., Rahman, M. M., König, D., and Schanz, T. (2016). Influence of non-plastic fines content on maximum shear modulus of granular materials. *Soils and Foundations*, 56(6):973–983.

Graton, L. C. and Fraser, H. (1935). Systematic packing of spheres: with particular relation to porosity and permeability. *The Journal of Geology*, 43(8, Part 1):785–909.

Harder Jr, L. F. and Boulanger, R. (1997). Application of k0 and ka correction factors. *Izzat M. Idriss*, page 167.

Hardin, B. O. and Black, W. L. (1966). Sand stiffness under various triaxial stresses. *Journal of Soil Mechanics & Foundations Div*, 92(ASCE# 4712 Proceeding).

Hardin, B. O. and Drnevich, V. P. (1972). Shear modulus and damping in soils: measurement and parameter effects. *Journal of Soil Mechanics & Foundations Div*, 98(sm6).

Hardin, B. O. and Richart Jr, F. (1963). Elastic wave velocities in granular soils. *Journal of Soil Mechanics & Foundations Div*, 89(Proc. Paper 3407).

Hazirbaba, K. and Rathje, E. M. (2004). A comparison between in situ and laboratory measurements of pore water pressure generation. In *Proceedings of the 13th World Conference on Earthquake Engineering, paper*, number 1220.

Héloïse, C., Bard, P.-Y., Duval, A.-M., and Bertrand, E. (2012). Site effect assessment using kik-net data: part 2—site amplification prediction equation based on f 0 and vsz. *Bulletin of Earthquake Engineering*, 10(2):451–489.

Housner, G. (1952). Spectrum intensities of strong-motion earthquakes.

Hsiao, D.-H. and Phan, V. T.-A. (2016). Evaluation of static and dynamic properties of sand–fines mixtures through the state and equivalent state parameters. *Soil Dynamics and Earthquake Engineering*, 84:134–144.

Huang, A.-B. and Chuang, S.-Y. (2011). Correlating cyclic strength with fines contents through state parameters. *Soils and foundations*, 51(6):991–1001.

Huang, Y. and Yu, M. (2013). Review of soil liquefaction characteristics during major earthquakes of the twenty-first century. *Natural hazards*, 65(3):2375–2384.

Huang, Y.-T., Huang, A.-B., Kuo, Y.-C., and Tsai, M.-D. (2004). A laboratory study on the undrained strength of a silty sand from central western taiwan. *Soil Dynamics and Earthquake Engineering*, 24(9-10):733–743.

Hughes, T. J. (1987). *The finite element method: linear static and dynamic finite element analysis*. Prentice Hall. New Jersey.

Hynes, M. E., Olsen, R. S., and Yule, D. (1998). The influence of confining stress on liquefaction resistance. *NIST SPECIAL PUBLICATION SP*, pages 167–184.

Hyodo, M., Nakata, Y., Yoshimoto, N., Kuwajima, K., Kato, Y., et al. (2002). Effect of fines and crushability on liquefaction of volcanic soil 'shirasu'. In *The Twelfth International Offshore and Polar Engineering Conference*. International Society of Offshore and Polar Engineers.

Iai, S., Matsunaga, Y., and Kameoka, T. (1990a). Parameter identification for a cyclic mobility model. *Report of the Port and harbour Research Institute*, 29(4):57–83.

Iai, S., Matsunaga, Y., and Kameoka, T. (1990b). Strain space plasticity model for cyclic mobility. *Report of the Port and harbour Research Institute*, 29(4).

Igwe, O., Fukuoka, H., and Sassa, K. (2012). The effect of relative density and confining stress on shear properties of sands with varying grading. *Geotechnical and Geological Engineering*, 30(5):1207–1229.

Ishihara, K. (1985). Stability of natural deposits during earthquakes. In *11th International Conference on Soil Mechanics and Foundation Engineering*, volume 2, page 321–376.

Ishihara, K. (1993). Liquefaction and flow failure during earthquakes. *Geotechnique*, 43(3):351–451.

Ishihara, K. (1996). Soil behaviour in earthquake geotechnics.

Ishihara, K., Araki, K., and Bradley, B. (2011). Characteristics of liquefaction induced damage in the 2011 great east japan earthquake.

Ishihara, K. and Koga, Y. (1981). Case studies of liquefaction in the 1964 niigata earthquake. *Soils and foundations*, 21(3):35–52.

Ishihara, K., Tatsuoka, F., and Yasuda, S. (1975). Undrained deformation and liquefaction of sand under cyclic stresses. *Soils and foundations*, 15(1):29–44.

Iwan, W. D. (1967). On a class of models for the yielding behavior of continuous and composite systems.

Iwasaki, T. (1986). Soil liquefaction studies in japan: state-of-the-art. *Soil Dynamics and Earthquake Engineering*, 5(1):2–68.

Iwasaki, T. and Tatsuoka, F. (1977). Effects of grain size and grading on dynamic shear moduli of sands. *Soils and foundations*, 17(3):19–35.

Iwasaki, T., Tatsuoka, F., and Takagi, Y. (1978). Shear moduli of sands under cyclic torsional shear loading. *Soils and Foundations*, 18(1):39–56.

Jamiolkowski, M., Lancellotta, R., LO PRESTI, D. C., and Pallara, O. (1995). Stiffness of toyoura sand at small and intermediate strain. In *XIII ICSMFE, New Delhi*, volume 1, pages 169–172. Oxford & IBH Publishing Co. PVT. LTD.

JGS-0111-2009 (2009). Laboratory testing standards of geomaterials: tests for physical properties–test method for density of soil particles. *Tokyo,Japan: The Japanese Geotechnical Society.*

Joyner, W. B. (1975). A method for calculating nonlinear seismic response in two dimensions. *Bulletin of the Seismological Society of America*, 65(5):1337–1357.

Joyner, W. B. and Chen, A. T. (1975). Calculation of nonlinear ground response in earthquakes. *Bulletin of the Seismological Society of America*, 65(5):1315–1336.

Karim, M. E. and Alam, M. J. (2014). Effect of non-plastic silt content on the liquefaction behavior of sand–silt mixture. *Soil Dynamics and Earthquake Engineering*, 65:142–150.

Kawase, H. (2011). Strong motion characteristics and their damage impact to structures during the off pacific coast of tohoku earthquake of march 11, 2011: How extraordinary was this m9. 0 earthquake. In *Proceedings, 4th IASPEI/IAEE International Symposium*.

Kayen, R. E. and Mitchell, J. K. (1997). Assessment of liquefaction potential during earthquakes by arias intensity. *Journal of Geotechnical and Geoenvironmental Engineering*, 123(12):1162–1174.

Kishida, H. (1969). Characteristics of liquefied sands during mino-owari, tohnankai and fukui earthquakes. *Soils and Foundations*, 9(1):75–92.

Kiyota, T., Ikeda, T., Konagai, K., and Shiga, M. (2017). Geotechnical damage caused by the 2016 kumamoto earthquake, japan. *International Journal of Geoengineering Case Histories*, 4(2):78–94.

Koester, J. P. (1994). The influence of fines type and content on cyclic strength. In *Ground failures under seismic conditions*, pages 17–33. ASCE.

Kokusho, T. (1980). Cyclic triaxial test of dynamic soil properties for wide strain range. *Soils and foundations*, 20(2):45–60.

Konstadinou, M. and Georgiannou, V. (2014). Prediction of pore water pressure generation leading to liquefaction under torsional cyclic loading. *Soils and Foundations*, 54(5):993–1005.

Kotha, S. R., Cotton, F., and Bindi, D. (2018). A new approach to site classification: Mixed-effects ground motion prediction equation with spectral clustering of site amplification functions. *Soil Dynamics and Earthquake Engineering*, 110:318–329.

Kramer, S. and Elgamal, A. (2001). Modeling soil liquefaction hazards for performance based earthquake engineering. report 2001/13, pacific earthquake engineering research center. *University of California, Berkeley*.

Kramer, S. L. (1996). *Geotechnical earthquake engineering*. Pearson Education India.

Kramer, S. L. and Seed, H. B. (1988). Initiation of soil liquefaction under static loading conditions. *Journal of Geotechnical Engineering*, 114(4):412–430.

Kuerbis, R., Negussey, D., and Vaid, Y. (1988). Effect of gradation and fines content on the undrained response of sand. *Geotechnical special publication*, (21):330–345.

Kutter, B. L., Carey, T. J., Hashimoto, T., Zeghal, M., Abdoun, T., Kokkali, P., Madabhushi, G., Haigh, S. K., d'Arezzo, F. B., Madabhushi, S., et al. (2018). Leap-gwu-2015 experiment specifications, results, and comparisons. *Soil Dynamics and Earthquake Engineering*, 113:616–628.

Kutter, B. L., Carey, T. J., Stone, N., Bonab, M. H., Manzari, M. T., Zeghal, M., Escoffier, S., Haigh, S. K., Madabhushi, G. S., Hung, W.-Y., et al. (2020). Leap-ucd-2017 v. 1.01 model specifications. In *Model Tests and Numerical Simulations of Liquefaction and Lateral Spreading*, pages 3–29. Springer.

Ladd, R. (1978). Preparing test specimens using undercompaction. *Geotechnical testing journal*, 1(1):16–23.

Lade, P. V. (1992). Static instability and liquefaction of loose fine sandy slopes. *Journal of Geotechnical Engineering*, 118(1):51–71.

Lade, P. V. (1993). Initiation of static instability in the submarine nerlerk berm. *Canadian Geotechnical Journal*, 30(6):895–904.

Lade, P. V. and Ibsen, L. B. (1997). A study of the phase transformation and the characteristic lines of sand behaviour. In *Proc. Int. Symp. on Deformation and Progressive Failure in Geomechanics, Nagoya*, pages 353–359.

Lade, P. V., Liggio, C., Yamamuro, J. A., et al. (1998). Effects of non-plastic fines on minimum and maximum void ratios of sand. *Geotechnical testing journal*, 21:336–347.

Lade, P. V., Nelson, R. B., and Ito, Y. M. (1988). Instability of granular materials with nonassociated flow. *Journal of engineering mechanics*, 114(12):2173–2191.

Lade, P. V. and Pradel, D. (1990). Instability and plastic flow of soils. i: Experimental observations. *Journal of engineering mechanics*, 116(11):2532–2550.

Lade, P. V. and Yamamuro, J. A. (1997). Effects of nonplastic fines on static liquefaction of sands. *Canadian Geotechnical Journal*, 34(6):918–928.

Lashkari, A. (2016). Prediction of flow liquefaction instability of clean and silty sands. *Acta Geotechnica*, 11(5):987–1014.

Lee, K. L. (1965). *Triaxial compressive strength of saturated sand under seismic loading conditions*. PhD thesis, University of California, Berkeley.

Lee, K. L. and Albaisa, A. (1974). Earthquake induced settlements in saturated sands. *Journal of Geotechnical and Geoenvironmental Engineering*, 100(Proc Paper 10496).

Leong, W., Chu, J., and Teh, C. (2000). Liquefaction and instability of a granular fill material. *Geotechnical Testing Journal*, 23(2):178–192.

Li, X.-S. and Wang, Y. (1998). Linear representation of steady-state line for sand. *Journal of geotechnical and geoenvironmental engineering*, 124(12):1215–1217.

Lin, M.-L., Huang, T.-H., and You, J.-C. (1996). The effects of frequency on damping properties of sand. *Soil dynamics and earthquake engineering*, 15(4):269–278.

Ling, Y. (1992). Liquefaction of granular soils with non-cohesive and cohesive fines. In *Proceedings of the Tenth World Conference on Earthquake Engineering: 19-24 July 1992, Madrid, Spain*, volume 3, page 1491. CRC Press.

Liu, X. and Yang, J. (2018). Shear wave velocity in sand: effect of grain shape. *Géotechnique*, 68(8):742–748.

Lombardi, D., Bhattacharya, S., and Wood, D. M. (2013). Dynamic soil–structure interaction of monopile supported wind turbines in cohesive soil. *Soil Dynamics and Earthquake Engineering*, 49:165–180.

Luong, M. (1978). Etat caractéristique du sol. *Compte Rendu del'Académie des Sciences*, 287:305.

Luzi, L., Puglia, R., Pacor, F., Gallipoli, M., Bindi, D., and Mucciarelli, M. (2011). Proposal for a soil classification based on parameters alternative or complementary to vs, 30. *Bulletin of Earthquake Engineering*, 9(6):1877–1898.

Manzari, M. T. and Dafalias, Y. F. (1997). A critical state two-surface plasticity model for sands. *Geotechnique*, 47(2):255–272.

Manzari, M. T., El Ghoraiby, M., Zeghal, M., Kutter, B. L., Arduino, P., Barrero, A. R., Bilotta, E., Chen, L., Chen, R., Chiaradonna, A., et al. (2020). Leap-2017 simulation exercise: Calibration of constitutive models and simulation of the element tests. In *Model Tests and Numerical Simulations of Liquefaction and Lateral Spreading*, pages 165–185. Springer.

Massa, M., Pacor, F., Luzi, L., Bindi, D., Milana, G., Sabetta, F., Gorini, A., and Marcucci, S. (2010). The italian accelerometric archive (itaca): processing of strong-motion data. *Bulletin of Earthquake Engineering*, 8(5):1175–1187.

McGeary, R. (1961). Mechanical packing of spherical particles. *Journal of the American ceramic Society*, 44(10):513–522.

Missoum, H., Belkhatir, M., and Bendani, K. (2013). Undrained shear strength response under monotonic loading of chlef (algeria) sandy soil. *Arabian Journal of Geosciences*, 6(3):615–623.

Mitchell, J. K., Soga, K., et al. (2005). *Fundamentals of soil behavior*, volume 3. John Wiley & Sons New York.

Mohammadi, A. and Qadimi, A. (2015). A simple critical state approach to predicting the cyclic and monotonic response of sands with different fines contents using the equivalent intergranular void ratio. *Acta Geotechnica*, 10(5):587–606.

Montgomery, J., Boulanger, R. W., and Harder Jr, L. F. (2014). Examination of the k σ overburden correction factor on liquefaction resistance. *Journal of Geotechnical and Geoenvironmental Engineering*, 140(12):04014066.

Mucciarelli, M., Gallipoli, M. R., et al. (2006). Comparison between vs30 and other estimates of site amplification in italy. In *First European Conference on Earthquake Engineering and Seismology*.

Mukunoki, T., Kasama, K., Murakami, S., Ikemi, H., Ishikura, R., Fujikawa, T., Yasufuku, N., and Kitazono, Y. (2016). Reconnaissance report on geotechnical damage caused by an earthquake with jma seismic intensity 7 twice in 28 h, kumamoto, japan. *Soils and foundations*, 56(6):947–964.

Murthy, T., Loukidis, D., Carraro, J., Prezzi, M., and Salgado, R. (2007). Undrained monotonic response of clean and silty sands. *Géotechnique*, 57(3):273–288.

Naeini, S. and Baziar, M. (2004). Effect of fines content on steady-state strength of mixed and layered samples of a sand. *Soil Dynamics and Earthquake Engineering*, 24(3):181–187.

Naeini, S. and Ziaie-Moayed, R. (1994). Effect of inter-granular void ratio on undrained shear strength of loose silty sand. *Computer Meth Geom*, 2:135.

Newmark, N. and Hall, W. (1982). Earthquake spectra and design, earthquake engineering research center.

NF-P94-059 (2000). Détermination des masses volumiques minimale et maximale des sols non cohérents. *Reconnaissance et essais, AFNOR*.

Nguyen, T.-K., Benahmed, N., and Hicher, P.-Y. (2017). Determination of the equivalent intergranular void ratio-application to the instability and the critical state of silty sand. In *EPJ Web of Conferences*, volume 140, page 02019. EDP Sciences.

Ni, Q., Tan, T., Dasari, G., and Hight, D. (2004). Contribution of fines to the compressive strength of mixed soils. *Géotechnique*, 54(9):561–569.

NZS (2004). Structural design actions, part 5: Earthquake actions-new zealand.

Ohsaki, Y. (1970). Effects of sand compaction on liquefaction during the tokachioki earthquake. *Soils and Foundations*, 10(2):112–128.

Oztoprak, S. and Bolton, M. (2013). Stiffness of sands through a laboratory test database. *Géotechnique*, 63(1):54–70.

Papadimitriou, A. G., Bouckovalas, G. D., and Dafalias, Y. F. (2001). Plasticity model for sand under small and large cyclic strains. *Journal of Geotechnical and Geoenvironmental Engineering*, 127(11):973–983.

Papadopoulou, A. and Tika, T. (2008). The effect of fines on critical state and liquefaction resistance characteristics of non-plastic silty sands. *Soils and foundations*, 48(5):713–725.

Park, D. and Hashash, Y. M. (2004). Probabilistic seismic hazard analysis with non linear site effects in the mississippi embayment. In *Proceedings of the 13th world conference on earthquake engineering, Vancouver, Paper*, number 1549.

Park, T., Park, D., and Ahn, J.-K. (2015). Pore pressure model based on accumulated stress. *Bulletin of Earthquake Engineering*, 13(7):1913–1926.

Peacock, W. H. and Seed, B. (1968). Sand liquefaction under cyclic loading simple shear conditions. *Journal of Soil Mechanics & Foundations Div.*

PEER (2014). Peer (pacific earthquake engineering research center) ground motion database.

Pitilakis, K., Riga, E., and Anastasiadis, A. (2013). New code site classification, amplification factors and normalized response spectra based on a worldwide ground-motion database. *Bulletin of Earthquake Engineering*, 11(4):925–966.

Pitman, T., Robertson, P., and Sego, D. (1994). Influence of fines on the collapse of loose sands. *Canadian Geotechnical Journal*, 31(5):728–739.

Polito, C. P., Green, R. A., and Lee, J. (2008). Pore pressure generation models for sands and silty soils subjected to cyclic loading. *Journal of Geotechnical and Geoenvironmental Engineering*, 134(10):1490–1500.

Polito, C. P. and Martin, J. R. (2003). A reconciliation of the effects of nonplastic fines on the liquefaction resistance of sands reported in the literature. *Earthquake Spectra*, 19(3):635–651.

Polito, C. P. and Martin II, J. R. (2001). Effects of nonplastic fines on the liquefaction resistance of sands. *Journal of Geotechnical and Geoenvironmental Engineering*, 127(5):408–415.

Porcino, D. D. and Diano, V. (2017). The influence of non-plastic fines on pore water pressure generation and undrained shear strength of sand-silt mixtures. *Soil Dynamics and Earthquake Engineering*, 101:311–321.

Poulos, S. J. (1981). The steady state of deformation. *Journal of Geotechnical and Geoenvironmental Engineering*, 107(ASCE 16241 Proceeding).

Prevost, J. H. (1985). A simple plasticity theory for frictional cohesionless soils. *International Journal of Soil Dynamics and Earthquake Engineering*, 4(1):9–17.

Qadimi, A. and Mohammadi, A. (2014). Evaluation of state indices in predicting the cyclic and monotonic strength of sands with different fines contents. *Soil Dynamics and Earthquake Engineering*, 66:443–458.

Quigley, M. C., Bastin, S., and Bradley, B. A. (2013). Recurrent liquefaction in christchurch, new zealand, during the canterbury earthquake sequence. *Geology*, 41(4):419–422.

Rahman, M. M., Baki, M., and Lo, S. (2014a). Prediction of undrained monotonic and cyclic liquefaction behavior of sand with fines based on the equivalent granular state parameter. *International Journal of Geomechanics*, 14(2):254–266.

Rahman, M. M., Cubrinovski, M., and Lo, S. (2012). Initial shear modulus of sandy soils and equivalent granular void ratio. *Geomechanics and Geoengineering*, 7(3):219–226.

Rahman, M. M. and Lo, S. (2012). Predicting the onset of static liquefaction of loose sand with fines. *Journal of Geotechnical and Geoenvironmental Engineering*, 138(8):1037–1041.

Rahman, M. M., Lo, S., and Baki, M. A. L. (2011). Equivalent granular state parameter and undrained behaviour of sand–fines mixtures. *Acta Geotechnica*, 6(4):183–194.

Rahman, M. M., Lo, S., and Gnanendran, C. (2008). On equivalent granular void ratio and steady state behaviour of loose sand with fines. *Canadian Geotechnical Journal*, 45(10):1439–1456.

Rahman, M. M., Lo, S.-C., and Dafalias, Y. (2014b). Modelling the static liquefaction of sand with low-plasticity fines. *Géotechnique*, 64(11):881–894.

Rahman, M. M. and Sitharam, T. (2020). Cyclic liquefaction screening of sand with non-plastic fines: Critical state approach. *Geoscience Frontiers*, 11(2):429–438.

Rangaswamy, K., Boominathan, A., and Rajagopal, K. (2010). Influence of initial conditions on liquefaction resistance of silty sands. *Geomechanics and Geoengineering: an International Journal*, 5(3):199–211.

Rees, S. D. (2010). Effects of fines on the undrained behaviour of christchurch sandy soils.

Régnier, J., Bonilla, L.-F., Bard, P.-Y., Bertrand, E., Hollender, F., Kawase, H., Sicilia, D., Arduino, P., Amorosi, A., Asimaki, D., et al. (2016a). International benchmark on numerical simulations for 1d, nonlinear site response (prenolin): Verification phase based on canonical cases. *Bulletin of the Seismological Society of America*, 106(5):2112–2135.

Régnier, J., Bonilla, L.-F., Bard, P.-Y., Bertrand, E., Hollender, F., Kawase, H., Sicilia, D., Arduino, P., Amorosi, A., Asimaki, D., et al. (2018).

Prenolin: International benchmark on 1d nonlinear site-response analysis—validation phase exerciseprenolin: International benchmark on 1d nonlinear site-response analysis—validation phase exercise. *Bulletin of the Seismological Society of America*, 108(2):876–900.

Régnier, J., Bonilla, L. F., Bertrand, E., and Semblat, J.-F. (2014). Influence of the vs profiles beyond 30 m depth on linear site effects: Assessment from the kik-net data. *Bulletin of the Seismological Society of America*, 104(5):2337–2348.

Régnier, J., Cadet, H., and Bard, P.-Y. (2016b). Empirical quantification of the impact of nonlinear soil behavior on site responseempirical quantification of the impact of nonlinear soil behavior on site response. *Bulletin of the Seismological Society of America*, 106(4):1710–1719.

Régnier, J., Cadet, H., Bonilla, L. F., Bertrand, E., and Semblat, J.-F. (2013). Assessing nonlinear behavior of soils in seismic site response: Statistical analysis on kik-net strong-motion data. *Bulletin of the Seismological Society of America*, 103(3):1750–1770.

Rey, J., Faccioli, E., and Bommer, J. J. (2002). Derivation of design soil coefficients (s) and response spectral shapes for eurocode 8 using the european strong-motion database. *Journal of seismology*, 6(4):547–555.

Rollins, K. M., Evans, M. D., Diehl, N. B., and III, W. D. D. (1998). Shear modulus and damping relationships for gravels. *Journal of Geotechnical and Geoenvironmental Engineering*, 124(5):396–405.

Sadrekarimi, A. (2013). Influence of fines content on liquefied strength of silty sands. *Soil Dynamics and Earthquake Engineering*, 55:108–119.

Salgado, R., Bandini, P., and Karim, A. (2000). Shear strength and stiffness of silty sand. *Journal of Geotechnical and Geoenvironmental Engineering*, 126(5):451–462.

Santamarina, J. and Cho, G.-C. (2004). Soil behaviour: The role of particle shape. In *Advances in geotechnical engineering: The Skempton conference: Proceedings of a three day conference on advances in geotechnical engineering, organised by the Institution of Civil Engineers and held at the Royal Geographical Society, London, UK, on 29–31 March 2004*, pages 604–617. Thomas Telford Publishing.

Santisi d'Avila, M. P., Lenti, L., Martino, S., and Romeo, R. W. (2019). Nonlinear numerical simulation of the soil seismic response to the 2012 mw

5.9 emilia earthquake considering the variability of the water table position. *Bulletin of the Seismological Society of America*, 109(2):505–524.

Santisi d'Avila, M. P., Lenti, L., and Semblat, J.-F. (2012). Modelling strong seismic ground motion: three-dimensional loading path versus wavefield polarization. *Geophysical Journal International*, 190(3):1607–1624.

Santisi d'Avila, M. P., Pham, V. A., Lenti, L., and Semblat, J.-F. (2018). Extended iwan-iai (3dxii) constitutive model for 1-directional 3-component seismic waves in liquefiable soils: applicationto the kushiro site (japan). *Geophysical Journal International*, 215(1):252–266.

Santisi d'Avila, M. P., Semblat, J.-F., and Lenti, L. (2013). Strong ground motion in the 2011 tohoku earthquake: A one-directional three-component modeling. *Bulletin of the Seismological Society of America*, 103(2B):1394–1410.

Sassa, S. and Takagawa, T. (2019). Liquefied gravity flow-induced tsunami: first evidence and comparison from the 2018 indonesia sulawesi earthquake and tsunami disasters. *Landslides*, 16(1):195–200.

Seed, B. (1979). Soil liquefaction and cyclic mobility evalution for level ground during earthquakes. *Journal of Geotechnical and Geoenvironmental Engineering*, 105(ASCE 14380).

Seed, B. and Lee, K. L. (1966). Liquefaction of saturated sands during cyclic loading. *Journal of Soil Mechanics & Foundations Div*, 92(ASCE# 4972 Proceeding).

Seed, H. B. (1983). Earthquake resistant design of earthdams. In *Proceedings of the symposium on seismic design of embankments and caverns*, page 41–46. ASCE.

Seed, H. B., Martin, P. P., and Lysmer, J. (1975). *The generation and dissipation of pore water pressures during soil liquefaction*. College of Engineering, University of California.

Seed, H. B., Wong, R. T., Idriss, I., and Tokimatsu, K. (1986). Moduli and damping factors for dynamic analyses of cohesionless soils. *Journal of geotechnical engineering*, 112(11):1016–1032.

Semblat, J. F., Kham, M., Parara, E., Bard, P.-Y., Pitilakis, K., Makra, K., and Raptakis, D. (2005). Seismic wave amplification: Basin geometry vs soil layering. *Soil dynamics and earthquake engineering*, 25(7-10):529–538.

Seyhan, E. and Stewart, J. P. (2014). Semi-empirical nonlinear site amplification from nga-west2 data and simulations. *Earthquake Spectra*, 30(3):1241–1256.

Seyhan, E., Stewart, J. P., Ancheta, T. D., Darragh, R. B., and Graves, R. W. (2014). Nga-west2 site database. *Earthquake Spectra*, 30(3):1007–1024.

Shen, C., Vrymoed, J., and Uyeno, C. (1997). The effects of fines on liquefaction of sands. proceedings of the 9th international conference on soil mech.. and foundation eng.

Shengcong, F. and Tatsuoka, F. (1984). Soil liquefaction during haicheng and tangshan earthquake in china; a review. *Soils and foundations*, 24(4):11–29.

Shibuya, S., Hwang, S., and Mitachi, T. (1997). Elastic shear modulus of soft clays from shear wave velocity measurement. *Geotechnique*, 47(3):593–601.

Skempton, A. (1954). The pore-pressure coefficients a and b: Geotechnique. *Institutions of Civil Engineers, Great Britain*, 4:143–147.

Sladen, J., D'hollander, R., and Krahn, J. (1985). The liquefaction of sands, a collapse surface approach. *Canadian geotechnical journal*, 22(4):564–578.

Stamatopoulos, C. A. (2010). An experimental study of the liquefaction strength of silty sands in terms of the state parameter. *Soil Dynamics and Earthquake Engineering*, 30(8):662–678.

Stambouli, A. B., Zendagui, D., Bard, P.-Y., and Derras, B. (2017). Deriving amplification factors from simple site parameters using generalized regression neural networks: implications for relevant site proxies. *Earth, Planets and Space*, 69(1):99.

Steidl, J. H. (2000). Site response in southern california for probabilistic seismic hazard analysis. *Bulletin of the Seismological Society of America*, 90(6B):S149–S169.

Tao, M., FUGUEROA, J., and Saada, A. (2004). Influence of nonplastic fines content on the liquefaction resistance of soils in terms of the unit energy. In *Cyclic behaviour of soils and liquefaction phenomena*, pages 223–231.

Terzaghi, K. (1943). Theoretical soil mechanics, wiley, new york.

Thevanayagam, S. (1998). Effect of fines and confining stress on undrained shear strength of silty sands. *Journal of Geotechnical and Geoenvironmental Engineering*, 124(6):479–491.

Thevanayagam, S. (2007). Intergrain contact density indices for granular mixes—i: Framework. *Earthquake engineering and engineering vibration*, 6(2):123.

Thevanayagam, S., Fiorillo, M., and Liang, J. (2000). Effect of non-plastic fines on undrained cyclic strength of silty sands. In *Soil Dynamics and Liquefaction 2000*, pages 77–91.

Thevanayagam, S. and Martin, G. (2002). Liquefaction in silty soils-screening and remediation issues. *Soil Dynamics and Earthquake Engineering*, 22(9-12):1035–1042.

Throncoso, J. and Verdugo, R. (1985). Silt content and dynamic behavior of tailing sands. In *International conference on soil mechanics and foundation engineering. 11*, pages 1311–1314.

Tohno, I. and Yasuda, S. (1981). Liquefaction of the ground during the 1978 miyagiken-oki earthquake. *Soils and Foundations*, 21(3):18–34.

Tokimatsu, K., Yamazaki, T., and Yoshimi, Y. (1986). Soil liquefaction evaluations by elastic shear moduli. *Soils and Foundations*, 26(1):25–35.

Tokimatsu, K. and Yoshimi, Y. (1983). Empirical correlation of soil liquefaction based on spt n-value and fines content. *Soils and Foundations*, 23(4):56–74.

Towhata, I. and Ishihara, K. (1985). Shear work and pore water pressure in undrained shear. *Soils and foundations*, 25(3):73–84.

Vaid, Y. and Chern, J. (1985). Cyclic and monotonic undrained response of saturated sands. In *Advances in the art of testing soils under cyclic conditions*, pages 120–147. ASCE.

Vaid, Y., Chung, E., and Kuerbis, R. (1990a). Stress path and steady state. *Canadian Geotechnical Journal*, 27(1):1–7.

Vaid, Y., Fisher, J., Kuerbis, R., and Negussey, D. (1990b). Particle gradation and liquefaction. *Journal of Geotechnical Engineering*, 116(4):698–703.

Vaid, Y. and Sivathayalan, S. (1996). Static and cyclic liquefaction potential of fraser delta sand in simple shear and triaxial tests. *Canadian Geotechnical Journal*, 33(2):281–289.

Vaid, Y. and Thomas, J. (1995). Liquefaction and postliquefaction behavior of sand. *Journal of Geotechnical Engineering*, 121(2):163–173.

Vaid, Y. P., Byrne, P., and Hughes, J. (1981). Dilation angle and liquefaction potential.

Vaid, Y. P., Chern, J. C., and Tumi, H. (1985). Confining pressure, grain angularity, and liquefaction. *Journal of Geotechnical Engineering*, 111(10):1229–1235.

Verdugo, R. (1992). *Characterization of sandy soil behavior under large deformation*. PhD thesis, University of Tokyo.

Verdugo, R. and Ishihara, K. (1996). The steady state of sandy soils. *Soils and foundations*, 36(2):81–91.

Wang, Y.-H. and Santamarina, J. (2007). Attenuation in sand: an exploratory study on the small-strain behavior and the influence of moisture condensation. *Granular Matter*, 9(6):365.

White, H. and Walton, S. (1937). Particle packing and particle shape. *Journal of the American Ceramic Society*, 20(1-12):155–166.

Wichtmann, T. and Triantafyllidis, T. (2004). Influence of a cyclic and dynamic loading history on dynamic properties of dry sand, part i: cyclic and dynamic torsional prestraining. *Soil Dynamics and Earthquake Engineering*, 24(2):127–147.

Wichtmann, T. and Triantafyllidis, T. (2014). Stiffness and damping of clean quartz sand with various grain-size distribution curves. *Journal of Geotechnical and Geoenvironmental Engineering*, 140(3):06013003.

Wood, D. M. (1990). *Soil behaviour and critical state soil mechanics*. Cambridge university press.

Xenaki, V. and Athanasopoulos, G. (2003). Liquefaction resistance of sand–silt mixtures: an experimental investigation of the effect of fines. *Soil Dynamics and Earthquake Engineering*, 23(3):1–12.

Yamamuro, J. A. and Lade, P. V. (1997). Static liquefaction of very loose sands. *Canadian Geotechnical Journal*, 34(6):905–917.

Yamamuro, J. A. and Lade, P. V. (1998). Steady-state concepts and static liquefaction of silty sands. *Journal of geotechnical and geoenvironmental engineering*, 124(9):868–877.

Yang, J. (2002). Non-uniqueness of flow liquefaction line for loose sand. *Géotechnique*, 52(10):757–760.

Yang, J. and Luo, X. (2015). Exploring the relationship between critical state and particle shape for granular materials. *Journal of the Mechanics and Physics of Solids*, 84:196–213.

Yang, J. and Wei, L. (2012). Collapse of loose sand with the addition of fines: the role of particle shape. *Géotechnique*, 62(12):1111–1125.

Yang, S., Sandven, R., and Grande, L. (2006). Steady-state lines of sand–silt mixtures. *Canadian Geotechnical Journal*, 43(11):1213–1219.

Yang, Z., Elgamal, A., and Parra, E. (2003). Computational model for cyclic mobility and associated shear deformation. *Journal of Geotechnical and Geoenvironmental Engineering*, 129(12):1119–1127.

Yasuda, S., Harada, K., Ishikawa, K., and Kanemaru, Y. (2012). Characteristics of liquefaction in tokyo bay area by the 2011 great east japan earthquake. *Soils and Foundations*, 52(5):793–810.

Yilmaz, Y., Mollamahmutoglu, M., Ozaydin, V., and Kayabali, K. (2008). Experimental investigation of the effect of grading characteristics on the liquefaction resistance of various graded sands. *Engineering geology*, 100(3-4):91–100.

Yin, Z.-Y., Zhao, J., and Hicher, P.-Y. (2014). A micromechanics-based model for sand-silt mixtures. *International journal of solids and structures*, 51(6):1350–1363.

Yokota, K., Imai, T., and Konno, M. (1981). Dynamic deformation characteristics of soils determined by laboratory tests. *OYO Tec. Rep*, 3:13–37.

Yoshida, N., Tokimatsu, K., Yasuda, S., Kokusho, T., and Okimura, T. (2001). Geotechnical aspects of damage in adapazari city during 1999 kocaeli, turkey earthquake. *Soils and foundations*, 41(4):25–45.

Yoshimine, M. and Ishihara, K. (1998). Flow potential of sand during liquefaction. *Soils and foundations*, 38(3):189–198.

Yoshimine, M., Robertson, P., and Wride, C. (1999). Undrained shear strength of clean sands to trigger flow liquefaction. *Canadian Geotechnical Journal*, 36(5):891–906.

Youd, T., Idriss, I., Andrus, R., Arango, I., Castro, G., Christian, J., Dobry, R., Finn, W., Harder Jr, L., Hynes, M., et al. (2001). Liquefaction resistance of soil: Summary report from the 1996 nceer and 1998 nceer. In *NSF Workshop on Evaluation of Liquefaction Resistance of Soils. Journal of Geotechnical and Geoenvironmental Engineering*, volume 124.

Youd, T. L. and Idriss, I. M. (2001). Liquefaction resistance of soils: summary report from the 1996 nceer and 1998 nceer/nsf workshops on evaluation of liquefaction resistance of soils. *Journal of geotechnical and geoenvironmental engineering*, 127(4):297–313.

Yuan, H., Yang, S. H., Andrus, R. D., and Juang, C. H. (2004). Liquefaction-induced ground failure: a study of the chi-chi earthquake cases. *Engineering Geology*, 71(1-2):141–155.

Zhao, J. X., Irikura, K., Zhang, J., Fukushima, Y., Somerville, P. G., Asano, A., Ohno, Y., Oouchi, T., Takahashi, T., and Ogawa, H. (2006). An empirical site-classification method for strong-motion stations in japan using h/v response spectral ratio. *Bulletin of the Seismological Society of America*, 96(3):914–925.

Zhu, C., Pilz, M., and Cotton, F. (2020). Which is a better proxy, site period or depth to bedrock, in modelling linear site response in addition to the average shear-wave velocity? *Bulletin of Earthquake Engineering*, 18(3):797–820.

Zlatović, S. and Ishihara, K. (1995). On the influence of nonplastic fines on residual strength. In *First International Conference on Earthquake Geotechnical Engineering*, volume 95, pages 239–244.